

© 2020 Richard Dicky Liu

CUBIC PHASE GALLIUM NITRIDE PHOTONICS INTEGRATED ON
SILICON(100) FOR NEXT-GENERATION SOLID STATE LIGHTING

BY

RICHARD DICKY LIU

DISSERTATION

Submitted in partial fulfillment of the requirements
for the degree of Doctor of Philosophy in Electrical and Computer Engineering
in the Graduate College of the
University of Illinois at Urbana-Champaign, 2020

Urbana, Illinois

Doctoral Committee:

Assistant Professor Can Bayram, Chair
Professor Lynford Goddard
Professor John Dallesasse
Associate Professor Minjoo Lawrence Lee
Dr. Anthony Yu, NASA Goddard Space Flight Center

ABSTRACT

Semiconductors made of gallium nitride (GaN) and its compounds (AlIn-GaN) have transformed the visible light emitting diode (LED) industry thanks to their direct bandgap across the entire visible and ultraviolet spectra. Despite its success, the conventional hexagonal-phase GaN has fundamental disadvantages in performance and cost that hinder market adoption. These include: internal polarization field (\sim MV/cm²), high acceptor activation energy (260 meV), low hole mobility (20 cm²/V), and expensive substrates (Al₂O₃, SiC). Gallium nitride also crystallizes in the cubic crystal that has a higher degree of symmetry. This leads to some advantageous properties for light emitting applications: polarization-free, lower acceptor energy (200 meV), and higher hole mobility (150 cm²/V). These advantages are critical for the development of the next-generation solid state lighting. Difficulty in its synthesis stemming from the large crystal lattice mismatch, chemical incompatibility, and phase metastability has prohibited the growth of high-quality semiconductor crystals that are device-worthy.

This thesis explores a method of synthesizing phase-pure, high-quality cubic GaN crystals on nanopatterned Si(100) substrates via hexagonal-to-cubic phase transition, and the thesis presents a comprehensive material characterization of the crystals. Crystal growth geometry modeling of GaN on nanopatterned Si(100) substrates is used to estimate the necessary patterning parameters to facilitate complete phase transition. The cubic GaN material is then studied using structural characterization techniques including scanning electron microscopy, electron backscatter diffraction, and transmission electron microscopy. The carrier recombination properties are studied using photoluminescence, Raman spectroscopy, and cathodoluminescence. The cubic GaN synthesized using the phase transition method on carefully patterned Si(100) substrates is shown to be phase-pure, defect-free, and optically superior. Material properties such as internal quantum efficiency,

Varshni coefficients, and defect levels are extracted from the experiments.

Other work on hexagonal GaN light emitters on silicon substrates, chamber conditioning for metalorganic chemical vapor deposition of III-nitrides, and space-based laser instruments for NASA missions is also discussed. Class lab module development and outreach activities are included.

To those fighting COVID-19, systemic racism, and climate change.

ACKNOWLEDGMENTS

To begin, I must express my sincerest gratitude to my advisor, Associate Professor Can Bayram, who has put the well-being and success of the graduate careers of his advisees as the first priority through the many emails about external opportunities, check-ins, and extraordinary ideas.

I would like to acknowledge my family, professors, colleagues, friends, and Claire for their never-ending support and encouragement. I would also like to acknowledge and thank Seattle Genetics, Inc., for AdcetrisTM (Brentuximab Vedotin) and Loyola University Medical Center. My work here would not be possible without them.

I would like to acknowledge Dr. James Mabon, Dr. Julio Soares, and Dr. Changqiang Chen of the University of Illinois at Urbana-Champaign, and Dr. Richard Schaller of Argonne National Laboratory, for sharing and teaching their expertise on conducting scientific research.

I would like to acknowledge the education, training, and support I have received from the Lasers and Optics branch at NASA Goddard Space Flight Center, especially from Dr. Anthony Yu and Molly Fahey. They have given me the once-in-a-lifetime opportunity to work on a cutting edge space scientific instrument.

This work was supported by the National Science Foundation Faculty Early Career Development (CAREER) Program under award number NSF-ECCS-16-52871, and by the NASA Space Technology Research Fellowship (NSTRF17) under award number 80NSSC17K0150. Use of the Center for Nanoscale Materials, Argonne National Laboratory, an Office of Science user facility, is supported by the U. S. Department of Energy, Office of Science, Office of Basic Energy Sciences, under Contract number DE-AC02-06CH11357. I also acknowledge the UIUC-MRL seed project number 8016 for structural microanalysis.

TABLE OF CONTENTS

CHAPTER 1	INTRODUCTION	1
1.1	Motivation: Solid State Lighting	2
1.2	History of the Semiconductor Gallium Nitride	3
1.3	Overview of the Gallium Nitride Material System	3
1.4	Fundamentals of Light Emitting Diodes	8
1.5	History of the Development of LEDs	10
1.6	Issue with Phosphor Down-converted White LEDs	11
CHAPTER 2	FUNDAMENTALS OF THE CUBIC PHASE GAL- LIUM NITRIDE	18
2.1	Motivation: Advantages of Cubic GaN	18
2.2	History of Cubic Phase GaN Research	21
2.3	Phase Transition of GaN: V-groove Nanopatterns	22
2.4	Phase Transition of GaN: U-groove Nanopatterns	24
CHAPTER 3	FABRICATION AND GROWTH OF CUBIC PHASE GALLIUM NITRIDE	26
3.1	Hexagonal-to-cubic Phase Transition	26
3.2	Dimension Definition of U-Groove Nanopatterns	27
3.3	Modeling of U-groove Nanopatterns for Complete Phase Transition	29
3.4	Fabrication of U-groove Nanopatterns on Si(100) Substrates	31
CHAPTER 4	STRUCTURAL CHARACTERIZATION OF CU- BIC PHASE GALLIUM NITRIDE	37
4.1	Scanning Electron Microscopy and Atomic Force Microscopy	37
4.2	Transmission and Scanning Transmission Electron Microscopy Study	42
4.3	Electron Backscatter Diffraction and Raman Spectroscopy	47
CHAPTER 5	FUNDAMENTAL OPTICAL TRANSITIONS IN PHASE TRANSITION CUBIC GALLIUM NITRIDE	52
5.1	Room Temperature Photoluminescence	52
5.2	Temperature-dependent Cathodoluminescence	55
5.3	Time-Resolved Photoluminescence	69

CHAPTER 6	EFFECT OF SUBSTRATES AND STRAIN ON HEXAGONAL PHASE INGAN EMITTERS ON SILICON(111) . .	73
6.1	Introduction	73
6.2	Experimental Approach	74
6.3	Photoluminescence Intensity and Uniformity Correlation . . .	76
6.4	Crystallinity and Strain Study	79
6.5	Internal Quantum Efficiency and Carrier Lifetime Calculations	85
6.6	Discussion	93
CHAPTER 7	MOCVD CHAMBER CONDITIONING	94
7.1	Introduction	94
7.2	Structural Characterization	96
7.3	Optical Characterization	100
7.4	Data Analysis	104
7.5	Conclusion	109
CHAPTER 8	LASER DESIGNS FOR SPACE-BASED SCIENTIFIC EXPERIMENTS AND APPLICATIONS	110
8.1	Introduction: Ultraviolet Laser	110
8.2	Laser Design	111
8.3	Laser Performance	113
8.4	Laser Power Modulation	117
8.5	Beam Steering	117
CHAPTER 9	OUTREACH ACTIVITIES AND COURSE DEVELOPMENT	121
9.1	Course Development	121
9.2	Research Experience for Undergraduates	124
9.3	Research Experience for Teachers	125
9.4	Intra-Institutional Educational Outreach	125
CHAPTER 10	SUMMARY AND FUTURE WORK	127
10.1	Conclusion	127
10.2	Future Work	128
REFERENCES	132
APPENDIX A	INSTRUMENTS AND EQUIPMENT	149
A.1	X-Ray Diffraction	149
A.2	Reactive Ion Etching	152
A.3	Dynatex DX-III Scribe Breaker	154
A.4	Scanning Electron Microscopy and Electron Backscatter Diffraction	157
A.5	Silicon Anisotropic Etching Recipe	159
A.6	KOH Etch Setup with Temperature Feedback Loop	161

A.7	Atomic Force Microscopy	162
A.8	Transmission Electron Microscopy	162
A.9	Raman Spectroscopy	163
A.10	Cathodoluminescence	164
A.11	Photoluminescence	165
A.12	Cryo-Photoluminescence	167
A.13	Time-resolved Photoluminescence	169
APPENDIX B COURSE LAB MODULES		171
B.1	Lab 1: NanoLab Walkthrough and Safety	171
B.2	Lab 2: Scanning Electron Microscopy	173
B.3	Lab 3: Light Emitting Diodes 1	176
B.4	Fab 4: LED Temperature and Efficiency Droop	181
B.5	Fab 5: Solar Cells	184
B.6	Fab 6: Design of Experiment: Temperature Dependence of Solar Cells	186

CHAPTER 1

INTRODUCTION

Research in photonics aims to understand the physics of the generation and detection of light in semiconductors and to use engineering measures to manipulate these materials to produce light in the desired wavelength at a high efficiency. Since the invention of the blue light emitting diode (LED) in the 1990s, gallium nitride-based photonic devices have revolutionized the light industry by providing an energy-efficient general lighting source. The cost of these devices is still relatively high, and prohibits their market-wide adoption to supplant the conventional light sources such as incandescent light bulbs and compact fluorescent lamps. For the next advancement in the field of gallium nitride-based photonics, a significant cost reduction is required. This thesis discusses a novel approach to synthesize a different photonic semiconductor material, cubic phase gallium nitride, to supersede the conventional hexagonal gallium nitride as the semiconductor of choice for general lighting. The growth of cubic phase gallium nitride is pursued via modeling and extensive structural and optical characterization.

This doctoral thesis is divided into nine chapters as follows: Chapter 1 introduces the history and the physics of LEDs beginning with the invention of the first visible LED by Prof. Nick Holonyak Jr. This is followed by a summary and overview of the semiconductor material system contrasting the differences between hexagonal (h-) and cubic (c-) phase gallium nitride (GaN), and the conventional method of obtaining c-GaN and its disadvantages. Finally, the novel approach of this thesis to the synthesis of c-GaN is discussed. In Chapter 2, the proposed solution, the cubic phase GaN, is introduced.

In Chapter 3, the growth dynamics and crystallographic modeling are presented to predict and estimate the conditions for optimal c-GaN growth. In Chapter 4, structural analysis and phase purity investigation of the phase transition c-GaN are explored extensively to demonstrate the reliability and

quality of this new technology. In Chapter 5, optical properties of the material are studied to document the emission characteristics of the c-GaN obtained through this approach and to compare it against other methods to quantify the gain in performance. In Chapter 6, conventional hexagonal phase LEDs are grown on Si(111) substrates as a benchmark for III-nitride photonic devices on silicon, and comparison between these devices and those grown on the industry-standard sapphire substrates is carried out. In Chapter 7, optimization of the metalorganic vapor deposition for conventional LED growth using Cp_2Mg conditioning is carried out. In Chapter 8, ultraviolet laser construction for satellite- and lander-based space missions conducted at the National Aeronautics and Space Administration Goddard Space Flight Center is discussed. In Chapter 9, photonic outreach activities, including mentorship and accomplishments, are outlined to show the broader impact of the work completed in this doctoral thesis. In Chapter 10, a summary of the work accomplished and potential future research directions are presented.

1.1 Motivation: Solid State Lighting

The white light emitting diode (LED) has transformed lighting technology since the beginning of the 21st century. The solid state devices are capable of emitting light in the visible and near-visible range for a wide range of applications: handheld flash lamps, communication, medical, dental, sanitation, and general lighting. Solid state devices are significantly more power efficient than the conventional light sources such as the incandescent bulbs and compact fluorescent lamps, and simultaneously more compact, robust, and long-lasting due to their design and the lack of glass, high-voltage circuits, and high-temperature filaments. By virtue of their high efficiency, supplanting the conventional light sources with LEDs can curtail the energy consumption and greenhouse emission. The US Department of Energy estimates an annual saving of \$50 billion US dollars per year and an energy saving of 5.1 quadrillion BTU by 2035. As of 2019, solid state general lighting has a market penetration of $\sim 30\%$ in the outdoor applications, and only $\sim 12\%$ in the more cost-conscious indoor market. The biggest hurdle to a rapid market adoption of LED as the source for lighting is the high upfront cost, which is the result of the expensive engineering solutions devised to

overcome the material limitations of the GaN semiconductor at the core of these LEDs.

1.2 History of the Semiconductor Gallium Nitride

The first successful growth of gallium nitride was accomplished in 1932 using gallium tribromide and dry ammonia gas [1]. In 1969, single crystalline GaN was synthesized on single crystalline c-plane sapphire substrates using vapor-phase growth with Ga-halide and ammonia [2]. It exhibited a direct bandgap at 3.39 eV; other properties such as lattice constants, coefficient of thermal expansion, chemical stability (water, acid and base insolubility) etc. were also reported. The material was shown to be highly n-type (electron concentration $> 10^{19} \text{ cm}^{-2}$) due to the high concentration of nitrogen vacancy. However, the usefulness of the material as a light emitter was hindered by early researchers' inability to grow high-quality crystals and to p-dope the material.

In 1986, crack-free GaN was demonstrated on sapphire by using an AlN nucleation layer and metalorganic chemical vapor deposition (MOCVD) [3]. The novel AlN layer mitigates the large lattice mismatch (-13.8%) between GaN and sapphire, and the optimized MOCVD growth greatly reduced the density of vacancies and thus the free background carrier concentration. A breakthrough in the p-doping technology was made when low-energy electron-beam irradiation was applied to Mg-doped GaN. The irradiation removes the hydrogen passivating the dopants and activates the acceptor [4]. This process was also demonstrated by a straightforward thermal annealing at 700°C in N_2 -ambient in 1992; it achieved a hole concentration of $3 \times 10^{17} \text{ cm}^{-3}$ [5]. These discoveries led to the successful fabrication of the high-efficiency blue LED, which subsequently enabled the white LED and thus the solid state lighting revolution. For this accomplishment, the blue LED inventors were awarded the 2014 Nobel Physics Prize.

1.3 Overview of the Gallium Nitride Material System

Gallium nitride is a binary compound semiconductor with a bandgap energy that is considered “wide”. The semiconductor preferentially crystallizes

Table 1.1: Bandgap (E_g), and lattice constants (a, c) of the two phases of GaN

	E_g (eV) at 300 K	a (Å)	c (Å)
h-InN [6, 7]	0.68	3.545	5.703
h-GaN [6, 8]	3.42	3.189	5.185
h-AlN [6]	6.0	3.112	4.982
c-InN [6, 9]	0.60	4.98	-
c-GaN [10, 11, 8]	3.22	4.50	-
c-AlN [6, 12]	5.3*	4.38	-

*Indirect bandgap

in the hexagonal (wurtzite) phase (h-GaN), although it can also form in the cubic (zinc blende) phase (c-GaN) under specific conditions. Similar to many other III-V semiconductors, GaN can form alloys with Al and In to form $\text{Al}_x\text{Ga}_y\text{In}_{1-x-y}\text{N}$ with a tunable bandgap that spans from the UV-C to infrared range of the optical spectrum (6.0 \sim 0.68 eV). The bandgap energies and lattice constants of the binary hexagonal and cubic III-nitrides are shown in Table 1.1. A ball and stick model of h-GaN is shown in Figure 1.1. The bandgap energies as a function of lattice constant of common III-V semiconductors are shown in Figure 1.2.

Due to its natural tendency to form in the h- phase, GaN-based photonics and electronics are conventionally heterogeneously fabricated on the (0001) c-plane of the thermodynamically stable hexagonal (wurtzite) material phase on non-native substrates such as Al_2O_3 [13], 6H-SiC [14], and Si(111) with multiple graded buffer layers [15, 16]. The use of stable crystal phase ensures the defectivity of the material is minimized.

The wurtzite crystal has a three-fold symmetry in the horizontal plane; the crystal is self-repeating when rotated by 60° in the a-plane. It is, however, not symmetric in the (0001) c-direction; the crystal is different when flipped in the vertical direction. As a result, spontaneous and piezoelectric (when strained) polarization fields are generated [17, 18]. The polarization fields will have the opposite effect on the charge carriers (electrons and holes) due to their opposite charge. The fields will exert a columbic force on the carriers towards the opposite direction along the c-axis. This phenomenon, quantum confined Stark effect (QCSE), spatially separates the carriers. The effect is a reduction in the wave function overlap between the carriers in the quantum

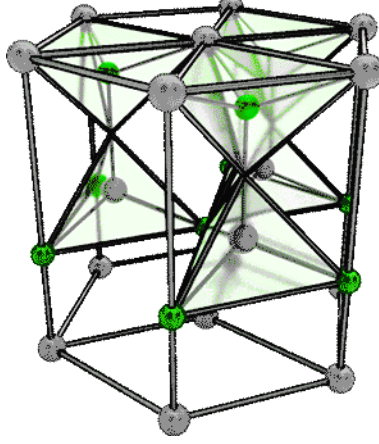


Figure 1.1: Atomic arrangement of h-GaN crystal. Grey atoms are gallium, green atoms are nitrogen. Selected tetrahedrons are shown.

wells of the active regions of a multiple quantum well (MQW) LED. As a consequence of the reduced wavefunction overlap, the radiative recombination rate is reduced, as shown in Figure 1.3 [19]. The reduced recombination rate result in an accumulation of carriers waiting to recombine. Under high injection level, the high concentration of carriers piling up in the opposite corners of the quantum wells is conducive to Auger recombination, which is a nonradiative three-particle recombination mechanism by which an electron in the conduction band is promoted to a higher level by the energy released by a nearby electron-hole recombination. This three-particle process has a third-order dependence on the carrier density and rapidly becomes more prominent in LEDs under a high injection regime that results in the generation of heat instead of photons [20]. The combined effect is an undesired heat-generating recombination mechanism that competes with the intended photon-generating recombination path.

The h-GaN crystal also possesses additional disadvantages that limit the effectiveness and the potential of photonic devices fabricated on this material. The low p-doping efficiency, due to the large activation energy of Mg (260 meV), necessitates a very high doping concentration to achieve a usable hole concentration. The high impurity concentration increases impurity scattering, which is undesirable as it reduces the carrier mobility and increases the ohmic loss of the material.

The large difference in carrier mobility (low mobility symmetry) causes the electrons to overshoot and the holes to undershoot in the active layer,

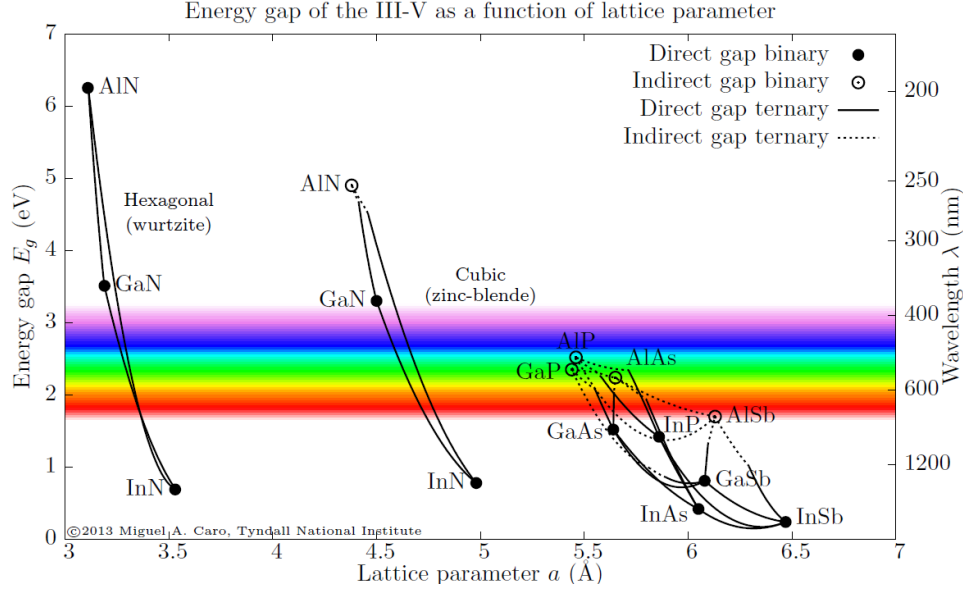


Figure 1.2: Bandgap energies of III-V semiconductors. Reprinted with permission from Á.M. Caro Bayo, Theory of Elasticity and Electric Polarization Effects in the Group-III Nitrides, University College Cork, 2013.

causing uncontrolled recombination to happen outside the active layer. This would result in either the emission of photons in the unintended wavelength or heat in the form of phonons. The countermeasures to mitigate the electron overshoot (more quantum wells) lead to the exacerbation of poor hole injection into the quantum wells, as the low-mobility holes tend to be captured in the first few quantum wells and not evenly across all wells. Concession must be made to accommodate the high degree of mobility asymmetry.

Another issue that is unique to the III-nitride material system is the problem with growing an alloy with high indium content. The larger bandgap in h-GaN means that a higher indium composition is needed to create an InGaN active layer with a suitable bandgap to emit in the green part (~ 555 nm) of the spectrum compared to c-GaN. The high indium content InGaN has been shown to exhibit a high degree of inhomogeneity, which leads to local clusters of lower bandgap, high-indium-content clusters and lowered crystal quality. This is especially problematic in the active layer, in which most carriers are confined.

The material inhomogeneity leads to an elevated level of nonradiative recombination. Increasing current density causes these minima to become sat-

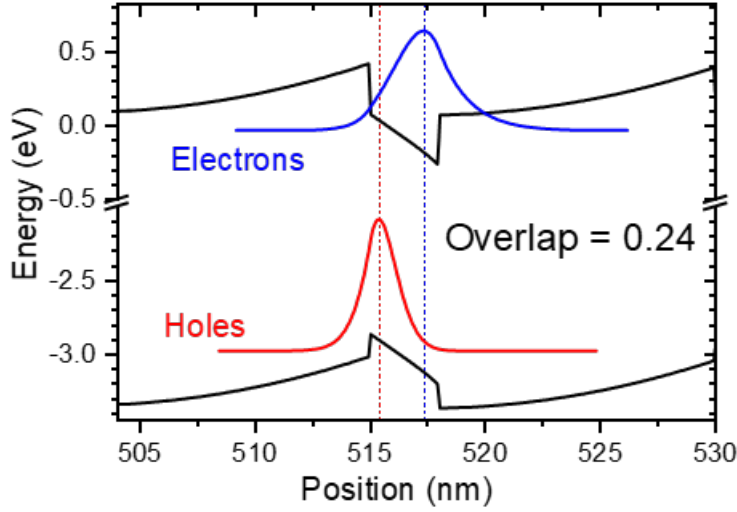


Figure 1.3: LED energy diagram under polarization fields.

urated and the carriers to spill over to the low indium region, which emits in a short wavelength. Due to the larger lattice mismatch with the GaN layer, higher indium content InGaN also induces a stronger piezoelectric field, which further aggravates the detrimental effect of QCSE. A photoluminescence (PL) spectrum of a InGaN/GaN LED is shown in Figure 1.4, which shows the typical behavior of InGaN-based blue emitting multiple quantum wells.

At low carrier injection level by laser (< 1 mW), a Gaussian peak can be observed at 2.8 eV. A low-energy shoulder at 2.74 eV, which indicates a local clustering of indium, is also observed. Under high laser power (> 1 mW), a shoulder appears on the high energy (or blue) side of the main peak at 2.8 eV. At this level, carriers are spilling over from the local energy minima to emit higher photons. Saturation of these minima can be seen through the drastic reduction in the marginal intensity gain of the 2.8 eV peak, as shown in the inset. The wavelength instability in InGaN-based emitters is a manifestation of the inability of the current state-of-the-art growth technology to provide a homogeneous, high-quality InGaN crystal.

For laser applications, the lack of ideal natural cleaving planes that could act as the mirrors of the Fabry-Perot cavity in h-GaN means the laser cavity requires a higher population inversion to reach lasing threshold. The quality factor of the laser cavity obtained from using h-GaN is therefore low. Laser diodes (LDs) based on InGaN must therefore be injected with a much higher

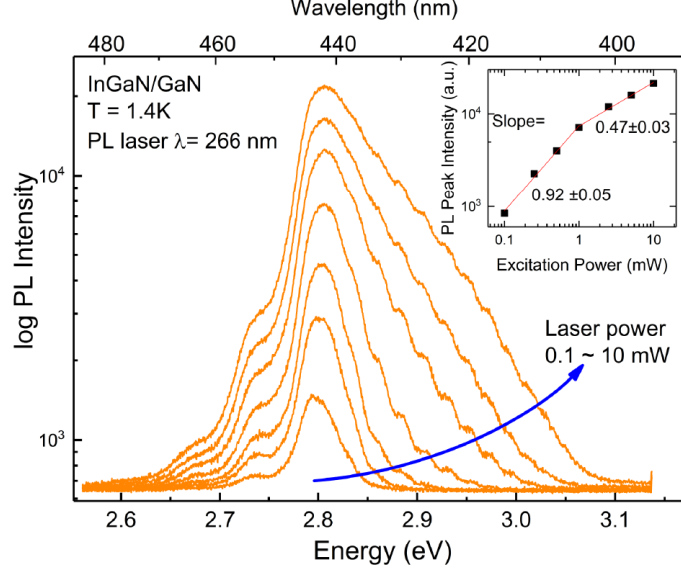


Figure 1.4: Photoluminescence spectrum of an InGaN/GaN blue LED showing the emergence of a “blue shoulder” at higher injection level. The inset shows the 2.8 eV peak intensity as a function of laser power.

current in order to lase.

To circumvent some of these detrimental effects, the non-polar m-plane ($10\bar{1}0$) and the a-plane ($11\bar{2}0$) of the h-GaN crystal have also been explored for polarization-free photonic devices (Figure 1.5). However, GaN grown in this direction suffers from small and prohibitively expensive substrates, lack of scalability and poor material quality. Therefore commercialization of this approach is limited [21, 22]. The optimal design and performance of modern solid state lighting based on the h-GaN semiconductor is therefore constrained by these material properties.

1.4 Fundamentals of Light Emitting Diodes

Light emitting diodes (LEDs) are regular diodes that deploy a direct bandgap semiconductor. They are two-terminal electrical devices that emit light via electroluminescence when a forward electrical current is applied. When electrons and holes recombine, photons are generated. The energy diagram of a blue-emitting GaN-based LED under 3 V of forward bias is shown in Figure 1.6. The LED, similar to a rectifying diode, consists of a p-doped region ($z > 600$ nm) and an n-doped region ($z < 500$ nm) that together form a p-n

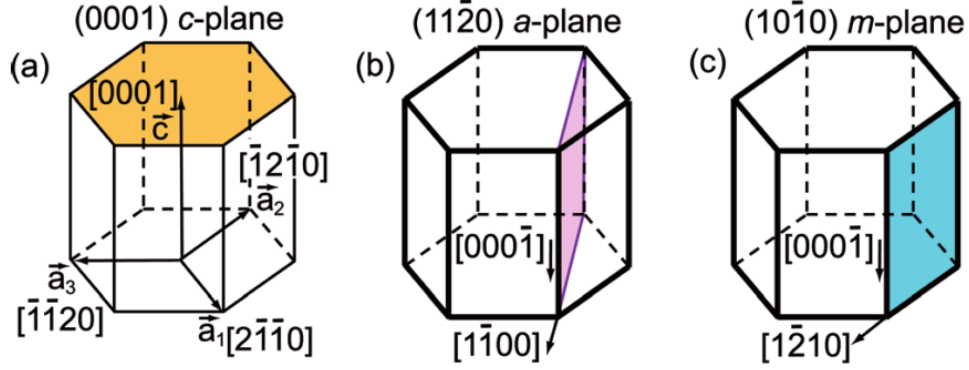


Figure 1.5: Planes of h-GaN. (a) The conventional polar (0001) c-plane, and the non-polar (b) $(11\bar{2}0)$ and (c) $(10\bar{1}0)$ planes of the hexagonal crystals. Reprinted from A.E. Romanov *et al.*, J. Appl. Phys. 109, (2011), with the permission of AIP Publishing.

junction with the addition of an intrinsic region ($500 < z < 600$) that has multiple quantum wells (MQW) made of InGaN with an indium content of 15% and an electron blocking layer (EBL) made of AlGaIn with an aluminum content of 25%.

The injection of holes (red arrow) from the positive terminal on the right and electrons (blue arrow) from the negative terminals on the left causes the carriers to get trapped in the MQW region and recombine, and if the material has a direct bandgap, a photon with its energy corresponding to the transition from conduction band (CB) to valence band (VB) is emitted. The photon emitted from this region is determined by the material properties (bandgap, recombination rate, recombination mechanism) and the confinement energies of the quantum wells. Under a forward electrical bias, the holes and electrons from the p- and n-type regions, respectively, are confined to the active region and undergo either radiative recombination to emit a photon or nonradiative recombination to emit heat in the form of lattice vibration called phonons.

In the III-V semiconductor family, which is composed of elements from column three (Al, Ga, In) and elements from column five (N, P, As, Sb), an array of compound semiconductors can form with a wide range of bandgap and lattice combinations (Figure 1.2). Depending on the combination of the elements, the resulting binary semiconductor can have bandgap energies range from 0.35 eV (InAs) to 6 eV (AlN) with either a direct or indirect bandgap. The combination of two of the elements from either group III or V

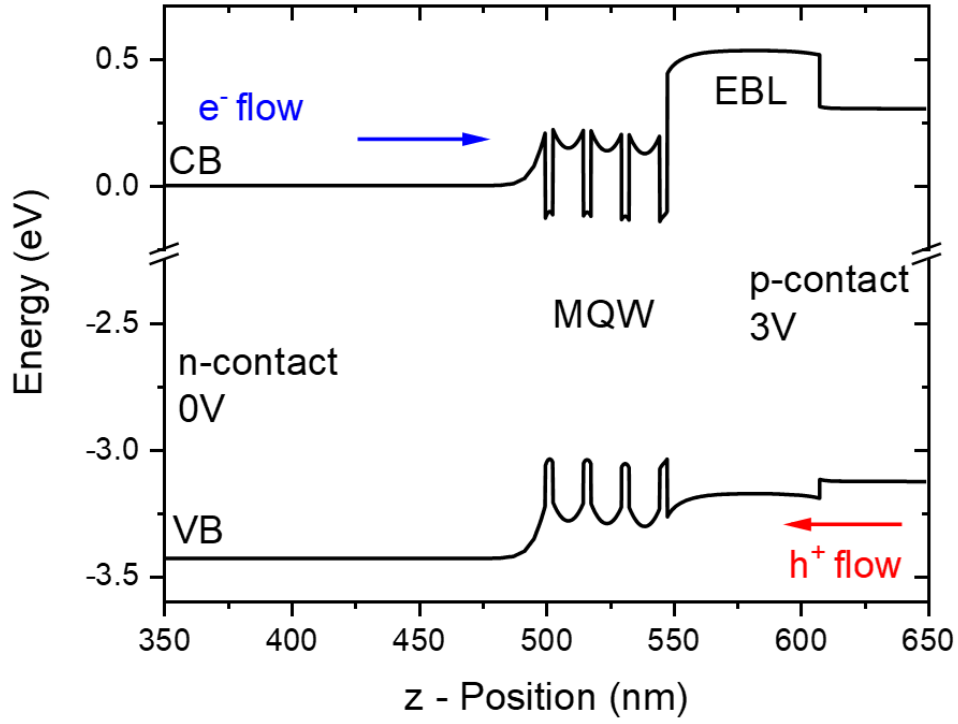


Figure 1.6: Energy diagram of a blue-emitting LED.

and one element from the other group forms a ternary alloy. It will have a bandgap energy that is a nonlinear combination of the bandgap energies of the underlying binary semiconductors. The visible range of photon energies is highlighted by the rainbow to demonstrate the corresponding color.

To make an emitter for the visible range, a semiconductor with bandgap energy in the visible range (400-700 nm or 1.77-3.1 eV) is required. In the III-V family, this leads to III-nitrides (full visible spectrum coverage), and III-arsenides-phosphides (yellow-red). This makes the III-nitrides, and particularly GaN, of great interest, as alloying with a small fraction of In to form $\text{In}_x\text{Ga}_{1-x}\text{N}$ can form an emitter that covers the entire visible range, which would enable full-spectrum solid state lighting.

1.5 History of the Development of LEDs

In 1961, the first LED was invented by James Biard and Gary Pittman at Texas Instruments using GaAs emitting in the infrared (900 nm) [23]. Their LED was based on a semi-insulating GaAs substrate and used a p-

n junction without quantum wells to facilitate the radiative recombination. One year later in 1962 at General Electric, Nick Holonyak, a University of Illinois doctoral graduate, demonstrated the first visible LED and laser diode that emitted in the red using $\text{GaAs}_{1-x}\text{P}_x$, which is the first time a ternary alloy was used. [24]. In 1972, George Craford, also a University of Illinois doctoral graduate, improved the brightness of the red LED by a factor of ten and invented the first yellow LED using GaAsP-based semiconductors [25]. He then continued to develop the AlInGaP-based LEDs that enabled the implementation and commercialization of solid state lighting to replace the conventional red/yellow sources such as incandescent and neon lamps in indicators (e.g. seven-segment digit displays).

On the other side of the visible spectrum, the first high-brightness blue LED was demonstrated by Shuji Nakamura, Isamu Akasaki and Hiroshi Amano in 1994 using the $\text{In}_x\text{Ga}_{1-x}\text{N}$ ternary alloy [26]. Their discovery of p-doping in the nitride material system allowed pn junctions to be formed in the material by activating the magnesium acceptors using electron beam or thermal anneal to remove the passivating hydrogen atoms. The blue LED is of particular importance since the energy of its photons is the highest in the visible range. Generation of white light is made possible by down-converting some of the high-energy blue photons into lower energy green, yellow, and red photons to achieve the full visible spectrum coverage. One of the most successful implementations of this approach is using the yellow phosphor cerium doped yttrium aluminum garnet (Ce:YAG), which has an exceptional performance in terms of blue light absorption and quantum efficiency [27].

1.6 Issue with Phosphor Down-converted White LEDs

The yellow phosphor-converted white LED transformed the general lighting industry by providing a light source that is capable of an electrical luminescence efficacy of 190+ lm/W (theoretical limit ~ 300 for white LED with color rendering index >90). This surpasses the most efficient conventional light source, the sodium vapor lamps. Beyond efficiency, the white LED also has additional advantages such as better color rendition, longer lifetime, robustness, being nonhazardous. The three inventors of the blue LED, Amano, Akasaki, and Nakamura, were awarded the 2014 Nobel Prize in Physics for

their discovery of p-doping of III-nitride semiconductors.

This approach to white solid state lighting is not ideal despite its success. The yellow Ce:YAG phosphor introduces Stokes losses as the blue photons are being converted to yellow photons despite the very high quantum yield ($>97\%$) [28]. This inherent quantum loss ($\sim 20\%$) cannot be mitigated, and a certain ratio of heat is generated. Additionally, the yellow phosphor experiences thermal quenching [29] – loss of efficiency at higher temperature – and chemical instability that reduces the efficiency of down-conversion and luminescence intensity as the device ages. The lack of emission in the red (>650 nm) from the Ce:YAG phosphor makes the color rendition of this approach to general lighting poor (CRI ~ 70 -80) as the light produced often seems too harsh and lacks in warmth compared to conventional sources. To overcome this, red phosphor such as europium-based phosphor is added to the phosphor coating. However, this type of phosphor is more problematic as it introduces stronger Stokes losses, its thermal quenching is more severe, and the cost is significantly higher.

Additionally, the color of these phosphor white LEDs is not independently tunable, as there is essentially only one active blue LED with passive phosphor coating that is always active. In display applications, polarizers and polarization rotating crystals in a thin-film transistor (TFT) filter are necessary to modulate the color of the phosphor down-converted white LED. Therefore, for each red, green, and blue (RGB) subpixel in a LED-backlit liquid crystal display (LCD), two thirds of the light has already been lost to heat. Another disadvantage of this type of backlighting is the poor contrast between the pixels with maximum (white) and minimum (black) brightness caused by the incomplete filtration of the TFT filters. The blacks in the LCD often look grey. These disadvantages of the phosphor down-converted white LEDs have fueled the research into the phosphor-free full spectrum RGB LEDs that have no Stokes losses.

For phosphor-free full spectrum solid state lighting, three individual LEDs with the colors RGB are needed. Unlike the efficient blue and red semiconductor emitters, which are readily available and have quantum efficiency (QE) of $>70\%$, green emitters are lacking in their performance. This creates the “green gap” in LED efficiency [30]. The external quantum efficiency (EQE) of LEDs near the visible range is shown in Figure 1.7.

The mechanisms behind the drop in efficiency while emitting in the green

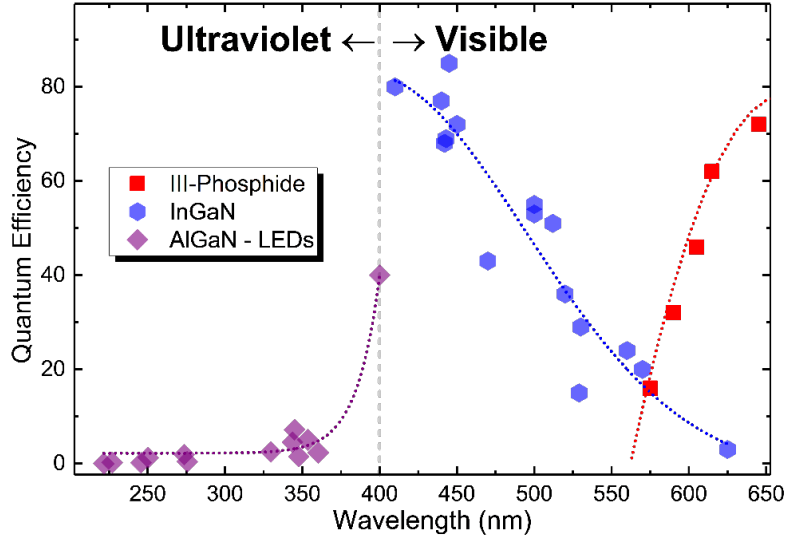


Figure 1.7: External quantum efficiencies of nitride and phosphide LEDs showing a lack of efficient emitter in the “green gap”. Plotted with data provided in Auf Der Maur et al. [30] and Zhang et al. [32].

part of the visible spectrum are different for the phosphide and nitride families. For the III-phosphides, their bandgap transitions from a direct to indirect transition as the aluminum composition is increased to increase the energy from red towards green [31]. When the bandgap becomes indirect, the AlInGaP semiconductor stops emitting photons. Instead, it starts to emit undesired heat in the form of phonons. The phosphide semiconductor family is unable to emit in the green.

The bandgap transition for III-phosphides transitions from direct to indirect as the aluminum composition increases (to reduce the wavelength from red λ green); this makes the phosphide unsuitable for light emission as indirect transition results in the emission of heat rather than photons.

For the III-nitrides, the issue lies in the lack in the growth technology for high indium-content InGaN. The crystal quality of the III-nitrides suffers as the composition of indium increases (to increase the wavelength from the bandgap energy of GaN in the UV to green) caused by a phenomenon called indium clustering [33]. These characteristics of the two semiconductor families create a precipitous drop in the EQE around $\lambda \sim 570$ nm, which is near the wavelength of green, an integral component for full spectrum phosphor-free white LED.

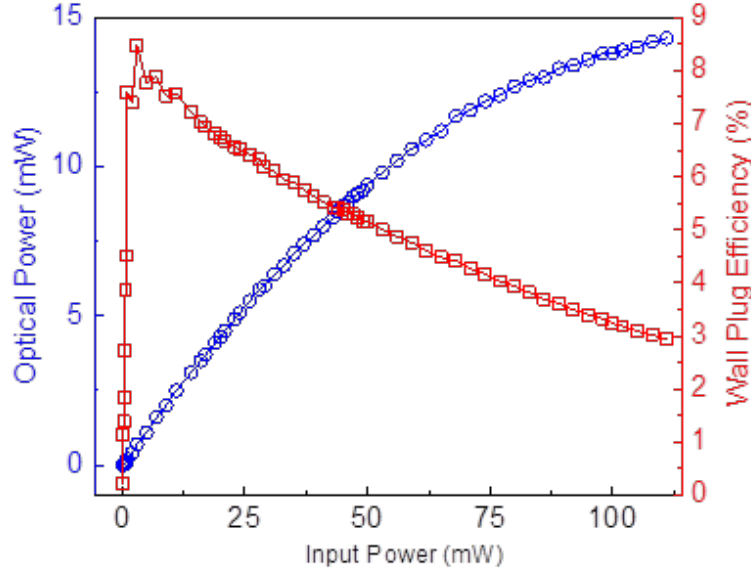


Figure 1.8: Efficiency droop of the blue III-nitride LED at various forward current.

For the phosphor down-converted white LED using the blue LED + yellow phosphor approach, the performance of the blue LED is at the very root of the efficiency of the white LEDs until a suitable green LED is found for the RGB white LEDs. The efficiency of a InGaN-based blue LED under various injection current is shown in Figure 1.8. Under low injection power (<10 mW) – the low injection current regime – blue LEDs exhibit higher overall efficiency. However, under high-power operation (>100 mW) with high injection current density, the efficiency of the LEDs is reduced by more than two thirds.

This phenomenon, termed “efficiency droop”, in which the efficiency of blue LEDs decreases sharply with increasing input power, limits the exploitation of the InGaN-based LEDs [34, 35]. There exists a trade-off between light output density and efficiency. Studies have proposed many origins of efficiency droop including: poor hole injection [36], carrier overflow [37, 38], polarization [39], Auger recombination [20], carrier delocalization [40], high defect density [41], etc. However, researchers have not reached a consensus, and droop-free LEDs have not yet been demonstrated [42]. In order to have more light output, more and/or larger LEDs are required to maintain a level of ef-

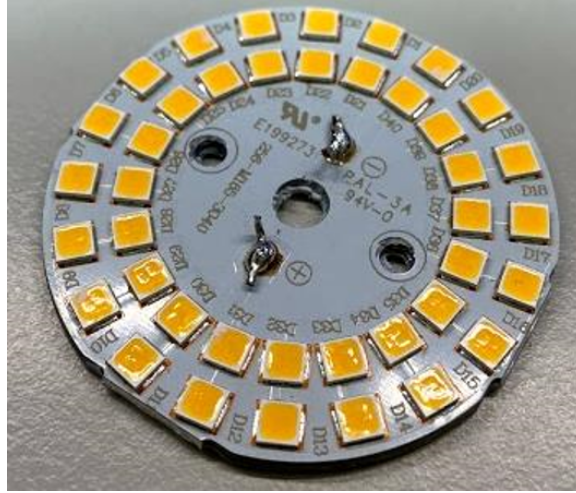


Figure 1.9: A commercially available 100 W equivalent 1600 lumen white LED light bulb.

efficiency; therefore, the upfront equipment cost and device footprint increase as the consequences. A commercially available 16 W (100 W equivalent), 1600 lumen phosphor down-converted LED light bulb is shown in Figure 1.9. Forty LED chips are required to maintain a luminous efficacy of at least 100 lm/W. A reduction in efficiency droop can potentially decrease the number of LEDs chips required, and therefore decrease the cost of solid state lighting by a similar magnitude.

The use of phosphor in the white LEDs also induces efficiency loss and aging effects under prolonged operation at elevated temperature. The added complexity in the manufacturing involving phosphor increases the cost on top of its raw material cost (Figure 1.10). The combination of efficiency droop and the necessary use of phosphor creates an upfront cost that is often prohibitively high. The result is an efficient lighting solution that is economically uncompetitive without copious subsidies.

Beyond visible light, ultraviolet (UV) radiation has shown important applications in space technology, such as mass spectroscopy, light detection and ranging (LIDAR), lidar in-space technology experiment (LITE) and lidar atmospheric sensing experiment (LASE) for planetary atmospheric measurements (e.g. ‘dust devils’ on Mars), fluorescence spectroscopy, etc. Conventional UV laser sources such as the gas lasers (XeF, He-Cd, XeCl, ArF), and solid state lasers (Nd:YAG (3rd and 4th harmonics), frequency-tripled Ti:sapphire) either have a very large form factor, require external pumping,

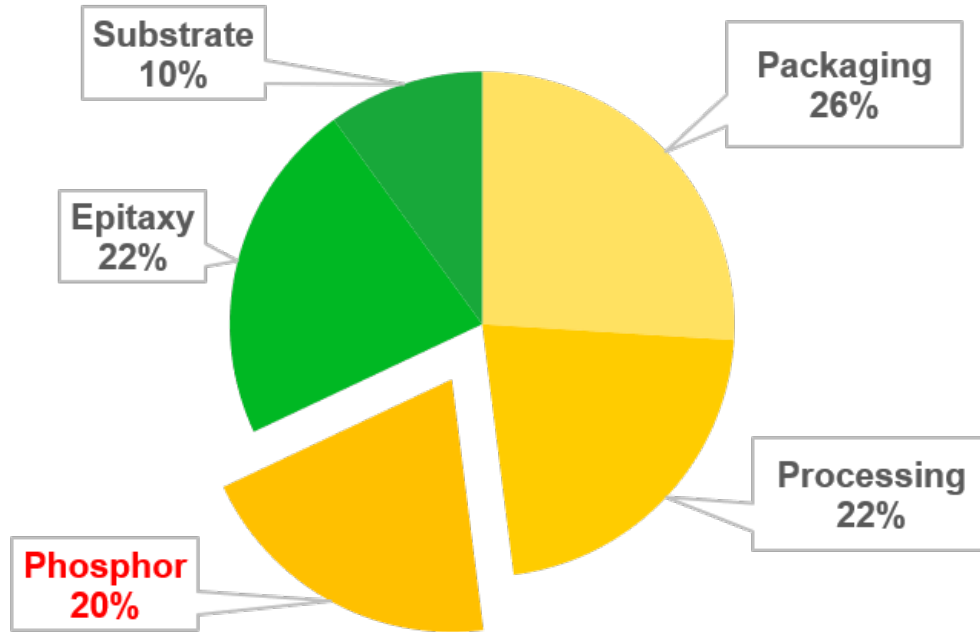


Figure 1.10: Cost breakdown of a modern white LED light bulb. Raw material cost for phosphor makes up to 20% of the total cost.

are very inefficient (require frequency up-conversion), and/or are difficult to modulate. Their overall efficiency is on the order of 1%. On the other hand, semiconductor lasers and laser diodes (LDs) offer extremely compact (<1 cm in length), inexpensive and simple designs that can achieve high power, high efficiency ($>30\%$), high gain, high modulation speed, high monochromaticity, and excellent reliability and longevity. LDs in the infrared~red range have already been commercialized and have changed the capability of long distance communication to handheld presenters.

For shorter wavelengths of light (≤ 405 nm), gallium nitride (GaN) and its alloys with aluminum and indium nitride (AlInGaN) with its wide range of bandgap energies, ranging from near infrared to vacuum UV, are used. GaN light emitting diodes (LEDs) have already been shown to operate in wavelengths as short as 257 nm at room temperature [43]. Studies have shown that GaN is several orders of magnitude more resistant to radiation damage, such as from protons, electrons, neutrons, and gamma-rays, than other semiconductors like gallium arsenide, making it suitable for the harsh extraterrestrial environment [44]. Lasing with InGaN at 405 nm has been commercialized with success, but lasing in the deeper part of the UV spec-

trum (< 355 nm) using AlGaN has not been realized with satisfying results. This is in part due to GaN's inherent material properties and the unavailability of a suitable substrate. The goal of improving the performance of AlGaN for the UV LEDs and LDs makes the study of the GaN material essential for the next-generation photonics.

CHAPTER 2

FUNDAMENTALS OF THE CUBIC PHASE GALLIUM NITRIDE

The material characteristics of h-GaN make it a challenging semiconductor to fabricate devices on as special considerations need to be taken. These measures are sometimes mutually exclusive (polarization-free vs. crystal quality) or simply do not exist (efficient P-dopants, high hole conductivity). However, its closely related material, the c-GaN, offers many desirable properties that promise to overcome the challenges h-GaN faces.

2.1 Motivation: Advantages of Cubic GaN

With a higher symmetry in its crystal structure, cubic (zinc-blende) phase GaN (c-GaN) is inherently polarization-free in the $\langle 100 \rangle$ growth direction. Literature has shown these internal polarization fields to be absent in c-GaN [45]. The crystal structure of the c-GaN is shown in Figure 2.1. The polarization-free nature of c-GaN therefore does not encounter the design limitations of conventional h-GaN based emitters.

The polarization-free nature of c-GaN leads to properties that are beneficial for photonic applications. The absence of internal polarization fields in the material growth direction allows for a more even carrier distribution, which leads to a greater wavefunction overlap in the active layer that results in a fast radiative recombination (Figure 2.2). This prevents the build-up of a high concentration of carriers that leads to Auger recombination [46]. Additionally, the population inversion in the active layer is also enhanced, which leads to a much higher optical gain observed in c-GaN [47]. The availability of cleavage planes in the cubic crystal permits the creation of atomic flat edges, which can be used as the high-reflectivity cavity mirrors of an edge emitting Fabry-Perot laser. Due to its weak spin-orbital coupling, very long room-temperature electron-spin relaxation lifetime has been observed in

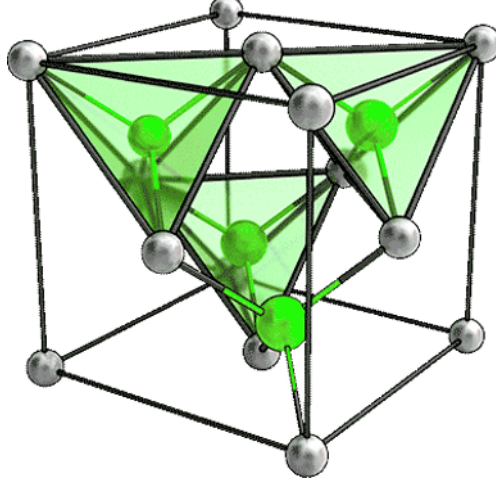


Figure 2.1: Atomic arrangement of c-GaN crystal. Grey atoms are gallium, green atoms are nitrogen.

c-GaN. The higher symmetry of the crystal results in a low carrier scattering rate [48]. This means a higher hole mobility and conductivity [49], and a higher electron drift velocity [50]. The hole mobility has been reported to be more than 10 times that of its h-GaN counterpart (30 vs. 350 cm²/Vs) [51]. Selected material properties are tabulated in Table 2.1 to compare the two material phases.

Table 2.1: Selected material properties of h- and c-GaN

	h-GaN	c-GaN	c-GaN's advantage
E_g (eV)	3.42	3.22	Less indium for longer λ
μ_n (cm ² /Vs)	1000	1000	Higher injection symmetry
μ_p (cm ² /Vs)	30	350	
$E_{acceptor}$ (meV)	200	145	Higher doping efficiency
Polarization (MV/cm)	3.5	0	No QCSE, simplified design
Auger Recombination	strong	weak	Efficient high power operation
Optical gain (cm ⁻¹) TE mode	1500	4000	Lower lasing threshold
Cleaving plane	no (Al ₂ O ₃)	Yes (Si)	Less lossy laser cavity

The smaller bandgap of c-GaN (E_g = 3.22 eV) means a smaller indium content is required to form the InGaN alloy with a bandgap that emits at wavelengths in the green. In comparison to the InGaN alloy based on h-GaN, which has greater bandgap energy (E_g = 3.42 eV), a 10-15% higher indium

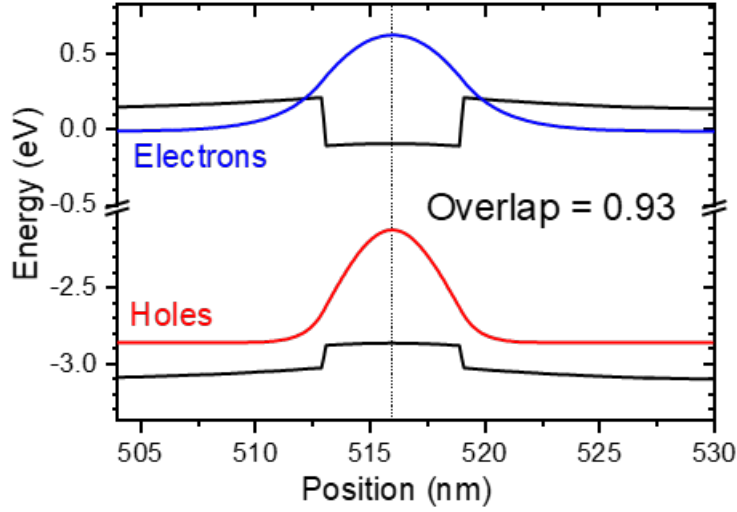


Figure 2.2: A c-GaN based quantum well showing no QCSE and a very high carrier wavefunction overlap.

content is required to achieve the same emission wavelength [52]. Higher indium content InGaN often leads to poor material quality that degrades the radiative efficiency of the LED. Published work has shown microcrystals of c-GaN to have a smaller efficiency droop, and to exhibit output power that is 50% stronger than their h-GaN counterpart [53]. These reported properties make the c-GaN fundamentally a superior photonic semiconductor than h-GaN, and a promising material for improving the performance of contemporary photonic devices [54].

Besides polarization-free photonics, polarization-free wide bandgap electronics using c-GaN such as normally-off transistors [55], room-temperature ferromagnetism [56], high-temperature spintronics [57], and single photon emitters have also been explored [58]. Yet, c-GaN is one of the least studied materials due to the lack of a reliable, high-quality commercialization method to grow this material. This is mainly due to the crystal's phase instability and its tendency to relax to the thermodynamically stable h-GaN when heterogeneously grown on foreign substrates.

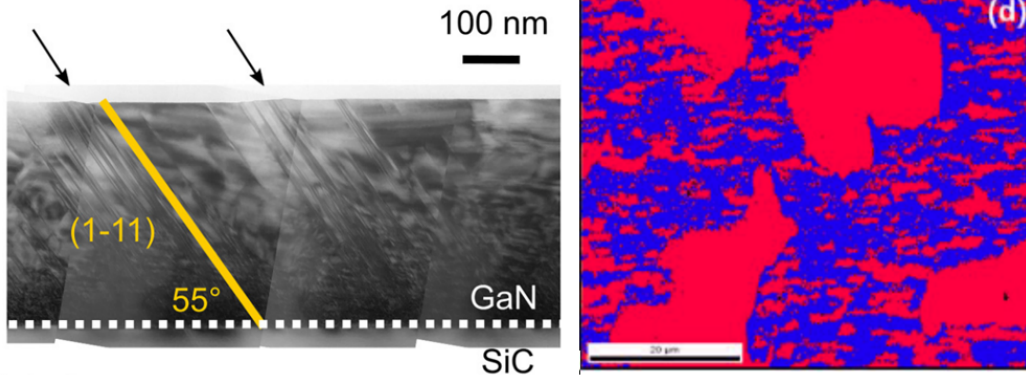


Figure 2.3: (Left) TEM image of MOCVD growth of c-GaN on 3C-SiC. Reprinted from Lee et. al., J. Appl. Phys. 125, 105303 (2019), with the permission of AIP Publishing.. (Right) Phase distribution of MBE grown GaN on 3C-SiC showing cubic (blue) and hexagonal (red) phases. Reprinted from R.M. Kemper, et al., J. Cryst. Growth 323, 84 (2011), with the permission of Wiley Publishing.

2.2 History of Cubic Phase GaN Research

Given the advantageous inherent material properties of c-GaN, researchers in the 2000s have begun to explore the possibility of exploiting the material for photonic devices. However, the material's phase instability on foreign planar substrates (GaAs [59], 3C-SiC [60], Si(100) [61], and MgO [62]) has hindered the synthesis of high-quality, phase pure c-GaN crystals. GaN grown via this planar heteroepitaxy approach often results in highly defective and mixed phase GaN as the crystal has a predilection to relax and form the more stable h-GaN [63]. The result is a very rough surface and random regions of c-GaN and h-GaN that are unsuitable for device fabrication [64].

Figure 2.3 (left) shows a transmission electron microscopy (TEM) image of a MOCVD grown c-GaN on 3C-SiC, which is the available substrate with the smallest lattice mismatch to c-GaN (3.5%). A high density of stacking faults along the (111) planes is observed. On the right, electron backscatter diffraction (EBSD) crystal phase detection of molecular beam epitaxy grown GaN on GaAs, which also has cubic crystal structure, shows c-GaN (blue) regions with h-GaN (red) inclusions, while the large h-GaN regions is phase pure and free of c-GaN inclusion. This demonstrates the one-way relaxation of GaN from its cubic phase to the hexagonal phase. The high defectivity and the permeating phase mixing show the shortcomings of the current growth

technology in providing a high-quality c-GaN crystal that is device-ready. Therefore, an alternative, improved approach is needed.

2.3 Phase Transition of GaN: V-groove Nanopatterns

The difficulty in its growth and the unsatisfying outcome of c-GaN planar heteroepitaxy have sparked researchers to pursue alternative methods to the synthesis of the material. Recently, the most promising alternative approach is through the hexagonal-to-cubic phase transition. This method utilizes the crystal equivalence between hexagonal and cubic at the (111) plane to induce the h-GaN growth to the c-GaN growth. The cubic and hexagonal crystals share a plane equivalence of the cubic (111) and the hexagonal (0001). Therefore, h-GaN and h-AlN will nucleate on the (111) planes of cubic substrates, such as silicon. Indeed, LEDs based on the conventional h-GaN can be fabricated on Si(111) wafers, albeit with a poorer performance than its sapphire equivalent due to the worse crystal quality as a result of a larger lattice mismatch [65].

The first phase transition in GaN discovered is the V-groove approach. This approach uses the Si(100) wafer, and uses anisotropic KOH etching technique to expose the (111) planes. To create the V-shaped grooves, KOH solution is used to preferentially etch the 100 planes of the Si(100) substrates at a rate that is approximately 900 times more quickly than that of the 111 planes [66]. The result is the formation of V-shaped grooves with the (111) planes on the either sides that make a 54.7° angle to the substrate when the groove is oriented in the 110 directions. Using standard photolithography techniques, such as contact lithography or stepper aligners, periods of passivation materials can be deposited on top of the Si(100) wafer to act as a protective hard mask for the KOH etching. Predefined periods of V-grooves can then be etched onto the wafer. Figure 2.4 shows the Si(100) wafer etched with V-grooves [67].

In a MOCVD chamber, h-GaN will selectively nucleate on the exposed 111 planes due to the cubic-hexagonal plane equivalence. This results in the growth of two opposing h-GaN “wings” on the V-grooves’ surfaces that are angled 109.47° with respect to each other. Studies have demonstrated that when two h-GaN wings coalesce at the tetrahedron bonding angle, which

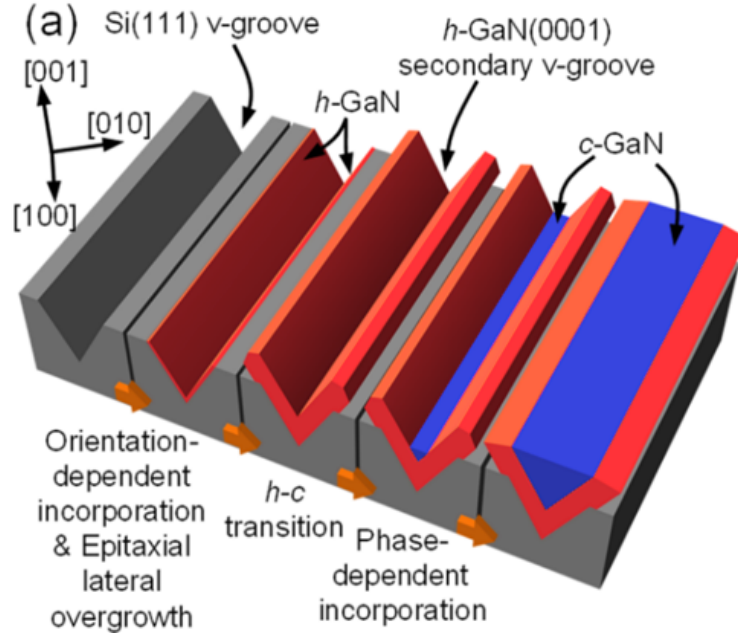


Figure 2.4: A single period V-groove. Adapted with permission from S. C. Lee et al., Cryst. Growth Des. 19, 5046 (2019). Copyright 2019 American Chemical Society.

coincides with the angle provided by the geometry of the V-groove, the crystals will be forced to adopt another degree of symmetry about the center line of the V-groove. This axis is absent in the hexagonal crystal, and therefore the material relaxes to the cubic phase, which does have this symmetry when oriented in the same direction as the Si(100) substrate [68] Therefore the material grown after the coalescence point will phase transition from hexagonal to cubic phase (the phase transition approach). A single period V-groove demonstrating the crystal geometry of the hexagonal-to-cubic phase transition is shown in Figure 2.4. The phase transitioned c-GaN (blue) plateau is flanked by two h-GaN (red) wings that are buried underneath.

This approach has shown excellent phase purity and crystal quality as no phase mixing is observed. However, the V-grooves do leave the h-GaN wings that have not undergone phase transition intact [69] Employing multiple periods of the V-groove on a substrate results in the h-GaN wings penetrating through neighboring c-GaN plateaus, as shown in Figure 2.5. The V-groove approach to phase transition does provide high-quality c-GaN crystallites, but the periodically phase mixing makes device fabrication difficult on this surface. The inability of the V-groove approach to suppress the h-GaN wings

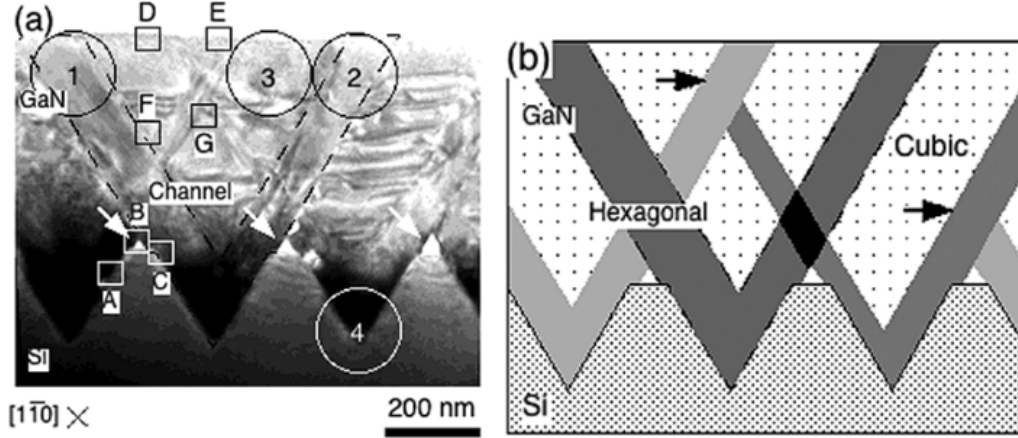


Figure 2.5: Multiple V-grooves showing periodic h-GaN mixing. Reprinted from S. C. Lee et al., IEEE J. Quantum Electron. 41, 596 (2005), with the permission of IEEE.

necessitate remedies in order to make the phase transition c-GaN usable for device fabrication.

This approach shows some promise for the synthesis of c-GaN, but the lack of growth suppression of the h-GaN on the sides and the seemingly randomly distributed c-GaN regions necessitate a more refined method to control the phase transition.

2.4 Phase Transition of GaN: U-groove Nanopatterns

In order to limit the growth of the h-GaN wings, an inert sidewall is required to choke off the flow of MOCVD precursor gas to the h-GaN crystal. To reliably predict the location of where hexagonal-to-cubic phase transition occurs, small Si(111) planes are required. These two improvements over the V-groove approach are the basis of the U-groove approach [70]. By preventing the KOH solution from etching the silicon all the way to form a V-shape, a U-shaped can be formed by carefully controlling the time the substrate is submerged in the etchant. Therefore, the overall shape of these U-shaped grooves consists of SiO_2 – Si(111) – Si(100) – Si(111) – SiO_2 surfaces. Barriers made of dielectrics, such as SiN_x or SiO_2 , placed between each period suppress the growth of the unwanted h-GaN. With the correct patterning and growth parameters, the c-GaN can cover the h-GaN wings completely. The result is

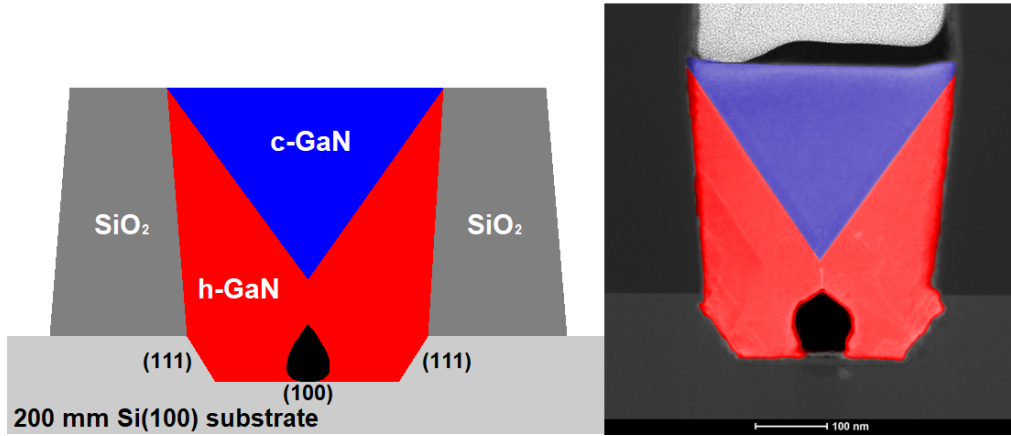


Figure 2.6: (Left) Illustration of a U-groove and (right) the corresponding transmission electron micrograph of the same structure.

a purely cubic surface, as shown by an illustration in Figure 2.6 (left) and transmission electron micrograph (right).

With the disadvantages of the V-groove approach addressed, the U-groove approach to phase transition can form a purely cubic surface. The ability of this technology to form a surface composed entirely of c-GaN using industry-standard fabrication techniques and substrates makes this approach to the illusive, metastable, and high-performing c-GaN promising. The c-GaN grown this way is poised to have a big impact on the semiconductor industry, and therefore is worthy of extensive research in order to fully capitalize on the superior properties of c-GaN.

CHAPTER 3

FABRICATION AND GROWTH OF CUBIC PHASE GALLIUM NITRIDE

The geometry of the U-groove nanopatterned silicon substrate, the nonplanar nature of growing h-GaN on the anisotropically etched Si(111) surfaces, and the growth-limiting SiO₂ dielectric sidewalls must be taken into consideration when modeling the growth dynamics of the phase transitioning GaN materials. The goal is to have the SiO₂ sidewalls tall enough to fully suppress the growth of h-GaN while not limiting that of c-GaN. This chapter explains the methodology of optimizing the silicon patterning to take all the dimensions of the U-groove into account as well as the nitride growth.

Section 3.1 explains the geometry required for phase transition. Section 3.2 describes the growth dynamics and phase transition of the two phases of GaN. Section 3.3 explains the geometry of a nanopatterned U-groove. Section 3.4 derives the critical conditioning in which the desired result, fully suppressed h-GaN growth and pure c-GaN surface, can be attained.¹

3.1 Hexagonal-to-cubic Phase Transition

This phase transition process can be visualized using a ball and stick model (Figure 3.1). When two h-GaN crystals with the ABAB stacking order (blue and green dashed lines) meet at $\sim 110^\circ$, c-GaN crystal, which is symmetric about the centerline, forms. This is based on the fact that the $\langle 0001 \rangle$ planes of the h-GaN crystals are equivalent to the $\langle 111 \rangle$ planes of the c-GaN crystal, which has an ABCABC stacking order with the C-stack shown in red dotted lines.

This c-GaN then grows in a triangular fashion bounded by h-GaN wings separated by two (111) planes. The h-GaN wings will eventually be encased

¹Portions of this chapter were previously published as [10, 71, 72, 73] and are reprinted with permission. (Copyright 2016 by AIP Publishing, and 2018 by American Chemical Society)

by the SiO_2 sidewalls, and leave the U-groove composed of entire c-GaN on the surface. However, if the c-GaN touches the SiO_2 sidewalls, defects will form and cause the crystal to revert back to h-GaN. Therefore, precaution in U-groove patterning must be taken to limit the height of the SiO_2 sidewall in relation to the location and geometry of c-GaN to prevent this defect formation and phase transition reversal.

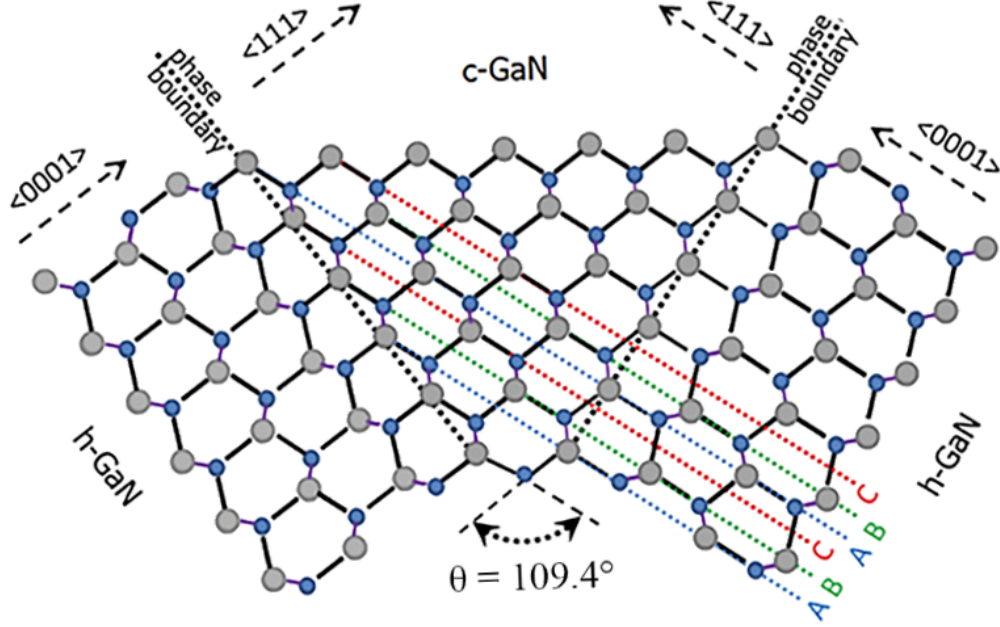


Figure 3.1: Cross-sectional sketch depicting wurtzite to cubic phase transition observed in the groove. Reprinted from C. Bayram et al., Adv. Funct. Mater. 24, 4492 (2014), with the permission of Wiley Publishing.

3.2 Dimension Definition of U-Groove Nanopatterns

To achieve the critical dimension for complete c-GaN coverage in a U-groove, the heights of the c-GaN triangle and the SiO_2 sidewalls must match. To achieve this desired patterning condition, crystal modelling of the dimensions of the U-groove patterning is needed. The geometry of the GaN growth in a U-groove is shown in Figure 3.2 [70]. The SiO_2 sidewalls are omitted in the drawing, but its height (h) will coincide with the top of the c-GaN triangle (blue). The turquoise line indicates the boundary between h-GaN and Si(111) on the sides and Si(100) in the horizontal part. The anisotropically KOH-

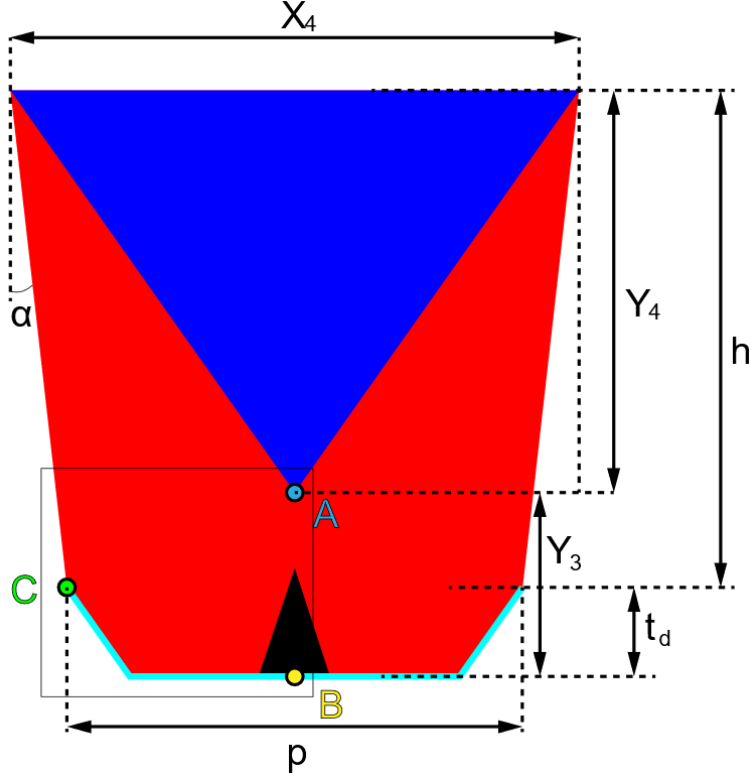


Figure 3.2: U-groove model and patterning parameter definition showing c-GaN (blue), h-GaN (red), void (black), and silicon interfaces (turquoise).

etched silicon surfaces consists of two (111) planes at 54.7° angles to the middle (100) surface. This etch depth (t_d) is measured vertically from the unetched silicon surface. The opening between the SiO_2 sidewalls at the base is measured from the top of the $\text{Si}(111)$ surface to the other. Under the previously mentioned selective growth conditions [74], h-GaN nucleates on the $\text{Si}(111)$ surfaces and coalesces at a 109.47° angle in the middle of the groove (point A). This is the initial point for phase transition to c-GaN, which grows in a triangular manner and bounded by two diverging cubic (111)/h-GaN (001) phase boundaries. Additionally, the SiO_2 sidewalls can exhibit an angle (α). Taking these geometries into consideration, the critical condition where the height of the c-GaN triangle (Y_4) plus the height of point A (Y_3) is equal to the height of the SiO_2 sidewall.

To determine the height of point A, a closer look at the h-GaN nucleation site on the $\text{Si}(111)$ planes is required (Figure 3.3). The h-GaN crystal grows perpendicular to the $\text{Si}(111)$ surface in its $\langle 0001 \rangle$ direction and is flanked by two (1101) semi-polar planes.

$$Y_2 = X_3 \tan 35.3^\circ \quad (3.5)$$

$$X_1 = \frac{t_d}{2 \tan 54.7^\circ} \quad (3.6)$$

$$X_3 = \frac{P}{2} - X_1 \quad (3.7)$$

Placing Equation (3.6) into (3.7) yields:

$$X_3 = \frac{P}{2} - X_1 = \frac{P}{2} - \frac{t_d}{2 \tan 54.7^\circ} \quad (3.8)$$

Combining (3.8) and (3.5):

$$Y_2 = X_3 \tan 35.3^\circ = \left(\frac{P}{2} - \frac{t_d}{2 \tan 54.7^\circ} \right) \tan 35.3^\circ \quad (3.9)$$

From Figure 3.2:

$$X_4 = P + 2h_c \tan \alpha \quad (3.10)$$

$$Y_1 + Y_3 = h_c + t_d \quad (3.11)$$

$$\tan 35.3^\circ = \frac{X_4}{2Y_1} \quad (3.12)$$

Rearranging:

$$Y_1 = \frac{X_4}{2 \tan 35.3^\circ} = \frac{P + 2h_c \tan \alpha}{2 \tan 35.3^\circ} \quad (3.13)$$

$$h = Y_1 + Y_3 - t_d = Y_1 + Y_2 - \frac{t_d}{2} \quad (3.14)$$

Substituting into (3.14):

$$h_c = \frac{P + 2h_c \tan \alpha}{2 \tan 35.3^\circ} + \left(\frac{P}{2} - \frac{t_d}{2 \tan 54.7^\circ} \right) \tan 35.3^\circ - \frac{t_d}{2} \quad (3.15)$$

Solving for h_c :

$$h_c = \left(1 - \frac{\tan \alpha}{\tan 35.3^\circ} \right)^{-1} \left[\frac{P}{2} - \frac{t_d}{2 \tan 54.7^\circ} \right] \tan 35.3^\circ - \frac{t_d}{2} \quad (3.16)$$

Equation 3.16 can be simplified by substituting the values for the tangents. To achieve the complete c-GaN coverage condition, the U-groove parameters – oxide opening width (P), silicon etch depth (t_d), dielectric sidewall angle (α), and deposition thickness (h) of GaN deposited above the Si(100) substrate surface – have to obey [71, 75]:

$$h = h_c = \frac{(1.06P - 0.75t_d)}{1 - \frac{\tan \alpha}{0.71}} \quad (3.17)$$

3.4 Fabrication of U-groove Nanopatterns on Si(100) Substrates

Anisotropic nano-patterning of Si(100) substrates is accomplished by utilizing the vastly different etch rates of the (100) and (111) planes of silicon in aqueous KOH solutions. The two opposing silicon (111) and ($\bar{1}\bar{1}\bar{1}$) planes, which are at a 109.47° angle to each other, can be used to facilitate the phase transition of GaN. This section explains the fabrication steps used to create the nanopatterns.

The photolithography and hard mask deposition on the substrate are shown in Figure 3.4. Firstly, (a) float-zone on-axis Si(100) substrate is used, then (b) a thin layer of SiO₂ with a predetermined thickness is grown using dry oxidation at 1150 °C, followed by (c) photolithography patterning of photoresist with predetermined opening and line widths, and (d) electron beam evaporation of 40 nm thick nickel in a vacuum chamber. Finally, (e) photoresist stripper lifts off the unwanted nickel and leaves lines of hard mask on the SiO₂. Scanning electron microscopy (SEM) images of the cross sections of the samples are shown on the right.

Nickel metal hard mask is used in order to achieve a nearly vertical SiO₂ sidewall as photoresist softmask in the corners experiences an etch rate that is much too fast. Therefore a triangular profile is often transferred from the softmask to the SiO₂ layer. Additionally, any nonvertical sidewalls in the photoresist will also be transferred to the SiO₂. A cross-sectional SEM image of as-developed photoresist is shown in Figure 3.5. Since the photolithography was completed using a stepper aligner, this level of nonuniformity on a 4-inch wafer is expected. When photoresist of this profile is used in a reactive

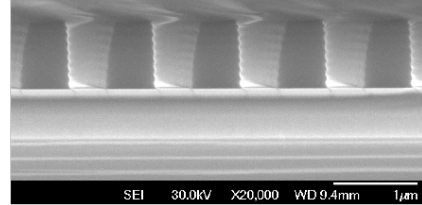
(a) Float-zone on-axis Si(100) wafer



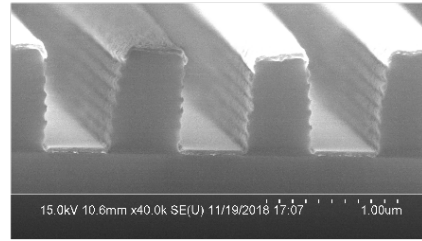
(b) Dry oxidation to grow SiO₂



(c) Photolithography deposition of patterned photoresist



(d) Nickel hardmask evaporation



(e) Metal liftoff

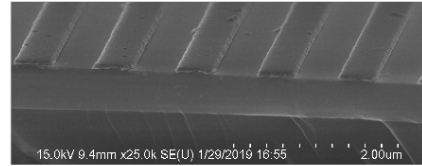


Figure 3.4: Photolithography of the silicon substrate to form the U-grooves.

ion etcher (RIE), the profile is transferred, too (Figure 3.6).

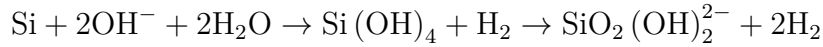
The etching of the substrate is shown in Figure 3.7: (f) Freon 23 (CHF_3) reactive ion etching (RIE) of the SiO_2 . CHF_3 was chosen as the etchant gas due to its ability to form an inhibitor layer on the sides of the opening. This inhibits the etching of the SiO_2 sidewall. While the overall etching rate is reduced, a near-vertical sidewall can be achieved. The etching parameters are: 35 sccm flow, 30 mTorr chamber pressure, and 93 W of RIE power. The etching rate is measured to be approximately $140 \text{ \AA}/\text{min}$. Therefore, to etch through 500 nm of SiO_2 , 37 minutes was required (g). The nickel metal mask is jettisoned (h) by wet etching in 40 °C nitric acid (Transene™ TFB). The removal of fluorocarbon polymer etching inhibitors is achieved using an O_2 plasma in an inductively coupled plasma reactive ion etch (ICPRIE) to ash.



Figure 3.5: As-developed photoresist cross sectional profile.

These processes leave a thin layer of SiO_2 on the surface, so a 10 second wet etching using 10:1 buffered oxide etch (10 NH_4F : 1 HF) is used to expose the Si. Then the sample is immersed in aqueous KOH to etch the exposed silicon (100) to form a U-shaped surface.

The KOH etching required a high degree of finesse. It is a very temperature-sensitive reaction; every 10°C increase in temperature increases the etch rate by a factor of two. Hydrogen gas is also released as a byproduct of the chemical reaction:



These hydrogen gas bubbles will then form on the $\text{Si}(100)$ surface and act as an etch mask. To minimize this effect, isopropanol alcohol is added to the solution to act as a surfactant [76]. Additionally, the sample is gently agitated in the solution with Teflon-based sample carrier and polymethylpentene-based tweezers. The (100) etch rate was found to be approximately 140 nm per minute. The detailed fabrication recipe is found in Appendix A.5. The samples are then placed in a MOCVD chamber for III-nitride growth (Figure 3.8).

In the MOCVD chamber, a thin layer of AlN is deposited everywhere on the sample at a low temperature (600°C). The temperature is then raised

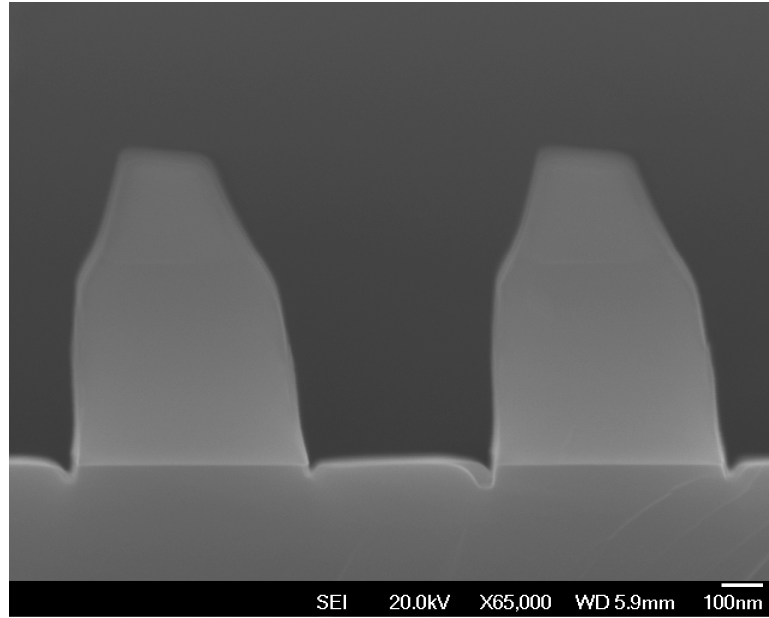
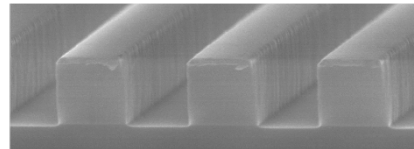


Figure 3.6: Cross-sectional SEM image of RIE etch profile using the as-developed photoresist as a soft mask resulting in nonvertical sidewalls.

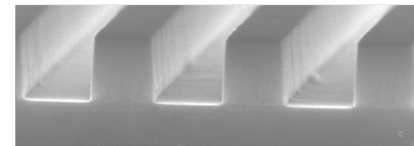
(f) Freon23 reactive ion etch



(g) Etch to expose bare Si(100) surface



(h) Remove Nickel hardmask, remove fluorocarbon polymer



(i) KOH anisotropic etch of Si(100) to partially expose Si(111) planes

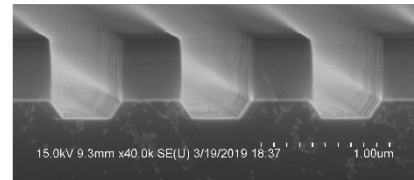


Figure 3.7: Anisotropic reactive ion etching of the sample with lines of Ni hardmask, and KOH wet etching.

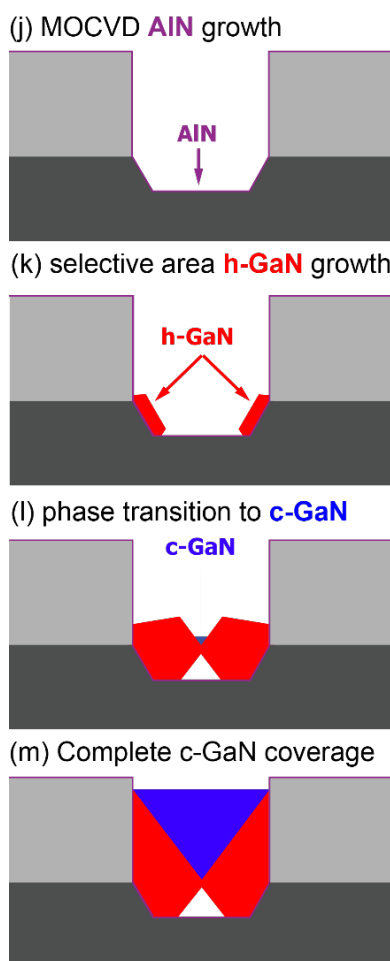


Figure 3.8: (j) An AlN nucleation layer is deposited everywhere via MOCVD. (k) h-GaN is selectively grown on the Si(111) planes at 54.7° to the substrate. (l) When the two h-GaN “wings” coalesce, the material is phase transitioned to c-GaN. (m) Further MOCVD growth allows the c-GaN to cover the entire surface.

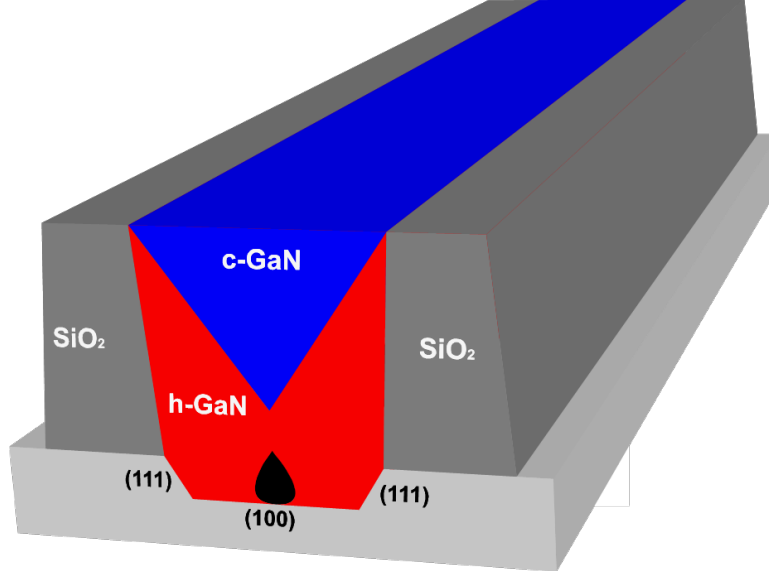


Figure 3.9: Phase transition in a U-grooves with GaN grown to the critical condition that allows c-GaN (blue) to cover the entire surface.

to 1100 °C to allow the AlN that is deposited on the Si(111) surfaces to selectively recrystallize (j). The crystalline AlN allows h-GaN to selectively grow on these surfaces (k). The two opposing h-GaN wings, each making a 54.74° angle to the Si(100) surface, will continue to grow perpendicular to the Si(111) surfaces until they coalesce in the middle of the U-groove. Their growth vectors make a $54.74^\circ \times 2 = 109.47^\circ$ angle. This angle is unsurprisingly also the angle between the two bonds in a tetravalent bonding structure, which is also found in III-V semiconductors. This forces the crystal to adopt a symmetry about the center line of the U-groove and phase transitions the h-GaN into c-GaN (l).

An illustration of the phase-transition of GaN in a U-groove is shown in Figure 3.9. When the height of the SiO₂ barriers (dark grey) coincides with the height of the inverted c-GaN triangle (blue), no h-GaN crystal can be seen from the top. This critical condition allows the surface to be composed of purely c-GaN, and thus the subsequent growth will be purely c-GaN also, without the adulteration of h-GaN. This approach is particularly interesting, due to a multitude of factors: ease of implementation due to the use of standard, scalable, and affordable processing techniques and substrates, and the ability to be integrated with Si-based devices such as CMOS.

The RIE and KOH etch recipes can be found in Appendix A.5.

CHAPTER 4

STRUCTURAL CHARACTERIZATION OF CUBIC PHASE GALLIUM NITRIDE

This chapter discusses the hexagonal-to-cubic phase transition of GaN in the U-groove using structural characterization techniques. The modeling from the previous chapter will be verified using scanning electron microscopy, cathodoluminescence, transmission electron microscopy, atomic force microscope, and Raman spectroscopy.¹

4.1 Scanning Electron Microscopy and Atomic Force Microscopy

Figure 4.1 shows the U-groove modeling from the previous chapter, and will act as the reference growth diagram for the critical condition for c-GaN phase transition. The critical GaN deposition thickness, which obeys Equation (3.17), has to be achieved in the U-groove for c-GaN to cover the entire surface. To observe how close each MOCVD growth outcome comes to the critical condition, a ratio, fill factor (ff) is defined as h/h_c , where a $ff = 1$ indicates the MOCVD growth is on target, $ff < 1$ means the sample is under-deposited, and $ff > 1$ shows an over-deposition of GaN. The actual growth height, h , is defined as GaN material growth above the nonetched Si(100) surface (Figure 4.1).

Scanning electron microscopy (SEM) was conducted using a JEOL 7000F Schottky field-emission scanning electron microscope. Figures 4.2, 4.3, 4.4 show cross-sectional SEM images of GaN in three U-grooves with different outcomes: critically-, under-, and overfilled. Figure 4.2 is close to an ideal case ($ff \approx 95\%$) where GaN has a near-critical fill ($h \approx h_c$) for the patterning

¹Portions of this chapter were previously published as [10, 71, 72, 73] and are reprinted with permission. (Copyright 2016 by AIP Publishing, and 2018 by American Chemical Society)

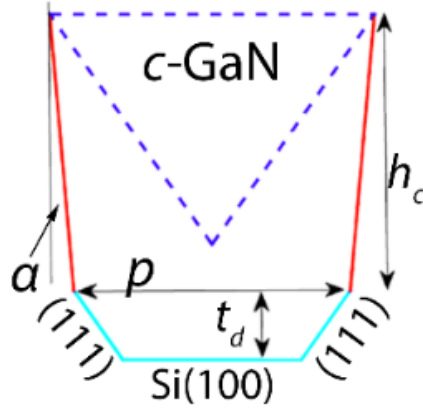


Figure 4.1: Schematic defining critical deposition thickness (h_c), etch depth (t_d), opening width (p), and sidewall angle (α). Reprinted from R. Liu and C. Bayram, Appl. Phys. Lett. 109, 38 (2016), with the permission of AIP Publishing.

parameters of $t_d = 80$ nm, $p = 300$ nm, and $\alpha \approx 2^\circ$. The top c-GaN(100) surface is seen to be very flat, which is a desirable property for device fabrication. Figure 4.3 shows an underfilled case ($h < h_c$, $ff \approx 45\%$) with $t_d = 70$ nm, $p = 640$ nm, and $\alpha \approx 4^\circ$. On the surface, a small amount of the flat c-GaN(100) can be seen in the center flanked by two h-GaN ($1\bar{1}01$) planes, which make a $\pm 7^\circ$ angle to the (100) planes of both the Si substrate and c-GaN in the center. For c-GaN to cover the entire surface in this scenario, more deposition is needed. However, the SiO_2 sidewalls are insufficiently tall to fully suppress the h-GaN (the red lines). Figure 4.4 shows an overfilled case ($h > h_c$, $ff \approx 170\%$), which has too much GaN deposited for $t_d = 70$ nm, $p = 190$ nm, and $\alpha \approx 1^\circ$. The top surface does not appear to be flat, which is an indication of amorphous material. This suggests that over-deposition of GaN ($h > h_c$) causes the overfilled GaN to become phase mixed and lose its high crystallinity.

Figure 4.5 shows the false-colored 45° tilted SEM view of (from left to right) 30%, 45%, 70% and 95% U-grooves consisting of different amounts of h-GaN (red) and c-GaN (blue). The progression of c-GaN growth is clear and predictable. As ff approaches 100%, the blue c-GaN plateau that originated in the center gradually grows to encompass an increasing amount of surface area eventually all of it, as seen in Figure 4.5 (d), in which no h-GaN is visible on the surface.

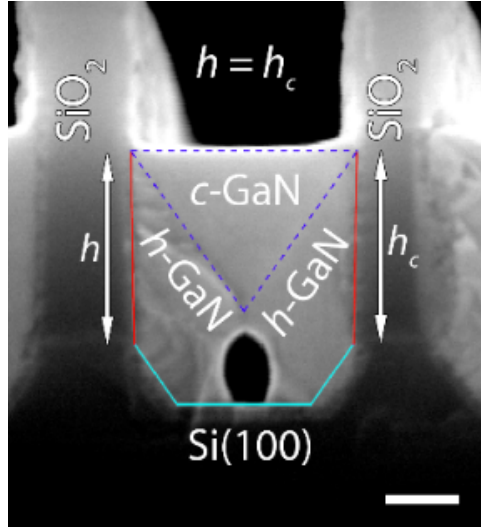


Figure 4.2: Cross-sectional SEM views of GaN deposited in a U-groove when ($h \approx h_c$). Complete c-GaN surface coverage is achieved. White scale bar = 100 nm. Reprinted from R. Liu and C. Bayram, Appl. Phys. Lett. 109, 38 (2016), with the permission of AIP Publishing.

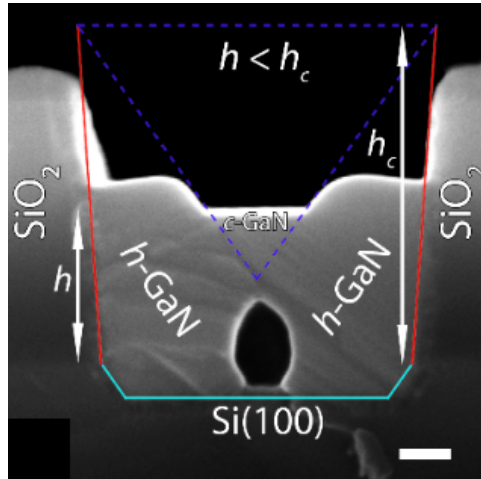


Figure 4.3: When ($h < h_c$) the U-groove is underfilled with GaN ($ff \approx 40\%$). White scale bar = 100 nm. Reprinted from R. Liu and C. Bayram, Appl. Phys. Lett. 109, 38 (2016), with the permission of AIP Publishing.

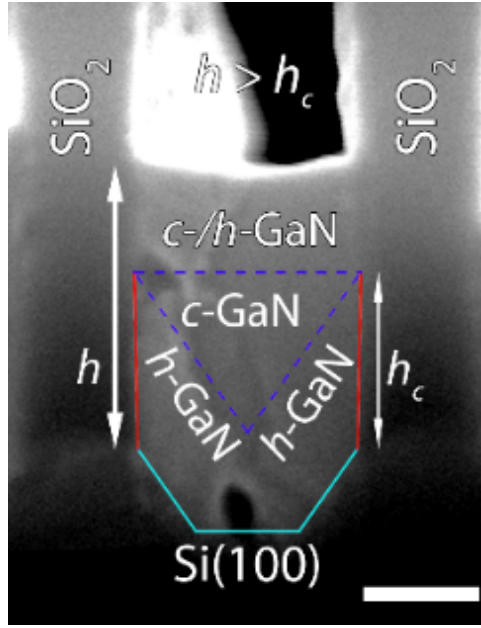


Figure 4.4: When ($h > h_c$) the U-groove is overfilled with GaN ($ff \approx 120\%$). This leads to phase-mixing. White scale bar = 100 nm. Reprinted from R. Liu and C. Bayram, Appl. Phys. Lett. 109, 38 (2016), with the permission of AIP Publishing.

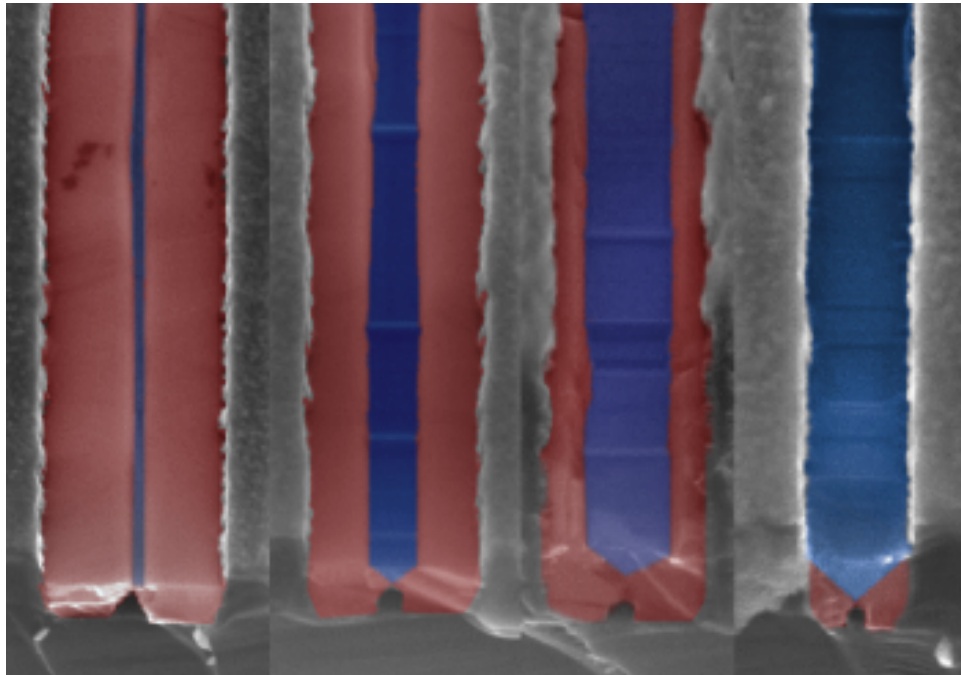


Figure 4.5: False-colored 45° SEM view of the U-grooves with ff of (a) 30%, (b) 45%, (c) 70%, (d) 95%. Blue = c-GaN, red = h-GaN. Scale bars all indicate 350 nm. Reprinted with permission from R. Liu et al., ACS Photonics 5, 955 (2018). Copyright 2018 American Chemical Society.

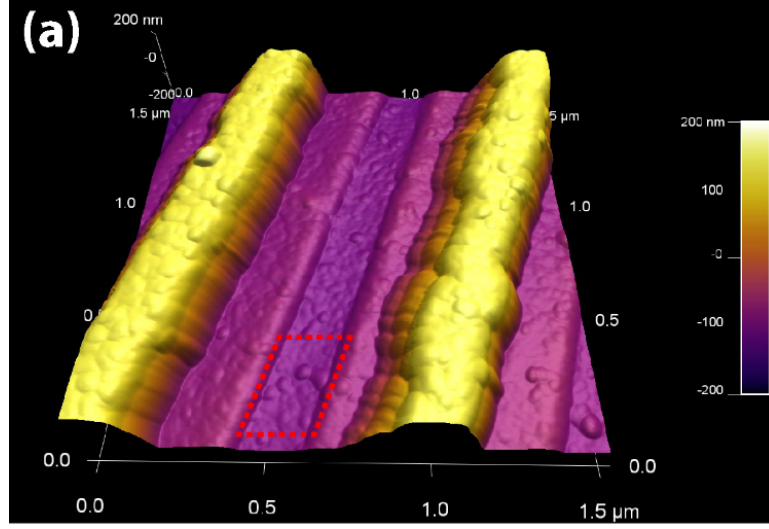


Figure 4.6: 3D rendering of the surface profile $f = 45\%$ U-groove using AFM.

To examine the surface morphology, atomic force microscopy (AFM) is used to study the crystal growth dynamics and defectivity. Figure 4.6 shows the 3D rendering of an incomplete phase transition U-groove ($f = 45\%$), which has incomplete c-GaN surface coverage with h-GaN wings exposed on the sides. The c-GaN can be seen sandwiched between two h-GaN wings, which themselves are confined by two taller oxide barriers (yellow). Figure 4.7 shows the high magnification AFM profile of the dotted area composed of purely GaN (Figure 4.6). The surface roughness (root-mean-square) of the c-GaN region is calculated to be 2.65 \AA , which is among the lowest reported for c-GaN. The AFM study shows the c-GaN is of high quality and device-ready.

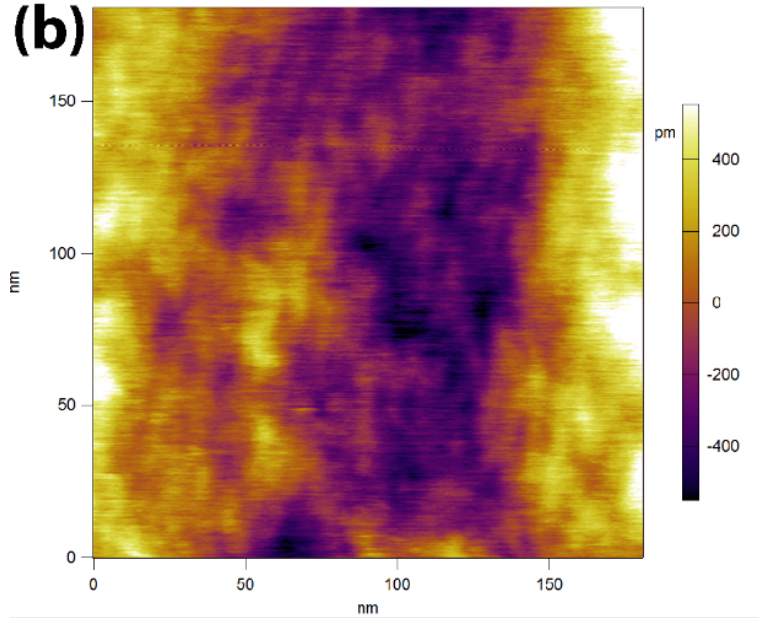


Figure 4.7: High-magnification AFM image of the marked c-GaN region in Figure 4.6.

4.2 Transmission and Scanning Transmission Electron Microscopy Study

Transmission electron microscopy (TEM) study is conducted to characterize the crystal quality of the GaN materials in a U-groove, as shown in Figure 4.8 bright field (BF) and Figure 4.9 dark field (DF) images. The zone axis $[\bar{1}210]$ of the dark field image is shown by the vector g , which corresponds to (0002) .

The thin (~ 15 nm) and highly defective AlN nucleation layer is seen covering the Si substrate and the amorphous oxide barriers. Near the h-GaN nucleation sites on the Si(111) planes, both TEM images show crystals containing dislocations and stacking faults. As the h-GaN crystals grow perpendicularly to the 111 planes of the silicon substrate by more than 50 nm, defectivity is greatly reduced, as indicated by the absence of dark spots in BF-TEM and bright spots in DF-TEM.

The coalescence of the two h-GaN wings can be observed as a ~ 20 nm long seam oriented perpendicular to the (100) plane of the silicon substrate directly above the void. This seam terminates into two distinctly straight interfaces extending in the $\langle 111 \rangle$ direction of the cubic crystals – same as

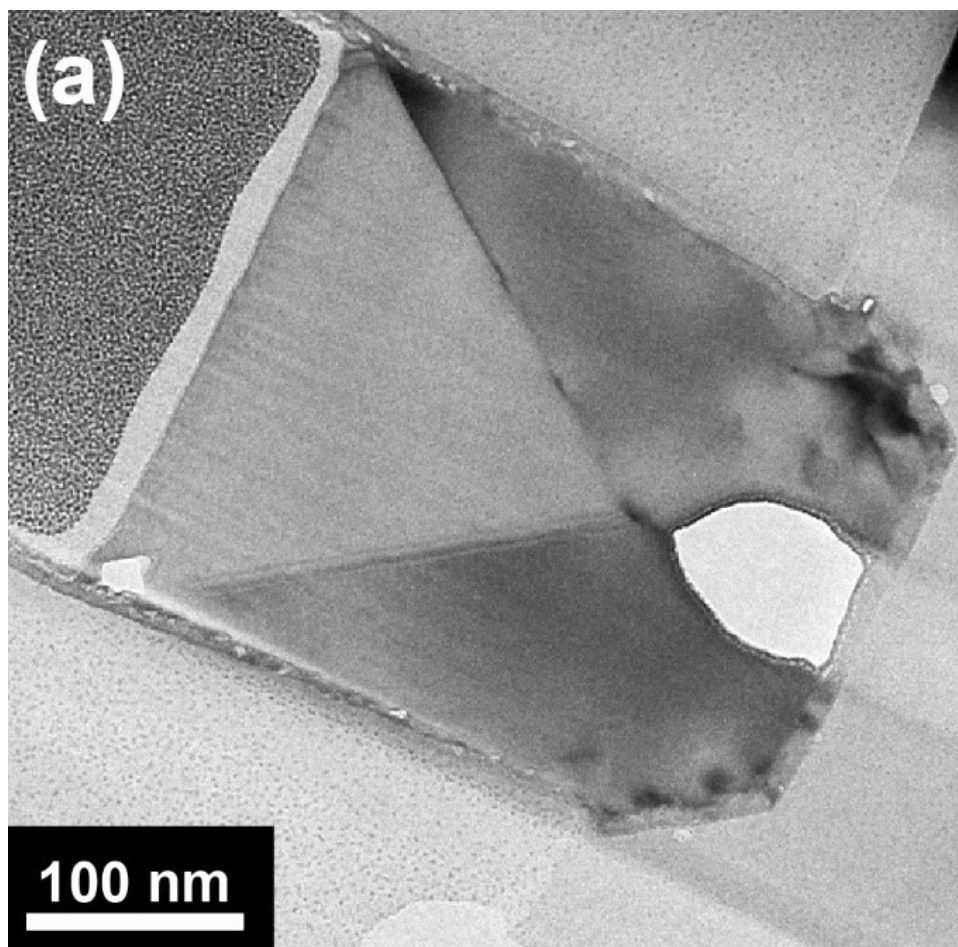


Figure 4.8: Bright field TEM image of GaN crystal in a U-groove. Reprinted with permission from R. Liu et al., ACS Photonics 5, 955 (2018). Copyright 2018 American Chemical Society.

the $\langle 0001 \rangle$ direction of the hexagonal crystal – toward the oxide sidewalls to form a distinct V-shaped phase boundary. Phase transitioned c-GaN is enclosed by the V-shaped phase boundary.

The growth dynamic of GaN in a U-groove is in good agreement with the crystallographic modeling in Chapter 3. The phase of the GaN material inside the phase boundary is confirmed to be cubic by TEM electron diffraction (Figure 4.12) taken from the triangular area shown in Figure 3.2.

The phase boundaries between the two phases of GaN, i.e. on the c-GaN (111) and h-GaN (0001) planes, are observed to be a series of parallel stacking faults. These defects are formed to accommodate the transition between the two crystal structures, but are limited to within a few layers of atoms thick (not shown). As such, the formation of these defects indicates that the

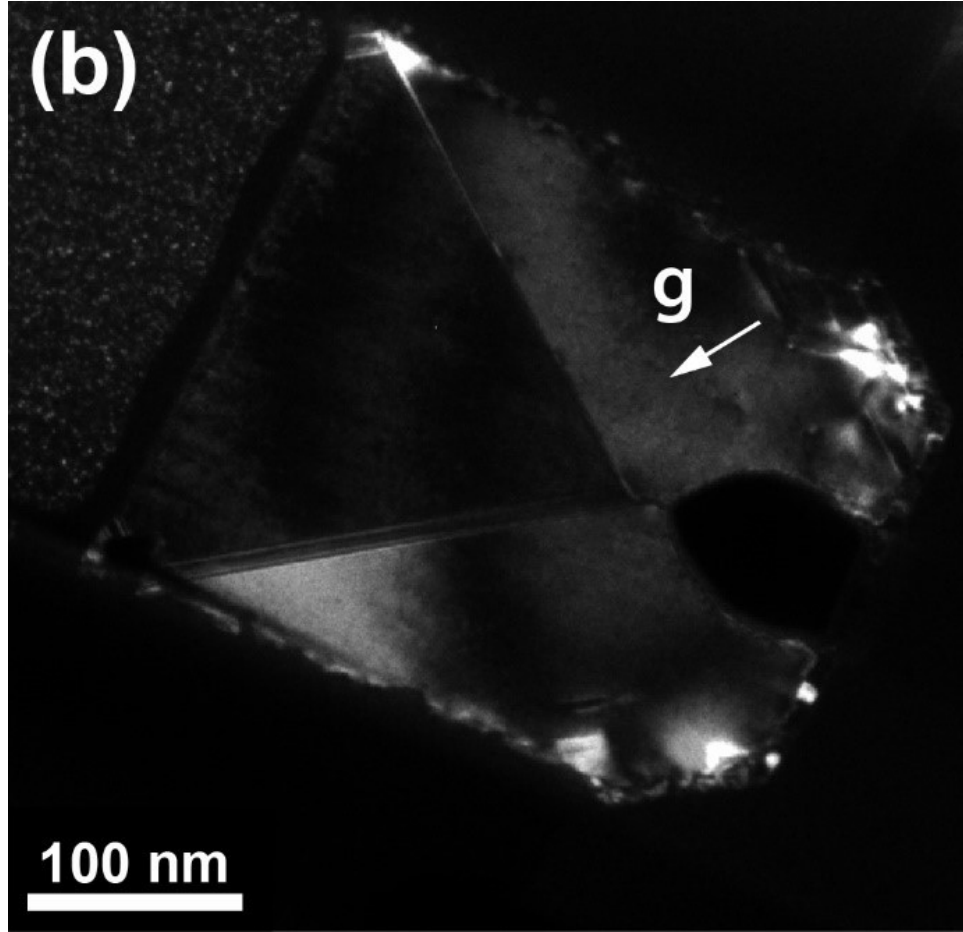


Figure 4.9: Dark field TEM image of GaN crystals in a U-groove taken at $g = (0002)$ near the $[1\bar{2}10]$ zone axis of the right-side h-GaN. Reprinted with permission from R. Liu et al., ACS Photonics 5, 955 (2018). Copyright 2018 American Chemical Society.

overall crystal energy is reduced; the hexagonal-to-cubic phase transition is thermodynamically stable/favorable. The crystal and phase stability breaks when the phase boundary reaches the c-GaN/oxide interface near the surface, as indicated by the formation of defects (stacking faults) oriented away from oxide (Figure 4.8 (b)). Defective and mixed-phase material are observed above these stacking faults and the aforementioned critical height, h_c . This suggests a critical U-groove design parameter: the phase boundary should not reach the oxide sidewall; the height of the sidewalls should be lower than that of the phase boundary.

To examine the crystal quality on the atomic level, scanning transmission electron microscopy is conducted. The state-of-the-art FEI Themis Z

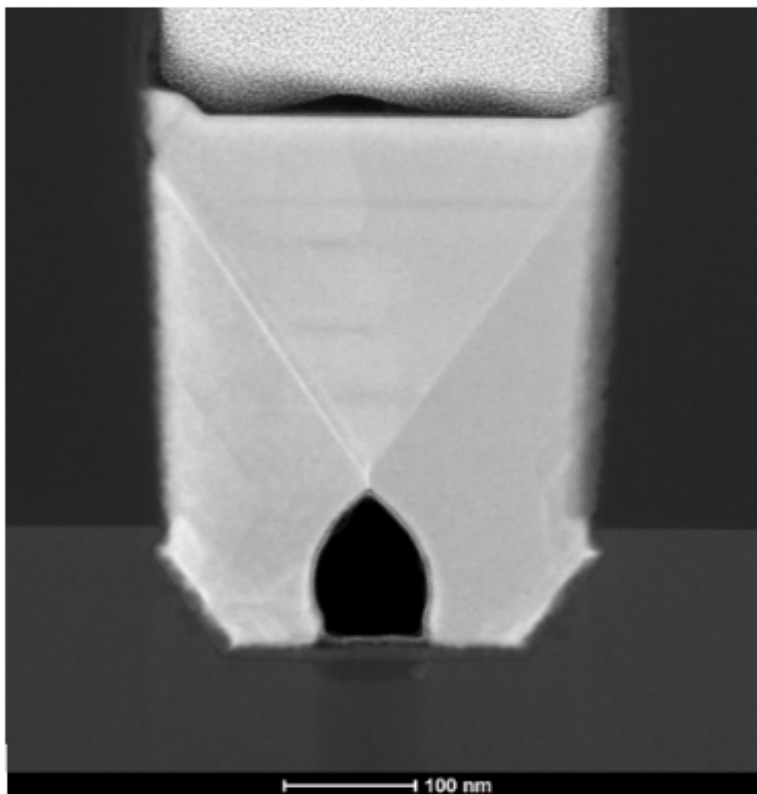


Figure 4.10: STEM image of GaN crystal in a U-groove

Advanced Probe Aberration Correct Analytical TEM/STEM in an acoustic enclosure with custom-designed metal shielded room using magnetic shields made of nickel-iron alloy sheets was used for the highest resolution atomic structure study. Figure 4.10 shows the (left) bright field STEM image of a U-groove using this tool. The phase boundaries between the two h-GaN/c-GaN interfaces can be clearly seen. Also, when the c-GaN reaches the SiO₂ side-walls, another phase boundary forms and travels towards the center of the groove. Figure 4.11 shows the high angle annular dark field image (HAADF) of the individual atoms of the phase transitioned c-GaN through the (110) direction. The larger atoms are the gallium atoms and the smaller ones are the nitrogen atoms. Due to the increase in thickness, the nitrogen atoms become less visible near the bottom of the image. No defects are observed in the scan; this indicates a defectivity of no higher than the mid 10^8 cm^{-3} .

The selective area electron diffraction (SAED) shows the single crystalline diffraction of the phase transition c-GaN in the (110) direction (Figure 4.12). When the SAED area is limited to the c-GaN triangle, single crystalline cubic

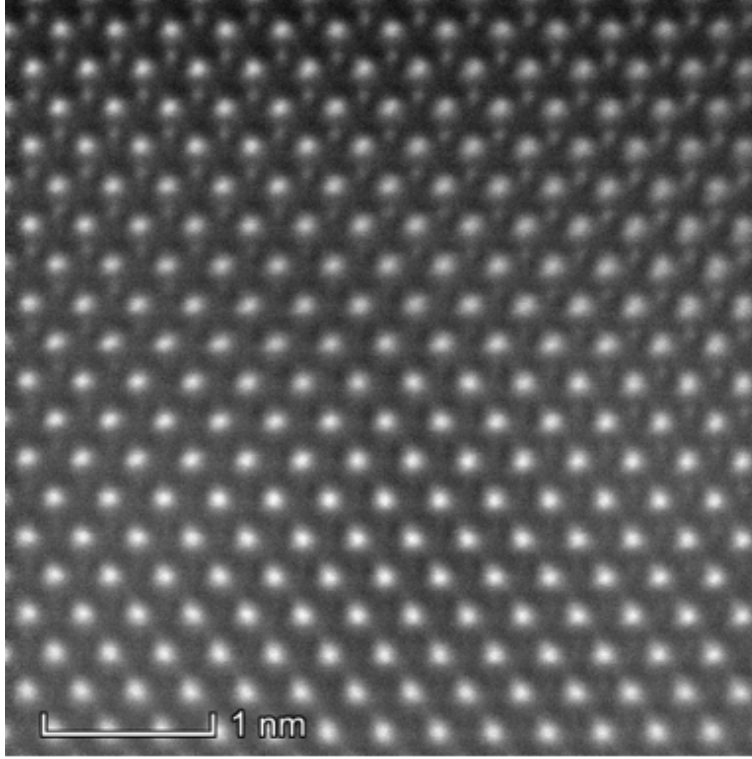


Figure 4.11: HAADF image of the phase transitioned c-GaN in the U-groove.

diffraction is observed in the (110) orientation. When the SAED is conducted on the left and right h-GaN wings, single crystalline hexagonal diffraction from the wurtzite (100) direction can be seen. When the SAED area is enlarged and collected from the entire U-groove, which includes the two h-GaN wings, the phase transition c-GaN, and the silicon (100) substrate, the resulting pattern can be used to approximate the lattice constant of c-GaN using Si as a reference.

Using the ratios between the (200) diffractions of c-GaN and Si, which sit closer to the zeroth diffraction center by a factor of 0.833, the lattice constant of c-GaN is calculated as:

$$a_{\text{c-GaN}} = a_{\text{Si}} \times 0.833$$

$$a_{\text{c-GaN}} = 5.431 \text{ \AA} \times 0.833$$

$$a_{\text{c-GaN}} = 4.523 \text{ \AA}$$

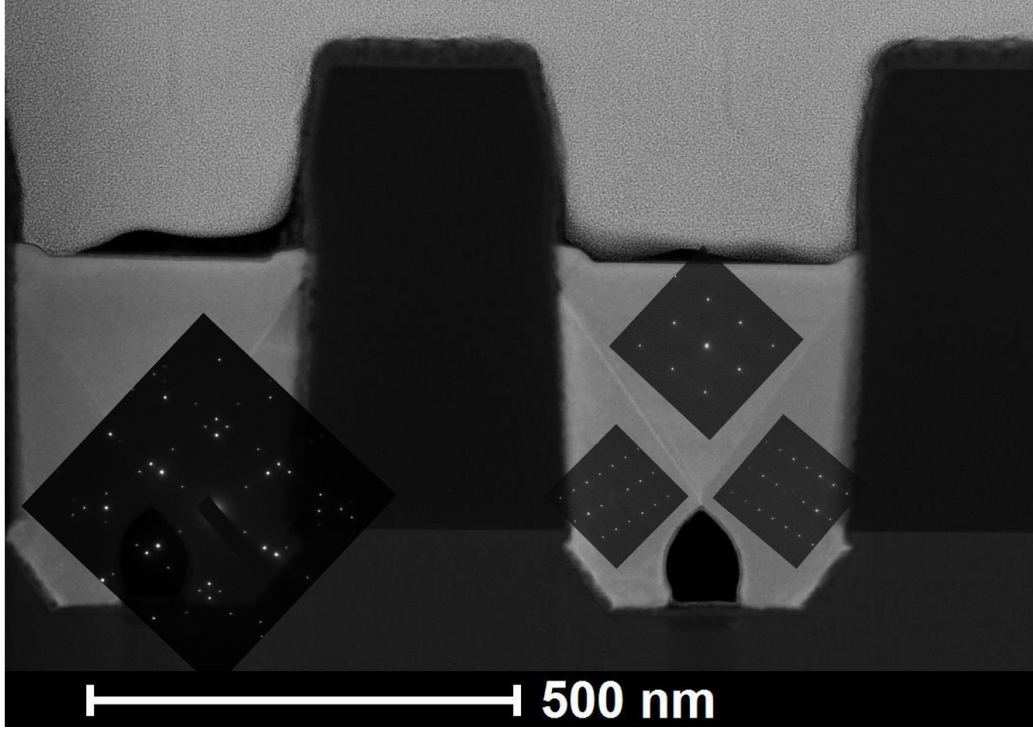


Figure 4.12: Selective area electron diffraction patterns of the U-grooves with overlays. The c-GaN crystals are showing a (110) orientation, the same as the Si(100) substrate.

This shows that the phase transition c-GaN on Si(100) exhibits a 0.4% tensile strain compared to the relaxed lattice constant of 4.5036 Å [62].

4.3 Electron Backscatter Diffraction and Raman Spectroscopy

To study the crystal phases of the GaN in the U-grooves, electron backscatter diffraction (EBSD) measurements are carried out. Crystal phase identification was completed on the same JEOL 7000F SEM fitted with a HKL Technology EBSD System and a high-resolution phosphorus screen/camera for crystallographic measurements. Real time high-speed texture mapping and phase identification were completed on a separate PC using HKL's Channel 5 Tango software.

The electron acceleration voltage is set to 15 kV with a current of 2 nA. The backscattered electrons come from the very top layer (~ 10 nm) of the

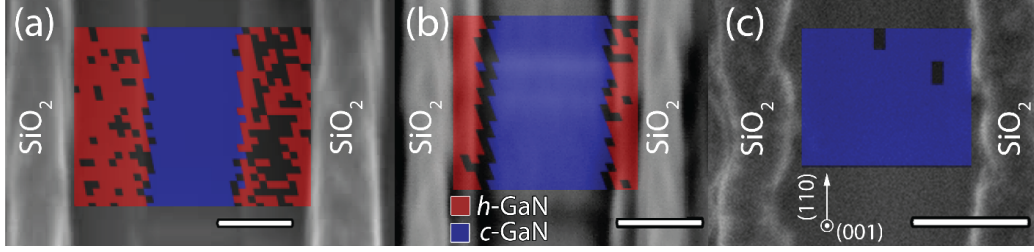


Figure 4.13: Top-view SEM images with EBSD overlay of GaN on U-grooves with (a) $ff = 40\%$, (b) $ff = 65\%$, and (c) $ff = 95\%$. Each pixel has resolution of 20×20 nm, and red, blue, gray colors correspond to h-GaN, c-GaN, and indistinguishable phases, respectively. The crystal orientation of c-GaN is identified and labeled in (c). The white scale bars in the bottom right of each figure correspond to 200 nm. Reprinted from R. Liu and C. Bayram, Appl. Phys. Lett. 109, 38 (2016) with the permission of AIP Publishing.

material in the U-grooves; therefore the information of the crystal is limited to the very surface of the material. The depth estimation is calculated using Monte Carlo simulation using the acceleration voltage.

Figure 4.13 shows the top-view SEM images with EBSD overlays of the U-grooves with different geometries grown in the same MOCVD chamber at the same time, i.e. at different stages of phase transition at (a) $ff = 40\%$, (b) $ff = 65\%$, and (c) $ff = 95\%$. The red and blue pixels indicate hexagonal and cubic, respectively, and have spatial dimension of 20 nm by 20 nm. EBSD identifies the GaN formed in the middle of the grooves as cubic phase with its (001) plane on the top surface and its (110), ($1\bar{1}0$) planes parallel and perpendicular to the U-grooves, respectively. As the ff of the U-groove approaches 100% in (b), the surface coverage of c-GaN increases, until the entire surface is composed of only c-GaN, as shown in Figure 4.13(c). Electron backscatter diffraction shows that the c-GaN formed through phase transition in a U-groove is of single phase, and the crystallographic modeling in Chapter 3 is corroborated.

The sample is then cleaved and placed at 90° for cross-sectional EBSD experiment. Figure 4.14 shows the cross-sectional EBSD phase detection of the $ff = 95\%$ U-groove, showing the GaN phases in red-crossed (hexagonal) and blue-striped (cubic) pixels. This experiment also corroborates the modeling (Figure 3.9(a)) and shows very clear phase separation at the visible V-shaped boundary after the h-phase crystals coalesced at the bottom of the

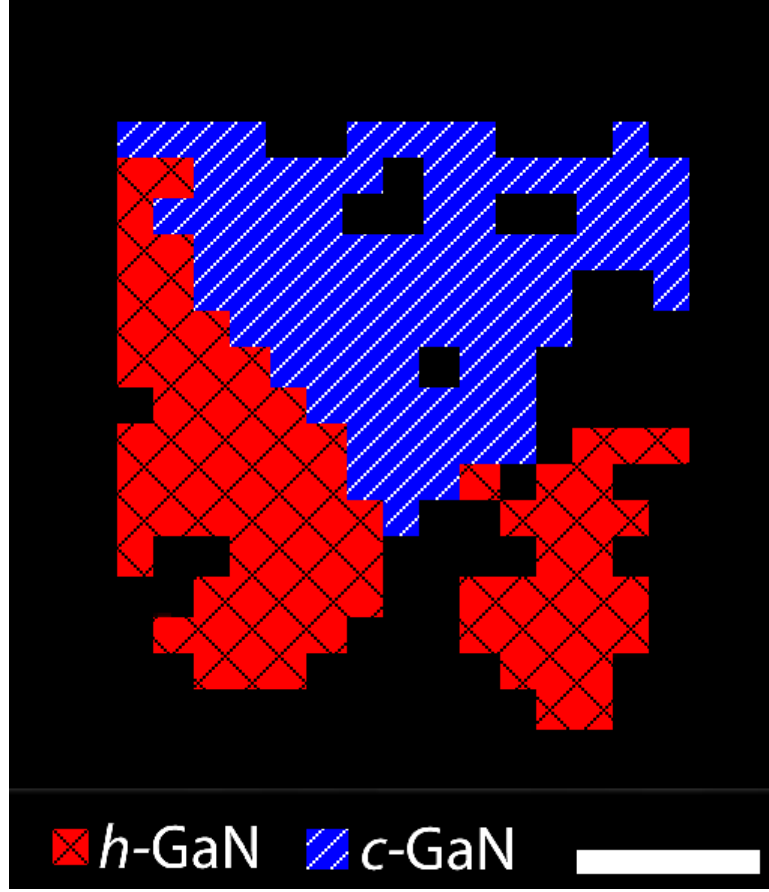


Figure 4.14: Cross-sectional EBSD image of the $ff = 95\%$ period. Reprinted from R. Liu and C. Bayram, J. Appl. Phys. 120, 25106 (2016), with the permission of AIP Publishing.

striped-blue triangle.

To study the crystallinity and strain of GaN materials grown in various-sized U-grooves, Raman spectroscopy is conducted using a Horiba Raman Confocal Imaging Microscope with a depolarized 405 nm laser and an 1800 lines/mm grating. Figure 4.15 shows the Raman shift of the U-grooves of ff from 0% (no phase transition) to 95% (near complete phase transition), to 205% (overfilling, phase mixing).

High-resolution Raman spectra of the TO-phonons are shown in Figure 4.15, in which the 558 cm^{-1} peak, attributed to the $E_1(\text{TO})$ Raman shift of h-GaN, is observed. Another peak at 551 cm^{-1} , attributed to TO-phonons of c-GaN, emerges as the ff value increases from 0% to 95%, signifying the increasing presence of c-GaN [77]. Both peaks of c-GaN show a red shift in their Stokes shift compared to published results (555 and 742 cm^{-1} for TO-

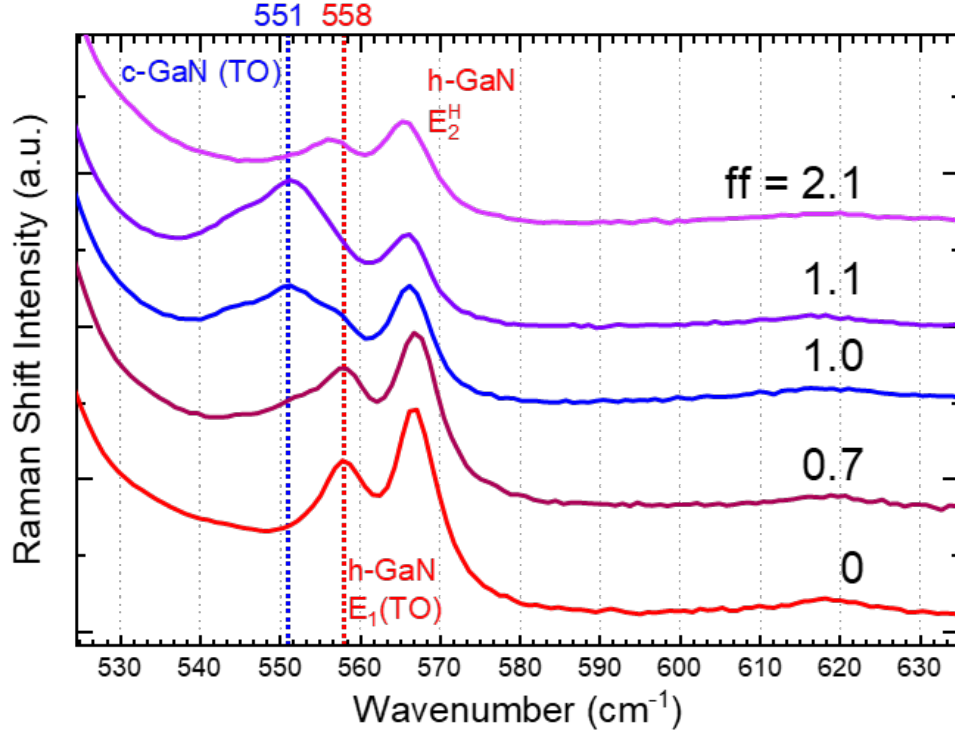


Figure 4.15: Confocal Raman spectroscopy of U-grooves with ff values ranging from 0% (purely h-GaN) to 210% (overgrown-mixed phase GaN). As phase transition occurs, c-GaN's TO-phonons can be observed. At $ff = 205\%$, the extremely over-deposited case, TO-phonon of c-GaN disappears, and the FWHM of h-GaN signal increases, indicating a reduction in crystallinity. Reprinted with permission from R. Liu et al., ACS Photonics 5, 955 (2018). Copyright 2018 American Chemical Society.

and LO-phonons, respectively), indicating c-GaN is under a tensile strain [77], which is in agreement with other studies [69, 78]. At the extreme case of over-deposition ($ff = 205\%$), all GaN related Raman signals decrease in intensity and increase in their FWHM, and the TO-phonon Raman mode of c-GaN becomes unobservable. This is attributed to the phase mixing of the GaN material on the surface as the result of defect formation near the SiO₂ sidewalls in over-growth samples [79]. The Raman spectra demonstrate the effect of optimization on the crystal quality – the near perfect case of phase transition shows the highest crystallinity for c-GaN. Overshooting the critical height (h_c) results in undesired formation of defects.

An accurate second alternative method to study the lattice spacing (and therefore the strain) is to use X-ray diffraction (XRD) conducted on a Bruker D8 using X-ray emissions from both Cu K- α 1 and Cu K- α 2. Figure 4.16

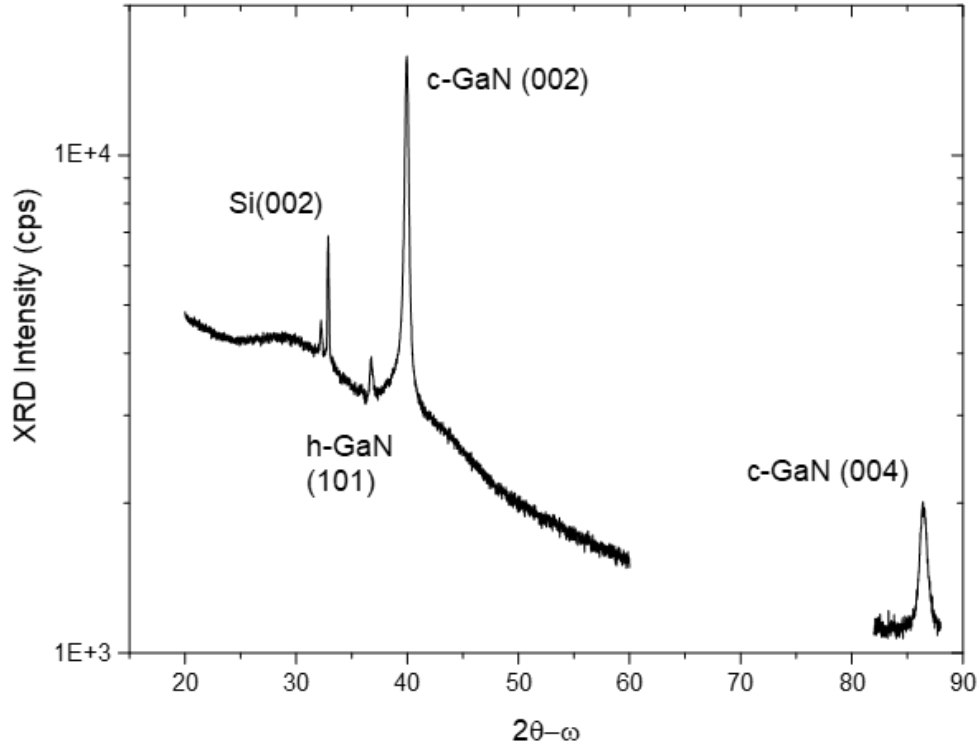


Figure 4.16: Symmetric XRD scan of phase transition c-GaN on Si(100) substrates. An extension of the scan at $82^\circ - 88^\circ$ was conducted to observe the c-GaN (004) reflection.

shows the symmetric $2\theta - \omega$ XRD scan of the U-grooves on Si(100). Four distinct peaks can be observed: Si (002), h-GaN (101), c-GaN (002), and c-GaN (004) in an extended scan. Comparing the measured angle of (002) of c-GaN (39.94°) with that 40.2° angle reported in [61], the c-GaN grown in a U-groove exhibits only a very small amount of tensile strain. The findings from XRD are in good agreement with the calculations from SAED (Figure 4.12) and Raman spectroscopy (Figure 4.15).

CHAPTER 5

FUNDAMENTAL OPTICAL TRANSITIONS IN PHASE TRANSITION CUBIC GALLIUM NITRIDE

This chapter explores the optical properties of the c-GaN using experimental methods. For photonic devices, the optical properties of the semiconductor they are based on dictates their performance. The optical properties indicate the possible quantum efficiency the devices can attain and the design parameters that must be taken into consideration prior to device fabrication. Therefore, detailed optical characterizations are carried out.

In Section 5.1, time-integrated room temperature PL studies are conducted to observe the luminescence characteristics of the phase transition c-GaN. Section 5.2 uses temperature-dependent CL to study the fundamental parameters of the novel c-GaN such as the Varshni coefficient and the defect levels. Using this experiment's data, the internal quantum efficiency is calculated. Section 5.3 switches focus to the optical performance in the time domain using time-resolved PL to study of carrier recombination dynamics in c-GaN.¹

5.1 Room Temperature Photoluminescence

Room temperature photoluminescence (PL) is conducted with a frequency quadrupled Nd:YAG laser emitting at $\lambda = 266$ nm with maximum power of 10 mW. The luminescence is collected by a pair of collimating lenses to guide the light through an adjustable slit with an opening width of 1 mm into a Princeton Instruments spectrometer with three pairs of gratings (300, 600, and 1200 lines/mm) and a 1024 by 100 pixel silicon CCD camera. The integration time was set to 10 seconds averaging over five exposures for a total time of 50 seconds (Figure 5.1). Due to the nonplanar nature of the

¹Portions of this chapter were previously published as [10, 71, 72, 73] and are reprinted with permission. (Copyright 2016 by AIP Publishing, and 2018 by American Chemical Society)

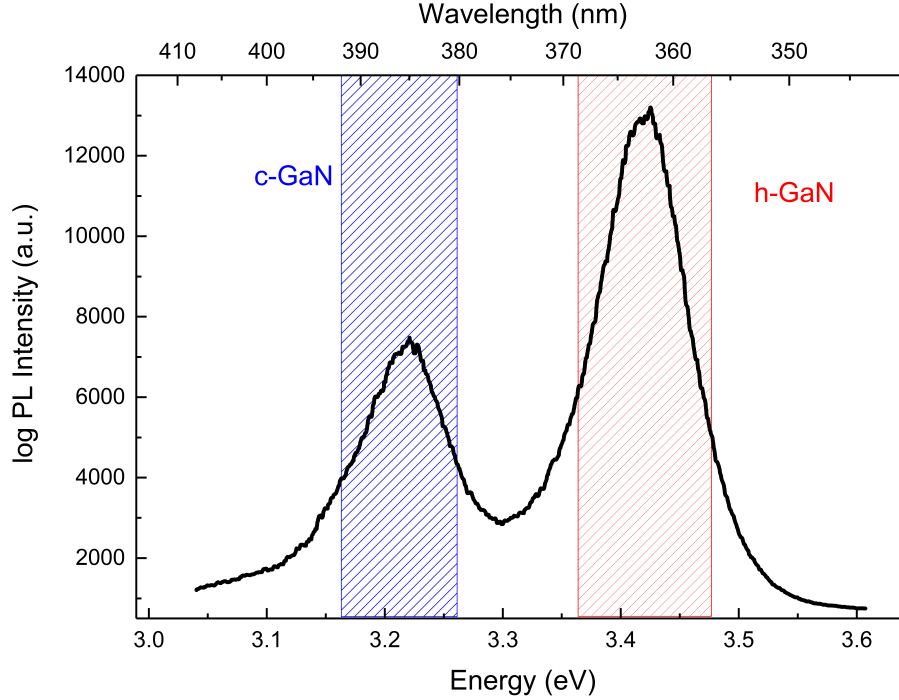


Figure 5.1: Room temperature PL spectra of the U-grooves. Near band edge emissions of h-GaN at 3.42 eV (362 nm, red) and c-GaN at 3.22 eV (385 nm, blue) are observed. Reprinted with permission from R. Liu et al., ACS Photonics 5, 955 (2018). Copyright 2018 American Chemical Society.

phase transition c-GaN on the U-grooves, its thinness, and scattering from the SiO₂ dielectric sidewalls, some UV light does reach the underlying h-GaN. Therefore the overall spectrum is a combination of luminescence from both phases of GaN at 3.42 eV (h-GaN, shaded red) and 3.22 eV (c-GaN, shaded blue).

To study the properties of the light emitted, a polaroid with an extinction ratio of 100:1 is placed between the collimating lenses and the slit for the polarization-dependent PL. The normalized intensities of h-GaN and c-GaN emissions at different polaroid angle with respect to the groove orientation is shown in Figure 5.2. Both phases of GaN show their maximum intensities when the passing axis of the polaroid is parallel to the U-grooves at 0 and 180° and minimum when the polaroid is perpendicular to the U-grooves at 90° and 270°. The orientation of the polarization corresponds to the $\langle 11\bar{2}0 \rangle$ and $\langle 110 \rangle$ directions of h-GaN and c-GaN/Si, respectively. Although the two phases of GaN are polarized in the same axis, their minimum intensities

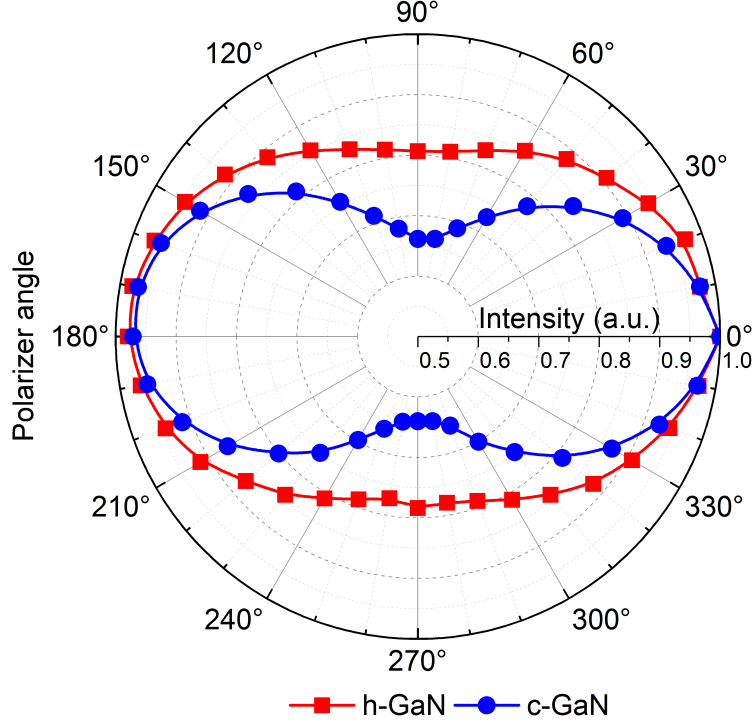


Figure 5.2: Normalized polarization-dependent photoluminescence of the PL emission from h-GaN (red squares) and c-GaN (blue circles). The passing axis of the polarizer angle is parallel to the direction of the U-grooves. The c-GaN shows a higher degree of polarization than h-GaN. Reprinted with permission from R. Liu et al., ACS Photonics 5, 955 (2018). Copyright 2018 American Chemical Society.

are different; c-GaN loses about 34% of its intensity at the minimum while h-GaN only lost 20%. The factors affecting the polarization of both phases of GaN could include the grating-like effect from the U-grooves and the SiO₂ dielectric sidewalls [80] and strain-induced valence band splitting [81].

The magnitude of the polarization of the emitter light can be quantified using

$$\rho = \frac{I_{\parallel} - I_{\perp}}{I_{\parallel} + I_{\perp}} \quad (5.1)$$

where ρ is the *degree of polarization*, I_{\parallel} is the intensity of luminescence when the polaroid is parallel to the U-grooves, whereas I_{\perp} is the intensity when the polaroid is perpendicular to the U-grooves. Polarization-dependent PL shows that h-GaN and c-GaN have a ρ 0.12 and 0.2, respectively. While

the luminescence from h-GaN has been reported to have a strong linear polarization parallel to the direction of the grating [82], uniaxial strain could also contribute to the polarization in c-GaN, too. Polarization-dependent PL therefore cannot conclusively distinguish the contributions from these two effects without the knowledge of strain. From the previous section on strain study conducted using Raman spectroscopy (Section 4.3), which shows c-GaN under a larger degree of tensile strain, the higher *degree of polarization* from c-GaN is likely caused by the additional tensile strain.

5.2 Temperature-dependent Cathodoluminescence

To study the luminescence from the GaN material spatially in both the horizontal plane and the vertical direction, cathodoluminescence (CL) is conducted on a JEOL 7000F Analytical SEM. Because of the excitation mechanism, the injection of high-energy electrons in CL, the location of the GaN crystals that are excited to emit photons can be finely controlled through acceleration voltage, magnification, and dwelling of the electron beam at a specific location. To examine the surface of the U-grooves, which have widths ranging from ~ 200 to ~ 1000 nm, a relatively low acceleration voltage of 2 kV can limit the average penetration depth of electrons to ~ 42 nm, according to Kanaya-Okayama formula [83]. This would minimize the energy loss to the creation of electron-hole pairs (EHPs) in the underlying h-GaN and maximize the signal from the GaN material on the surface, which can be h-GaN, domains of h- and c-GaN, purely c-GaN, or a mixed phase GaN. For the luminescence collection, a Gatan MonoCL3 spectrometer with a paraboloid mirror, a 1200 l/mm grating (blazed at 500 nm) diffraction grating, and silicon CCD thermoelectrically cooled to -17 °C are fitted to the JEOL SEM. This configuration allows for the detection of light from 300 to 900 nm and a spatial resolution limited by diffusion length. The sample is mounted on a liquid helium cold finger mount with a PID temperature controller capable of modulating and measuring the temperature from 5.65 to 400 K.

The CL study is conducted on the selected area grown h-GaN on the Si(111) surfaces without an opposing h-GaN wing to initiate the phase transition (Figure 5.3) and the near perfect, $f = 95\%$, phase transition c-GaN (Figure 5.4) at 280 K (black lines) and at 5.7 K (colored lines). The injection

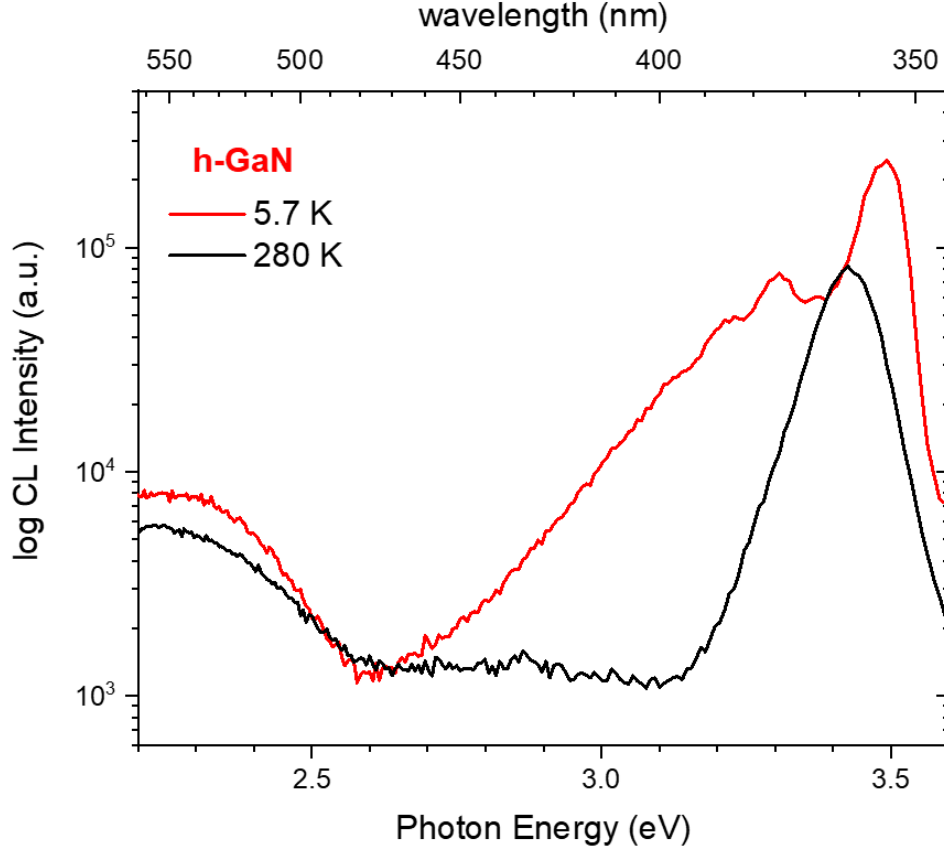


Figure 5.3: Cathodoluminescence (CL) spectra at 280 K (black line) and 5.7 K (red line) of h-GaN.

current is set to 2 nA, as measured by a Faraday cup, and the beam is set to raster over an area of 20 by 30 μm^2 .

At 280 K, h-GaN shows a near band edge (NBE) transition at 3.43 eV, and a broad, yellow luminescence (YL) at around 2.21 eV, whereas c-GaN shows a NBE transition at 3.22 eV, and another broader transition at 2.72 eV (blue luminescence (BL)). These spectra show that the two GaN materials grown in the same MOCVD chamber on the same silicon substrate at the same time are clearly very different. No h-GaN NBE luminescence is observed in the c-GaN spectrum. This suggests that no h-GaN is observed in the complete phase transitioned c-GaN, and the crystal is phase pure. Figure 5.5 shows the CL mapping overlaid on an SEM image of the c-GaN U-grooves.

At cryogenic temperatures, carriers from shallow acceptors and donors are not activated, and therefore transitions involving these impurity states can be observed, and the NBE transitions are dominated by exciton transitions (free

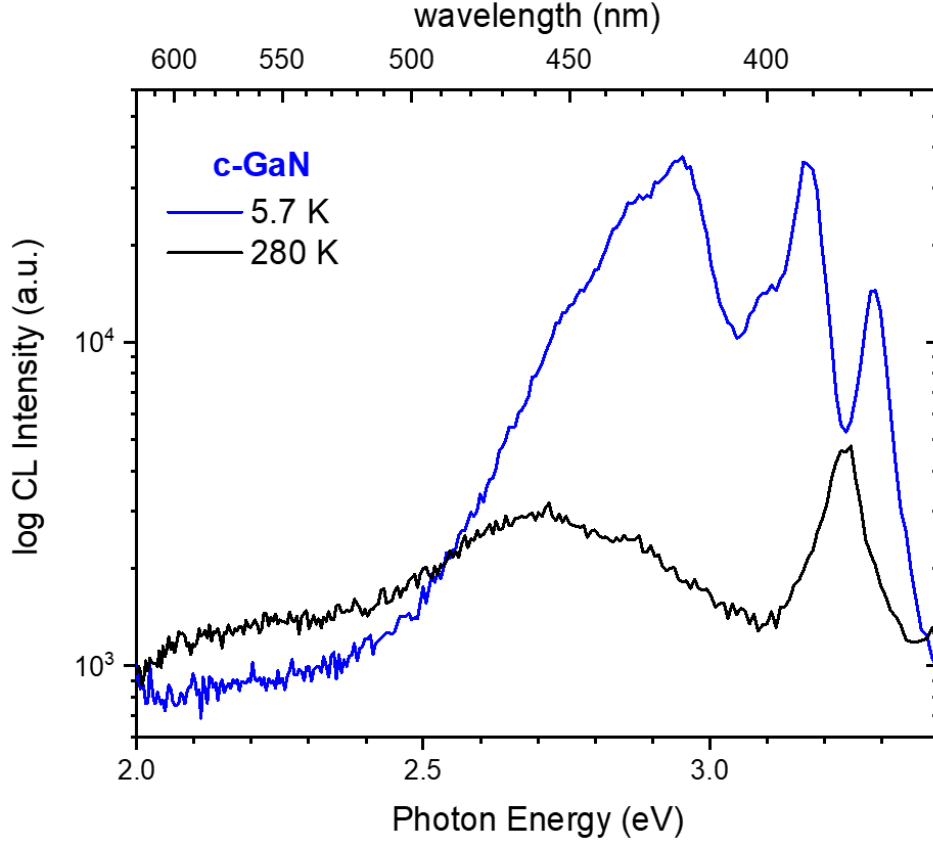


Figure 5.4: CL spectra at 280 K (black line) and 5.7 K (blue line) of c-GaN.

or bound). At 5.7 K, h-GaN shows a bound exciton (BX) transition at 3.49 eV and another transition at 3.31 eV (labeled as DAP_1), which other studies attribute to a donor-acceptor pair (DAP) transition [84]. The acceptor energy involved in DAP_1 can be calculated taking the energy of a typical shallow donor in h-GaN ($E_D \approx 25$ meV) and the excitonic binding energy ($E_{\text{exciton}} \approx 26$ meV) into account:

$$E_g = E_{\text{DAP}_1} + E_D + E_A \quad (5.2)$$

while the bandgap energy at 5.7 K can be calculated as:

$$E_g = E_{\text{BX} + E_{\text{exciton}}} \quad (5.3)$$

These relationships suggest a shallow acceptor level at ~ 180 meV is found in h-GaN that contributes to the CL spectra. LO-phonon replicas of this transition can also be seen at integer multiples of LO-phonon energy (~ 90

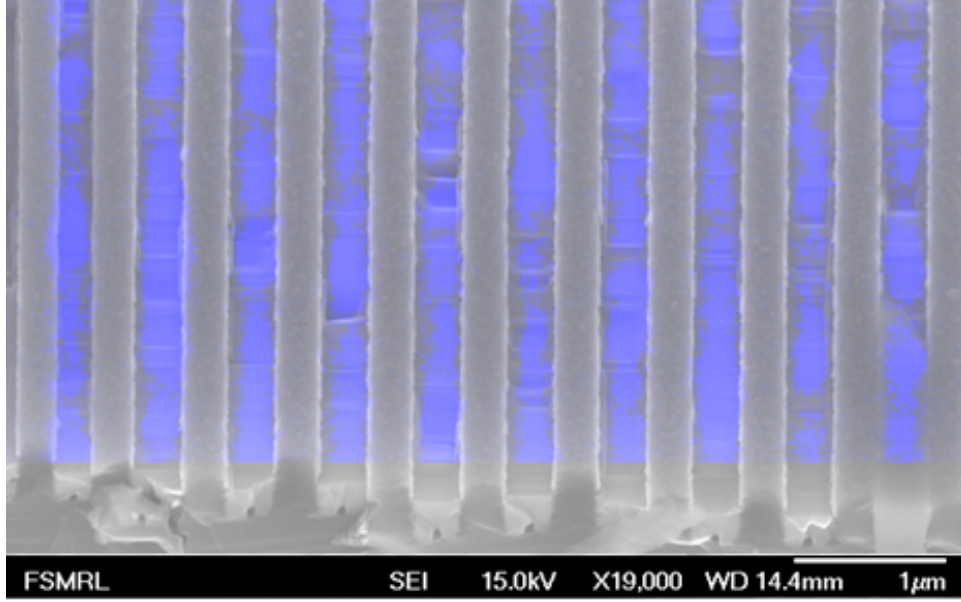


Figure 5.5: CL imaging overlaid on SEM image of the critical condition phase transitioned U-groove. Reprinted from R. Liu and C. Bayram, *J. Appl. Phys.* 120, 25106 (2016), with the permission of AIP Publishing.

meV) lower than the zero phonon line (3.31 eV). The YL at 2.1 eV persists at 5.7 K, and does not seem to have shifted in a measurable way.

The CL spectrum for c-GaN at 5.7 K is more complicated; it shows a BX transition at 3.28 eV, a DAP at 3.18 (DAP₁), and another DAP at 2.95 eV (DAP₂). The DAP₁ transition has been identified as the neutral donor to neutral acceptor (D⁰, A⁰) transition [85]. Using similar methodology as above, the acceptor energy for this transition is ~ 100 meV, which is in line with [86]. DAP₂ emission is observed at a lower energy (~ 230 meV) than DAP₁, suggesting another deep level transition.

In order to understand the origin of these radiative recombination centers, the temperature at which CL is conducted is varied from 5.7 K to 280 K. Figure 5.6 shows the CL spectra of h-GaN and c-GaN collected at 20 K intervals. The dashed lines are centered at the peak position of BX of each respective phase of GaN at 5.7 K for reference.

As the temperature decreases from room temperature to below 140 K, the DAP₁ peak of h-GaN becomes distinguishable along with very strong LO-phonon coupling (Figure 5.3). This transition is believed to be associated with shallow acceptors such as Si-N or C-N complexes [87]. At roughly the same temperature, DAP₂ of c-GaN also becomes visible (Figure 5.4). This

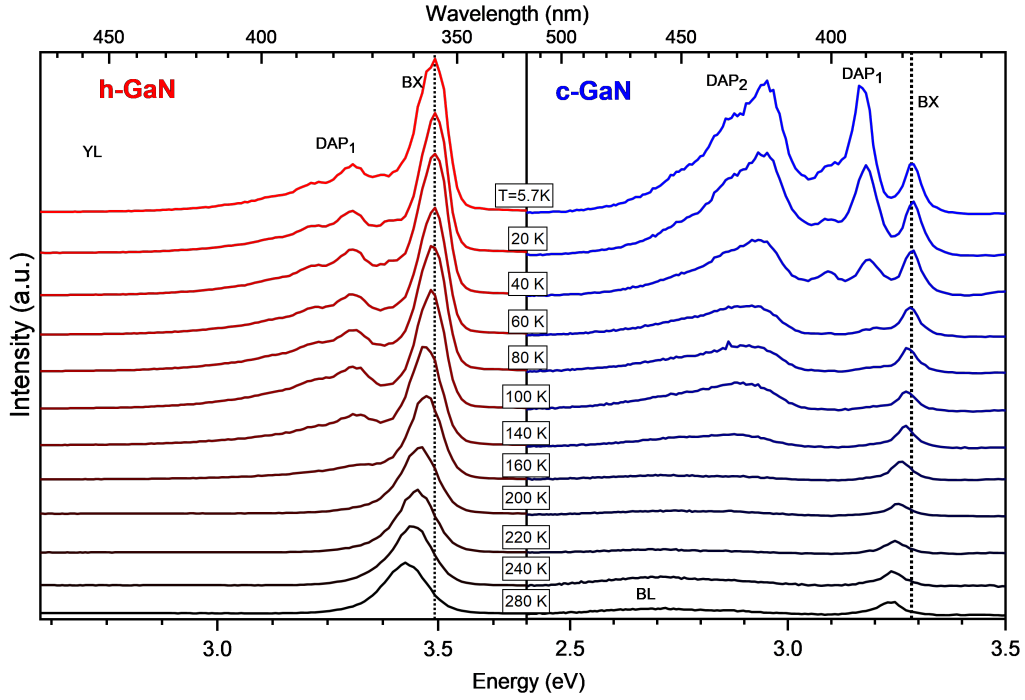


Figure 5.6: Temperature-dependent CL spectra of (left) h-GaN and (right) c-GaN from 280 K to 5.7 K. At 280 K, near band edge emission (BX) of c- (h-) GaN is observed at 3.22 (3.43) eV, whereas at 5.7 K it blueshifts to 3.28 (3.49) eV. At temperatures below 140 K, donor-to-acceptor emission peaks (DAP₁ and DAP₂) appear, and below 60 K, LO-phonon replica emissions become pronounced. The dashed lines are the peak position of BX at 5.7 K drawn across figures for guidance. Reprinted from R. Liu and C. Bayram, J. Appl. Phys. 120, 25106 (2016), with the permission of AIP Publishing.

suggests the origin of DAP₂ in c-GaN could be the same as that of DAP₁ in h-GaN, as they become visible at roughly the same temperature and share the same tendency to form LO-phonon replicas.

The DAP₁ in c-GaN appears to be unique and behaves very differently from these other two DAPs. It becomes observable at a much lower temperature ($T < 60$ K), has a weaker LO-phonon coupling, and grows in intensity much more quickly as temperature decreases. The peak energy of this transition also exhibits positive correlation with temperature. It has been reported that this blueshifting behavior is due to the thermalization of the shallow donors associated with this transition that shifts the recombination from a (D^0 , A^0) into a free electron to acceptor transition (e , A^0) [88].

At temperatures below 60 K in c-GaN, another peak at ~ 3.08 eV (unla-

beled) appears albeit with a much weaker intensity. In the literature, this peak has been attributed to free-to-bound (e, A^0) or another donor-acceptor pair (D^0 , A^0) associated with carbon residuals during MOCVD growth or arsenic from the substrate, since most of these studies were performed on c-GaN grown on planar cubic substrates such as GaAs [89]. The relatively weak emission at this wavelength on the c-GaN on nanopatterned Si(100) suggests the luminescence at 3.08 eV is more likely associated with an acceptor other than As.

It has been suggested that DAP_2 in c-GaN is a LO-phonon replica of the DAP at 3.08 eV on GaAs substrates [90], but this is clearly not the case in the data shown in Figure 5.4. The zero phonon line is usually much stronger than the phonon replicas, and the energy spacing between DAP_2 and 3.08 eV is not an integer multiple of the LO-phonon energy.

The YL emission of h-GaN at 2.3 eV, which has been reported to originate from native defects such as V_{Ga} and its complexes ($V_{Ga}O_N$, $V_{Ga}C_N$, $V_{Ga}Si_{Ga}$) [91], remained stable in intensity and peak energy throughout the temperature range. This behavior is similar to that reported in [92]. The BL of c-GaN, on the other hand, starts to overlap with DAP_2 and its LO-phonon replicas at temperatures below 140 K, and therefore becomes unobservable.

5.2.1 Donor-acceptor pair energy calculations

To accurately find the temperature dependence, and therefore their origins, of the three luminescence centers (BX, DAP_1 , DAP_2) in c-GaN, their energies are fitted using models against temperature in Figure 5.7. The exciton emission (BX) can be used to calculate the bandgap at a specific temperature in conjunction with the excitonic binding energy ($E_{exciton}$). The temperature dependence of the bandgap of h-GaN and c-GaN can be described empirically by Varshni's equation [93]:

$$E(T) = E_0 - \frac{\alpha T^2}{(T + \beta)} \quad (5.4)$$

where E_0 is the bandgap at 0 K, α is the Varshni's coefficient, and β is conventionally taken as the Debye temperature of GaN (600 K). The least square fit yields $E_0=3.31 (\pm 0.01)$ eV and $\alpha = (6.83 \pm 0.22) \times 10^{-4}$ eVK⁻¹ for c-GaN ($E_0=3.51 (\pm 0.01)$ eV and $\alpha = (7.37 \pm 0.13) \times 10^{-4}$ eVK⁻¹ for h-GaN),

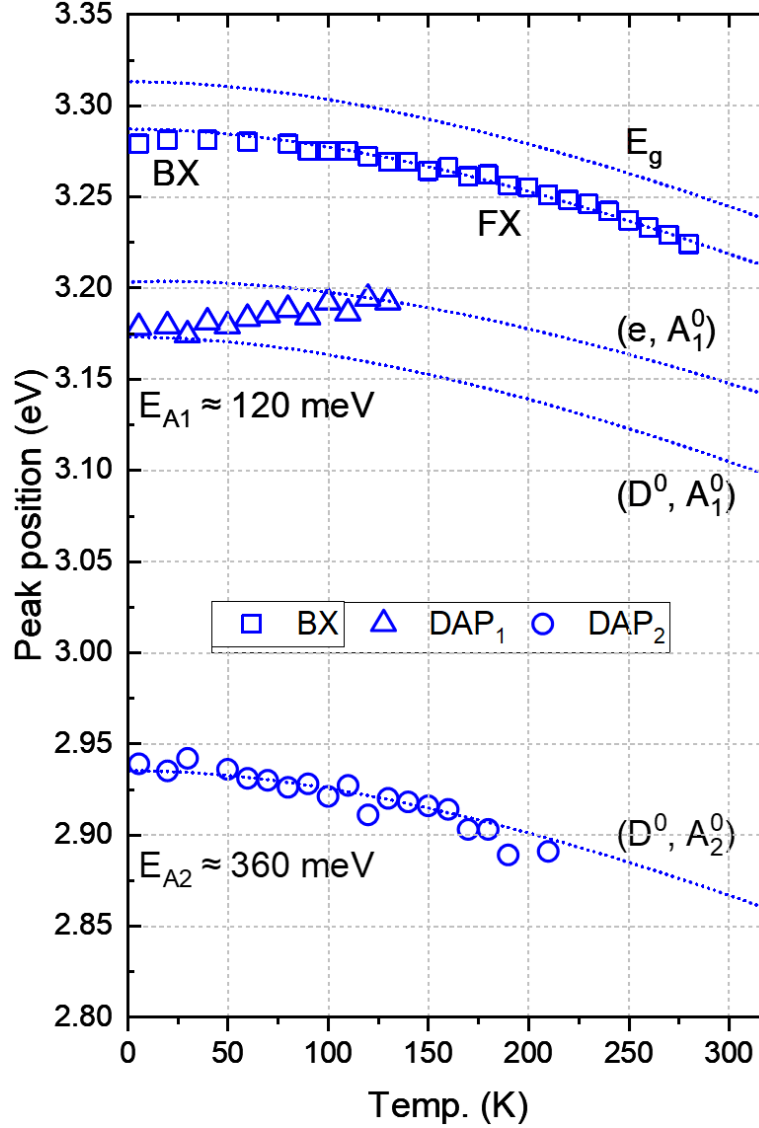


Figure 5.7: Temperature-dependent CL peak positions of excitonic (bound, BX, and free, FX) transitions (squares) and DAP₁ (circles) and DAP₂ (triangle) of c-GaN. The bandgap energy (E_g) is calculated and fitted by Varshni's equation. At temperatures below 20 K, FX transition shifts to a BX transition with a binding energy of ~ 9 meV. DAP₁ transitions from a donor-acceptor pair (D^0, A_1^0), with an acceptor energy of 110 meV and a donor energy of ~ 25 meV, to a free-to-acceptor (e, A_1^0) transition as the temperature increases. DAP₂ shows a donor-acceptor pair (D_0, A_1^0) transition with acceptor energy of $E_{A2} = 360$ meV. Reprinted from R. Liu and C. Bayram, J. Appl. Phys. 120, 25106 (2016), with the permission of AIP Publishing.

similar to that of c-GaN grown on other substrates such as GaAs [94, 95, 96]. The small deviation of the data from the FX fitted line at temperatures below 20 K indicates a transition from FX-dominated transition to a BX-dominated one.

The DAP₁ transition requires taking two different types of transitions into consideration: free electron to acceptor (e, A⁰) at higher temperatures, shown as triangles, and the neutral donor to neutral acceptor transition (D⁰, A⁰), shown as circles. Their energies are calculated using:

$$h\nu (e, A^0) = E_g(T) - E_D + \frac{kT}{2} \quad (5.5)$$

for the free-electron-to-acceptor transitions, and

$$h\nu (D^0, A^0) = E_g(T) - E_D - E_A + \alpha N^{\frac{1}{3}} \quad (5.6)$$

for the neutral-donor-to-neutral-acceptor transitions, where

$$\alpha = \left(\frac{4\pi}{3} \right)^{\frac{1}{3}} \times \frac{e^2}{4\pi\epsilon\epsilon_0} \quad (5.7)$$

in which N is the dopant concentration and α is a material property (for GaN ($\epsilon = 9.7$), $\alpha = 2.39 \times 10^{-8}$ eV cm).

Using a typical unintentionally doped impurity concentration of 10^{16} cm⁻³ for unintentionally doped MOCVD-grown GaN, the last term in Equation (5.6) is about 5.1 meV. Least square fitting with these parameters reveals an acceptor level of $E_{A1} \approx 110$ meV for DAP₁ (squares), and $E_{A2} \approx 360$ meV for DAP₂ (circles). DAP₂ is attributed to intrinsic defects such as gallium vacancy (V_{Ga}), as it is a common defect in MOCVD-grown material [84]. Its transition remains as a donor-to-acceptor transition, and never shifts to a free electron-to-acceptor pair.

Injection power-dependent CL (PDCL) at 5.7 K is conducted (Figure 5.8) to observe any possible saturation of these luminescence centers to verify their origins. Defect or impurity originated luminescence often has a limited density of states for recombination that can be overfilled when too many injected EHPs are present. The study is conducted on the $\bar{f}\bar{f} = 95\%$ c-GaN U-grooves, as these are shown by structural characterization techniques (Section 4.3) to be the most optimized U-groove for the growth of fully phase transitioned c-GaN, and provide the largest surface coverage of phase-

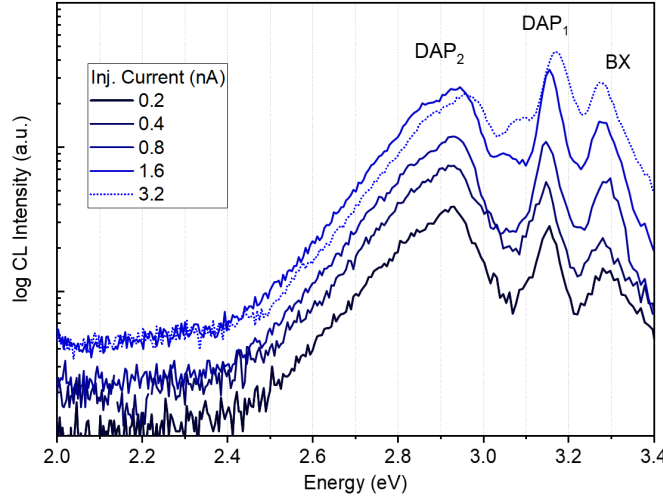


Figure 5.8: Logged low-temperature (5.7 K) CL spectra of c-GaN at increasing injection current from 0.1 to 3.2 nA. Bound exciton (BX) at 3.28 eV, two donor-acceptor pairs at 3.18 (DAP₁) and 2.95 (DAP₂) eV, as well as their LO-phonon replicas, of c-GaN are observed. Both DAPs show saturation and blueshift at high injection current.

transition c-GaN with the highest crystal quality. The experiment was done with the SEM in rastering scan mode, which would reveal any possible h-GaN inclusion in a $20 \times 30 \mu\text{m}^2$ area on the surface (Figure 5.5).

The three previously identified luminescence centers, BX, DAP₁ and DAP₂, can be seen behaving differently under increasing injection current from 0.1 to 3.2 nA. The peak intensities of both DAPs increase linearly with injection current. However, between 1.6 and 3.2 nA, the trend goes from linear increase to sublinear for DAP₁ and negative for DAP₂. Additionally, the peak centers also experienced a strong blueshift to higher energies. These phenomena are the manifestation of the saturation of defect related recombination centers and strongly suggest their defect-originated nature. As the injection of EHPs exceeds the rate at which the DAPs can absorb them to emit photons, excess carriers are recombined via different and higher energy recombination mechanisms. The BX peak exhibits neither of these behaviors, as a band-to-band transition has a density of states that is orders of magnitude greater than those of DAPs, and usually cannot be saturated using electron beam injections in CL [97].

One of the advantages of CL over other forms of luminescence study is its ability to physically image the spatial distribution of the luminescence centers

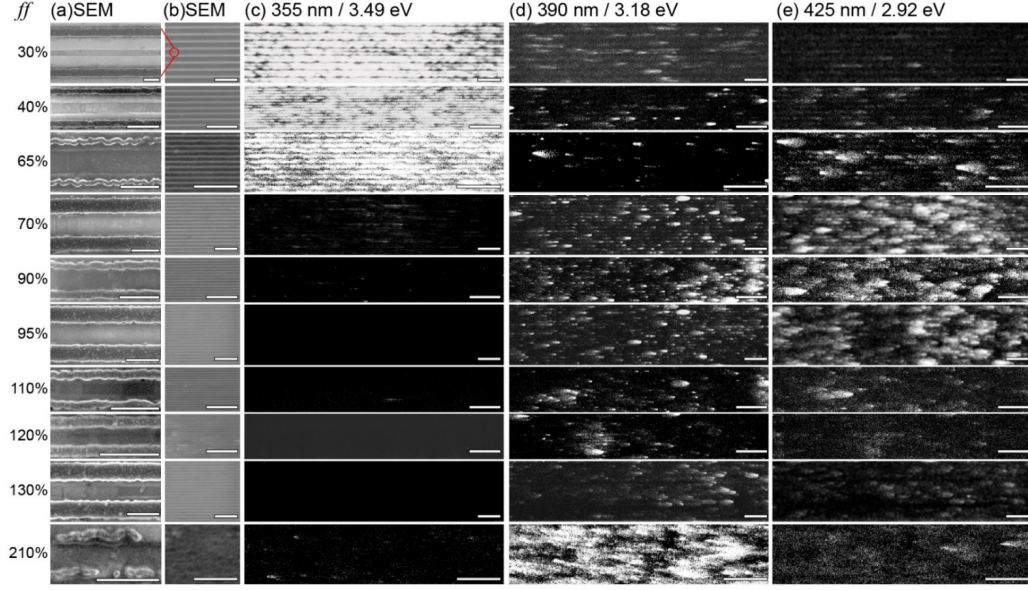


Figure 5.9: Plane view SEM and CL images of GaN on various U-grooves. (a) High-magnification SEM images with scale bar of 500 nm. (b) Low-magnification SEM image, and its corresponding monochromatic CL images at (c) the bandgap of h-GaN at 355 nm, (d) DAP₁ of c-GaN at 390 nm, and (e) DAP₂ of c-GaN at 425 nm. Reprinted with permission from R. Liu et al., ACS Photonics 5, 955 (2018). Copyright 2018 American Chemical Society.

with a resolution less than 1 μm . Figure 5.9 shows (a) high-magnification and (b) low-magnification SEM images of the U-grooves with various $f\text{-}f$ values ranging from 30% to 205%. The monochromatic CL images of the grooves shown in Figure 5.9 (b) at $\lambda = 355$ nm (3.49 eV, (h-GaN BX)), 390 nm (3.18 eV, c-GaN DAP₁) and 425 nm (2.95 eV, c-GaN DAP₂), are shown in Figure 5.9(c), (d), (e), respectively.

The luminescence of h-GaN BX (Figure 5.9 (c)) in the underfilled U-grooves ($f\text{-}f = 30\%$, 40% , 65%) is very uniform and intense, which indicates the presence of h-GaN on the surface. In contrast, the intermediate U-grooves ($f\text{-}f = 65\%$, 70% , 90%) only show sparsely lit spots in this wavelength. This indicates the GaN materials on the top ~ 47 nm layer of these U-grooves are not composed of h-GaN and have already undergone phase transition. The distribution of the c-GaN DAPs is point-like and randomly distributed. This is an indication of defect or impurity-originated emissions.

The most optimized U-grooves ($f\text{-}f = 95\%$) show no observable h-GaN emission, similar to the observation made in their CL spectrum (Figure 5.4).

This indicates the excellent spatial uniformity of c-GaN on the surface of these U-grooves in these grooves over a large area. In contrast, the U-grooves with $ff > 100\%$, which indicates overfilling of the U-grooves (Figure 4.4), exhibit small traces of h-GaN BX luminescence scattered randomly across the image. This suggests the relaxation of the c-GaN crystal to h-GaN in a randomly distributed fashion.

The distribution of DAP_1 (Figure 5.9 (d)) of c-GaN at 3.18 eV is scattered randomly across the images in point-like clusters. The intensity and concentration of these clusters seem to have a weak dependence on the optimization of c-GaN (strongest at $ff = 100\%$), but increase greatly when there is a large extent of phase mixing and defect formation ($ff = 210\%$). This suggests the defect could be linked to the phase boundary (stacking faults), near which carriers from each phase of GaN recombine near the type II alignment of bandgap (staggered) [98]. Since the growth condition is the same across all U-grooves, impurity concentration is unlikely to have changed. Therefore DAP_1 is more likely related to intrinsic defects. Given the trend across various ff s, stacking faults in the (111) planes are the most likely explanation of this luminescence [99]. The formation of these stacking faults near the c-GaN/SiO₂ interfaces can be observed in Figure 4.9.

The distribution of DAP_2 in c-GaN (Figure 5.9 (e)) is different from that of DAP_1 . Even though the two centers do show the same point-like clusters, their correlations between the intensity and the phase transition optimization (ff) are different. They are both the strongest near $ff = 100\%$, but only DAP_1 is present in the greatly overfilled case ($ff \gg 100\%$). This suggests that DAP_2 coexists only with c-GaN, whereas DAP_1 likely originates from the interaction between h-GaN and c-GaN. Given the energy level calculated previously, DAP_2 in c-GaN and DAP_1 in h-GaN are likely the same DAPs in different crystal lattice that manifest different transition energies.

5.2.2 DAP activation energy calculation

The intensities of the peaks in c-GaN measured by temperature-dependent CL across the temperature range can be used to calculate the energies of the donors and acceptors involved. As the temperature increases, the thermalization of the donors/acceptors, and therefore the dissociation of the DAP,

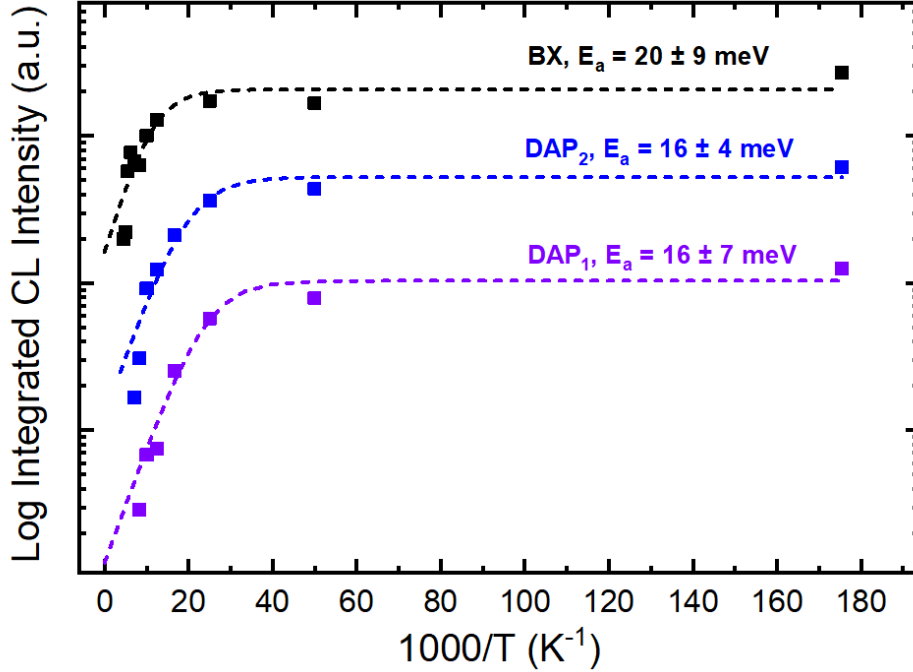


Figure 5.10: Arrhenius plot of c-GaN CL emissions at 5.7 K. Fitting shows activation energy of 20 ± 9 , 16 ± 7 , 16 ± 4 meV for BX (exciton binding energy), DAP₁ (shallow donor), DAP₂ (shallow donor) respectively. Reprinted with permission from R. Liu et al., ACS Photonics 5, 955 (2018). Copyright 2018 American Chemical Society.

reduces their intensities. By extracting the temperature at which this dissociation occurs using the Arrhenius equation, the activation energy of the donors can be found (Figure 5.10). The integrated intensity obeys [100]:

$$I(T) = \frac{I_0}{1 + C \exp(-E_{act}/k_B T)} \quad (5.8)$$

where I_0 , C are fitting constants, k_B is the Boltzmann's constant, and T is the temperature. Fitting of the experimental data reveals donor activation energy (E_a) of 20, 16, and 16 meV for BX (black), DAP₁ (violet), and DAP₂ (blue), respectively.

The activation energy for BX corresponds to the excitonic binding energy of ~ 20 meV [101]. The similarity between the activation energies obtained for the DAPs suggests these transitions involve the same shallow donor species. In the case of U-grooves on Si(100), silicon desorption and doping of the GaN crystal is a likely source for the shallow donor [102]. Using the extracted donor activation energy, bandgap of c-GaN at 0 K [8], and

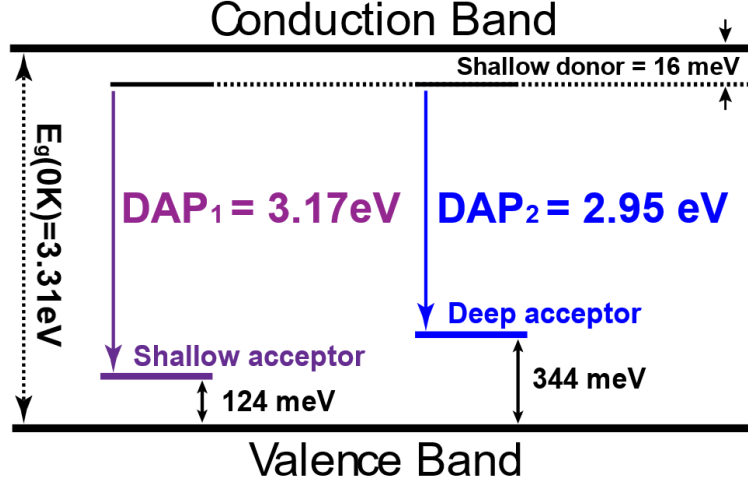


Figure 5.11: Band diagram for the phase transition c-GaN with radiative defects observable at cryogenic temperatures. Reprinted with permission from R. Liu et al., ACS Photonics 5, 955 (2018). Copyright 2018 American Chemical Society.

the energies of photon emitted (Figure 5.4), the revised acceptor energies for these DAP transitions are 124 meV (DAP₁) and 344 meV (DAP₂). The shallow acceptor at 124 meV above the valence band is of particular interest, as it demonstrates the possibility of a much higher p-type doping efficiency and conductivity of c-GaN than that of h-GaN. A proposed band diagram of c-GaN is shown in the inset in Figure 5.11.

5.2.3 Thermal approach to IQE calculation

The internal quantum efficiency (IQE) for photonic devices is a measure of the ratio of carriers that undergo the desired radiative recombination over all recombination. These other recombination paths include defect-assisted trapping called Shockley-Reed-Hall (SRH) recombination, and the three particle (direct and indirect) Auger recombinations. IQE provides an insight to how efficient a photonic device is, and is often used to gauge the performance of a device or a fabrication technique against one another.

Using the results from the temperature-dependent CL study, IQE of the band-to-band transition of h-GaN (3.48 eV) and c-GaN (3.28 eV) is calculated using:

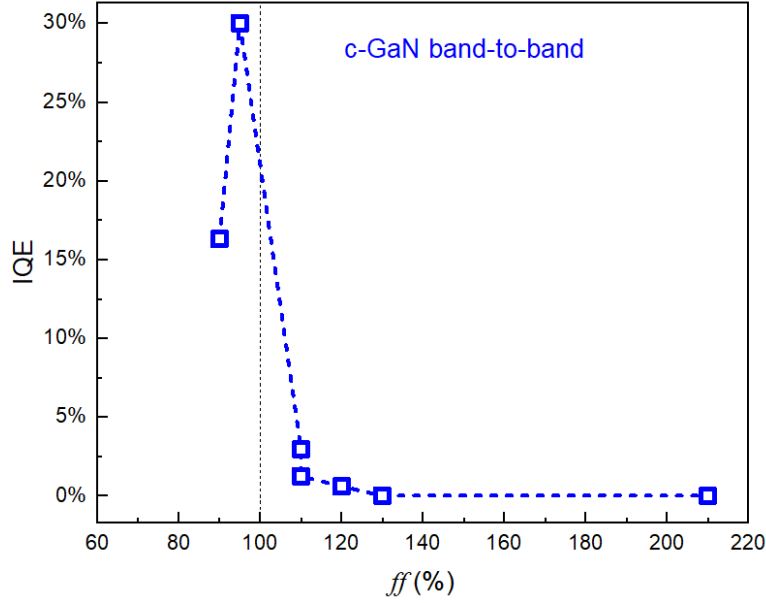


Figure 5.12: Effect of optimization (ff) on the internal quantum efficiency of the c-GaN band-to-band emission. Reprinted from R. Liu and C. Bayram, Appl. Phys. Lett. 109, 38 (2016), with the permission of AIP Publishing.

$$\eta_{QE}(T) = \frac{I(T)}{I(5.7K)} \quad (5.9)$$

where $I(T)$ is the integrated intensity as a function of temperature and $\eta_{QE}(T)$ is the internal quantum efficiency, assuming the nonradiative recombination centers are fully deactivated at 5.7 K [103]. Figure 5.12 shows the IQE of c-GaN across U-grooves with various ff s from 0% (pure h-GaN) to 210% (the U-grooves shown in the bottom row of Figure 5.9). The IQE for c-GaN increases very rapidly as the value of ff approaches 100%, and drops precipitously to very small values once the value of ff exceeds 100%. It is clear that the highest IQE (29%) is only obtained with U-grooves at or near the critical condition ($ff = 100\%$).

The estimated IQE for the $ff = 95\%$, the U-groove closest to perfect phase transition, c-GaN band-to-band transition is plotted as a function of temperature in Figure 5.13. A similar experiment is conducted on planar, bulk h-GaN on commercial Al_2O_3 substrate for comparison.

The IQE and CL imaging reinforces the importance of U-pattern optimization; any deviation from the critical condition of $ff = 100\%$ is going to degrade the performance sharply.

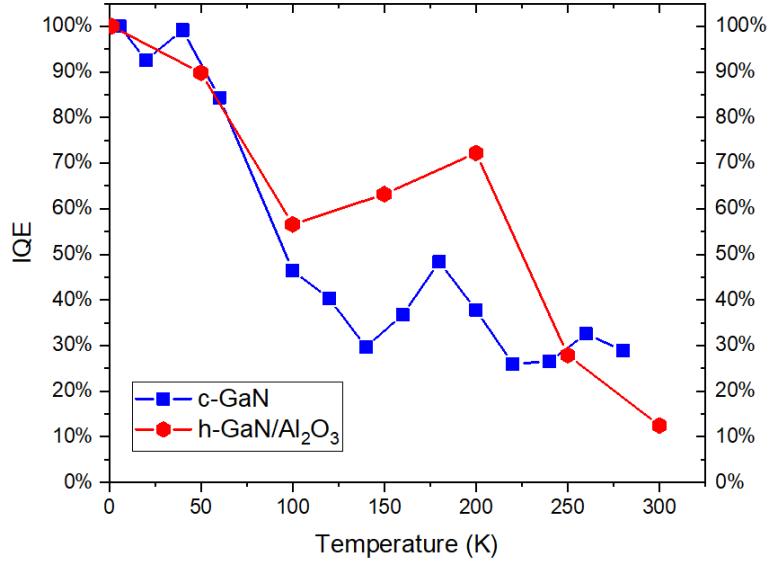


Figure 5.13: The temperature dependence of the IQE of the $\mathcal{f} = 95\%$ U-grooves and conventional h-GaN on Al₂O₃ substrates. Reprinted from R. Liu and C. Bayram, Appl. Phys. Lett. 109, 38 (2016), with the permission of AIP Publishing.

5.3 Time-Resolved Photoluminescence

To study the carrier recombination dynamics in the c-GaN, time-resolved photoluminescence (TRPL) studies are carried out. Carrier recombination lifetime can provide insight into the efficiency of each recombination mechanism. For LEDs, the radiative recombination lifetime should be as short as possible (and therefore making the rate high) to make it the most efficient recombination pathway in order to out-compete other undesired nonradiative mechanisms such as SRH and Auger recombinations.

The experiment was completed at the Center for Nano Materials, Argonne National Laboratory, using a frequency-tripled Ti:sapphire laser lasing at $\lambda = 266$ nm with a pulse duration of ~ 150 fs and a repetition rate of 80 MHz. Data collection was completed using a Hamamatsu streak camera with a < 1 ps temporal resolution. Figure 5.14 shows the TRPL data for h-GaN (left) and c-GaN (right), which correspond to the free exciton transitions of h-GaN (3.42 eV) and c-GaN (3.22 eV), respectively [8]. Time-resolved PL intensity shows a monoexponential decay with a PL lifetime of 20 ps for h-GaN and 11 ps for c-GaN.

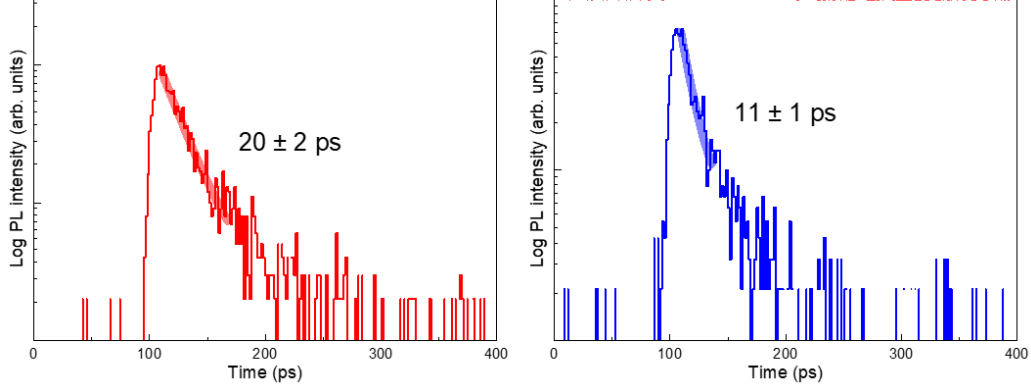


Figure 5.14: Time-resolved photoluminescence of the bandgap emission of (left) h-GaN and (right) c-GaN. Reprinted with permission from R. Liu et al., ACS Photonics 5, 955 (2018). Copyright 2018 American Chemical Society.

The measured PL lifetime τ_{PL} is a combination of radiative τ_{rad} and non-radiative recombination lifetime τ_{nr} through the following relationship:

$$\tau_{PL}^{-1} = \tau_{nr}^{-1} + \tau_{rad}^{-1}. \quad (5.10)$$

It has been reported that the radiative lifetime in semiconductors is determined by the scattering from the excitonic branch to the photonic branch of the exciton-polariton dispersion curves [104]. Therefore, theory suggests that radiative lifetime for a 200 nm thick GaN film can be expressed as:

$$\tau_{rad} = \frac{1}{2} \left(\frac{5\pi}{3} \right)^{\frac{3}{5}} \left(\frac{M}{\nu_0} \right)^{\frac{2}{5}} \left\{ \frac{\hbar^2 c^7 \alpha_p L^3}{C^4 \omega^6} \right\}^{\frac{1}{5}} \quad (5.11)$$

where M/ν_0 is the mass per unit volume of the unit cell (3 kgm^{-3}), α_p is the polarizability (4×10^{-5}), L is the thickness of the excited layer ($\sim 200 \text{ nm}$), $\hbar\omega$ is the photon energy of the excitonic transition (3.42 eV), and C is the deformation potential (4 eV) [105].

Equation (5.11) yields a theoretical radiative lifetime of $\sim 470 \text{ ps}$ for h-GaN. The corresponding predicted radiative lifetime of c-GaN is estimated to be $\sim 47 \text{ ps}$. The theory predicts c-GaN would have a radiative recombination lifetime one tenth that of h-GaN, and this prediction has been corroborated by experiments [106, 107]. This is mainly due to the greater electron-hole wavefunction overlap, which results in a greater oscillator strength, in the absence of the MV/cm level of polarization fields in c-GaN.

It has been reported that the internal electric field in h-GaN strongly decreases the oscillator strength via quantum confined stark effect [107]. The absence of internal polarization effect is very evident in c-GaN based devices. Studies conducted on c-GaN and h-GaN quantum dots (QDs) concluded that the QCSE are the cause of the 10 times longer PL lifetime in h-GaN. Additionally, increasing the diameter of c-GaN QDs does not significantly decrease the radiative recombination rate, whereas h-GaN QDs experiences a very dramatic decrease (IQE decreased from 80% to 25%) [108]. This demonstrates the effect of the polarization field, and the detrimental effect of QCSE in wavefunction overlap. Therefore QDs and QW-based LEDs have a design limitation to keep the carriers confined as tightly as possible. The disadvantage of this approach is small active volume and difficulty in carrier transport, as discussed previously in Chapter 1.

For the nonradiative lifetimes, c-GaN has been reported to have one that is about an order of magnitude shorter than those of h-GaN mainly due to the much higher defect density [106].

Studies have reported that high-quality lateral epitaxial overgrowth (LEO) grown h-GaN on sapphire exhibits a radiative lifetime in the range of 80 ~ 210 ps at room temperature [109, 110], and 530 ps for bulk, freestanding GaN grown by hydride phase vapor epitaxy (HVPE) [111]. These values are much longer than the one shown in Figure 5.14 for h-GaN. The difference likely stems from the fact that the h-GaN crystals are very small, are surrounded by semiconductors with smaller bandgap, and are adjacent to interfaces and surfaces that do act as recombination centers.

For c-GaN, the lifetime observed in Figure 5.14 is similar to that of studies conducted on 1 μm thick c-GaN films on 3C-SiC at ≈ 15 ps [112]. This demonstrates the similarity in crystal quality between the 300 nm thick phase transition c-GaN and the molecular beam epitaxy (MBE) grown c-GaN on the expensive 3C-SiC substrate. This demonstrates the improvement in growth technology of c-GaN using U-groove phase transition over conventional planar epitaxy.

Using the τ_{rad} predicted theoretically and the measured PL lifetime, τ_{nr} can be calculated using Equation (5.10). For h-GaN, τ_{nr} is calculated to be 21 ps, which implies the recombination in h-GaN is dominated by nonradiative recombination. The stacking faults along the hexagonal-cubic phase transition interfaces may act as nonradiative recombination centers [98]. The

h-GaN–silicon and c-GaN–air interfaces may also provide another carrier loss mechanism.

On the other hand, a fast PL lifetime could also be the result of a strong radiative recombination resulting from the higher degree of confinement provided by quasi 1D nature of the U-grooves. It has been reported that c-GaN has a significantly higher oscillator strength with its smaller bandgap and lack of polarization fields [106].

5.3.1 IQE approach to radiative recombination lifetime

Another approach to estimate τ_{rad} of c-GaN is to utilize the IQE calculated from temperature-dependent CL from Section 5.2.3. Using IQE = 29% and the measured $\tau_{PL} = 11$ ps for c-GaN, the τ_{rad} is extracted using:

$$\eta_{IQE} = \frac{\tau_{PL}}{\tau_{rad}} \quad (5.12)$$

which yields a τ_{rad} of 38 ps, which is ~ 12.4 times shorter than the value for h-GaN. The finding in the TRPL for c-GaN is in good agreement with the other studies in the literature and is remarkably similar to the value (47 ps) calculated using Equation (5.11).

The observed radiative lifetime of 38 ps in c-GaN can be used to extract fundamental material properties. Assuming similar mass density and deformation potential as h-GaN, the polarizability of c-GaN, α_p , can be calculated using Equation (5.11). This value is estimated to be 8.3×10^{-11} , which is $\approx 10^7$ times smaller than that of h-GaN.

CHAPTER 6

EFFECT OF SUBSTRATES AND STRAIN ON HEXAGONAL PHASE INGAN EMITTERS ON SILICON(111)

This chapter explores the hexagonal InGaN multiple quantum wells grown on various conventional substrates using MOCVD. These substrates include Al_2O_3 and Si(111). While Si(111) appears to be the more appropriate comparison to c-GaN on Si(100) due to the scalability of the silicon substrates thanks to the available substrate diameters and cost, the industry standard substrate is Al_2O_3 . While determining which substrate is the more suitable comparison, differences between emitters grown on Al_2O_3 and Si(111) substrates yielded significant differences in their optical performances. This is expected as the strain difference between h-GaN, Al_2O_3 , and Si(111) is a significant -16% and +17%. The change in the sign of strain (from compressive to tensile) and the sheer magnitude will impact the crystal quality, and thus the device performance. In order to quantify the differences between these two benchmark h-GaN devices, six periods of 2-nm-thick $\text{In}_{0.15}\text{Ga}_{0.85}\text{N}$ /13-nm-thick GaN blue emitting multi-quantum-well (MQW) layers are grown on sapphire (Al_2O_3) and silicon (Si) substrates.¹

6.1 Introduction

Indium gallium nitride (InGaN) / gallium nitride (GaN) multiple quantum well (MQW)-based blue light emitting diodes (LEDs) and their white LED derivatives have transformed the lighting industry thanks to their superior power efficiency, longevity, and compactness. The lack of commercially viable native GaN substrates necessitates InGaN/GaN LEDs to be grown on foreign substrates such as sapphire (Al_2O_3) [114]. LEDs can also be grown on Si(111) substrates, which are widely available in very high quality and in wafer sizes

¹Portions of this chapter were previously published as [113, 65] and are reprinted with permission. (Copyright 2019 by AIP Publishing and 2019 by SPIE)

as large as 450 mm at lower than one-fifth of the price per unit area. In the latter, the absorptive silicon substrate can then be removed after a flip-chip bonding scheme is employed. This approach can significantly reduce the cost and increase the market penetration of LED [115]. In addition, recent advances in III-nitrides growth on silicon have mitigated the thermal expansion and lattice mismatch issues with the use of stress management layers such as AlN buffer layers and SiN interlayers [116, 16, 117]. Recent studies on electrically injected and packaged LEDs showed instances where LEDs on Si outperform those on Al₂O₃ [118, 119]. However, such studies have not been done for LEDs on Al₂O₃ and Si substrates with identical blue emitting MQWs, inhibiting direct comparison of structural and optical properties of the blue emitting MQWs.

6.2 Experimental Approach

In this chapter, identical blue-emitting MQW layers without p-GaN caps are grown on c-plane Al₂O₃ (MQW-Al₂O₃) and Si(111) (MQW-Si) substrates. Structural studies using X-ray diffraction (XRD), Raman spectroscopy, and atomic force microscopy (AFM), and optical studies using micro-photoluminescence (μ PL), temperature-dependent PL (TDPL), and time-resolved PL (TRPL) are carried out in order to compare the structural and optical properties of MQWs on Al₂O₃ and Si substrates.

Figure 6.1 illustrates the cross section of (a) MQW-Al₂O₃ and (b) MQW-Si grown by metalorganic chemical vapor deposition (MOCVD). The blue-emitting active layers on the surface of both samples consist of six periods of 2 nm thick In_{0.15}Ga_{0.85}N / 13 nm thick GaN well-barrier pairs. The overall thickness of the epitaxial layers of MQW-Si (3.3 μ m) is less than that of MQW-Al₂O₃ (4.6 μ m). No cracks are observed on the surface of either sample.

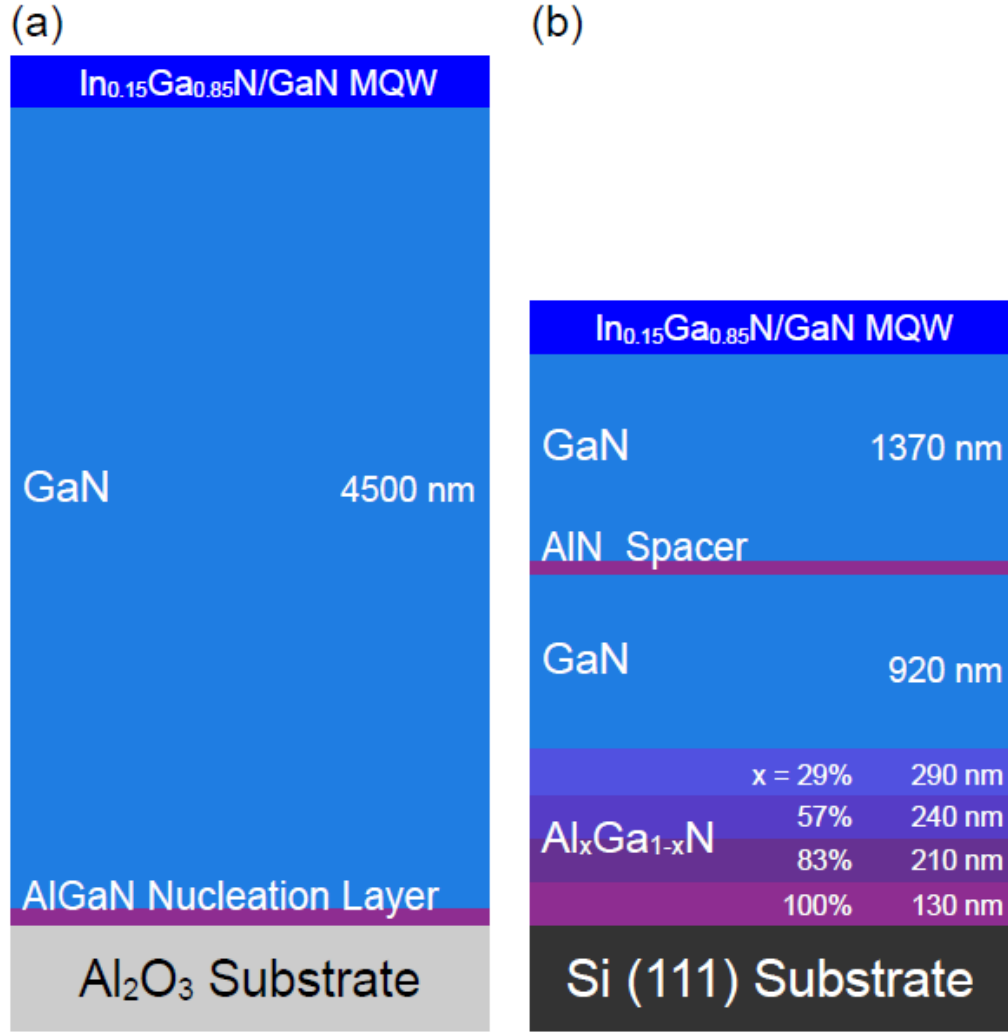


Figure 6.1: Cross-sectional illustration of the MOCVD-grown (a) MQW- Al_2O_3 , and (b) MQW-Si. The MQW- Al_2O_3 is a 4.6 μm thick GaIn on Al_2O_3 substrate with a thin AlN nucleation layer. The MQW-Si uses multiple AlGaIn buffer layers with decreasing Al-composition and a thick GaIn underlayer with a thin AlN spacer. Reprinted from R. Liu, C. McCormick, and C. Bayram, AIP Adv. 9, 025306 (2019), with the permission of AIP Publishing.

6.3 Photoluminescence Intensity and Uniformity Correlation

Figure 6.2 shows the $200\text{ }\mu\text{m} \times 200\text{ }\mu\text{m}$ μPL mapping of (a) MQW- Al_2O_3 and (b) MQW-Si with the top row showing the MQW emission intensity variation and the bottom row showing the peak emission energy variation relative to their respective averages using a continuous wave HeCd 325 nm laser. MQW- Al_2O_3 and MQW-Si exhibit integrated intensity uniformities of 5.1% and 4.1%, and average peak emission energies of $2.791\text{ eV} \pm 3.7\text{ meV}$ (444 nm) and $2.823\text{ eV} \pm 1.4\text{ meV}$ (439 nm), respectively. One noteworthy observation is that the strongly blue-shifted regions of MQW- Al_2O_3 coincide accurately with the high PL intensity regions, and conversely the red-shifted clusters overlap with the low PL intensity spots. Closer inspection of the spectra of these locations shows that the brighter regions emit additional photons only in the high-energy shoulder when compared to the dimmer regions. This is attributed to the screening of the quantum confined stark effect (QCSE) and filling of the states in the emission centers [120, 121].

MQW- Al_2O_3 exhibits integrated intensity uniformity of 5.1% and average peak position of $2.791\text{ eV} \pm 3.7\text{ meV}$. In comparison, MQW-Si shows a similar intensity distribution with a uniformity of 4.1%, and an average peak position that has a slightly higher energy at 2.823 eV with a smaller distribution of $\pm 1.4\text{ meV}$. MQW- Al_2O_3 shows a strong and positive correlation between the peak position and intensity ($R^2 = 0.75$), whereas this correlation is not observed in MQW-Si ($R^2 = 0.11$) (Figure 6.3). Comparing a typical dimmer location with a brighter one on MQW- Al_2O_3 shows that the brighter location emits roughly the same number of photons in the low-energy part of the spectrum, but more intensely in the higher energy shoulder along with a shift in peak position (Figure 6.4). This kind of intensity-energy correlation has been reported in the literature as the screening of the quantum confined stark effect (QCSE) and filling of the states in the emission centers [120, 122]. The lack of this correlation in MQW-Si suggests these effects are less pronounced.

Raman spectroscopy is then conducted to verify the stress of the samples to examine the origin of the differences observed in micro PL. To further explore the differences between the samples, surface analysis using atomic force microscopy (AFM) is conducted.

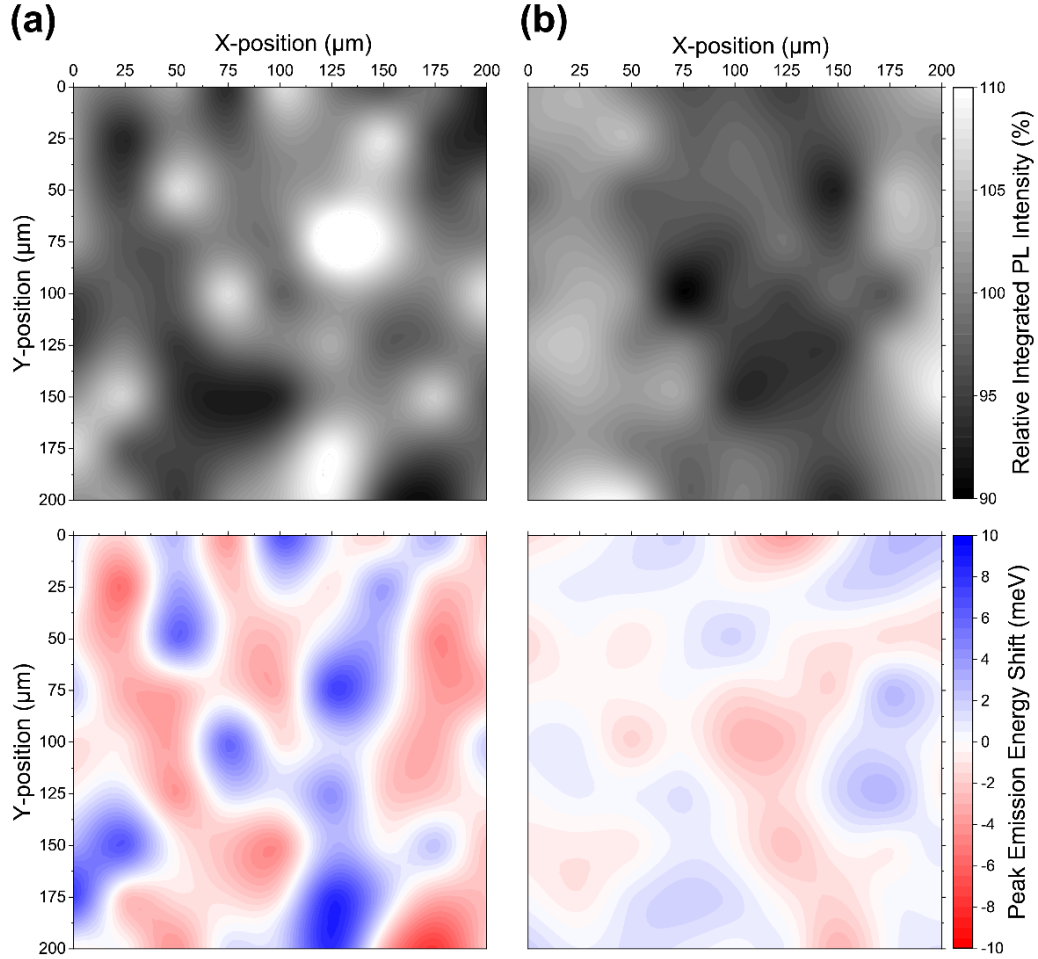


Figure 6.2: Micro-photoluminescence mapping of (a) MQW-Al₂O₃ and (b) MQW-Si. The relative intensity is shown in the top row and peak emission energy in bottom row. MQW-Al₂O₃ exhibits a correlation between the intensity and the peak emission energy mapping with the high-intensity locations showing a blue shift and vice versa. Reprinted from R. Liu, C. McCormick, and C. Bayram, AIP Adv. 9, 025306 (2019), with the permission of AIP Publishing.

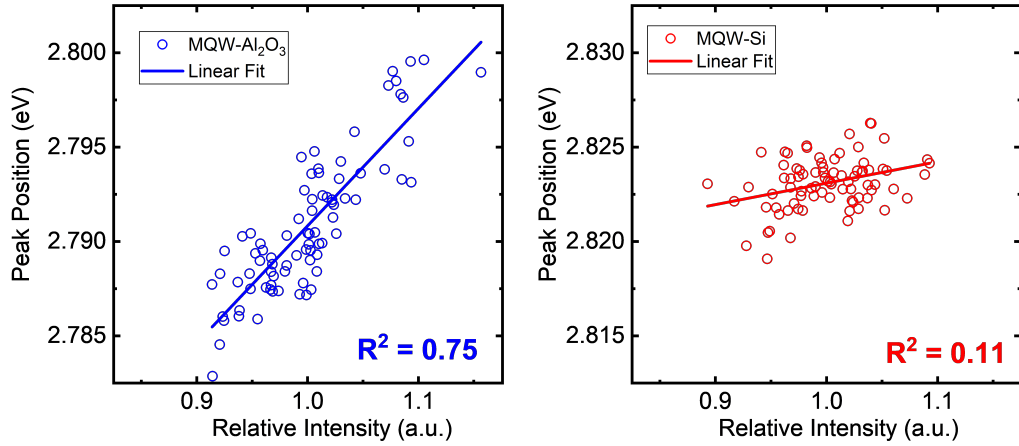


Figure 6.3: The peak position and relative intensity distribution of μ PL of (left) MQW-Al₂O₃ and (right) MQW-Si. A strong linear correlation is found in MQW-Al₂O₃, but not in MQW-Si. Reprinted from R. Liu, C. McCormick, and C. Bayram, Gall. Nitride Mater. Devices XIV 1091822, 73 (2019), with the permission of SPIE.

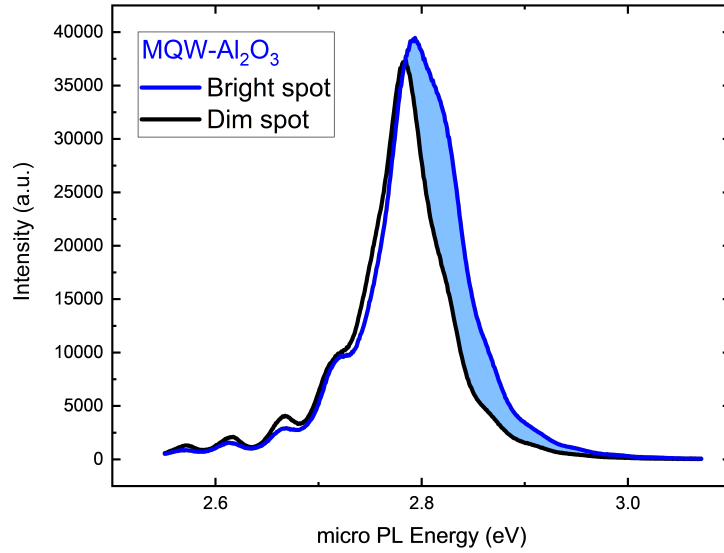


Figure 6.4: A typical “bright” spot and a typical “dim” spot of the MQW-Al₂O₃ sample. The extra intensity coming from the bright spot comes entirely from the higher energy shoulder (colored area). This indicates the band filling effect and QCSE. Reprinted from R. Liu, C. McCormick, and C. Bayram, Gall. Nitride Mater. Devices XIV 1091822, 73 (2019), with the permission of SPIE.

6.4 Crystallinity and Strain Study

Tapping mode AFM is conducted on the samples to quantify the crystal quality at the surface. Figure 6.5 shows $5\text{ }\mu\text{m} \times 5\text{ }\mu\text{m}$ AFM scans of MQW-Al₂O₃ and MQW-Si in Figure 6.6. The surface of MQW-Al₂O₃ shows step-flow terraces with atomic step heights of $\sim 3\text{ }\text{\AA}$, a threading dislocation density of $\sim 2.87 \times 10^8\text{ cm}^{-2}$, and a root-mean-square (RMS) surface roughness of 1.12 nm. The surface of MQW-Si shows hexagonal spiral hillocks that are approximately $2\text{ }\mu\text{m}$ apart with a mixed-type dislocation in their centers, a threading dislocation density of $\sim 3.20 \times 10^8\text{ cm}^{-2}$, and a RMS roughness of 0.51 nm [123]. Due to the different type of strain experienced by the GaN layer, they exhibit a different form of epitaxial growth. However, the results from AFM show the crystal quality of MQW-Al₂O₃ is better than that of MQW-Si, but not by a significant amount.

Figure 6.7 shows the symmetric $\omega/2\theta$ XRD spectra. The (004) GaN reflections are observed at $\theta \approx 73^\circ$ with InGa_{0.98}N/GaN MQW fringe peaks on the left for both samples and AlGa_{0.98}N buffer layers' peaks on the right for MQW-Si. The 0th peak position of InGa_{0.98}N implies an average indium composition of $\sim 2\%$ across the MQW. The thickness of each well-barrier period is calculated from the fringe spacing using the relationship [124]:

$$T = \frac{(n_i - n_j)\lambda}{2(\sin\theta_i - \sin\theta_j)} \quad (6.1)$$

where n_i and n_j are the order of the i^{th} and j^{th} fringe peaks, respectively, and λ is the wavelength of the X-ray (Copper K- α , 0.154056 nm). This yields a well-barrier pair thickness of 14.8 nm. Asymmetric scan on the (102) reflection is conducted to evaluate composition of the Al_{1-x}Ga_xN buffer layers. The lattice constants, a and c , are calculated using the d-plane spacing (d_{hkl}), which is the interplanar spacing of the lattice plane (hkl) that satisfies Bragg's condition:

$$\left(\frac{1}{d_{hkl}}\right)^2 = \frac{4}{3} \left(\frac{h^2 + hk + k^2}{a^2}\right) + \frac{l^2}{c^2} \quad (6.2)$$

and Poisson-Vegard's law:

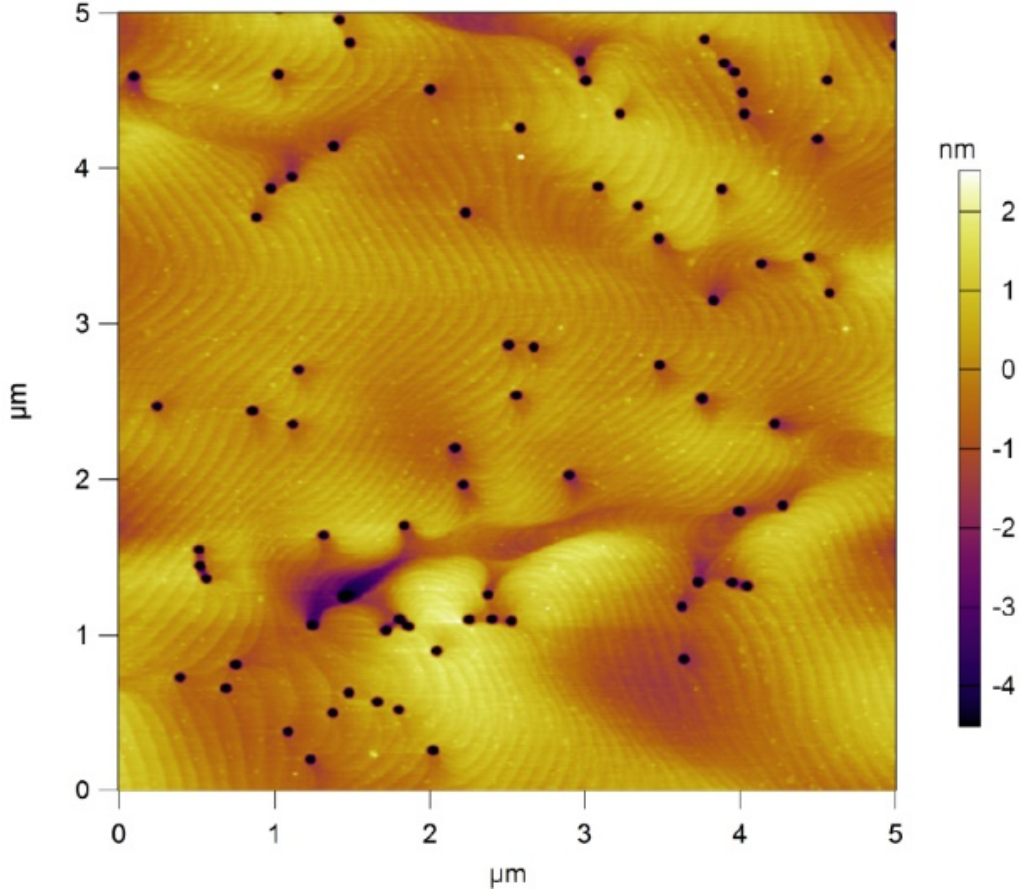


Figure 6.5: $5 \times 5 \mu\text{m}^2$ AFM scan of MQW- Al_2O_3 . The surface of MQW- Al_2O_3 shows step-flow terraces. Reprinted from R. Liu, C. McCormick, and C. Bayram, Gall. Nitride Mater. Devices XIV 1091822, 73 (2019), with the permission of SPIE.

$$\begin{aligned} \frac{c_m(x) - c_0(x)}{c_0(x)} &= -\frac{2\nu(x)}{1 - \nu(x)} \times \frac{a_m(x) - a_0(x)}{a_0(x)} \\ c_0(x) &= (1 - x)c_{\text{GaN}} + xc_{\text{AlN}} + \delta_c x(1 - x) \\ a_0(x) &= (1 - x)a_{\text{GaN}} + xa_{\text{AlN}} + \delta_a x(1 - x) \\ \nu(x) &= (1 - x)\nu_{\text{GaN}} + x\nu_{\text{AlN}} \end{aligned}$$

where $c_m(x)$ and $a_m(x)$ are the measured lattice constants, $c_0(x)$ and $a_0(x)$ are the relaxed lattice constants, $\nu(x)$ is the Poisson's ratio, $\delta_a(x)$ and $\delta_c x$ are the lattice bowing parameters [125, 126]. The compositions of the $\text{Al}_{1-x}\text{Ga}_x\text{N}$

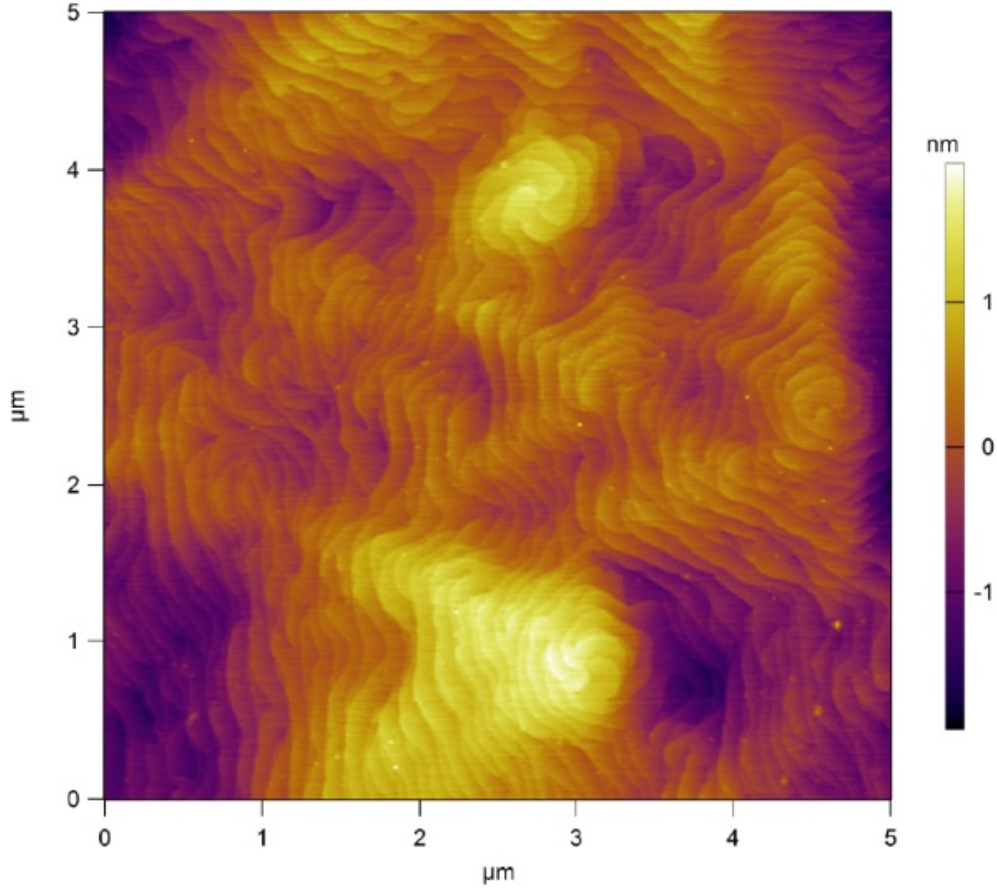


Figure 6.6: $5 \times 5 \mu\text{m}^2$ AFM scan of MQW-Si. The surface of MQW-Si is populated with hillocks. Reprinted from R. Liu, C. McCormick, and C. Bayram, Gall. Nitride Mater. Devices XIV 1091822, 73 (2019), with the permission of SPIE.

buffer layers are calculated in order from the substrate to the surface to be 1.00, 0.83, 0.57, and 0.29. Additionally, the lattice constants and strain of the GaN layers are also calculated and tabulated in Tables 6.1 and 6.2. The XRD shows the GaN layers of MQW- Al_2O_3 and MQW-Si are under compressive (-0.17%) and tensile (0.19%), respectively.

The ω scan of the GaN peaks (002) and (102) reflections are used to quantify the defectivity of the GaN material. The densities of screw- and edge-type dislocations are related to the ω scan FWHM of the (002) plane (β_{002}) and the (102) plane (β_{102}) through the Burgers vector lengths of the edge type dislocation ($b_{edge} = 0.3189 \text{ nm}$), and of the screw type dislocation

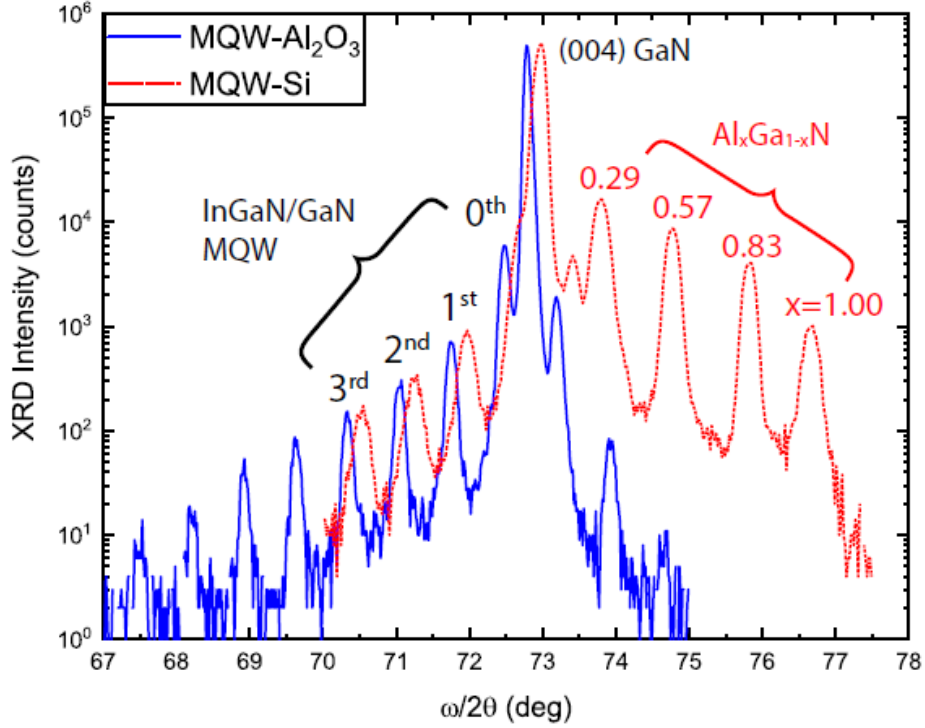


Figure 6.7: Symmetric $\omega/2\theta$ XRD showing the (004) reflections from AlGaIn buffer layers, GaN, and InGaIn MQWs. GaN peak in MQW-Si exhibits a broader FWHM (732 vs. 460 arcsec) than MQW-Al₂O₃. Reprinted from R. Liu, C. McCormick, and C. Bayram, AIP Adv. 9, 025306 (2019), with the permission of AIP Publishing.

($b_{screw} = 0.5185$ nm) using the following relations [124]:

$$D_{screw} = \frac{\beta_{002}^2}{4.35 \times b_{screw}^2} \quad (6.3)$$

$$D_{edge} = \frac{\beta_{102}^2 - \beta_{002}^2}{4.35 \times b_{edge}^2} \quad (6.4)$$

The results are tabulated in Table 6.1 and Table 6.2, which show that MQW-Si contains approximately four times more screw- and edge-type dislocations than MQW-Al₂O₃.

Raman spectroscopy is conducted with a Horiba Confocal Raman Microscope with an 1800 l/mm grating and a $\lambda = 532$ nm laser using a Z(XX) \bar{Z} configuration to calculate strain in the GaN layers of the InGaIn/GaN MQW.

Table 6.1: Lattice constants and strain calculated from the XRD and AFM data

Samples	a (Å)	c (Å)	Strain (%)	(002) ω -FWHM (arcsec)	(102) ω -FWHM (arcsec)
MQW-Al ₂ O ₃	3.1819	5.1929	+0.128	195.1	293.6
MQW-Si	3.1911	5.1819	-0.162	386.2	573.1

Table 6.2: Screw and edge type defect density calculated from the XRD and AFM data

Samples	D_{screw} (10^8 cm^{-2})	D_{edge} (10^8 cm^{-2})	TDD (10^8 cm^{-2})
MQW-Al ₂ O ₃	0.77	1.73	2.87
MQW-Si	3.00	6.60	3.20

Raman spectroscopy results of the MQW-Al₂O₃ (blue, solid line) and on Si (red, dashed line) are shown in Figure 6.8. MQW-Al₂O₃ shows three distinct Raman shifts: 417 cm⁻¹, which is attributed to the A_{1g} phonon mode from the Al₂O₃ substrate [127], and 569.7 and 735.3 cm⁻¹, which are associated with the E₂^H and A₁(LO) phonons of GaN [128, 129]. MQW-Si shows four Raman shifts: a saturated peak at 520 cm⁻¹ from the Si substrate, 565.7 and 732.1 cm⁻¹ from the E₂^H and A₁(LO) phonons of GaN, and a weak 646 cm⁻¹ peak, which is likely a E₂^H phonon mode associated with a AlGaN buffer layer [130]. The E₂^H and A₁(LO) Raman shifts of GaN in the MQW-Al₂O₃ exhibit a blue shift in energy from its relaxed value (567.5 cm⁻¹, 734.0 cm⁻¹, respectively); this indicates a compressive strain experienced in the GaN layer. MQW-Si exhibits the opposite shifts, indicating the presence of a tensile strain. The E₂^H peak is used to calculate the stress based on its deviation from the relaxed value due to its high strain sensitivity [131]. The in-plane biaxial stress is then calculated using [132]:

$$\Delta\omega = 4.3\sigma_{xx} \text{ cm}^{-1} \text{ GPa}^{-1} \quad (6.5)$$

where $\Delta\omega$ is the Raman shift and σ_{xx} is the stress. The in-plane strain is calculated using [133]:

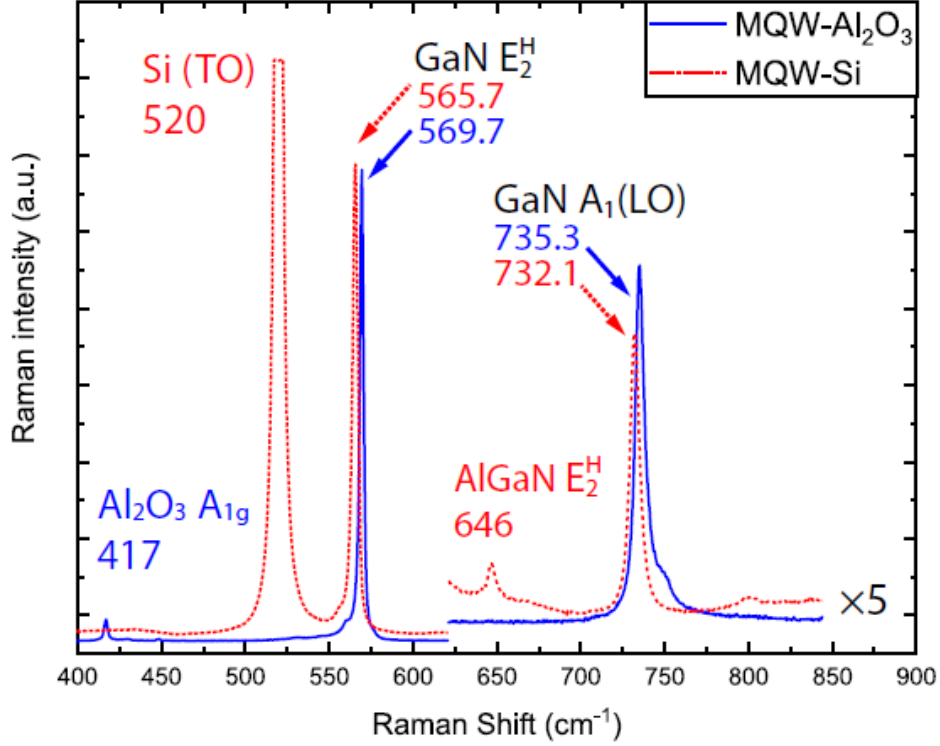


Figure 6.8: Raman spectroscopy shows a blue shift in both the E_2^H and $A_1(LO)$ peaks of GaN of MQW- Al_2O_3 , whereas these are red-shifted in MQW-Si. These shifts indicate that GaN on MQW- Al_2O_3 experiences a compressive strain, and a tensile strain for MQW-Si. Reprinted from R. Liu, C. McCormick, and C. Bayram, AIP Adv. 9, 025306 (2019), with the permission of AIP Publishing.

$$\varepsilon_{xx} = \sigma_{xx} / [(C_{11} + C_{12}) - 2C_{13}^2/C_{33}] \quad (6.6)$$

where C_{ij} are the elastic constants of GaN ($C_{11} = 390$ GPa, $C_{12} = 145$ GPa, $C_{13} = 106$ GPa, and $C_{33} = 398$ GPa) [134], which give a proportionality factor of 478 GPa. The calculated in-plane stress and strain values are tabulated in Table 6.3. Raman spectroscopy shows a compressive strain (-0.107%) in MQW- Al_2O_3 and tensile strain (+0.088%) in MQW-Si, in line with XRD results.

Table 6.3: Strain and stress of the GaN buffer layers calculated from the Raman spectroscopy data

Samples	E_2^H (cm^{-1})	$\Delta\omega$ (cm^{-1})	Stress (GPa)	Strain ω -FWHM (%)
MQW- Al_2O_3	569.7	2.2	+0.512	+0.107
MQW-Si	565.7	-1.8	-0.419	-0.088
GaN (relaxed)	567.5			

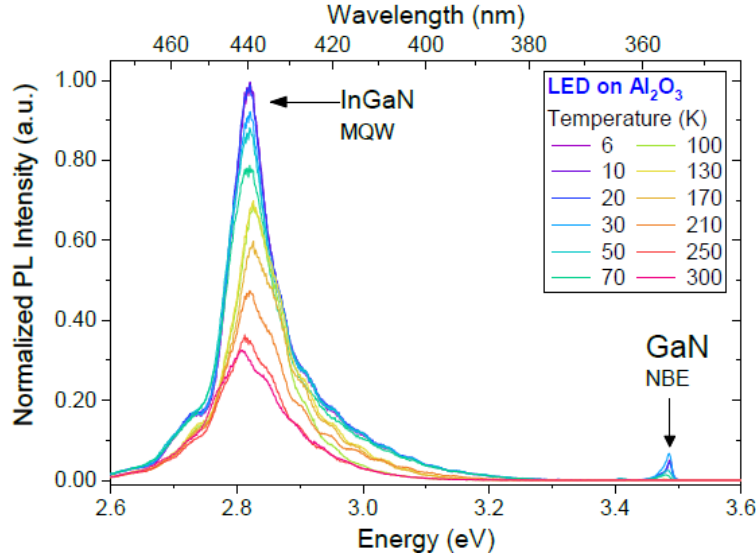


Figure 6.9: Temperature-dependent PL spectra of MQW- Al_2O_3 6 K (purple) to 300 K (red). Reprinted from R. Liu, C. McCormick, and C. Bayram, AIP Adv. 9, 025306 (2019), with the permission of AIP Publishing.

6.5 Internal Quantum Efficiency and Carrier Lifetime Calculations

Figures 6.9 and 6.10 show the PL spectra of MQW- Al_2O_3 and MQW-Si, respectively, from 6 ~ 300 K obtained using a 10 mW frequency-tripled laser ($\lambda = 266$ nm) and a helium-bath cryostat. The extracted temperature-dependent internal quantum efficiency (IQE) is shown in Figure 6.11 and peak emission energy in Figure 6.12. MQW- Al_2O_3 exhibits InGaN multiple quantum well peak (MQW) centered at 2.812 eV at 300 K. At low temperature ($T < 100$ K), a shoulder on the low-energy (2.728 eV) side of the MQW

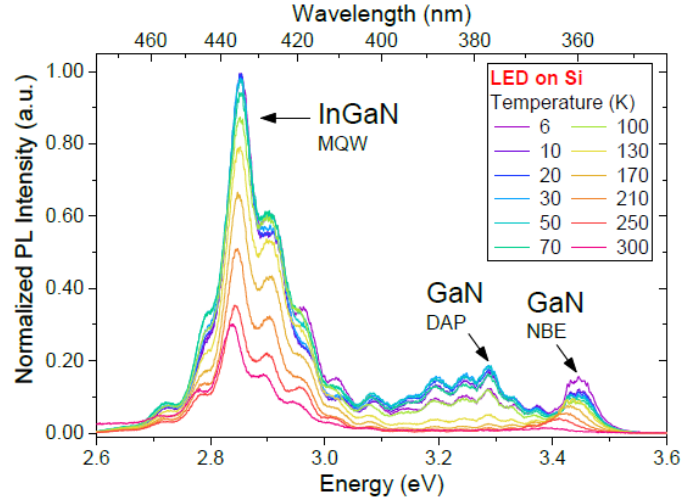


Figure 6.10: Temperature-dependent PL spectra of MQW-Si from 6 K (purple) to 300 K (red). MQW-Si shows more carrier recombination via NBE and DAP in GaN. Reprinted from R. Liu, C. McCormick, and C. Bayram, AIP Adv. 9, 025306 (2019), with the permission of AIP Publishing.

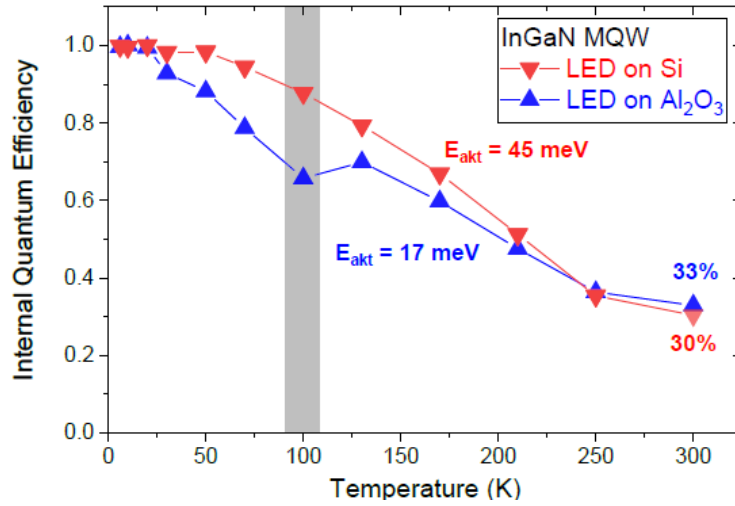


Figure 6.11: Temperature-dependent IQE of (red) MQW-Si and (blue) MQW- Al_2O_3 . The two samples exhibit similar IQE at 300 K. However, MQW-Si exhibits a higher IQE at temperature below 250 K. Arrhenius activation energy is calculated to be 17 meV (45 meV) for MQW- Al_2O_3 (on Si). Reprinted from R. Liu, C. McCormick, and C. Bayram, AIP Adv. 9, 025306 (2019), with the permission of AIP Publishing.

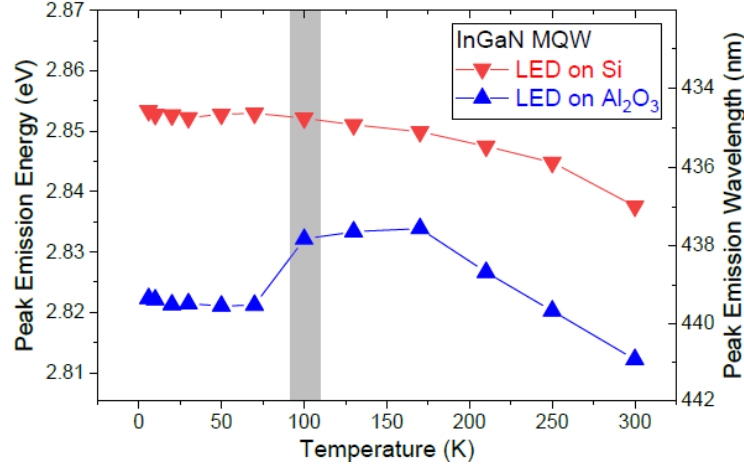


Figure 6.12: Temperature-dependent peak emission energy of (blue) MQW-Al₂O₃ and (red) on Si. While the MQW-Si peak emission red-shifts monotonically with increasing temperature due to the bandgap shrinkage, MQW-Al₂O₃ peak emission exhibits an S-curve. An increase in IQE of MQW-Al₂O₃ with increasing temperature at 100 K coincides with a blue shift in the peak emission energy. Reprinted from R. Liu, C. McCormick, and C. Bayram, AIP Adv. 9, 025306 (2019), with the permission of AIP Publishing.

peak and a peak in the ultraviolet range (3.486 eV) appear. The low-energy peak is attributed to the localized indium clusters [135], which are caused by the phase separation as a result of lattice mismatch [136], whereas the UV peak is attributed to near-band-edge (NBE) emission from excitons recombining in the GaN layer [84]. The PL spectra for MQW-Si show three major emission centers: the MQW at 2.853 eV, donor-acceptor-pair (DAP) transition of GaN at 3.288 eV [84], and NBE emissions from GaN at 3.446 eV. These emissions are convolved with the Fabry-Perot interference caused by the thinner films on the silicon substrate. The DAP emission exhibits the commonly seen LO-phonon replicas that are spaced at 90 meV apart [137]. The DAP recombination indicates the elevated impurity concentration in MQW-Si, while the stronger GaN NBE emission suggests the carrier confinement is poorer due to the lower crystal quality.

The difference of ~ 41 meV in the main MQW emissions from the samples throughout the temperature range (Figure 6.9), despite the same physical structure shown by XRD, is attributed to the reduced quantum confined stark effect (QCSE) in the InGaN active layers. The compressive strain

experienced by the GaN layer in the MQW-Al₂O₃ leads to an even larger compressive strain in the InGaN wells. This leads to a stronger piezoelectric polarization field in the InGaN layer, and thus a reduction in the QW ground state energies. The tensile strain in the GaN layer of the MQW-Si leads to a reduced compressive strain in the InGaN layer, which in turn exhibits a reduced piezoelectric polarization [138]. The reduced QCSE is believed to increase the electron-hole wavefunction overlap, which should increase the efficiency of radiative recombination.

Figure 6.9 (c) shows the temperature-dependent IQE, which is calculated using the following:

$$\text{IQE}(T) = \frac{I(T)}{I(6\text{K})} \quad (6.7)$$

where $I(T)$ is the integrated intensity of the PL emission at temperature T , and assuming at 6 K all the recombination mechanisms are radiative. The IQE of the LEDs are shown in Figure 6.9 (c). MQW-Si shows a steady decrease in IQE as the temperature increases, whereas Al₂O₃ exhibits a dip in IQE at 100 K. At room temperature, the IQE of the MQW-Al₂O₃ and MQW-Si are very similar at 33 and 30%, respectively, despite the difference in crystal quality observed by AFM and XRD. In fact, the IQE of MQW-Si exceeds that of MQW-Al₂O₃ at all temperatures below 250 K. This indicates that the activation energies of their respective carrier loss mechanisms, either band filling or nonradiative recombination centers, are significantly different. This can be evaluated via Arrhenius activation energy analysis using [100]:

$$I = \frac{I_0}{1 + C \exp(-E_{act}/kT)} \quad (6.8)$$

where I is the integrated intensity, I_0 and C are fitting constants, k is the Boltzmann's constant, T is temperature, and E_{act} is the activation energy. This yields a E_{act} of 17 ± 3 meV for MQW-Al₂O₃ and 45 ± 4 meV for MQW-Si. This analysis shows that the carriers in the local energy minima of MQW-Al₂O₃ require very little thermal energy to escape to other higher energy emission centers, while MQW-Si requires 2.6 times more energy to activate a carrier loss mechanism.

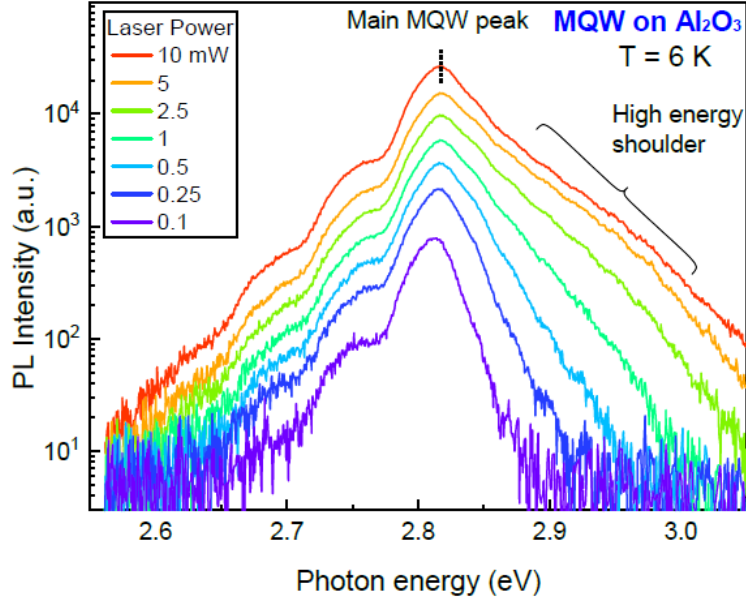


Figure 6.13: Injection power-dependent photoluminescence at 6 K with laser power from 0.1 to 10 mW of MQW-Al₂O₃, which shows a sublinear relationship (0.73 ± 0.04) with injection laser power and an indistinct blue shoulder. Reprinted from R. Liu, C. McCormick, and C. Bayram, AIP Adv. 9, 025306 (2019), with the permission of AIP Publishing.

The peak MQW emission energies from 6 to 300 K are plotted in Figure 6.9. The MQW emission from the MQW-Al₂O₃ exhibits a distinct S-shape shift in peak energy with increasing temperature in addition to the overall bandgap shrinkage, which is described by the Varshni coefficient [93]. The peak energy remains stable between 6 and 100 K, but then rapidly blue-shifts by 10 meV at 100 K, and then red-shifts by 21 meV steadily from 170 to 300 K. The S-shaped peak shift has been reported to be caused by the temperature-dependent carrier dynamics in the self-organized inhomogeneous InGaN local minima [139]. The coincidence of a blue shift in the peak energy and an increase in the IQE of the MQW of the MQW-Al₂O₃ at 130 K suggests a change in the emission center as carriers gain enough thermal energy to freely move between the low-energy minima and the higher energy minima as the temperature increases [140]. On the other hand, the MQW emission from MQW-Si monotonically red-shifts by 16 meV with increasing temperature. To verify the reduced QCSE and the higher density of states in MQW-Si, power-dependent PL is conducted.

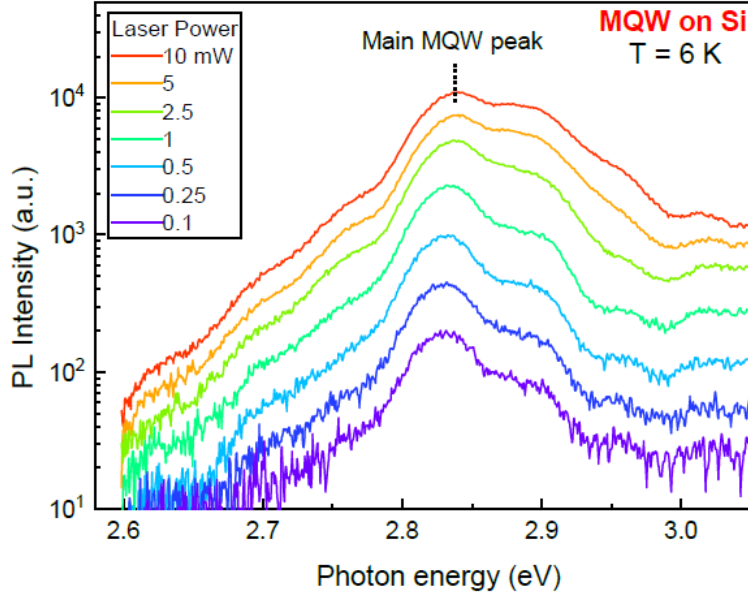


Figure 6.14: Injection power-dependent photoluminescence at 6 K with laser power from 0.1 to 10 mW of MQW-Si, which shows a linear relationship (0.91 ± 0.05) with laser power. Reprinted from R. Liu, C. McCormick, and C. Bayram, AIP Adv. 9, 025306 (2019), with the permission of AIP Publishing.

Figures 6.13 and 6.14 show the injection power-dependent PL of MQW- Al_2O_3 and MQW-Si with laser power varying from 0.1 to 10 mW at 6 K, respectively. With 0.1 mW of laser power (purple spectrum), MQW- Al_2O_3 shows a main LED peak at 2.813 eV, a red shoulder at 2.755 eV, and a broad, undefined blue shoulder, whereas MQW-Si shows a main LED peak at 2.830 eV. A power-law dependence of the PL peak intensities on the laser power is fitted to quantify the difference between the two LEDs [97]:

$$I \propto P^m \quad (6.9)$$

where I is the intensity of the emission, P is the power of the incident laser, and m is the power dependence. The fitting yields power dependence of 0.73 ± 0.04 (MQW- Al_2O_3 main peak), 0.75 ± 0.04 (MQW- Al_2O_3 red shoulder), and 0.91 ± 0.05 (MQW-Si main peak). The sublinear power dependence observed in both emission centers for MQW- Al_2O_3 indicates the band filling

of the low-energy minima. This happens when a high concentration of injected carriers occupies all the available states in the lowest emission center, causing some of the carriers to occupy otherwise higher energy states and subsequently emit photons with higher energies. The high-energy shoulder has been reported to be a combination of the filling of the band-tail states and the screening of the internal electric fields [120, 121].

The power-law fitting of the MQW-Al₂O₃ main peak is separated into two laser power regimes of 0.1~ 0.5 mW and 0.5 ~ 10 mW and the power dependencies are $m = 0.94 \pm 0.09$ and $m = 0.65 \pm 0.02$, respectively. This shows that the main peak of MQW-Al₂O₃ exhibits a band-to-band-like transition at laser power below 0.5 mW, whereas at laser power above 0.5 mW it exhibits defect-like band-filling behavior with a featureless high-energy shoulder. MQW-Si, on the other hand, shows an approximately linear ($m \approx 1$) power dependence. The intensity saturation observed in MQW-Al₂O₃ is not present in MQW-Si. This suggests the bands in the main emission centers of MQW-Si are not filled, and therefore the carrier spilling to higher energy states is not as pronounced. To observe the carrier recombination mechanisms in the MQW, time-resolved photoluminescence (TRPL) is conducted.

The experiment was conducted using a frequency-doubled Ti-Al₂O₃ laser ($\lambda = 390$ nm) to directly create electron-hole-pairs in the quantum well, and an avalanche photodiode with a bandpass filter to observe the LED emission. Figure 6.15 shows the TRPL spectra and mono-exponential decay fit of MQW-Al₂O₃ (blue) and MQW-Si (red). Using single exponential decay fitting (shaded regions), the PL lifetimes of MQW-Al₂O₃ and MQW-Si are calculated to be 4.9 ± 0.3 and 7.3 ± 0.1 ns, respectively. Given the relationship of lifetimes with IQE [103]:

$$\text{IQE} = \frac{\tau_{\text{rad}}^{-1}}{\tau_{\text{PL}}^{-1}} \quad (6.10)$$

where τ_{rad} and τ_{PL} are the radiative and photoluminescence lifetimes, the radiative lifetimes are calculated. Nonradiative recombination lifetimes (τ_{nr}) are calculated via:

$$\tau_{\text{PL}}^{-1} = \tau_{\text{rad}}^{-1} + \tau_{\text{nr}}^{-1} \quad (6.11)$$

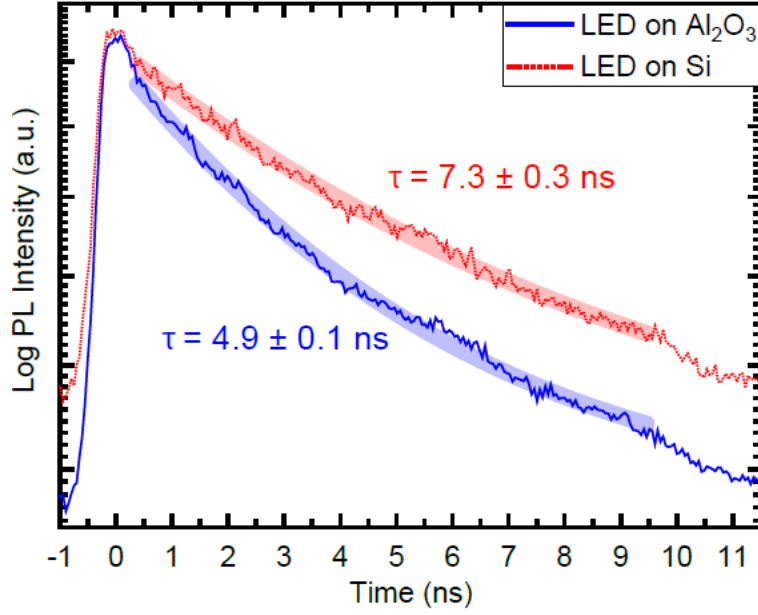


Figure 6.15: Time-resolved photoluminescence of (blue solid) MQW- Al_2O_3 and (red dashed) MQW-Si using a frequency-doubled Ti:sapphire laser at 390 nm to directly generate electron-hole-pairs in the InGaN quantum wells. Exponential decay fitting in the highlighted regions yields PL lifetimes of 7.3 ± 0.3 ns for MQW-Si and 4.9 ± 0.1 ns for MQW- Al_2O_3 . Reprinted from R. Liu, C. McCormick, and C. Bayram, AIP Adv. 9, 025306 (2019), with the permission of AIP Publishing.

Radiative (nonradiative) recombination lifetimes of 14.8 ns (7.3 ns) are calculated for the MQW- Al_2O_3 and 24.3 ns (10.4 ns) for MQW-Si. The shorter radiative lifetime in MQW- Al_2O_3 is attributed to the higher carrier concentration in the smaller indium clusters, while the shorter nonradiative lifetime is attributed to the carrier escape from these local potential minima. On the other hand, the longer radiative lifetime in MQW-Si suggests the recombination centers are operating in a lower carrier concentration regime, which has a lower probability of carrier escape. The net result of a reduced carrier escape probability and a lower crystal quality is a $\sim 40\%$ longer nonradiative lifetime.

6.6 Discussion

The carriers in MQW-Al₂O₃ and MQW-Si are shown to behave rather differently even though the MQW structures are grown under the same MOCVD configuration. MQW-Si does not exhibit the intensity-wavelength correlation and the S-shaped shift in the emission energy with decreasing temperature. The lack of these characteristics, which are associated with indium clustering and strong QCSE, indicate the MQW-Si is superior to MQW-Al₂O₃ in indium uniformity and emission stability. These differences are believed to originate from the different type of residual strain in the GaN layer; the results suggest the tensile strain in the GaN of MQW-Si could be beneficial as it reduces the compressive strain in the InGaN layer. The advantage of this reduction is twofold. First, the reduction in piezoelectric polarization allows the electrons and holes to achieve a greater wavefunction overlap, which should lead to an increased radiative efficiency [141]. This is supported by the IQE analysis, which shows that, despite the lower crystal quality, MQW-Si outperforms MQW-Al₂O₃ at most temperatures and is roughly equal at room temperature. Second, tensile strain is shown to be beneficial for indium atom incorporation during MOCVD growth due to strain compensation [138, 142]. This is shown by the lack of S-shaped shift in emission energy, low-energy shoulders at cryo-temperatures, and the intensity-wavelength correlation. This indicates that the tensile strain allows MQW-Si to incorporate a higher indium content during growth than MQW-Al₂O₃. This demonstrates the possibility of growing MQW-Si with a higher indium mole fraction for the emission of green light.

CHAPTER 7

MOCVD CHAMBER CONDITIONING

This chapter reports experimentation on the detrimental effects of Cp_2Mg -induced trace transition metal (iron, manganese) contamination on the optical performance of metalorganic chemical vapor deposition (MOCVD)-grown blue-emitting hexagonal phase InGaN/GaN multiple quantum wells (MQW). Five samples are grown at various stages of conditioning of a new MOCVD reactor with stainless steel gas lines. The metallic ion contamination is measured experimentally, and its correlation with the optical performance is important for bringing emitters grown in newly installed MOCVD reactors up to their expected quality. Acceleration in the conditioning of the reactors can lead to reduced labor and material cost, and is critical for commercial applications.

7.1 Introduction

Group III-nitride semiconductors have transformed the solid state lighting industry through the commercialization of the blue-emitting InGaN/GaN multiple quantum well (MQW) and its phosphor-coated variant white-emitting light emitting diode (LED) that have high efficiency, long service life, high brightness, and small footprint [143]. These devices are most often commercially grown on Al_2O_3 or SiC substrates using metal organic chemical vapor deposition (MOCVD) due to its high throughput. Typically, the main layers in the LED epi wafer consist of a p-i-n structure with the n-type GaN as the bottom layer, the InGaN/GaN MQW in the intrinsic region, and Mg-doped p-type GaN as the top layer.

The conventional precursor for Mg-doping in the p-type GaN layer is bis(cyclopentadienyl)magnesium (Cp_2Mg) [4]. Since Mg is the strongest reductant ($E_{\text{Mg}^{2+}}^0 = -2.382 \text{ eV}$) of the metal species found in a stainless steel

MOCVD reactor, it is capable of reducing the Cr_2O_3 , which is the self-healing passivation layer that forms on a typical 316 stainless steel to prevent oxidation of other transition metal constituents, such as Fe and Mn [144]. Therefore, introducing Cp_2Mg in a pristine MOCVD chamber for the first time could induce this transmetalation to form MgO , which itself limits further reaction once the lining is covered with it. The Cr ($E_{\text{Cr}^{3+}}^0 = -0.74$ eV), along with the underlying Fe ($E_{\text{Fe}^{3+}}^0 = -0.04$ eV) and Mn ($E_{\text{Mn}^{3+}}^0 = -0.74$ eV) ions that are now present on the lining of the gas lines can be entrained in the gas flow (TMAI, TMGa, TMIIn) of the next epitaxial run and transported inadvertently to the growth surface [145, 146].

These metallic ion impurities then act as traps with large capture cross sections in GaN (Fe_{Ga} : $2.1 \sim 2.5$ eV [147], Mn_{Ga} : 1.4 eV [148] above the valence band) to create efficient nonradiative recombination centers that reduce the devices' efficiency [149, 150, 151, 152, 153]. Suppressing the entrainment of these impurities usually takes numerous epitaxial growths to thoroughly season the MOCVD chamber since first-principles studies have shown that iron concentrations as low as 10^{15} cm^{-3} can have a significant negative impact on the device performance due to the large carrier capture cross section of its excited states [153]. This chapter examines this effect experimentally in a typical conditioning procedure carried out in a commercial MOCVD chamber using optical and structural characterization techniques.

Five samples (MQW1-5) each consisting of six pairs of $\text{In}_{0.15}\text{Ga}_{0.85}\text{N}$ / GaN quantum well-barriers on a 5 μm thick GaN buffer layer on 6-inch Al_2O_3 substrates are grown during various stages of the conditioning of a never-used MOCVD chamber. Each cycle of conditioning (Mg-conditioning) is composed of (i) high flux Cp_2Mg flow to initiate the transmetalation followed by (ii) opening the chamber for ambient air and humidity exposure to fully oxidize the Mg [154]. MQW1 is grown after the initial cycle high flux Cp_2Mg . MQW2 is grown after five additional cycles of Mg-conditioning. MQW3 is grown after one additional cycle. MQW4 is grown after multiple additional cycles. MQW5 is grown after yet more additional cycles.

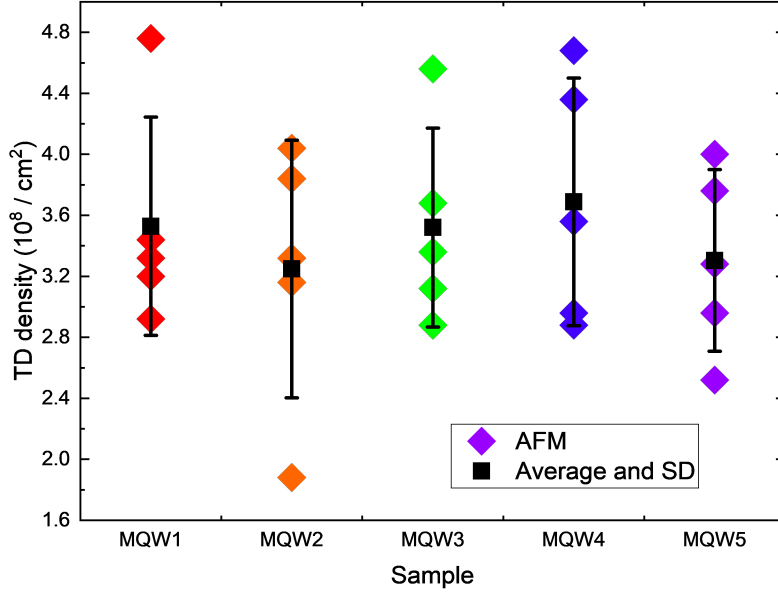


Figure 7.1: Threading dislocation densities measured using AFM.

7.2 Structural Characterization

Structural characterization techniques such as atomic force microscopy, X-ray diffraction, and reciprocal space mapping are conducted on the samples, and no observable differences are found among the samples (see Figures 7.1 – 7.4). Secondary ion mass spectroscopy is conducted on a Cameca IMS with O₂ plasma to measure the trace concentration of Fe and Mn impurities. MQW1 is found to contain approximately $3 \times 10^{14} \text{ cm}^{-3}$ of Mn and $3 \times 10^{15} \text{ cm}^{-3}$ of Fe. No other samples were found to contain more than $1 \times 10^{14} \text{ cm}^{-3}$ of Mn and $1 \times 10^{15} \text{ cm}^{-3}$ of Fe, which are the detection limit of the instrument (Figures 7.5 – 7.6). A similar level (10^{15} cm^{-3}) of unintentional Fe contamination has been reported in HVPE growth of GaN when Mg dopant is used [155]. Using electron paramagnetic resonance (EPR), signals from Fe impurities are observed; this corroborates the observation from the SIMS data.

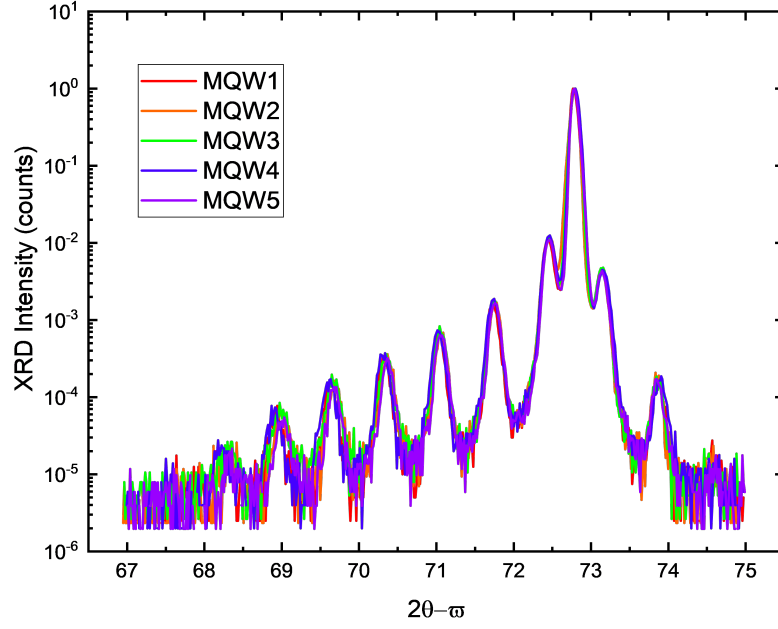


Figure 7.2: XRD shows no observable difference between the samples in terms of crystal quality or strain.

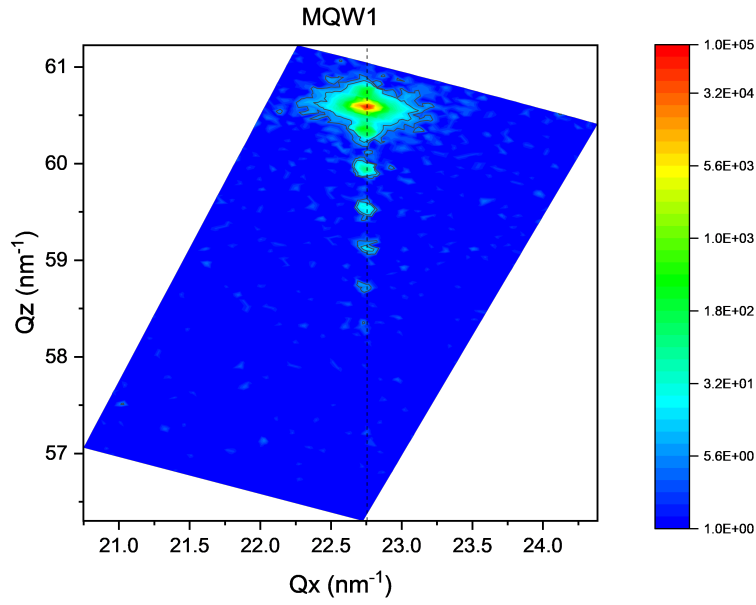


Figure 7.3: Reciprocal space mapping of MQW1 shows the InGaN layers are fully strained.

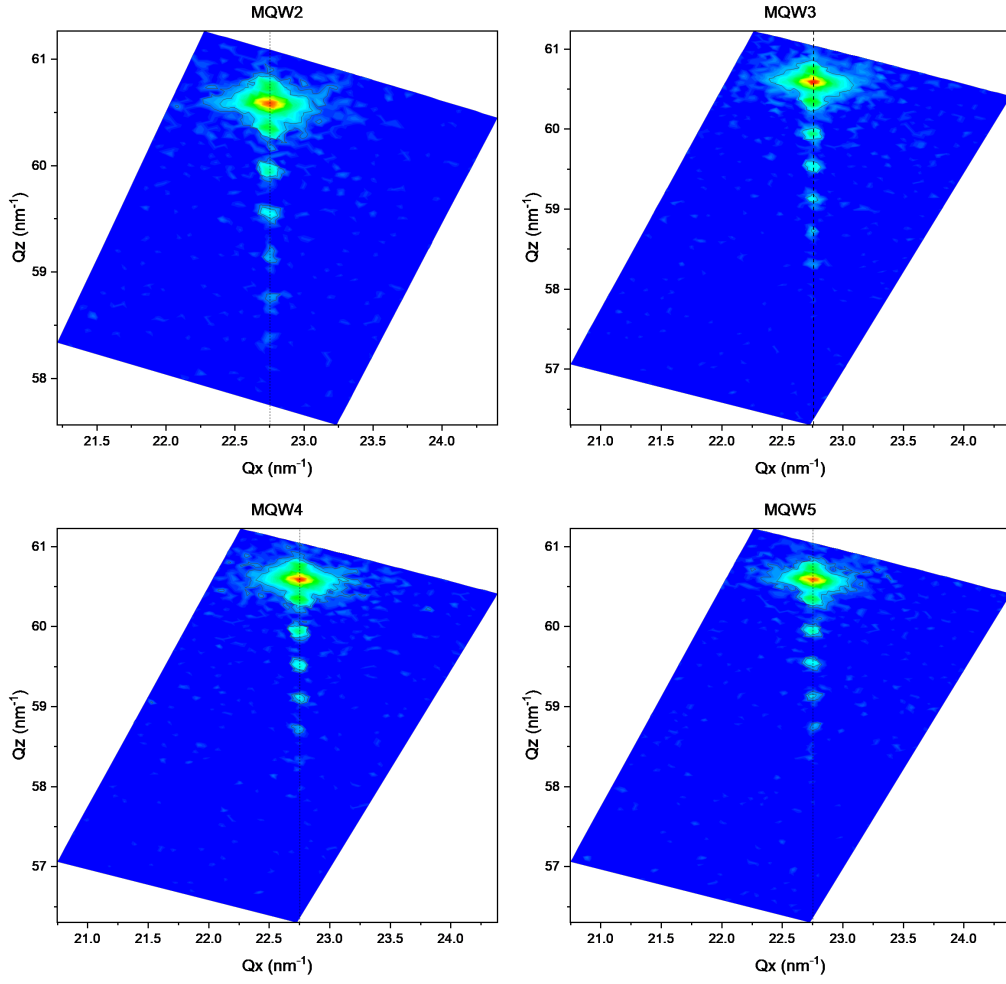


Figure 7.4: Reciprocal space mapping of the remaining samples shows no signs of quantum well relaxation.

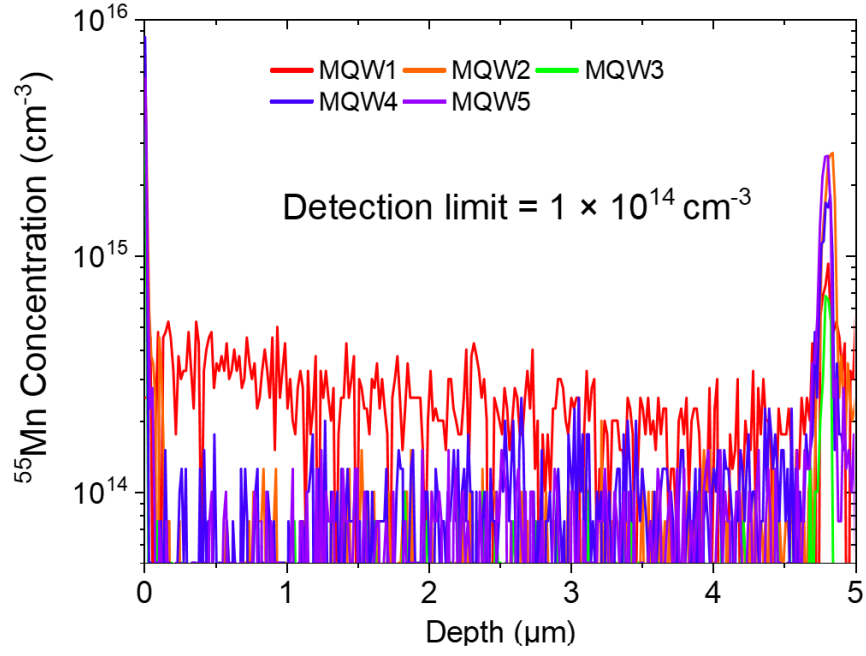


Figure 7.5: SIMS shows a trace amount of ^{55}Mn in MQW1.

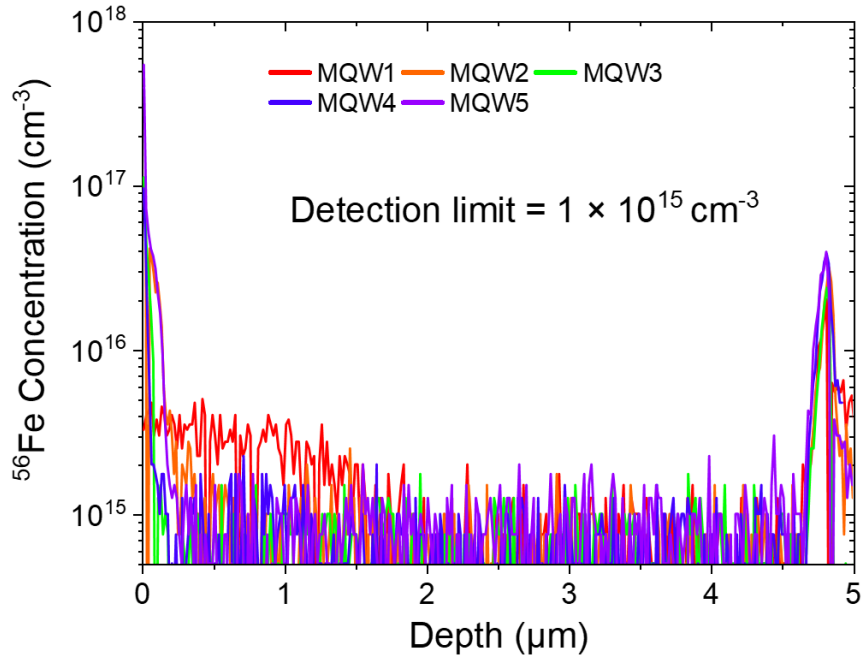


Figure 7.6: SIMS shows a trace amount of ^{56}Fe in MQW1.

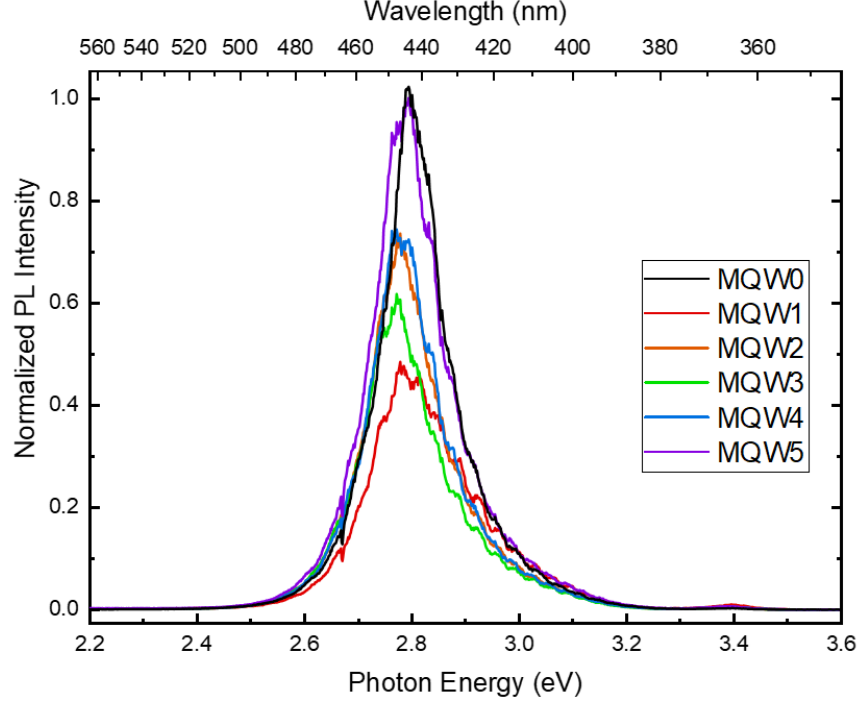


Figure 7.7: PL spectra of the MQW samples.

7.3 Optical Characterization

The optical properties of the MQW samples are measured using room temperature photoluminescence (PL) with a $\lambda = 266$ nm laser and spectrometer fitted with a CCD camera (Figure 7.7). All five samples show their peak emission energy at roughly 2.77 eV (448 nm). Overall, the PL intensity increases with successive cycles of Mg-conditioning with MQW1 (no conditioning) showing the lowest intensity and MQW5 (most extensive conditioning and air exposure) showing the highest. The samples show a maximum integrated PL intensity increase of 41% and peak intensity increase of 52% (MQW5). No defect-related luminescence (e.g. the yellow luminescence band) is observed. The effectiveness of chamber conditioning at increasing the PL intensity is significant; growing MQW structures in an unconditioned stainless steel chamber after initial Cp_2Mg exposure introduces Fe and Mn impurities that reduce the PL intensity. With multiple cycles of Mg-conditioning and MQW growth, the contamination mechanism is suppressed, and the PL intensity gradually recovers to the same intensity as the sample grown before Cp_2Mg was introduced in the chamber (Figures 7.7 and 7.8).

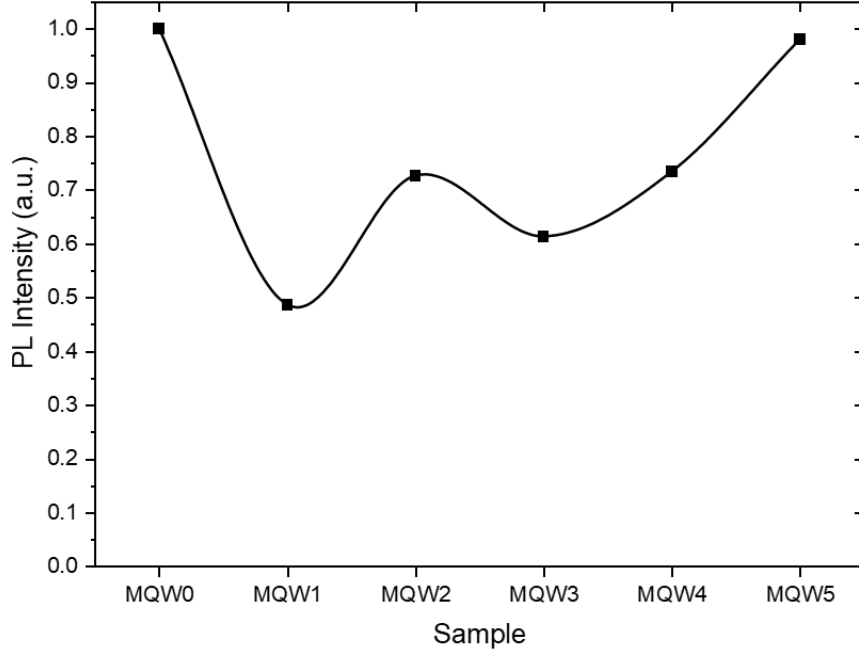


Figure 7.8: Integrated PL intensities of the samples showing improvement in performance with successive cycles of chamber conditioning.

In addition to the overall PL intensity, spatial and spectral emission uniformity is examined using a micro PL (μ PL) setup with a $\lambda = 325$ nm continuous wave laser. Figure 7.9 shows the integrated PL intensity mapping of the samples relative to their respective averages in a 200×200 μm area. The intensity distribution in MQW1, which has the most of Fe and Mn impurities and lowest PL intensity, shows the highest level of nonuniformity (σ) of 8.3% (Figure 7.9). This sample shows numerous dark spots as dim as 17% weaker than its average. With the five and six cycles of Mg-conditioning, MQW2 and MQW3 show reduced σ of 5.5% and 5.1%, respectively. The trend continues with MQW4 and MQW5, which show a σ of 3.6% and 3.9%, respectively. These data suggest the Fe and Mn impurities maybe the culprit in creating localized nonradiative recombination centers that reduce the overall PL intensity.

To study the optical properties of the samples in the temporal space, time-resolved PL is conducted (Figure 7.10) using a frequency-doubled, femtosecond Ti:sapphire laser ($\lambda = 385$ nm, 1 nJ pulses) and an avalanche photodiode with bandpass filters for data collection. MQW1 shows biexponential decay PL lifetimes (τ_{PL}) of 0.8 and 2.78 ns at time interval between 0~2 ns and 2~6 ns after laser pulse incidence, respectively, while MQW2 and MQW

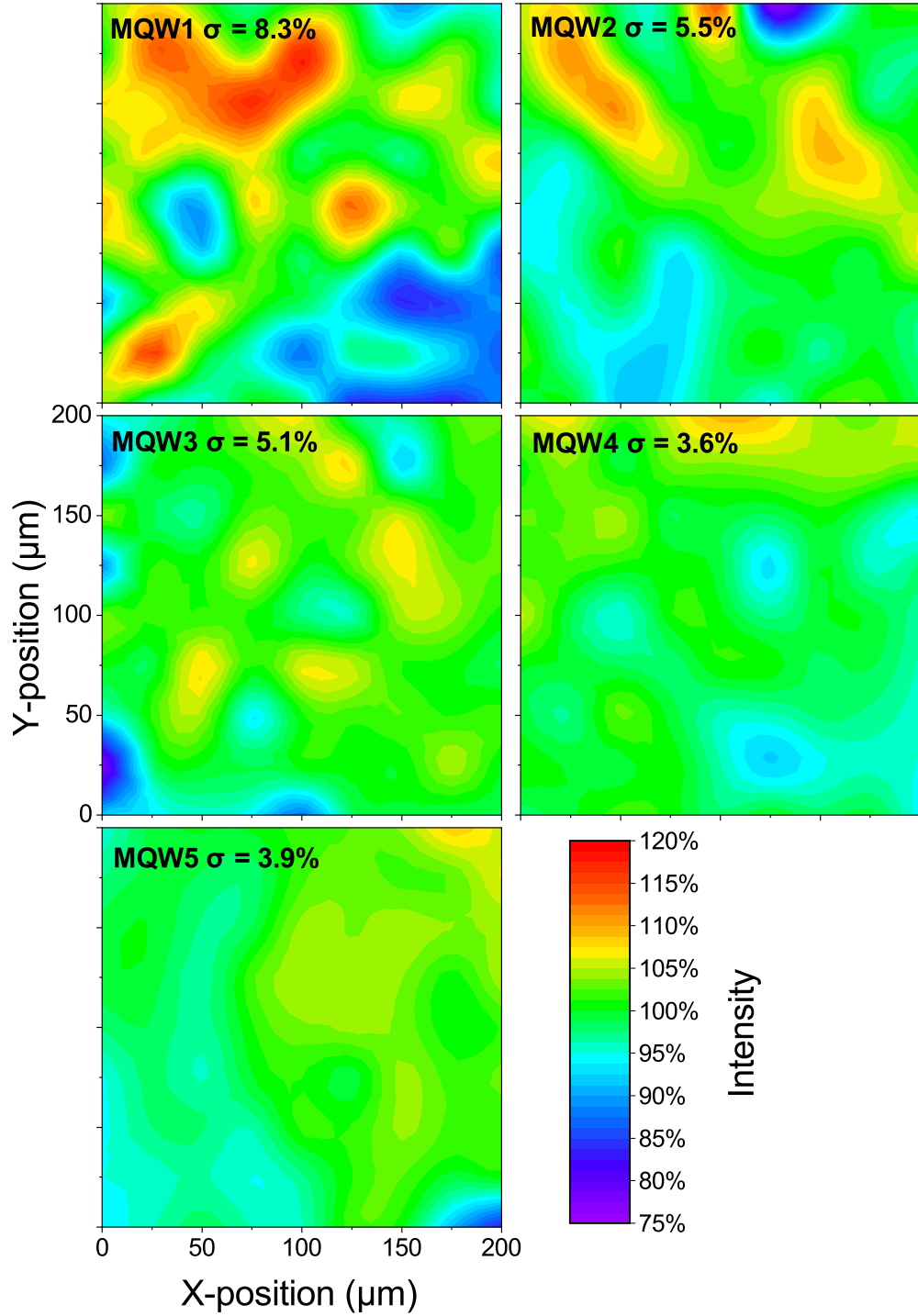


Figure 7.9: Micro PL mapping of the intensities of the samples over a $200 \times 200 \mu\text{m}$ area. Each figure is scaled relative to its own average. The standard deviations are also shown.

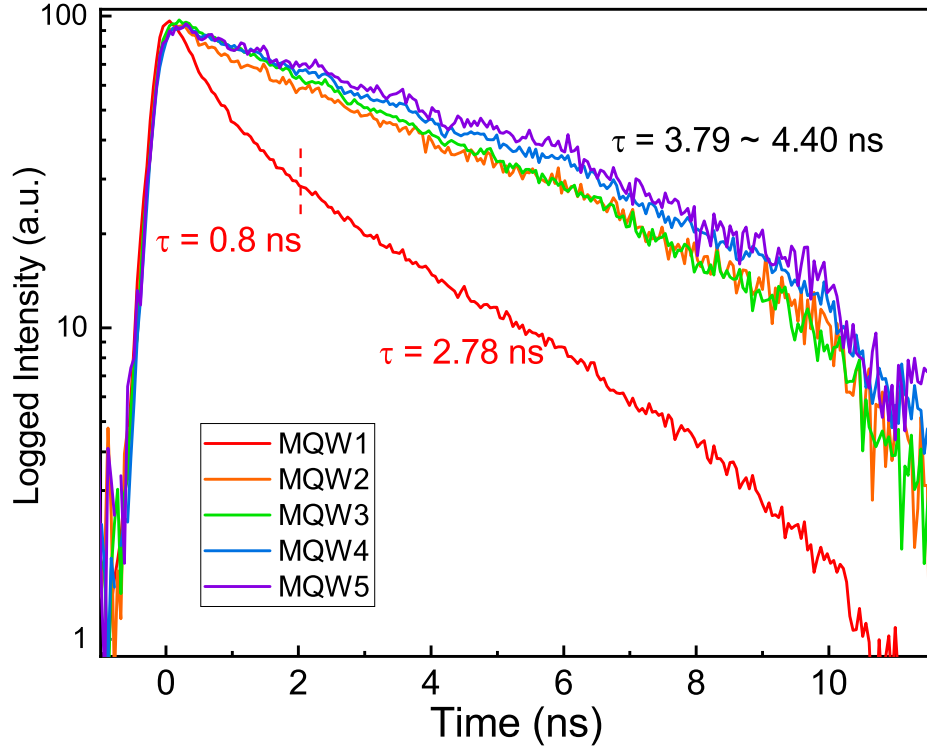


Figure 7.10: Time-resolved PL using a 385 nm laser shows that MQW1 exhibits a biexponential decay, whereas the remaining samples have monoexponential decays with much longer lifetimes.

3 show similar monoexponential τ_{PL} of ~ 3.79 ns, and MQW4 and MQW5 show an additional increase in τ_{PL} to ~ 4.43 ns. This suggests that the initial cycles of Mg-condition (MQW2) eliminated a vast majority of the nonradiative recombination centers, likely caused by the Fe and Mn impurities, that are responsible for the difference in the τ_{PL} . Meanwhile, a few additional cycles (MQW3, MQW4), and further cycles of Mg/air exposures (MQW5) yielded only small increases in over MQW2. This demonstrates the importance of eliminating these transition metal contaminants even at very low concentrations.

To study the effect of these nonradiative recombination centers in MQW1 and their reduction in the other samples, temperature-dependent (6 K – 300 K) PL is conducted using a $\lambda = 266$ nm laser and a liquid helium bath cryostat with a PID temperature controller (Figure 7.11). The temperature-

dependent internal quantum efficiency (IQE) is calculated using:

$$IQE(T) = \frac{I(T)}{I(6\text{ K})} \quad (7.1)$$

where $I(T)$ is the integrated intensity of the PL emission at temperature T , and assuming at 6 K the recombination mechanism is purely radiative [103]. MQW1 exhibits the lowest IQE of 39% at 300 K, whereas MQW2 and MQW3 exhibit similar IQEs at 53 and 51%, respectively. This suggests the chamber conditioning eliminates a significant number of the nonradiative recombination centers and increases the IQE. Multiple additional cycles of Mg-conditioning have a diminishing return (MQW4 and MQW5) with IQEs that show an additional 10% increase ($IQE > 60\%$). The observation made on the trend of IQE across the samples roughly mirrors that of the integrated PL intensities (Figure 7.6) and TRPL (Figure 7.10); chamber conditioning decreases the rate of nonradiative recombination. The similarities in the trends of these three characterization techniques suggest the differences in observed optical properties originate from the same nonradiative recombination centers introduced by the Fe and Mn impurities that reduce PL intensity, shorten PL lifetime, reduce IQE.

7.4 Data Analysis

Closer inspection of the temperature-dependent PL spectra revealed that all samples exhibit a low-energy PL peak at 2.7 eV at temperatures below 100 K. This emission center has been associated with potential minima caused by local indium clustering [156] and is especially prominent in MQW1, and becomes less prominent with successive Mg-conditioning. Studies have shown that some impurities (e.g. Si) in the InGaN/GaN MQW on Al_2O_3 can result in the formation of nano-scale high-indium-content clusters [157, 158]. The data here suggests this phenomenon may also occur with Fe or Mn impurities.

The extracted PL peak emission energy and peak emission energy shift from their 6 K values as a function of temperature are plotted in Figure 7.12. All five samples show a distinct blueshift in the peak emission energy as the temperature decreases from 300 K; the trend then reverses to red-shifting at temperatures below 170 K, and lastly the trend reverses again to blue-shifting

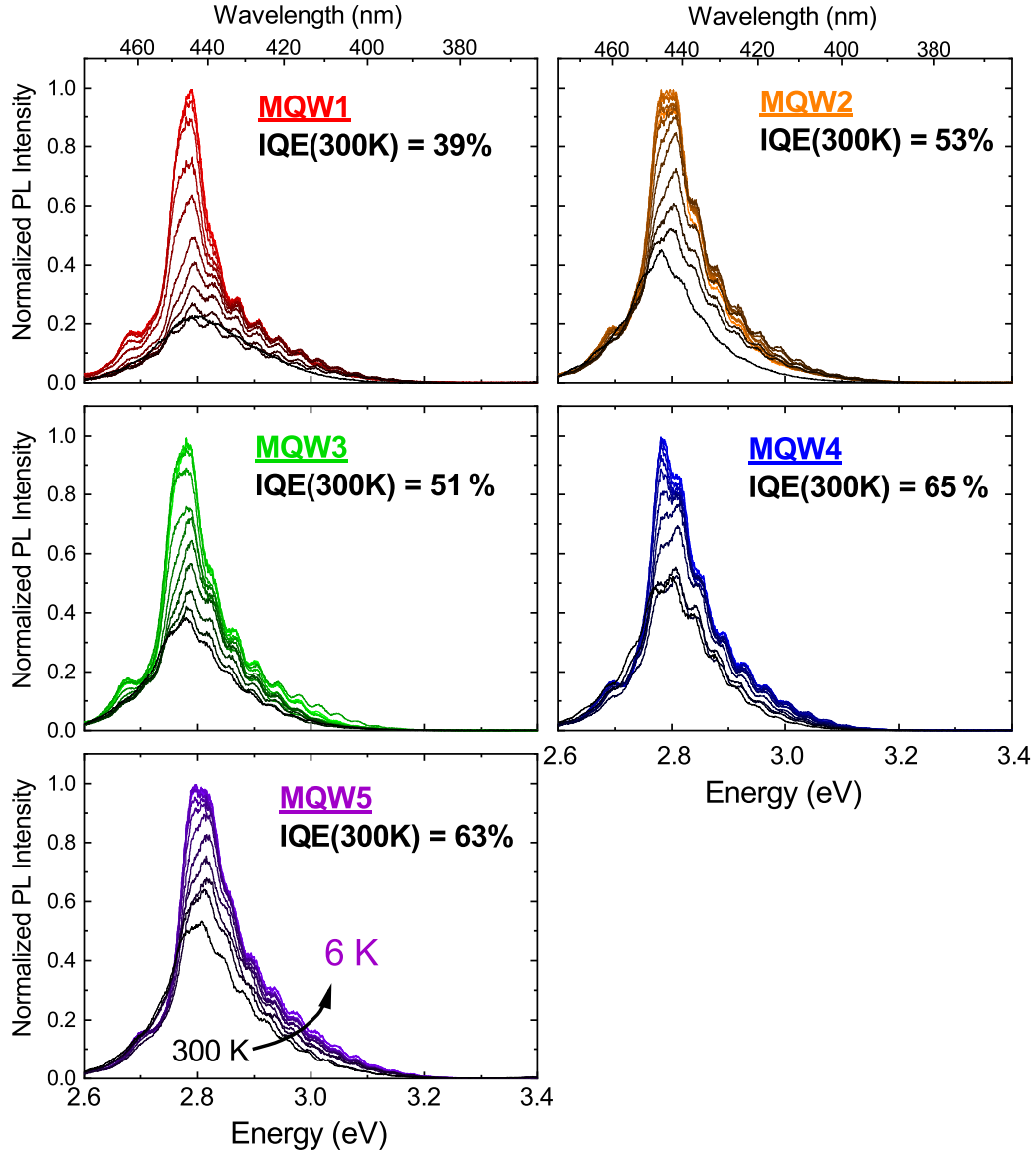


Figure 7.11: Temperature-dependent PL spectra of the samples from 6 K to 300 K. MQW1 has the lowest IQE (39% at room temperature) of all devices. Mg-conditioning improves the IQE from 39% to a maximum of 65%.

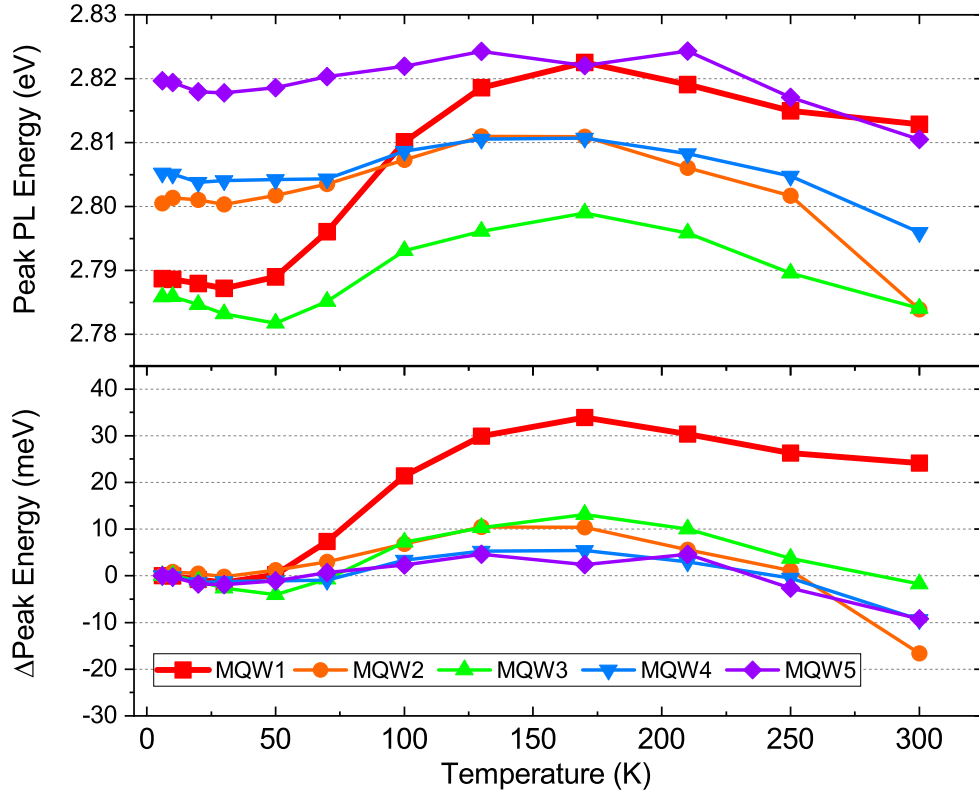


Figure 7.12: (top) Temperature-dependent Peak PL emission energies. (bottom) Peak emission energy shift from its 6 K value.

at temperatures below 20 K. This s-shaped redshift-blueshift-redshift behavior is attributed to the carrier localization in the inhomogeneity in the InGa_N MQWs [139]. Comparing the magnitudes of the blueshift at 170 K, MQW1 shows exceptionally strong shift at 36 meV. Meanwhile, MQW2 and MQW3 only blueshift by ~ 10 meV, and MQW4 and MQW5 blueshift by an even smaller amount at ~ 5 meV. At temperatures higher than 170 K, all samples redshift at the similar rate. This progressive reduction in the magnitude of the S-curve in the samples with increasing cycles of conditioning shows a correlation between Fe and Mn impurities and the carrier dynamics in the quantum wells; these atoms induce inhomogeneity in the InGa_N layer. This phenomenon does not appear to be significant when the impurity concentrations fall below the detection limit.

This relationship is consistent with the observations made in the μ PL uniformity measurements showing a decrease in integrated PL nonuniformity from MQW1 to MQW5 and mirrors the decrease in the intensity of the 2.7 eV

low-energy shoulder in low-temperature PL results from MQW1 to MQW5, in which the strongest effect is found in the sample with Fe and Mn impurity concentrations above 10^{15} cm^{-3} and 10^{14} cm^{-3} , respectively.

The IQE values can be used in conjunction with the carrier lifetime obtained from TRPL to calculate the radiative and nonradiative recombination lifetimes using [103]:

$$IQE = \frac{\tau_{rad}^{-1}}{\tau_{PL}^{-1}} \quad (7.2)$$

where τ_{rad} and τ_{PL} are the radiative and PL lifetimes, which allows the extraction of nonradiative recombination lifetimes (τ_{nr}) via:

$$\tau_{PL}^{-1} = \tau_{rad}^{-1} + \tau_{nr}^{-1} \quad (7.3)$$

The extracted lifetimes of the samples are shown in Figure 7.13.

The radiative lifetimes of the samples are calculated to be in the neighborhood of 7 ns. This is expected as the physical structures (QW layer thicknesses), strain, defectivity, and composition are statistically the same, and the values fall within the reported range for InGaN-based blue emitting MQWs [159]. The variation in τ_{nr} shows the detrimental effect of Fe and Mn impurities; MQW1 exhibits a very fast τ_{nr} (4.54 ns). Reducing their concentrations in MQW2 increases the τ_{nr} by a significant 3.54 ns. Under the low injection level presented here, nonradiative recombination can be assumed to be dominated by Shockley-Reed-Hall recombination (SRH), the A coefficient, which can be expressed as [101]:

$$A = \frac{1}{\tau_{nr}} \quad (7.4)$$

The increase in τ_{nr} between MQW1 and MQW2 corresponds to a decrease in the SRH coefficient from $2.2 \times 10^8 \text{ s}^{-1}$ to $1.2 \times 10^8 \text{ s}^{-1}$. The $1 \times 10^8 \text{ s}^{-1}$ reduction in the SRH recombination rate, coinciding with the reduction in the Fe impurity concentration from $3 \times 10^{15} \text{ cm}^{-3}$ to below detection limit, is in good agreement with the rate reported in the literature [153, 160].

One additional cycle of Mg-conditioning after the growth of MQW2 increases the τ_{nr} by another ~ 1 ns in MQW3. This suggests that the chamber conditioning is not yet complete even with the impurity concentrations below the detection limit. Additional extensive Mg-conditioning before MQW4 was

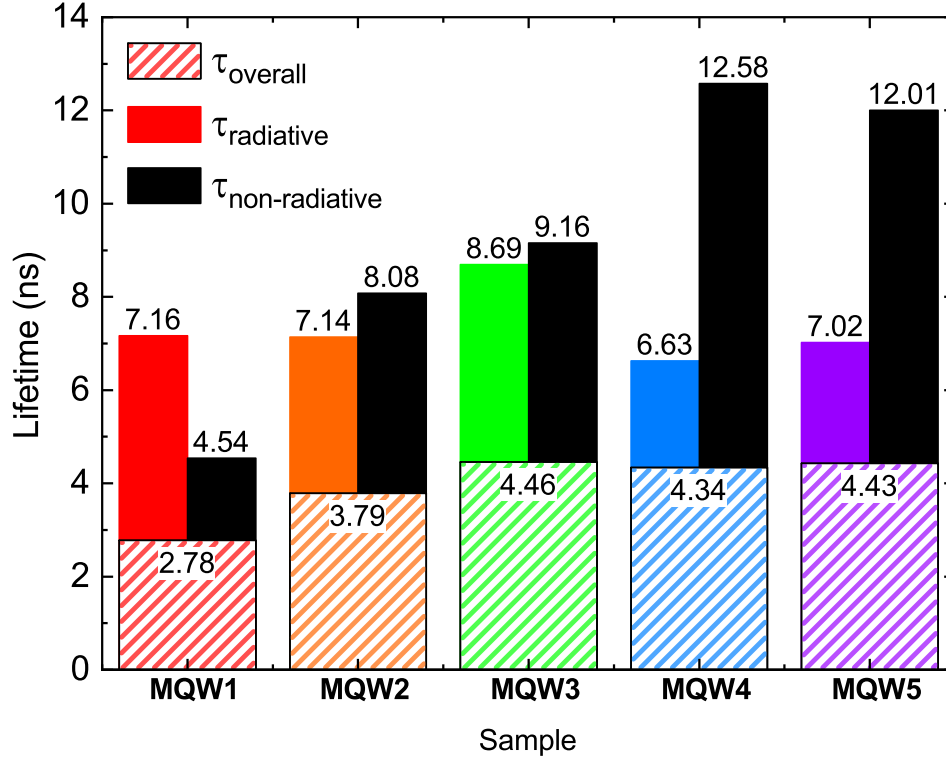


Figure 7.13: Radiative and nonradiative lifetimes calculated using the TRPL and IQE measurements.

grown increased its τ_{nr} by another ~ 3 ns, but further cycles did not yield a significant improvement in MQW5. These results suggest that the benefit of chamber conditioning has a diminishing return with the majority of the contaminants suppressed within the first five cycles of Mg-conditioning.

Conditioning of the MOCVD chamber appears to be complete somewhere between MQW3 and MQW4 using characterization techniques such as μ PL, IQE, and TRPL, which show no significant difference between MQW4 and MQW5. As far as these techniques show, the loss in optical performance seems to be fully suppressed after $\sim 10+$ cycles of Mg-conditioning. The largest performance gained was during the first five cycles that also coincide with the reduction in Fe and Mn impurity concentration. The data suggest these transition metal impurities are hurting the optical performance of blue-emitting InGaN/GaN MQWs at a concentration slightly below the SIMS detection limit of 10^{15} cm^{-3} .

7.5 Conclusion

In conclusion, through temperature-dependent, time-resolved, and μ PL, this chapter shows the detrimental effects of Fe and Mn impurities in blue-emitting InGaN/GaN grown in a new MOCVD reactor. Even at very low concentrations (3×10^{15} and $3 \times 10^{14} \text{ cm}^{-3}$, respectively), these impurities are capable of forming efficient nonradiative recombination centers with recombination rates in the 10^8 s^{-1} range. Through successive conditioning of the chamber, the impurities were reduced to below detection limit, IQE increased by 26%, μ PL intensity variation decreased by 4.7%, nonradiative recombination lifetime increased by 8 ns, and the magnitude of the S-curve shift decreased by 86%. Unintentional trace transition metal ion impurity contamination has been shown experimentally to play a significant role in the conditioning of MOCVD chambers. New installation of MOCVD reactors should take the suppression of the contamination from these metallic sources into consideration to accelerate the process of conditioning.

CHAPTER 8

LASER DESIGNS FOR SPACE-BASED SCIENTIFIC EXPERIMENTS AND APPLICATIONS

This chapter describes the work done at the Laser and Optics Branch (Code: 554) at National Space and Aeronautics Administration (NASA) Goddard Space Flight Center (GSFC) in Greenbelt, Maryland. This work includes the construction of a prototype UV laser for a lander-based mass spectrometer and its optimization over the years.¹

8.1 Introduction: Ultraviolet Laser

For surface chemistry experiments on planetary bodies such as the moon, Mars, and Europa, one of Jupiter’s Galilean moons, a mass spectrometers provides a progressive analytical platform for its ability to detect very specific molecules at a very high rate and with high accuracy. Currently, NASA has two ongoing missions, Characterization of Ocean Residues And Life Signatures (CORALS) and Characterization of Regolith And Trace Economic Resources (CRATER), to explore the potentially habitable environments in the solar system and search for signs of extraterrestrial life. The solid state laser-based spectrometer Orbitrap is currently under development for a compact, robust, and high technology readiness level (TRL) for the prospective lander-based instruments.

The solid state laser will serve as a desorption and ionizing source, and comes from the design of a previous mission, Mars Organic Molecule Analyzer (MOMA), onboard the ExoMAr rover. The laser will generate laser pulses of 4 ns width with total energy $> 450 \mu\text{J}/\text{pulse}$ at $\lambda = 266 \text{ nm}$ and a repetition rate between 1 and 10 Hz. Ability to attenuate the pulse energy from 1-100% is required, and the ability to redirect the beam to perform a raster

¹Portions of this chapter were previously published as M. Fahey, A. Yu, R. Liu, R. Arevalo, A. Grubisic, X. Li, S. Getty, “Ultraviolet Laser Development for Planetary Lander Missions,” IEEE Aerospace Conference, Big Sky, MT, USA, Mar 7-14 (2020).

scan should be built into the system to allow the lander to sample over a wider area and to accommodate the potentially uneven surfaces of the celestial bodies. The laser is chosen to be a Nd:YAG laser using a slab crystal and side pumped by an array of laser diodes to minimize footprint. The master oscillator power amplifier will lase at a fundamental wavelength of $\lambda=1064$ nm to be frequency quadrupled by nonlinear optics to ultraviolet. Improvement of this laser configuration, which has been flight-tested, will have a very high mission success-rate that requires fewer additional testing to achieve a high TRL.

8.2 Laser Design

The goal of the laser is to produce 500 μ J, nanosecond, frequency-quadrupled 266 nm laser pulses. The 2018 prototype of the laser uses a Nd:YAG slab to produce the fundamental laser, KTP and BBO crystals for the 2nd and 4th harmonics generation, and six pairs of mirrors (four of which are dichroic) to deliver the pulse energy required for the mass spectroscopy experiment (Figure 8.1). This approach is too cumbersome for battery-powered lander missions. The 2019 prototype improves the design of the laser to cut down on bulk by eliminating the six pairs of mirrors and putting all components in a linear arrangement with a dispersion prism for harmonics separation (Figure 8.2). This approach also benefits from an increased overall 266 nm conversion efficiency due to reduction in the effect of beam divergence from 17% to 20%, in spite of the reflection losses at the uncoated CaF_2 prism. This design allows for a lowered laser diode pump current (from 110 A to 106.4 A) and obviate the need for additional optics.

The new overall design is shown in Figure 8.3. The miniaturization of the Nd:YAG-based 4th harmonic (266 nm) laser breadboard is completed for the CORALS instrument proposal. The revised version utilizes a passive Q-switch (PQS), potassium titanyl phosphate (KTP), lead zirconate titanate (PLZT), barium borate (BBO), and dispersive prism to achieve the 4th harmonic generation, its conversion efficiency modulation, and harmonics separation.

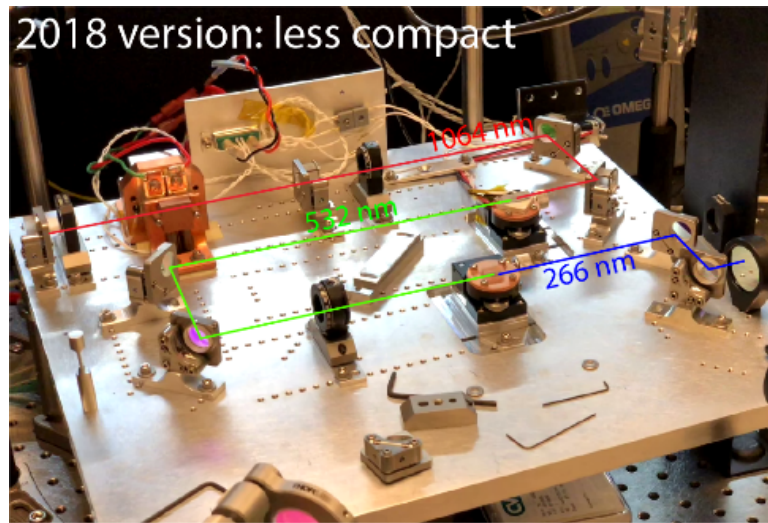


Figure 8.1: Standard UV laser configuration (2018) before miniaturization.

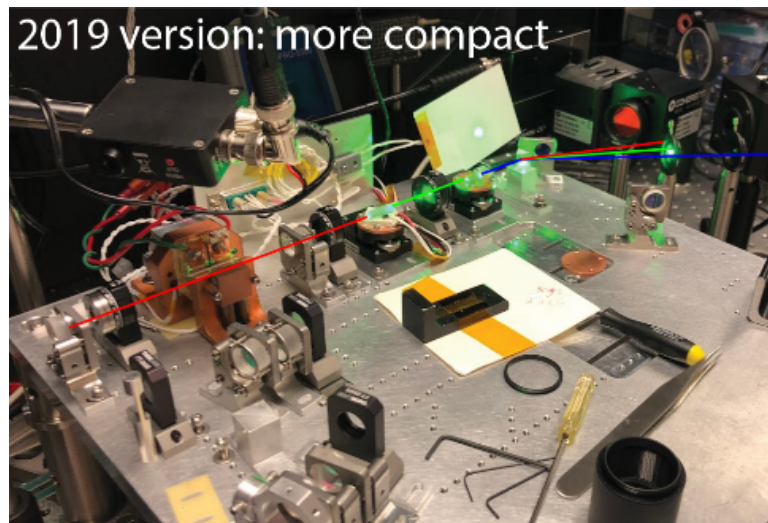


Figure 8.2: Advanced UV laser configuration (2019) after miniaturization implementing CaF_2 for harmonics separation.

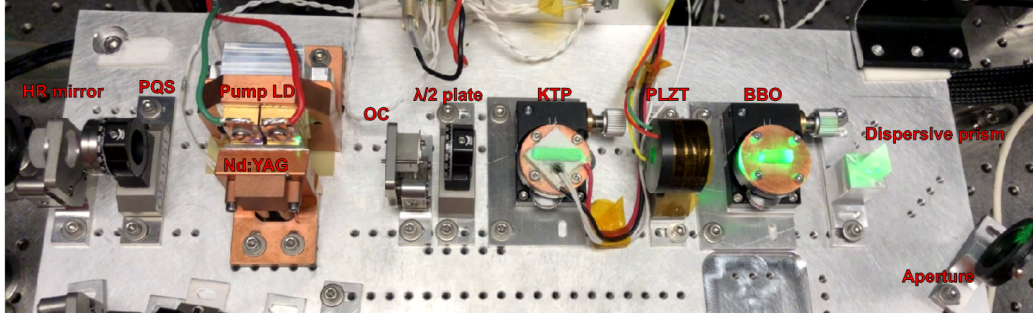


Figure 8.3: Laser setup: High reflective (HR) mirror, passive Q-switch (PQS), pump laser diode (LD), Nd:YAG slab, output coupler (OC), half waveplate ($\lambda/2$ plate), KTP crystal, PLZT crystal, BBO crystal, CaF₂ dispersive prism, and an aperture to select the harmonics for transmission.

8.3 Laser Performance

Overall conversion efficiency (1064 nm to 266 nm) is approximately 20%. A 266 nm pulse energy of 200 μ J is achieved. However, some BBO mounting stage instability led to a fluctuation of the conversion efficiency due to drifting in phase matching. Temperature related degradation of conversion efficiency was measured and ruled out. Over a one-hour period, the CORALS UV laser system exhibited a small temperature deviation; all the actively cooled components, except the Nd:YAG slab, stayed within 1 $^{\circ}$ C of their initial values (Figure 8.4). The BBO crystal, which is not cooled, only showed a 1 $^{\circ}$ C increase, which is the same as the increase in ambient temperature. Therefore, the temperature of the BBO crystal is not the cause of conversion efficiency fluctuation. The Nd:YAG slab does show a rapid increase in temperature from 23.6 $^{\circ}$ C to \sim 28 $^{\circ}$ C within the first 10 minutes. This rise in temperature also decreased the radiative efficiency of the crystal, and the switch-out time is increased as a result (Figure 8.5).

The UV laser power over the same period shows that the power decreases from 8.5 mW to 6.7 mW within the first 30 minutes, while the 532 nm and 1064 nm scattered power showed no variation. Realignment of the BBO crystal was completed around the 70 minute mark, which showed an increase of the UV laser power to 10 mW, but it also rapidly decreased (Figure 8.6). Ambient light was turned on, and the 1064 nm power reading became inaccurate.

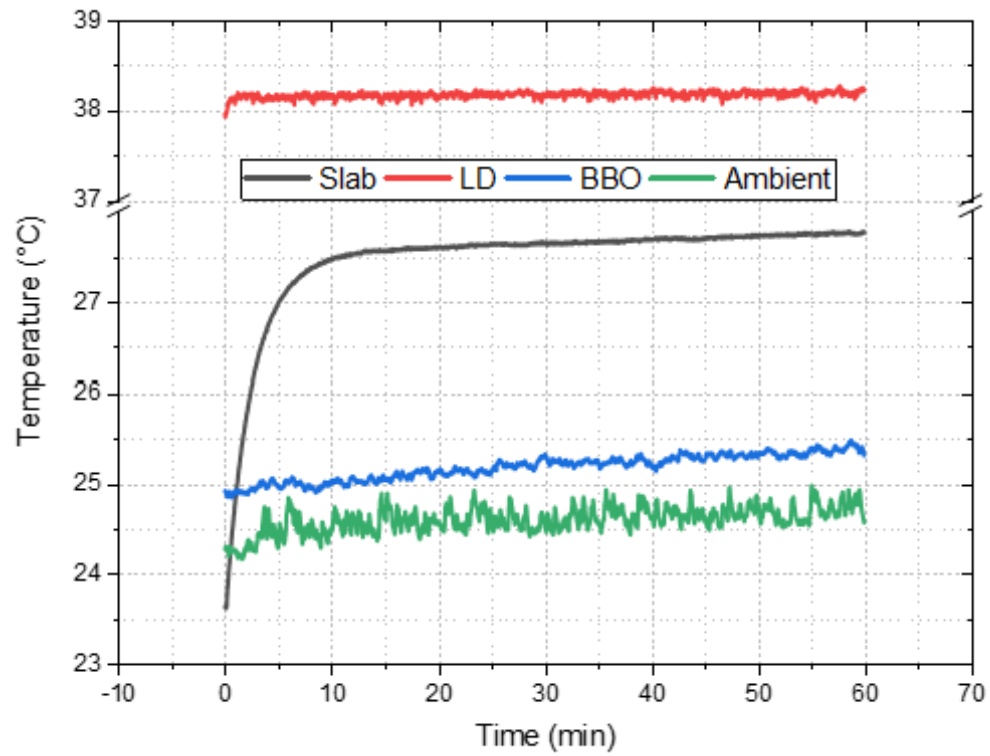


Figure 8.4: Temperature of the CORALS UV laser over one-hour period under continuous operation. (Left) temperature of Nd:YAG slab, pump LD, BBO crystal, and ambient temperature.

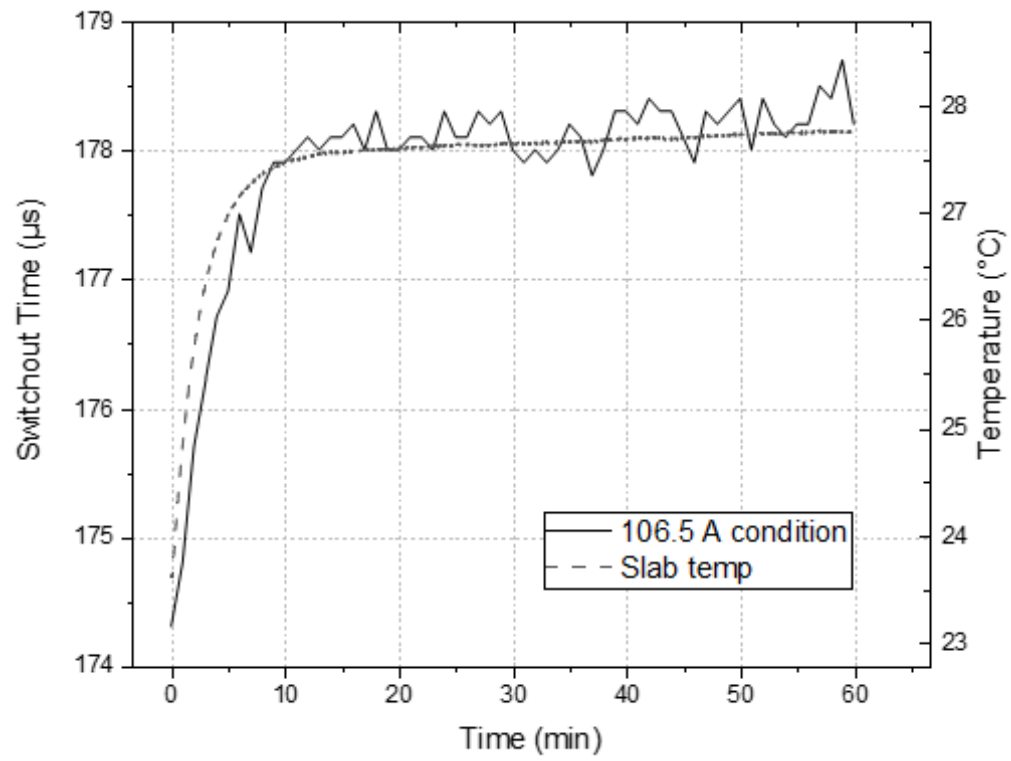


Figure 8.5: PQS switch-out time and slab temperature.

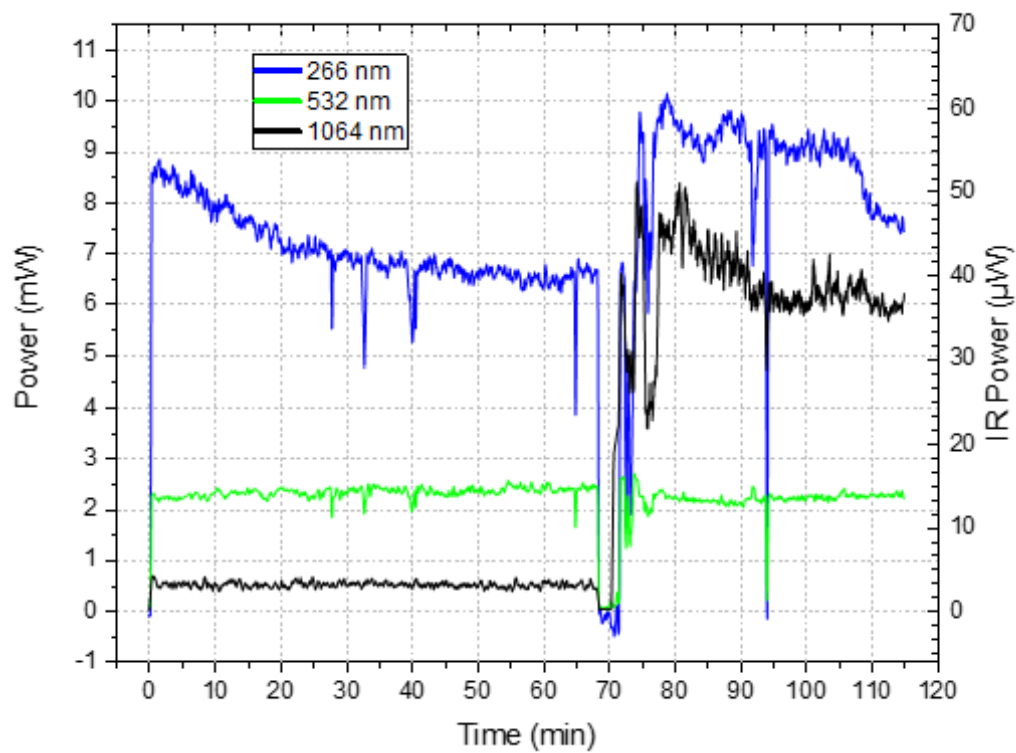


Figure 8.6: Temperature profile of the laser components over two hours of operation with one realignment at the 70 min mark.

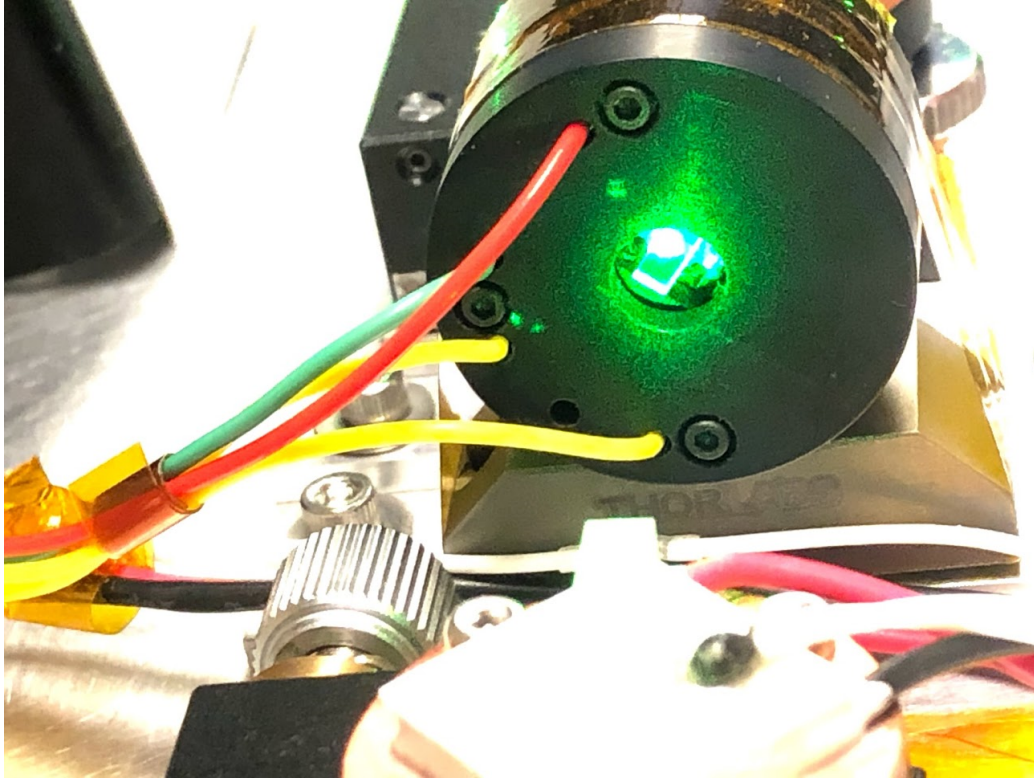


Figure 8.7: PLZT polarization rotator with the 532 nm laser beam landing roughly in the middle of the crystal. The KTP crystal is visible in the foreground.

8.4 Laser Power Modulation

To modulate the UV laser power, a PLZT polarization rotator was used to replace the 532 nm waveplate (Figure 8.7). The PLZT requires approximately 480 V to achieve a polarization rotation of 180° . A built-in thermo-electric controller and a high-voltage source were procured for the PLZT. The component was installed on an adapter plate using some Kapton tape, and good alignment was achieved. A full 0-100% UV laser power modulation was observed (Figure 8.8).

8.5 Beam Steering

The next step for the UV laser is to implement a micro-electro-mechanical semiconductor (MEMS) mirror to add the ability to steer the beam in a raster scan pattern to cover a surface that is not necessarily flat. A development kit

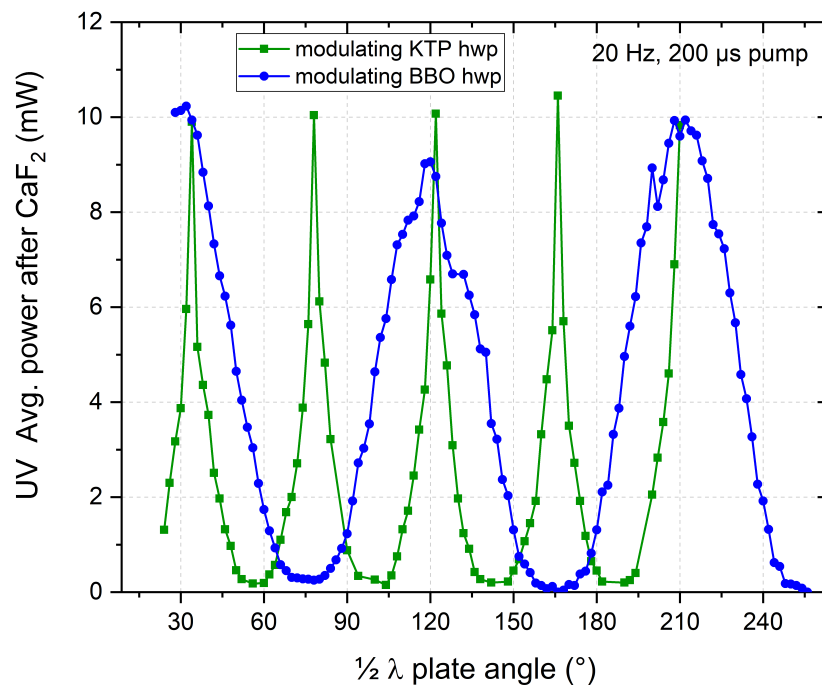


Figure 8.8: Modulation of the efficiencies of the 2nd and 4th harmonic generation using a PLZT polarization rotator.

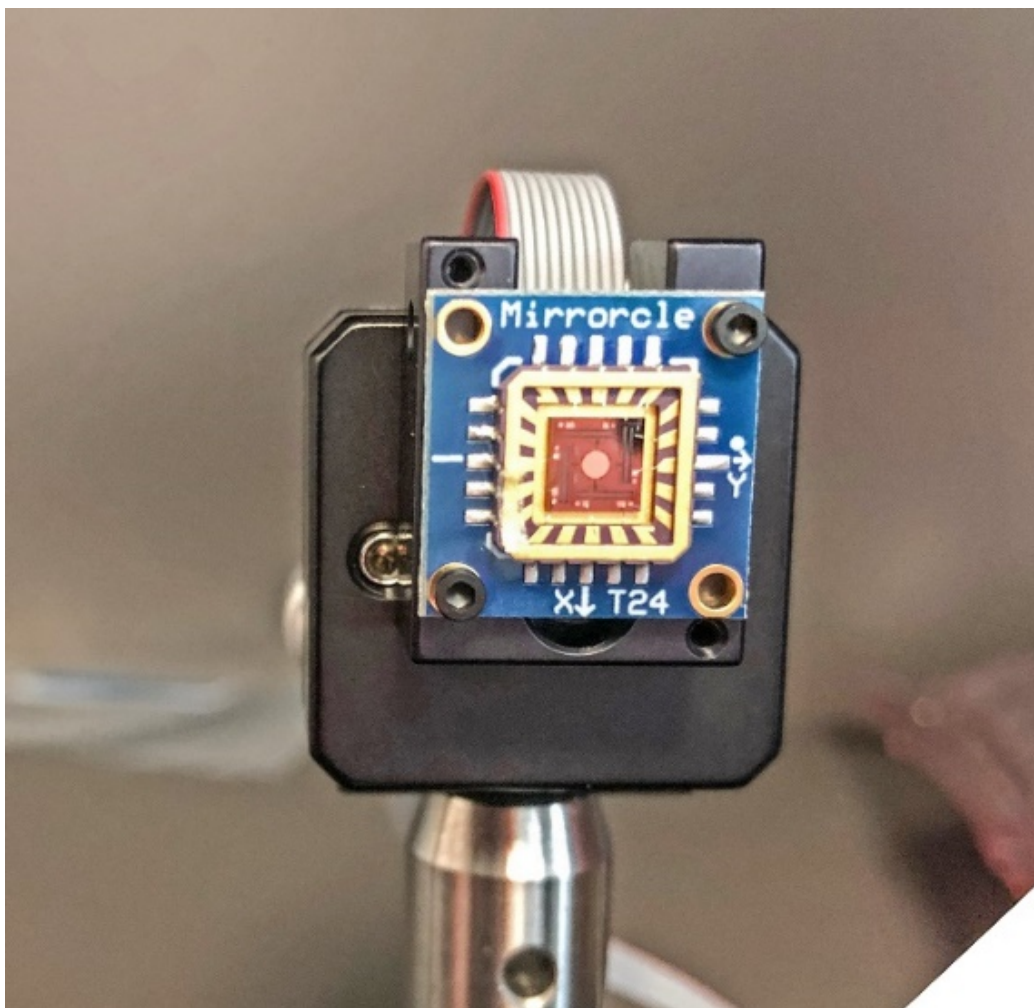


Figure 8.9: Mirrorcle MEMS mirror.

from Mirrorcle Technologies that includes a 5V USB-powered driver module, a laser pointer, and a MEMS mirror (Figure 8.9) is fitted at the end of the laser assembly for beam steering into arbitrary position following any nominal path as long as it is within the $\pm 5^\circ$ range. Preliminary results show that the commands sent to the MEMS were able to steer the beam to any arbitrary position following a path (Figure 8.10). Once the UV laser design is finalized and approved, the mirror will be integrated to the laser system for a complete deliverable for further testing (thermal vacuum) and capability demonstration.

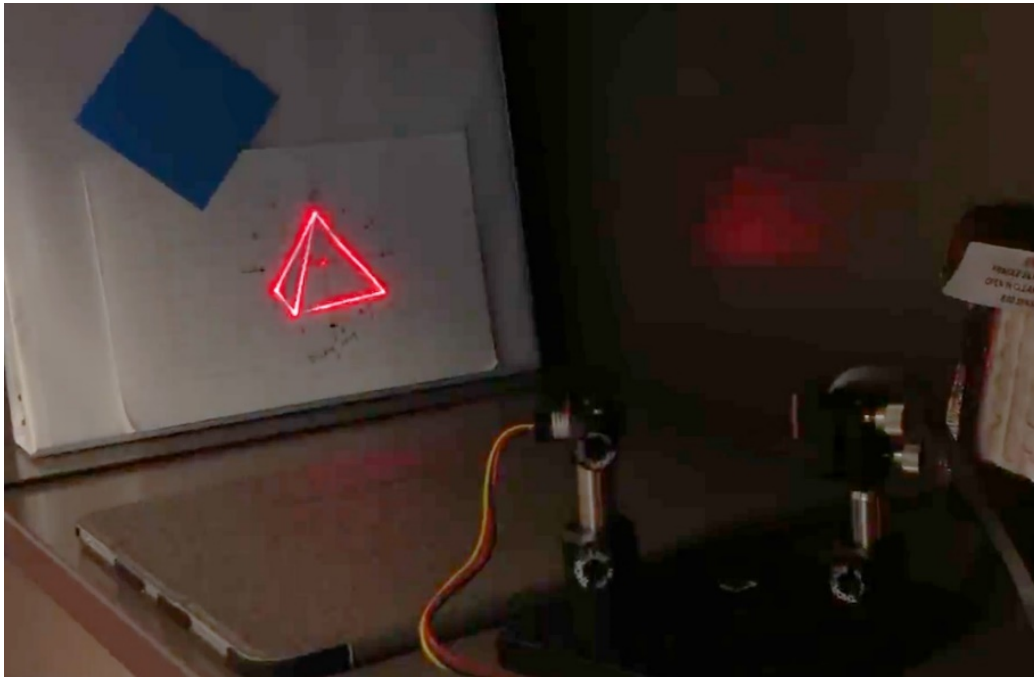


Figure 8.10: An animated trace of a pyramid produced using vector scans from the mirror and a laser pointer at 60 Hz.

CHAPTER 9

OUTREACH ACTIVITIES AND COURSE DEVELOPMENT

This chapter describes the activities pertaining the outreach for solid state lighting research. These include a course developed for hand-on characterization of LEDs and solar cells, and collaboration with external researchers funded by the National Science Foundation.

9.1 Course Development

A new course (ECE443) within the Department of Electrical and Computer Engineering of the University of Illinois Urbana-Champaign focused on the LED and solar cell device operation theory, design, growth, fabrication, characterization, and verification was drafted, proposed, piloted, refined, and approved for the permanent curriculum in 2019. The lab modules of the course were designed, revised, and launched. The planning and procurement of the necessary equipment (scanning electron microscope, parametric analyzer, heating stage, and spectrometers, as shown in Figure 9.1) to conduct characterization of as-fabricated light emitting diodes on a piece of sapphire wafer (Figure 9.2) and solar cells (Figure 9.3) was started from the ground up. Over three years, these modules have been revised and the delivery of experimental techniques streamlined. The course, ECE443 LEDs and Solar Cells, is one of the most highly ranked courses in the Department of Electrical and Computer Engineering (ECE).

The lab modules consist of the following: safety training, scanning electron microscopy, LED electrical and optical characterization, temperature-dependent LED characterization, solar cell electrical and wavelength-dependent quantum efficiency characterization, and solar cell temperature-dependent quantum efficiency. The six lab modules can be found in Appendix B.



Figure 9.1: Three Keithley probe stations including one fitted with thermal stage and black box.

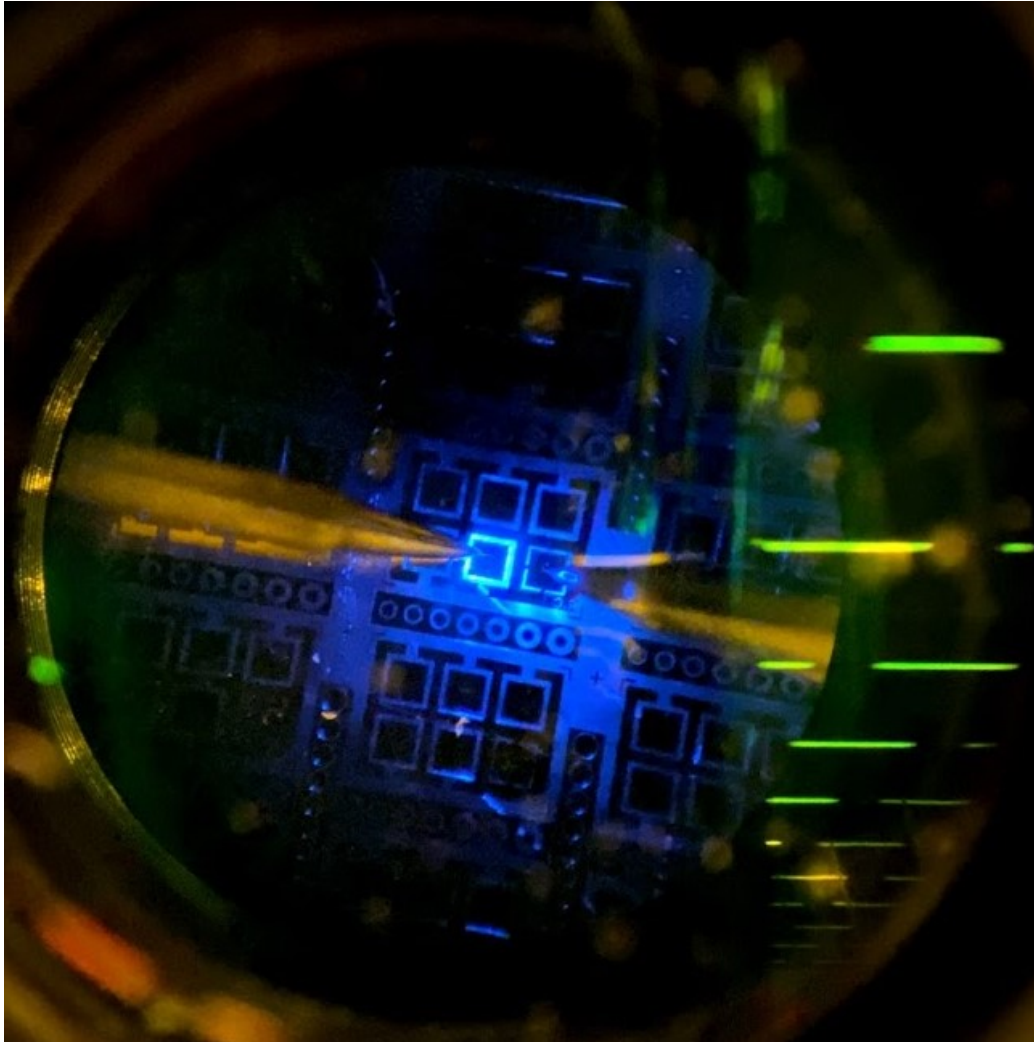


Figure 9.2: Lab setup for ECE443. On-wafer LED sample under testing as viewed through an optical microscope.

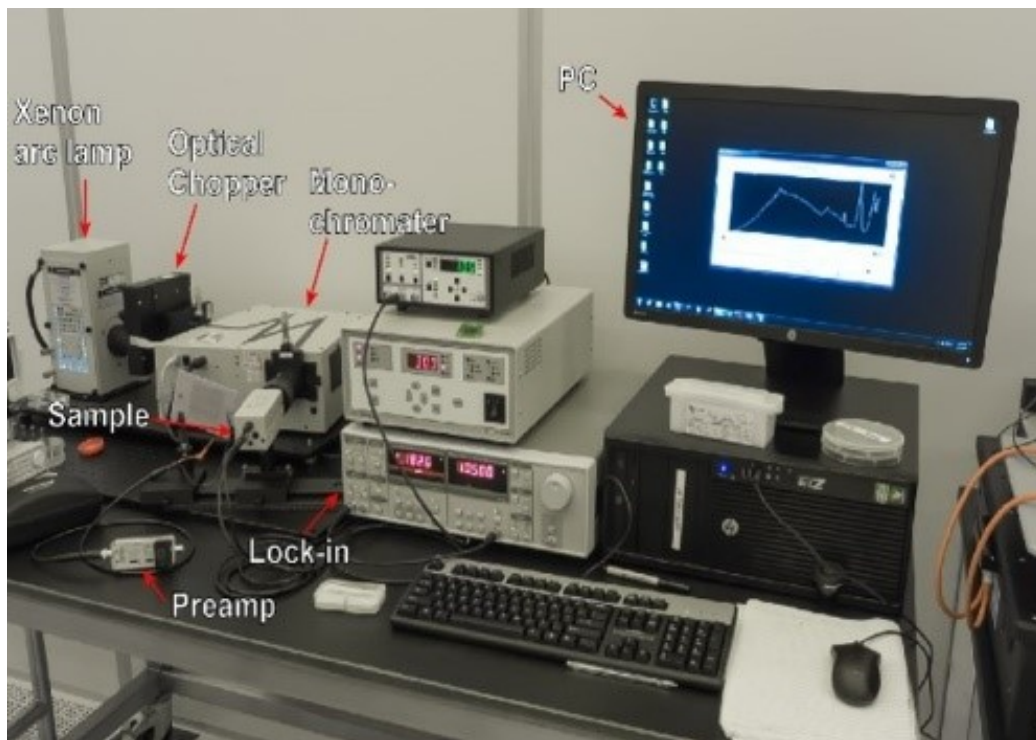


Figure 9.3: Solar cell EQE testing bench.

9.2 Research Experience for Undergraduates

The goal to advance the National Science Foundation's (NSF) mission to disseminate the knowledge about photonics has involved mentoring the NSF's Research Experience for Undergraduates (REU) program participants during the summers of 2016, 2017, 2018, and 2020 at the University of Illinois Urbana-Champaign. The mentorship consists of demonstrating graduate-level photonics research and supervising the participants as they engaged in hands-on research activities (cleanroom wet chemistry, low-temperature Hall effect measurements, and using the scanning electron microscope). The participants learned to perform data analysis in OriginPro and MATLAB. At the end of the program, the REU participants were assisted with poster presentation preparation, and program report preparation and writeup.

We collaborated with the physics department at Colorado College on setting up the NSF's REU program to host research for undergraduate level physics students to conduct solid state physics experiments. Over the summer we conducted temperature-dependent PL experiments and PL intensity mapping of as-grown InGaN LEDs. In addition to characterization experi-

ments, we conducted fabrication technique development such as silicon oxide growth optimization and potassium hydroxide anisotropic etching of silicon wafers. We also designed a photolithography mask for future fabrication of c-GaN LED. The collaboration has resulted in two publications in scientific journals [113, 161] and a conference presentation [65].

9.3 Research Experience for Teachers

In addition to the REU program, the Research Experience for Teachers (RET) was also hosted for two summers. Participants received help in developing a junior/senior high school level physics experiment in solid state lighting: measuring the width of a piece of hair using a laser pointer, and taking an LED chip apart to find the GaN semiconductor. This collaboration resulted in the funding and construction of a life-size atomic force microscope at a high school in Portland, Oregon.

9.4 Intra-Institutional Educational Outreach

To broaden our community outreach, we are developing a theme-based interactive solid state lighting outreach program, which we will be piloting at a local middle school with a large underrepresented student presence. A portable exhibit will be devised to educate K-12 students and the general public about solid state lighting. It involves making electrical contact with LED structures on an uncut wafer, then measuring the efficiency using an integrating sphere while comparing it with conventional light sources.

Expanding the effort to bring research to younger students, I am currently working with a junior undergraduate from the University of Illinois on the characterization of defect-dependence of carrier recombination in photonic semiconductors using time-resolved cryo-photoluminescence. Due to our proximity, the student and I are able to work together over a longer period of time to develop more in-depth experimental and analytical skills. We are planning on submitting a journal manuscript with this aspiring student as the lead author. In addition to research, I have also hosted basic light spectroscopy demonstrations for freshmen from the Underrepresented Pop-

ulations in STEM program. In the demonstrations, I used a spectrometer to scientifically determine whether the internet-famous dress is blue/black or white/gold.

CHAPTER 10

SUMMARY AND FUTURE WORK

Cubic phase gallium nitride has been shown to exhibit many advantageous properties for light emitting applications. The fabrication procedures for phase transition were optimized so that the critical condition of complete surface coverage is achieved. Structural studies showed that the crystal quality of the phase transition c-GaN is almost strain- and defect-free. The crystal's fundamental optical transitions including donor-acceptor pairs are quantified.

10.1 Conclusion

In conclusion, the hexagonal-to-cubic phase transition is shown to be a reliable method to form pure cubic phase GaN. The U-groove parameters, etch depth, opening width, and deposition thickness are shown to be important for complete cubic phase surface coverage. A crystallographic modeling is proposed that is validated by EBSD phase detection, which showed excellent phase uniformity. A highly crystalline and uniform phase transition c-GaN surface can be reproduced when the critical condition, $h_c = (1.06p - 0.75t_d)/(1 - \tan \alpha/0.71)$, is met. Phase transition c-GaN is observed to be under tensile-strain, and its light emission has a 0.2 *degree of polarization* (ρ) along the pattern direction.

Low-temperature CL spectroscopy identified two defect luminescence centers at 144 and 344 eV above the valence band, and imaging of the distribution of these acceptors suggests these are intrinsic defect and extrinsic impurity levels, respectively. At 280 K, c-GaN (h-GaN) shows a near band edge luminescence at 3.22 eV (3.43 eV) and a defect peak at 2.72 eV (2.21 eV), and at 5.7 K, bound exciton transition at 3.28 eV (3.48 eV), donor-to-acceptor transition at 3.18 eV (3.31 eV) and another peak identified as (D^0, A^0) transition at 2.95 eV. The bandgap energy for c-GaN (h-GaN) of

3.31 eV (3.51 eV) and the Varshni coefficient $\alpha=(6.83 \pm 0.22) \times 10^{-4}$ eV/K ($(7.37 \pm 0.27) \times 10^{-4}$ eV/K) are calculated.

These values are in good agreement with published reports. Additionally, the emission wavelength fitting yields acceptor energies of 110 meV and 360 meV for DAP₁ and DAP₂, respectively, in c-GaN. The band-to-band emission of phase-transition c-GaN internal quantum efficiency is calculated independently via temperature-dependent CL and time-resolved photoluminescence to be between 23% and 29%, making this technology suitable for next-generation photonic devices.

10.2 Future Work

Through the detailed structural and optical characterization of the phase transition, the U-groove approach has been demonstrated to be a reliable method of synthesizing high-quality, high-phase-purity, high-performance c-GaN. These are the requirements for the next-generation solid state lighting that is based on the polarization-free cubic phase III-nitrides.

The high IQE demonstrated by the c-GaN is a promising result for high-performing photonic devices. Future extension of this work is to capitalize on the high-quality crystal obtained using the phase transition approach on the silicon substrate nanopatterned with U-grooves. The first approach is to fabricate a vertical LED across multiple periods of U-groove, as shown in Figure 10.1.

The LED active layer stack can be grown on the c-GaN template grown at the critical condition, h_c , provided by the U-grooves. Standard dry etching techniques can etch away part of the LED stack to reveal the n-type layer. Electrical contact fingers and current spreading layer can then be deposited across multiple U-grooves to create an LED array with an arbitrary number of U-grooves. An interdigitated design for the contacts (Figure 10.2) allows the fabrication of large area devices with good electrical spreading efficiency.

Other photonic devices, such as a AlGaIn-based UV Fabry-Perot edge emitting laser, can also be fabricated in the U-grooves, as shown in Figure 10.3. A UV laser can be fabricated on the U-groove in a design similar to that of a ridge-wave guide laser. Depending on the AlGaIn guiding layers used, a direct injection of current to the quantum well may be needed, since the wave

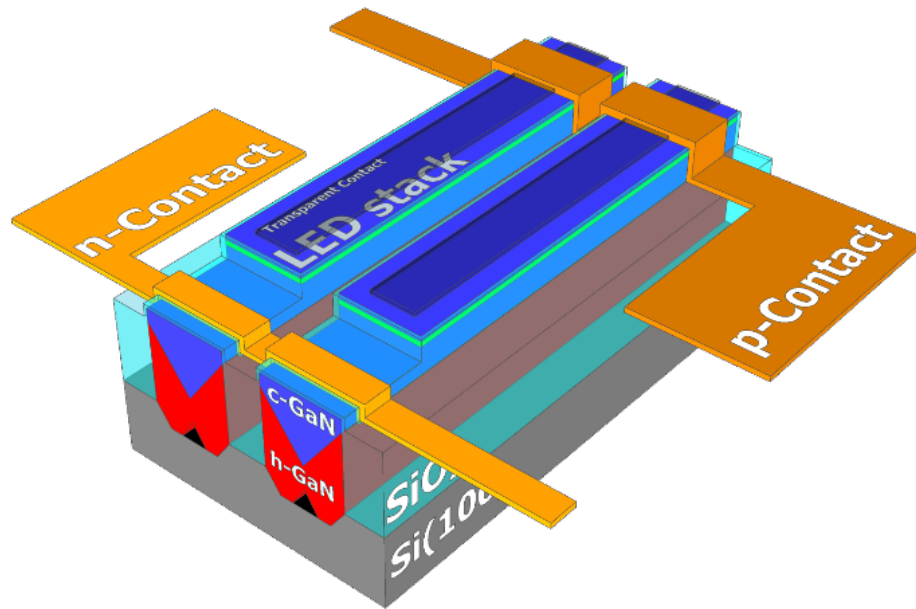


Figure 10.1: LEDs based on the phase transition c-GaN in U-grooves. N- and P-contact fingers can span multiple periods of U-groove to create a larger device.

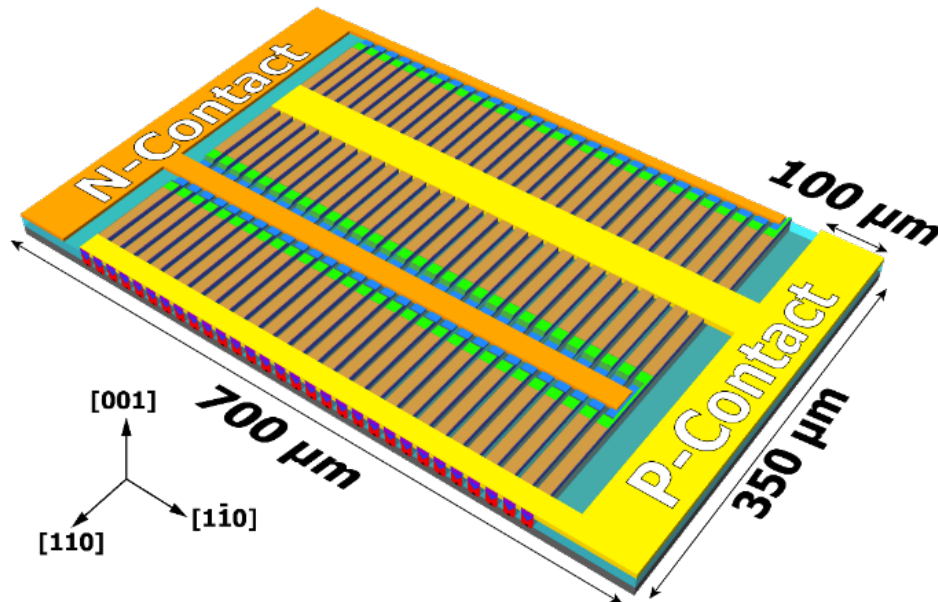


Figure 10.2: The contact fingers can span an area that is similar to standard LED chip size.

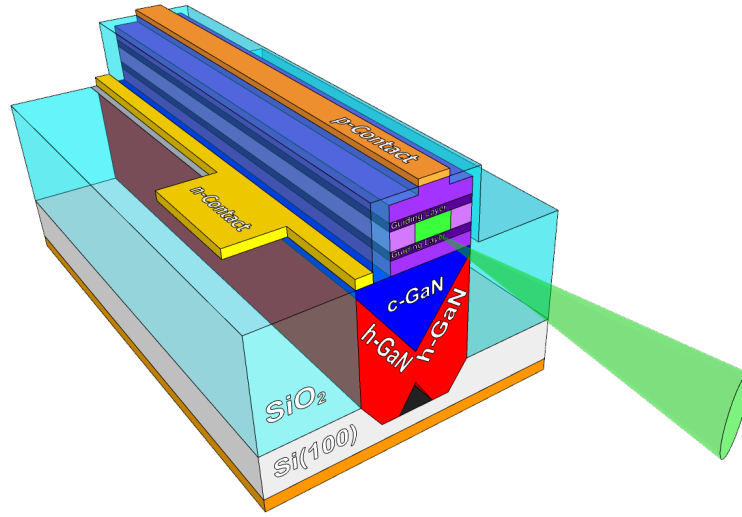


Figure 10.3: Fabry-Perot edge emitting laser diode fabricated on the phase transition c-GaN in a U-groove.

guiding layers might be too resistive. Since the substrate can be conducting silicon, it is possible to use the back side of the substrate as a contact, which is an improvement over III-nitrides on the traditional insulating Al_2O_3 substrates.

Reliability and stability testing can be carried out once these devices are fabricated. As one of the most advantageous properties of GaN is its resistance to radiation and low sensitivity to defects formed by environmental effects, space-based applications are of high interest and importance. The three areas which are of concern are the devices' ability to withstand a high dosage of gamma radiation and high-energy particles, behavior across a wide range of temperature, and projected lifetime/degradation.

For both of these potential devices, loss minimization is paramount and should be explored. Some of the possible directions include sidewall passivation using different materials, thickness, and deposition techniques. Since the substrate is silicon, an obvious augmentation to this technology is device lift-off and transfer to flexible films for novel applications such as intracranial implants.

Another possible extension of this work is to fabricate the U-grooves at a close proximity, overgrow the c-GaN to above the SiO_2 sidewalls, and coa-

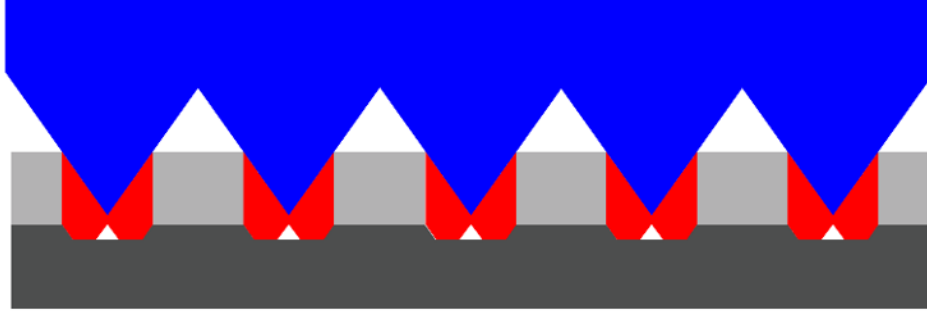


Figure 10.4: Coalescing many individual U-grooves to provide a continuous phase pure c-GaN to form a pseudo-substrate.

lesce each individual c-GaN crystallite into a continuous surface composed of purely c-GaN, forming a pseudo-substrate, as shown in Figure 10.4.

This approach would alleviate the design constraints imposed by the U-grooves and enable photonic and electronic devices of any size to be fabricated on the coalesced c-GaN. Additionally, the pseudo c-GaN substrate can be used as a seeding crystal/template for other faster growth technologies, such as HVPE, for a scalable production of free-standing c-GaN substrates for the next-generation solid state lighting and polarization-free III-nitride devices.

REFERENCES

- [1] W. C. Johnson and J. B. Parsons, “Nitrogen compounds of gallium. I, II,” *J. Phys. Chem.*, vol. 36, no. 10, pp. 2588–2594, 1931.
- [2] H. P. Maruska and J. J. Tietjen, “The preparation and properties of vapor-deposited single-crystal-line GaN,” *Appl. Phys. Lett.*, vol. 15, no. 10, pp. 327–329, 1969.
- [3] H. Amano, N. Sawaki, I. Akasaki, and Y. Toyoda, “Metalorganic vapor phase epitaxial growth of a high quality GaN film using an AlN buffer layer,” *Appl. Phys. Lett.*, vol. 48, no. 5, pp. 353–355, 1986.
- [4] H. Amano, M. Kito, K. Hiramatsu, and I. Akasaki, “P-type conduction in Mg-doped GaN treated with low-energy electron beam irradiation (LEEBI),” *Jpn. J. Appl. Phys.*, vol. 28, p. L2112, 1989.
- [5] S. Nakamura, T. Mukai, M. Senoh, and N. Iwasa, “Thermal annealing effects on P-type Mg-doped GaN films,” *Jpn. J. Appl. Phys.*, vol. 31, no. Part 2, No. 2B, pp. L139–L142, 1992.
- [6] I. Vurgaftman, J. R. Meyer, and L. R. Ram-Mohan, “Band parameters for III–V compound semiconductors and their alloys,” *J. Appl. Phys.*, vol. 89, no. 11, pp. 5815–5875, 2001.
- [7] P. Schley, R. Goldhahn, A. T. Winzer, G. Gobsch, V. Cimalla, O. Ambacher, H. Lu, W. J. Schaff, M. Kurouchi, Y. Nanishi, M. Rakel, C. Cobet, and N. Esser, “Dielectric function and Van Hove singularities for In-rich $\text{In}_x\text{Ga}_{1-x}\text{N}$ alloys: Comparison of N- and metal-face materials,” *Phys. Rev. B - Condens. Matter Mater. Phys.*, vol. 75, no. 20, pp. 1–8, 2007.
- [8] Y. C. Tsai and C. Bayram, “Structural and electronic properties of hexagonal and cubic phase AlGaInN alloys investigated using first principles calculations,” *Sci. Rep.*, vol. 9, no. 1, pp. 1–9, 2019.
- [9] P. Schley, R. Goldhahn, C. Napierala, G. Gobsch, J. Schörmann, D. J. As, K. Lischka, M. Feneberg, and K. Thonke, “Dielectric function of cubic InN from the mid-infrared to the visible spectral range,” *Semicond. Sci. Technol.*, vol. 23, no. 5, p. 055001, 2008.

- [10] R. Liu and C. Bayram, “Cathodoluminescence study of luminescence centers in hexagonal and cubic phase GaN hetero-integrated on Si(100),” *J. Appl. Phys.*, vol. 120, no. 2, p. 025106, 2016.
- [11] B. Qu, X. H. Zheng, Y. T. Wang, D. P. Xu, S. M. Lin, H. Yang, and J. W. Liang, “Orientation relationship between hexagonal inclusions and cubic GaN grown on GaAs(001) substrates,” *J. Cryst. Growth*, vol. 227, pp. 399–403, 2001.
- [12] M. Röppischer, R. Goldhahn, G. Rossbach, P. Schley, C. Cobet, N. Esser, T. Schupp, K. Lischka, and D. J. As, “Dielectric function of zinc-blende AlN from 1 to 20 eV: Band gap and van Hove singularities,” *J. Appl. Phys.*, vol. 106, no. 7, pp. 1–4, 2009.
- [13] S. Nakamura, M. Senoh, S.-i. Nagahama, N. Iwasa, T. Yamada, T. Matsushita, H. Kiyoku, and Y. Sugimoto, “InGa_N multi-quantum-well-structure laser diodes with cleaved mirror cavity facets,” *Jpn. J. Appl. Phys.*, vol. 35, no. Part 2, No. 2B, pp. L217–L220, 1996.
- [14] D. G. Zhao, S. J. Xu, M. H. Xie, S. Y. Tong, and H. Yang, “Stress and its effect on optical properties of GaN epilayers grown on Si(111), 6H-SiC(0001), and c-plane sapphire,” *Appl. Phys. Lett.*, vol. 83, no. 4, pp. 677–679, 2003.
- [15] J. Perozek, H.-P. Lee, B. Krishnan, A. Paranjpe, K. B. Reuter, D. K. Sadana, and C. Bayram, “Investigation of structural, optical, and electrical characteristics of an AlGa_N/Ga_N high electron mobility transistor structure across a 200 mm Si(1 1 1) substrate,” *J. Phys. D: Appl. Phys.*, vol. 50, no. 5, p. 055103, 2017.
- [16] H.-P. Lee, J. Perozek, L. D. Rosario, and C. Bayram, “Investigation of AlGa_N/Ga_N high electron mobility transistor structures on 200-mm silicon (111) substrates employing different buffer layer configurations,” *Sci. Rep.*, vol. 6, no. August, p. 37588, 2016.
- [17] H. Morkoç, “General properties of nitrides,” in *Handbook of nitride semiconductors and devices*. Weinheim, Germany: Wiley-VCH Verlag GmbH & Co. KGaA, 2009.
- [18] H.-P. Lee and C. Bayram, “Investigation of annealed, thin (~ 2.6 nm)-Al₂O₃ /AlGa_N/Ga_N metal-insulator-semiconductor heterostructures on Si(111) via capacitance-voltage and current-voltage studies,” *Mater. Res. Express*, vol. 6, no. 10, p. 105904, 2019.
- [19] F. Bernardini, V. Fiorentini, and D. Vanderbilt, “Spontaneous polarization and piezoelectric constants of III-V nitrides,” *Phys. Rev. B*, vol. 56, no. 16, pp. R10 024–R10 027, 1997.

- [20] E. Kioupakis, P. Rinke, K. T. Delaney, and C. G. Van De Walle, “Indirect Auger recombination as a cause of efficiency droop in nitride light-emitting diodes,” *Appl. Phys. Lett.*, vol. 98, no. 16, pp. 16–18, 2011.
- [21] S. Xu, Y. Hao, J. Zhang, T. Jiang, L. Yang, X. Lu, and Z. Lin, “Yellow luminescence of polar and nonpolar GaN nanowires on r-plane sapphire by metal organic chemical vapor deposition,” *Nano Lett.*, vol. 13, no. 8, pp. 3654–3657, 2013.
- [22] Y. Zhao, Q. Yan, C.-Y. Huang, S.-C. Huang, P. Shan Hsu, S. Tanaka, C.-C. Pan, Y. Kawaguchi, K. Fujito, C. G. Van de Walle, J. S. Speck, S. P. DenBaars, S. Nakamura, and D. Feezell, “Indium incorporation and emission properties of nonpolar and semipolar InGaN quantum wells,” *Appl. Phys. Lett.*, vol. 100, no. 20, p. 201108, 2012.
- [23] W. N. Carr and G. E. Pittman, “One-watt GaAs p-n junction infrared source,” *Appl. Phys. Lett.*, vol. 3, no. 10, pp. 173–175, 1963.
- [24] N. Holonyak and S. F. Bevacqua, “Coherent (visible) light emission from Ga(As_{1-x}P_x) junctions,” *Appl. Phys. Lett.*, vol. 1, no. 4, pp. 82–83, 1962.
- [25] T. Perry, “M. George Craford [biography],” *IEEE Spectr.*, vol. 32, no. 2, pp. 52–55, 1995.
- [26] S. Nakamura, T. Mukai, and M. Senoh, “Candela-class high-brightness InGaN/AlGaN double-heterostructure blue-light-emitting diodes,” *Appl. Phys. Lett.*, vol. 64, no. 13, pp. 1687–1689, 1994.
- [27] J. L. Wu, G. Gundiah, and A. K. Cheetham, “Structure-property correlations in Ce-doped garnet phosphors for use in solid state lighting,” *Chem. Phys. Lett.*, vol. 441, no. 4-6, pp. 250–254, 2007.
- [28] P. Gorrotxategi, M. Consonni, and A. Gasse, “Optical efficiency characterization of LED phosphors using a double integrating sphere system,” *J. Solid State Light.*, vol. 2, no. 1, p. 1, 2015.
- [29] J. Ueda, P. Dorenbos, A. J. J. Bos, A. Meijerink, and S. Tanabe, “Insight into the Thermal Quenching Mechanism for Y₃Al₅O₁₂:Ce³⁺ through Thermoluminescence Excitation Spectroscopy,” *J. Phys. Chem. C*, vol. 119, no. 44, pp. 25 003–25 008, 2015.
- [30] M. Auf Der Maur, A. Pecchia, G. Penazzi, W. Rodrigues, and A. Di Carlo, “Efficiency drop in green InGaN/GaN light emitting diodes: the role of random alloy fluctuations,” *Phys. Rev. Lett.*, vol. 116, no. 2, p. 027401, 2016.

- [31] K. A. Bulashevich, A. V. Kulik, and S. Y. Karpov, “Optimal ways of colour mixing for high-quality white-light LED sources,” *Phys. Status Solidi Appl. Mater. Sci.*, vol. 212, no. 5, pp. 914–919, 2015.
- [32] Y. Zhang, S. Krishnamoorthy, F. Akyol, A. A. Allerman, M. W. Moseley, A. M. Armstrong, and S. Rajan, “Design and demonstration of ultra-wide bandgap AlGa_N tunnel junctions,” *Appl. Phys. Lett.*, vol. 109, no. 12, p. 121102, 2016.
- [33] D. Schiavon, M. Binder, M. Peter, B. Galler, P. Drechsel, and F. Scholz, “Wavelength-dependent determination of the recombination rate coefficients in single-quantum-well GaInN/GaN light emitting diodes,” *Phys. Status Solidi Basic Res.*, vol. 250, no. 2, pp. 283–290, 2013.
- [34] J. Piprek, “Efficiency droop in nitride-based light-emitting diodes,” *Phys. Status Solidi Appl. Mater. Sci.*, vol. 207, no. 10, pp. 2217–2225, 2010.
- [35] G. Verzellesi, D. Saguatti, M. Meneghini, F. Bertazzi, M. Goano, G. Meneghesso, and E. Zanoni, “Efficiency droop in InGa_N/Ga_N blue light-emitting diodes: Physical mechanisms and remedies,” *J. Appl. Phys.*, vol. 114, no. 7, p. 071101, 2013.
- [36] J. Xie, X. Ni, Q. Fan, R. Shimada, Ü. Özgür, and H. Morkoç, “On the efficiency droop in InGa_N multiple quantum well blue light emitting diodes and its reduction with p-doped quantum well barriers,” *Appl. Phys. Lett.*, vol. 93, no. 12, pp. 91–94, 2008.
- [37] D. S. Meyaard, G.-B. Lin, Q. Shan, J. Cho, E. Fred Schubert, H. Shim, M.-H. Kim, and C. Sone, “Asymmetry of carrier transport leading to efficiency droop in GaInN based light-emitting diodes,” *Appl. Phys. Lett.*, vol. 99, no. 25, p. 251115, 2011.
- [38] M. H. Kim, M. F. Schubert, Q. Dai, J. K. Kim, E. F. Schubert, J. Piprek, and Y. Park, “Origin of efficiency droop in Ga_N-based light-emitting diodes,” *Appl. Phys. Lett.*, vol. 91, no. 18, pp. 1–4, 2007.
- [39] Y.-S. Yoo, J.-H. Na, S. J. Son, and Y.-H. Cho, “Effective suppression of efficiency droop in Ga_N-based light-emitting diodes: Role of significant reduction of carrier density and built-in field,” *Sci. Rep.*, vol. 6, no. October, p. 34586, 2016.
- [40] S. Hammersley, D. Watson-Parris, P. Dawson, M. J. Godfrey, T. J. Badcock, M. J. Kappers, C. McAleese, R. A. Oliver, and C. J. Humphreys, “The consequences of high injected carrier densities on carrier localization and efficiency droop in InGa_N/Ga_N quantum well structures,” *J. Appl. Phys.*, vol. 111, no. 8, p. 083512, 2012.

- [41] J. Hader, J. V. Moloney, and S. W. Koch, "Density-activated defect recombination as a possible explanation for the efficiency droop in GaN-based diodes," *Appl. Phys. Lett.*, vol. 96, no. 22, p. 221106, 2010.
- [42] J. Piprek, "How to decide between competing efficiency droop models for GaN-based light-emitting diodes," *Appl. Phys. Lett.*, vol. 107, no. 3, p. 031101, 2015.
- [43] H. Hirayama, "Quaternary InAlGaIn-based high-efficiency ultraviolet light-emitting diodes," *J. Appl. Phys.*, vol. 97, no. 9, p. 091101, 2005.
- [44] S. Pearton and A. Polyakov, "Effects of radiation damage in GaN and related materials," *Int. J. Mater. Struct. Integr.*, vol. 2, no. 1/2, p. 93, 2008.
- [45] S. Li, J. Schörmann, D. J. As, and K. Lischka, "Room temperature green light emission from nonpolar cubic InGaNGaN multi-quantum-wells," *Appl. Phys. Lett.*, vol. 90, no. 7, pp. 10–13, 2007.
- [46] K. T. Delaney, P. Rinke, and C. G. Van de Walle, "Auger recombination rates in nitrides from first principles," *Appl. Phys. Lett.*, vol. 94, no. 19, p. 191109, 2009.
- [47] C.-H. Kim and B.-H. Han, "Valence subbands and optical gain in wurtzite and zinc-blende strained GaN/AlGaIn quantum wells," *Solid State Commun.*, vol. 106, no. 3, pp. 127–132, 1998.
- [48] J. G. Kim, A. C. Frenkel, H. Liu, and R. M. Park, "Growth by molecular beam epitaxy and electrical characterization of Si-doped zinc blende GaN films deposited on β -SiC coated (001) Si substrates," *Appl. Phys. Lett.*, vol. 65, no. 1, pp. 91–93, 1994.
- [49] O. Brandt, H. Yang, H. Kostial, and K. H. Ploog, "High p-type conductivity in cubic GaN/GaAs(113) A by using Be as the acceptor and O as the codopant," *Appl. Phys. Lett.*, vol. 69, no. 18, pp. 2707–2709, 1996.
- [50] E. W. S. Caetano, R. N. Costa Filho, V. N. Freire, and J. A. P. Da Costa, "Velocity overshoot in zincblende and wurtzite GaN," *Solid State Commun.*, vol. 110, no. 9, pp. 469–472, 1999.
- [51] D. J. As, D. Schikora, A. Greiner, M. Lübbers, J. Mimkes, and K. Lischka, "p- and n-type cubic GaN epilayers on GaAs D." *Phys. Rev. B*, vol. 54, no. 16, pp. R11 118–R11 121, 1996.

- [52] T. Kitamura, Y. Suzuki, Y. Ishida, X. Q. Shen, H. Nakanishi, S. F. Chichibu, and M. Shimizu, “Optical properties of cubic In-GaN/GaN multiple quantum wells on 3C-SiC substrates by radio-frequency plasma-assisted molecular beam epitaxy,” *Phys. Status Solidi a-Applied Res.*, vol. 188, no. 2, pp. 705–709, 2001.
- [53] B. Lv, Y. Tang, S. Lou, Y. Xu, and S. Zhou, “Single p-n homojunction white light emitting diodes based on high-performance yellow luminescence of large-scale GaN microcubes,” *J. Mater. Chem. C*, vol. 4, no. 23, pp. 5416–5423, 2016.
- [54] D. J. As, “Cubic group-III nitride-based nanostructures-basics and applications in optoelectronics,” *Microelectronics J.*, vol. 40, no. 2, pp. 204–209, 2009.
- [55] R. Grady and C. Bayram, “Simulation of zincblende AlGaIn/GaN high electron mobility transistors for normally-off operation,” *J. Phys. D. Appl. Phys.*, vol. 50, no. 26, p. 265104, 2017.
- [56] V. A. Chitta, J. A. H. Coaquira, J. R. L. Fernandez, C. A. Duarte, J. R. Leite, D. Schikora, D. J. As, K. Lischka, and E. Abramof, “Room temperature ferromagnetism in cubic GaN epilayers implanted with Mn^{+} ions,” *Appl. Phys. Lett.*, vol. 85, no. 17, pp. 3777–3779, 2004.
- [57] J. H. Buß, A. Schaefer, T. Schupp, D. J. As, D. Hägele, and J. Rudolph, “High temperature electron spin dynamics in bulk cubic GaN: Nanosecond spin lifetimes far above room-temperature,” *Appl. Phys. Lett.*, vol. 105, no. 18, 2014.
- [58] S. Kako, M. Holmes, S. Sargent, M. Bürger, D. J. As, and Y. Arakawa, “Single-photon emission from cubic GaN quantum dots,” *Appl. Phys. Lett.*, vol. 104, no. 1, p. 011101, 2014.
- [59] D. J. As, A. Richter, J. Busch, M. Lübbers, J. Mimkes, and K. Lischka, “Growth and characterization of a cubic GaN p-n light emitting diode on GaAs (001) substrates,” *Phys. Status Solidi Appl. Res.*, vol. 180, no. 1, pp. 369–374, 2000.
- [60] S. F. Chichibu, T. Onuma, T. Aoyama, K. Nakajima, P. Ahmet, T. Chikyow, T. Sota, S. P. DenBaars, S. Nakamura, T. Kitamura, Y. Ishida, and H. Okumura, “Recombination dynamics of localized excitons in cubic $In_xGa_{1-x}N$ /GaN multiple quantum wells grown by radio frequency molecular beam epitaxy on 3C-SiC substrate,” *J. Vac. Sci. Technol. B Microelectron. Nanom. Struct.*, vol. 21, no. 4, pp. 1856–1862, 2003.

- [61] C. H. Wei, Z. Y. Xie, L. Y. Li, Q. M. Yu, and J. H. Edgar, "MOCVD growth of cubic GaN on 3C-SiC deposited on Si (100) substrates," *J. Electron. Mater.*, vol. 29, no. 3, pp. 317–321, 2000.
- [62] V. D. Compeán García, I. E. Orozco Hinojosa, A. Escobosa Echavarría, E. López Luna, A. G. Rodríguez, and M. A. Vidal, "Bulk lattice parameter and band gap of cubic $\text{In}_x\text{Ga}_{1-x}\text{N}$ (001) alloys on MgO (100) substrates," *J. Cryst. Growth*, vol. 418, pp. 120–125, 2015.
- [63] R. Kemper, M. Weinl, C. Mietze, M. Häberlen, T. Schupp, E. Tschumak, J. Lindner, K. Lischka, and D. As, "Growth of cubic GaN on nano-patterned 3C-SiC/Si (001) substrates," *J. Cryst. Growth*, vol. 323, no. 1, pp. 84–87, 2011.
- [64] R. M. Kemper, M. Häberlen, T. Schupp, M. Weinl, M. Bürger, M. Ruth, C. Meier, T. Niendorf, H. J. Maier, K. Lischka, D. J. As, and J. K. N. Lindner, "Formation of defects in cubic GaN grown on nano-patterned 3C-SiC (001)," *Phys. status solidi*, vol. 9, no. 3-4, pp. 1028–1031, 2012.
- [65] R. Liu, C. McCormick, and C. Bayram, "Suppression of indium clustering and quantum confined Stark effect of InGaN LED on silicon (111)," in *Gallium Nitride Materials and Devices XIV*, vol. 10918. International Society for Optics and Photonics, 2019, p. 1091822.
- [66] K. Sato, M. Shikida, Y. Matsushima, T. Yamashiro, K. Asaumi, Y. Iriye, and M. Yamamoto, "Characterization of orientation-dependent etching properties of single-crystal silicon: effects of KOH concentration," *Sensors Actuators A Phys.*, vol. 64, no. 1, pp. 87–93, 1998.
- [67] S. C. Lee, E. J. Peterson, Y.-B. Jiang, C. Wetzel, and S. R. J. Brueck, "Elastic variation of quasi-one-dimensional cubic-phase GaN at nanoscale," *Cryst. Growth Des.*, vol. 19, no. 9, pp. 5046–5053, 2019.
- [68] S. C. Lee, B. Pattada, S. D. Hersee, Y. B. Jiang, and S. R. J. Brueck, "Nanoscale spatial phase modulation of GaN on a V-grooved Si substrate - Cubic phase GaN on Si(001) for monolithic integration," *IEEE J. Quantum Electron.*, vol. 41, no. 4, pp. 596–605, 2005.
- [69] S. C. Lee, N. Youngblood, Y. B. Jiang, E. J. Peterson, C. J. M. Stark, T. Detchprohm, C. Wetzel, and S. R. J. Brueck, "Incorporation of indium on cubic GaN epitaxially induced on a nanofaceted Si(001) substrate by phase transition," *Appl. Phys. Lett.*, vol. 107, no. 23, p. 231905, 2015.

- [70] C. Bayram, J. A. Ott, K.-T. Shiu, C.-W. Cheng, Y. Zhu, J. Kim, M. Razeghi, and D. K. Sadana, "Cubic phase GaN on nano-grooved Si (100) via maskless selective area epitaxy," *Adv. Funct. Mater.*, vol. 24, no. 28, pp. 4492–4496, 2014.
- [71] R. Liu and C. Bayram, "Maximizing cubic phase gallium nitride surface coverage on nano-patterned silicon (100)," *Appl. Phys. Lett.*, vol. 109, no. 4, pp. 38–41, 2016.
- [72] R. Liu, R. Schaller, C. Q. Chen, and C. Bayram, "High internal quantum efficiency ultraviolet emission from phase-transition cubic GaN integrated on nanopatterned Si(100)," *ACS Photonics*, vol. 5, no. 3, pp. 955–963, 2018.
- [73] R. Liu, "Structural and optical properties of phase transition cubic phase gallium nitride for photonic devices," PhD Thesis, University of Illinois at Urbana-Champaign, 2017. [Online]. Available: <https://www.ideals.illinois.edu/handle/2142/99306>
- [74] C. Bayram, C.-W. Cheng, D. Sadana, and K.-T. Shiu, "Dual phase gallium nitride material formation on (100) silicon," *US Pat.*, vol. 9048173, 2015.
- [75] C. Bayram and R. Liu, "Maximizing Cubic Phase Group III-Nitride on Patterned Silicon," 2018.
- [76] I. Zobel and M. Kramkowska, "Etch rates and morphology of silicon (h k l) surfaces etched in KOH and KOH saturated with isopropanol solutions," *Sensors Actuators A Phys.*, vol. 115, no. 2-3, pp. 549–556, 2004.
- [77] H. Siegle, L. Eckey, A. Hoffmann, C. Thomsen, B. Meyer, D. Schikora, M. Hankeln, and K. Lischka, "Quantitative determination of hexagonal minority phase in cubic GaN using Raman spectroscopy," *Solid State Commun.*, vol. 96, no. 12, pp. 943–949, 1995.
- [78] M. T. Durniak, A. S. Bross, D. Elsaesser, A. Chaudhuri, M. L. Smith, A. A. Allerman, S. C. Lee, S. R. J. Brueck, and C. Wetzel, "Green Emitting Cubic GaInN/GaN Quantum Well Stripes on Micropatterned Si(001) and Their Strain Analysis," *Adv. Electron. Mater.*, vol. 2, no. 3, p. 1500327, 2016.
- [79] C. Bayram, K. T. Shiu, Y. Zhu, C. W. Cheng, D. K. Sadana, F. H. Teherani, D. J. Rogers, V. E. Sandana, P. Bove, Y. Zhang, S. Gautier, C.-Y. Cho, E. Cicek, Z. Vashaei, R. McClintock, and M. Razeghi, "Engineering future light emitting diodes and photovoltaics with inexpensive materials: Integrating ZnO and Si into GaN-based devices," *Oxide-based Mater. Devices IV*, vol. 8626, p. 86260L, 2013.

- [80] M. Athanasiou, R. M. Smith, S. Ghataora, and T. Wang, “Polarized white light from hybrid organic/III-nitrides grating structures,” *Sci. Rep.*, vol. 7, no. 1, p. 39677, 2017.
- [81] M. Feneberg, F. Lipski, R. Sauer, K. Thonke, P. Brückner, B. Neubert, T. Wunderer, and F. Scholz, “Polarized light emission from semipolar GaInN quantum wells on $\{11\bar{0}1\}$ GaN facets,” *J. Appl. Phys.*, vol. 101, no. 5, p. 053530, 2007.
- [82] Z. Zhuang, Y. Li, B. Liu, X. Guo, J. Dai, G. Zhang, T. Tao, T. Zhi, Z. Xie, H. Ge, Y. Shi, Y. Zheng, and R. Zhang, “Optical polarization characteristics of c-plane InGaN/GaN asymmetric nanostructures,” *J. Appl. Phys.*, vol. 118, no. 23, p. 233111, 2015.
- [83] K. Kanaya and S. Okayama, “Penetration and energy-loss theory of electrons in solid targets,” *J. Phys. D. Appl. Phys.*, vol. 5, no. 1, p. 308, 1972.
- [84] M. A. Reshchikov, M. Zafar Iqbal, S. S. Park, K. Y. Lee, D. Tsvetkov, V. Dmitriev, and H. Morkoç, “Persistent photoluminescence in high-purity GaN,” *Phys. B Condens. Matter*, vol. 340-342, pp. 444–447, 2003.
- [85] J. Wu, H. Yaguchi, K. Onabe, R. Ito, and Y. Shiraki, “Photoluminescence properties of cubic GaN grown on GaAs(100) substrates by metalorganic vapor phase epitaxy,” *Appl. Phys. Lett.*, vol. 71, no. 15, p. 2067, 1997.
- [86] C. Wang, D. J. As, B. Schöttker, D. Schikora, and K. Lischka, “Cathodoluminescence of homogeneous cubic GaN/GaAs(001) layers,” *Semicond. Sci. Technol.*, vol. 14, no. 2, pp. 161–167, 1999.
- [87] E. Glaser, J. Freitas, B. Shanabrook, D. Koleske, S. Lee, S. Park, and J. Han, “Optically detected magnetic resonance of (effective-mass) shallow acceptors in Si-doped GaN homoepitaxial layers,” *Phys. Rev. B*, vol. 68, no. 19, pp. 0–6, 2003.
- [88] D. J. As, F. Schmilgus, C. Wang, B. Schöttker, D. Schikora, and K. Lischka, “The near band edge photoluminescence of cubic GaN epilayers,” *Appl. Phys. Lett.*, vol. 70, no. 10, pp. 1311–1313, 1997.
- [89] H. Okumura, H. Hamaguchi, G. Feuillet, Y. Ishida, and S. Yoshida, “Arsenic surfactant effects and arsenic mediated molecular beam epitaxial growth for cubic GaN,” *Appl. Phys. Lett.*, vol. 72, no. 23, pp. 3056–3058, 1998.

- [90] J. Menniger, U. Jahn, O. Brandt, H. Yang, and K. Ploog, “Optical transitions in cubic GaN investigated by spatially resolved cathodoluminescence,” *Appl. Phys. Lett.*, vol. 69, no. 6, pp. 836–838, 1996.
- [91] M. A. Reshchikov and H. Morkoç, “Luminescence properties of defects in GaN,” *J. Appl. Phys.*, vol. 97, no. 6, p. 061301, 2005.
- [92] R. Zhang and T. F. Kuech, “Photoluminescence of carbon in situ doped GaN grown by halide vapor phase epitaxy,” *Appl. Phys. Lett.*, vol. 72, no. 13, pp. 1611–1613, 1998.
- [93] Y. Varshni, “Temperature dependence of the energy gap in semiconductors,” *Physica*, vol. 34, no. 1, pp. 149–154, 1967.
- [94] R. Dingle, D. D. Sell, S. E. Stokowski, and M. Ilegems, “Absorption, reflectance, and luminescence of GaN epitaxial layers,” *Phys. Rev. B*, vol. 4, no. 4, pp. 1211–1218, 1971.
- [95] G. Ramírez-Flores, H. Navarro-Contreras, A. Lastras-Martínez, R. C. Powell, and J. E. Greene, “Temperature-dependent optical band gap of the metastable zinc-blende structure β -GaN,” *Phys. Rev. B*, vol. 50, no. 12, pp. 8433–8438, 1994.
- [96] H. Teisseyre, P. Perlin, T. Suski, I. Grzegory, S. Porowski, J. Jun, A. Pietraszko, and T. D. Moustakas, “Temperature dependence of the energy gap in GaN bulk single crystals and epitaxial layer,” *J. Appl. Phys.*, vol. 76, no. 4, pp. 2429–2434, 1994.
- [97] W. Grieshaber, E. F. Schubert, I. D. Goepfert, R. F. Karlicek, M. J. Schurman, and C. Tran, “Competition between band gap and yellow luminescence in GaN and its relevance for optoelectronic devices,” *J. Appl. Phys.*, vol. 80, no. 8, pp. 4615–4620, 1996.
- [98] S. A. Church, S. Hammersley, P. W. Mitchell, M. J. Kappers, S. L. Sahonta, M. Frentrop, D. Nilsson, P. J. Ward, L. J. Shaw, D. J. Wallis, C. J. Humphreys, R. A. Oliver, D. J. Binks, and P. Dawson, “Photoluminescence studies of cubic GaN epilayers,” *Phys. status solidi*, vol. 254, no. 8, p. 1600733, 2017.
- [99] R. M. Kemper, L. Hiller, T. Stauden, J. Pezoldt, K. Duschik, T. Nien-dorf, H. J. Maier, D. Meertens, K. Tillmann, D. J. As, and J. K. Lindner, “Growth of cubic GaN on 3C-SiC/Si (001) nanostructures,” *J. Cryst. Growth*, vol. 378, pp. 291–294, 2013.
- [100] J. Krustok, H. Collan, and K. Hjelt, “Does the low-temperature Arrhenius plot of the photoluminescence intensity in CdTe point towards an erroneous activation energy?” *J. Appl. Phys.*, vol. 81, no. 3, pp. 1442–1445, 1997.

- [101] J. F. Muth, J. H. Lee, I. K. Shmagin, R. M. Kolbas, H. C. Casey, B. P. Keller, U. K. Mishra, and S. P. DenBaars, "Absorption coefficient, energy gap, exciton binding energy, and recombination lifetime of GaN obtained from transmission measurements," *Applied Physics Letters*, vol. 71, no. 18, pp. 2572–2574, 1997.
- [102] W. Götz, N. M. Johnson, C. Chen, H. Liu, C. Kuo, and W. Imler, "Activation energies of Si donors in GaN," *Appl. Phys. Lett.*, vol. 68, no. 22, pp. 3144–3146, 1996.
- [103] Y. Narukawa, Y. Kawakami, S. Fujita, and S. Nakamura, "Dimensionality of excitons in laser-diode structures composed of InGaN multiple quantum wells," *Phys. Rev. B*, vol. 59, no. 15, pp. 10 283–10 288, 1999.
- [104] Y. Toyozawa, "On the Dynamical Behavior of an Exciton," *Prog. Theor. Phys. Suppl.*, vol. 12, pp. 111–140, 1959.
- [105] S. Hess, F. Walraet, R. A. Taylor, J. F. Ryan, B. Beaumont, and P. Gibart, "Dynamics of resonantly excited excitons in GaN," *Phys. Rev. B*, vol. 58, no. 24, pp. R15 973–R15 976, 1998.
- [106] J. Simon, N. T. Pelekanos, C. Adelmann, E. Martinez-Guerrero, R. Andre, B. Daudin, L. S. Dang, and H. Mariette, "Direct comparison of recombination dynamics in cubic and hexagonal GaN/AlN quantum dots," *Phys. Rev. B*, vol. 68, no. 3, p. 35312, 2003.
- [107] V. A. Fonoberov and A. A. Balandin, "Excitonic properties of strained wurtzite and zinc-blende GaN/Al_xGa_{1-x}N quantum dots," *J. Appl. Phys.*, vol. 94, no. 11, pp. 7178–7186, 2003.
- [108] O. Marquardt, T. Hickel, and J. Neugebauer, "Polarization-induced charge carrier separation in polar and nonpolar grown GaN quantum dots," *J. Appl. Phys.*, vol. 106, no. 8, 2009.
- [109] S. F. Chichibu, H. Marchand, M. S. Minsky, S. Keller, P. T. Fini, J. P. Ibbetson, S. B. Fleischer, J. S. Speck, J. E. Bowers, E. Hu, U. K. Mishra, S. P. DenBaars, T. Deguchi, T. Sota, and S. Nakamura, "Emission mechanisms of bulk GaN and InGaN quantum wells prepared by lateral epitaxial overgrowth," *Appl. Phys. Lett.*, vol. 74, no. 10, pp. 1460–1462, 1999.
- [110] H. Ki Kwon, C. Eiting, D. Lambert, M. Wong, B. Shelton, T. Zhu, Z. Liliental-Weber, M. Benamara, and R. Dupuis, "Time-resolved photoluminescence study of GaN grown by metalorganic chemical vapor deposition," *J. Cryst. Growth*, vol. 221, no. 1-4, pp. 240–245, 2000.

- [111] G. E. Bunea, W. D. Herzog, M. S. Ünlü, B. B. Goldberg, and R. J. Molnar, “Time-resolved photoluminescence studies of free and donor-bound exciton in GaN grown by hydride vapor phase epitaxy,” *Appl. Phys. Lett.*, vol. 75, no. 6, pp. 838–840, 1999.
- [112] S. F. Chichibu, A. Uedono, T. Onuma, T. Sota, B. A. Haskell, S. P. DenBaars, J. S. Speck, and S. Nakamura, “Limiting factors of room-temperature nonradiative photoluminescence lifetime in polar and nonpolar GaN studied by time-resolved photoluminescence and slow positron annihilation techniques,” *Appl. Phys. Lett.*, vol. 86, no. 2, p. 021914, 2005.
- [113] R. Liu, C. McCormick, and C. Bayram, “Comparison of structural and optical properties of blue emitting $\text{In}_{0.15}\text{Ga}_{0.85}\text{N}$ / GaN multi-quantum-well layers grown on sapphire and silicon substrates,” *AIP Adv.*, vol. 9, no. 2, p. 025306, 2019.
- [114] E. Schmitt, T. Straubinger, M. Rasp, and A.-D. Weber, “Defect reduction in sublimation grown SiC bulk crystals,” *Superlattices Microstruct.*, vol. 40, no. 4-6, pp. 320–327, 2006.
- [115] D. Zhu, D. J. Wallis, and C. J. Humphreys, “Prospects of III-nitride optoelectronics grown on Si,” *Rep. Prog. Phys.*, vol. 76, no. 10, p. 106501, 2013.
- [116] M. Lee, M. Yang, K. M. Song, and S. Park, “InGaN/GaN blue light emitting diodes using freestanding GaN extracted from a Si Substrate,” *ACS Photonics*, vol. 5, no. 4, pp. 1453–1459, 2018.
- [117] A. Dadgar, T. Hempel, J. Bläsing, O. Schulz, S. Fritze, J. Christen, and A. Krost, “Improving GaN-on-silicon properties for GaN device epitaxy,” *Phys. Status Solidi Curr. Top. Solid State Phys.*, vol. 8, no. 5, pp. 1503–1508, 2011.
- [118] J.-Y. Kim, Y. Tak, J. Kim, H.-G. Hong, S. Chae, J. W. Lee, H. Choi, Y. Park, U.-I. Chung, J.-R. Kim et al., “Highly efficient InGaN/GaN blue LED on 8-inch Si (111) substrate,” in *Gallium Nitride Materials and Devices Vii*, vol. 8262. International Society for Optics and Photonics, 2012, p. 82621D.
- [119] H. Y. Ryu, K. S. Jeon, M. G. Kang, H. K. Yuh, Y. H. Choi, and J. S. Lee, “A comparative study of efficiency droop and internal electric field for InGaN blue lighting-emitting diodes on silicon and sapphire substrates,” *Sci. Rep.*, vol. 7, no. 1, p. 44814, 2017.

- [120] K. Kazlauskas, G. Tamulaitis, J. Mickevičius, E. Kuokštis, A. Žukauskas, Y.-C. C. Cheng, H.-C. C. Wang, C.-F. F. Huang, and C. C. Yang, “Excitation power dynamics of photoluminescence in In-GaN/GaN quantum wells with enhanced carrier localization,” *J. Appl. Phys.*, vol. 97, no. 1, p. 013525, 2005.
- [121] Y. J. Lee, C. H. Chiu, C. C. Ke, P. C. Lin, T. C. Lu, H. C. Kuo, and S. C. Wang, “Study of the excitation power dependent internal quantum efficiency in InGaN/GaN LEDs grown on patterned sapphire substrate,” *IEEE J. Sel. Top. Quantum Electron.*, vol. 15, no. 4, pp. 1137–1143, 2009.
- [122] T. Wang, D. Nakagawa, J. Wang, T. Sugahara, and S. Sakai, “Photoluminescence investigation of InGaN/GaN single quantum well and multiple quantum wells,” *Appl. Phys. Lett.*, vol. 73, no. 24, pp. 3571–3573, 1998.
- [123] B. Heying, E. J. Tarsa, C. R. Elsass, P. Fini, S. P. DenBaars, and J. S. Speck, “Dislocation mediated surface morphology of GaN,” *J. Appl. Phys.*, vol. 85, no. 9, pp. 6470–6476, 1999.
- [124] M. A. Moram and M. E. Vickers, “X-ray diffraction of III-nitrides,” *Reports Prog. Phys.*, vol. 72, no. 3, p. 036502, 2009.
- [125] A. Kadir, C. C. Huang, K. E. Kian Lee, E. A. Fitzgerald, and S. J. Chua, “Determination of alloy composition and strain in multiple Al-GaN buffer layers in GaN/Si system,” *Appl. Phys. Lett.*, vol. 105, no. 23, p. 232113, 2014.
- [126] B.-T. Liou, S.-H. Yen, and Y.-K. Kuo, “Vegard’s law deviation in band gaps and bowing parameters of the wurtzite III-nitride ternary alloys,” in *Proc. SPIE 5628, Semicond. Lasers Appl. II*, J.-q. Yao, Y. J. Chen, and S. Lee, Eds., Jan 2005, p. 296.
- [127] S. P. S. Porto and R. S. Krishnan, “Raman effect of corundum,” *J. Chem. Phys.*, vol. 47, no. 3, pp. 1009–1012, 1967.
- [128] H. Harima, “Properties of GaN and related compounds studied by means of Raman scattering,” *J. Phys. Condens. Matter*, vol. 14, no. 38, pp. R967–R993, 2002.
- [129] V. Y. Davydov, Y. E. Kitaev, I. N. Goncharuk, A. N. Smirnov, J. Graul, O. Semchinova, D. Uffmann, M. B. Smirnov, A. P. Mirgorodsky, and R. A. Evarestov, “Phonon dispersion and Raman scattering in hexagonal GaN and AlN,” *Phys. Rev. B*, vol. 58, no. 19, pp. 12 899–12 907, 1998.

- [130] M. Kuball, “Raman spectroscopy of GaN, AlGa_N and AlN for process and growth monitoring/control,” *Surf. Interface Anal.*, vol. 31, no. 10, pp. 987–999, 2001.
- [131] F. Demangeot, J. Frandon, M. A. Renucci, O. Briot, B. Gil, and R. L. Aulombard, “Raman determination of phonon deformation potentials in α -GaN,” *Solid State Commun.*, vol. 100, no. 4, pp. 207–210, 1996.
- [132] S. Tripathy, S. J. Chua, P. Chen, and Z. L. Miao, “Micro-Raman investigation of strain in GaN and Al_xGa_{1-x}N / GaN heterostructures grown on Si(111),” *J. Appl. Phys.*, vol. 92, no. 7, pp. 3503–3510, 2002.
- [133] J. Gleize, F. Demangeot, J. Frandon, M. A. Renucci, F. Widmann, and B. Daudin, “Phonons in a strained hexagonal GaN-AlN superlattice,” *Appl. Phys. Lett.*, vol. 74, no. 5, pp. 703–705, 1999.
- [134] A. Polian, M. Grimsditch, and I. Grzegory, “Elastic constants of gallium nitride,” *J. Appl. Phys.*, vol. 79, no. 6, pp. 3343–3344, 1996.
- [135] S. Chichibu, K. Wada, and S. Nakamura, “Spatially resolved cathodoluminescence spectra of InGa_N quantum wells,” *Appl. Phys. Lett.*, vol. 71, no. 16, pp. 2346–2348, 1997.
- [136] Y.-s. Lin, K.-j. Ma, C. Hsu, S.-W. Feng, Y.-C. Cheng, C.-C. Liao, C. C. Yang, C.-C. Chou, C.-M. Lee, and J.-I. Chyi, “Dependence of composition fluctuation on indium content in InGa_N/Ga_N multiple quantum wells,” *Appl. Phys. Lett.*, vol. 77, no. 19, pp. 2988–2990, 2000.
- [137] T. Azuhata, T. Sota, K. Suzuki, and S. Nakamura, “Polarized Raman spectra in GaN,” *J. Phys. Condens. Matter*, vol. 7, no. 10, pp. L129–L133, 1995.
- [138] Jae-Hyun Ryou, P. Yoder, Jianping Liu, Z. Lochner, Hyunsoo Kim, Suk Choi, Hee Jin Kim, and R. Dupuis, “Control of quantum-confined Stark effect in InGa_N-based quantum wells,” *IEEE J. Sel. Top. Quantum Electron.*, vol. 15, no. 4, pp. 1080–1091, 2009.
- [139] Y.-H. Cho, G. H. Gainer, A. J. Fischer, J. J. Song, S. Keller, U. K. Mishra, and S. P. DenBaars, ““S-shaped” temperature-dependent emission shift and carrier dynamics in InGa_N/Ga_N multiple quantum wells,” *Appl. Phys. Lett.*, vol. 73, no. 10, pp. 1370–1372, 1998.
- [140] Z. Wang, L. Wang, Y. Xing, D. Yang, J. Yu, Z. Hao, C. Sun, B. Xiong, Y. Han, J. Wang, H. Li, and Y. Luo, “Consistency on two kinds of localized centers examined from temperature-dependent and time-resolved photoluminescence in InGa_N/Ga_N multiple quantum wells,” *ACS Photonics*, vol. 4, no. 8, pp. 2078–2084, 2017.

- [141] M. Monavarian, A. Rashidi, A. A. Aragon, M. Nami, S. H. Oh, S. P. Denbaars, and D. Feezell, “Trade-off between bandwidth and efficiency in semipolar (2021) InGa_N/Ga_N single- and multiple-quantum-well light-emitting diodes,” *Appl. Phys. Lett.*, vol. 112, no. 19, 2018.
- [142] M. C. Johnson, E. D. Bourret-Courchesne, J. Wu, Z. Liliental-Weber, D. N. Zakharov, R. J. Jorgenson, T. B. Ng, D. E. McCready, and J. R. Williams, “Effect of gallium nitride template layer strain on the growth of In_xGa_{1-x}N/GaN multiple quantum well light emitting diodes,” *J. Appl. Phys.*, vol. 96, no. 3, pp. 1381–1386, 2004.
- [143] S. Nakamura and M. R. Krames, “History of gallium-nitride-based light-emitting diodes for illumination,” *Proc. IEEE*, vol. 101, no. 10, pp. 2211–2220, 2013.
- [144] A. Kimura, M. Shibata, K. Kondoh, Y. Takeda, M. Katayama, T. Kanie, and H. Takada, “Reduction mechanism of surface oxide in aluminum alloy powders containing magnesium studied by x-ray photo-electron spectroscopy using synchrotron radiation,” *Appl. Phys. Lett.*, vol. 70, no. 26, pp. 3615–3617, 1997.
- [145] B. Monemar and O. Lagerstedt, “Properties of VPE-grown GaN doped with Al and some iron-group metals,” *J. Appl. Phys.*, vol. 50, no. 10, pp. 6480–6491, 1979.
- [146] G. Milazzo, S. Caroli, and R. D. Braun, “Tables of standard electrode potentials,” *J. Electrochem. Soc.*, vol. 125, no. 6, pp. 261C–261C, 1978.
- [147] K. Pressel, S. Nilsson, R. Heitz, A. Hoffmann, and B. K. Meyer, “Photoluminescence study of the 1.047 eV emission in GaN,” *J. Appl. Phys.*, vol. 79, no. 6, pp. 3214–3218, 1996.
- [148] R. Y. Korotkov, J. M. Gregie, and B. W. Wessels, “Optical properties of the deep Mn acceptor in GaN:Mn,” *Appl. Phys. Lett.*, vol. 80, no. 10, pp. 1731–1733, 2002.
- [149] C. Y. Hwang, M. J. Schurman, W. E. Mayo, Y. C. Lu, R. A. Stall, and T. Salagaj, “Effect of structural defects and chemical impurities on hall mobilities in low pressure MOCVD grown GaN,” *J. Electron. Mater.*, vol. 26, no. 3, pp. 243–251, 1997.
- [150] S. Leone, F. Benkhelifa, L. Kirste, C. Manz, S. Mueller, R. Quay, and T. Stadelmann, “Suppression of iron memory effect in GaN epitaxial layers,” *Phys. Status Solidi Basic Res.*, vol. 255, no. 5, pp. 1–7, 2018.

- [151] C. Liu, E. Alves, A. D. Sequeira, N. Franco, M. F. da Silva, and J. C. Soares, “Fe ion implantation in GaN: Damage, annealing, and lattice site location,” *J. Appl. Phys.*, vol. 90, no. 1, pp. 81–86, 2001.
- [152] A. Y. Polyakov, N. B. Smirnov, A. V. Govorkov, N. V. Pashkova, A. A. Shlensky, S. J. Pearton, M. E. Overberg, C. R. Abernathy, J. M. Zavada, and R. G. Wilson, “Electrical and optical properties of Cr and Fe implanted n-GaN,” *J. Appl. Phys.*, vol. 93, no. 9, pp. 5388–5396, 2003.
- [153] D. Wickramaratne, J.-X. Shen, C. E. Dreyer, M. Engel, M. Marsman, G. Kresse, S. Marcinkevičius, A. Alkauskas, and C. G. Van de Walle, “Iron as a source of efficient Shockley-Read-Hall recombination in GaN,” *Applied Physics Letters*, vol. 109, no. 16, p. 162107, 2016.
- [154] C. Fotea, J. Callaway, and M. R. Alexander, “Characterisation of the surface chemistry of magnesium exposed to the ambient atmosphere,” *Surf. Interface Anal.*, vol. 38, no. 10, pp. 1363–1371, 2006.
- [155] M. E. Zvanut, J. Dashdorj, J. A. Freitas, E. R. Glaser, W. R. Willoughby, J. H. Leach, and K. Udway, “Incorporation of Mg in free-standing HVPE GaN substrates,” *Journal of Electronic Materials*, vol. 45, no. 6, pp. 2692–2696, 2016.
- [156] Y.-S. Lin, K.-J. Ma, C. Hsu, S.-W. Feng, Y.-C. Cheng, C.-C. Liao, C. C. Yang, C.-C. Chou, C.-M. Lee, and J.-I. Chyi, “Dependence of composition fluctuation on indium content in InGaN/GaN multiple quantum wells,” *Applied Physics Letters*, vol. 77, no. 19, pp. 2988–2990, 2000.
- [157] Y.-C. Cheng, S.-W. Feng, E.-C. Lin, C.-C. Yang, C.-H. Tseng, C. Hsu, and K.-J. Ma, “Quantum dot formation in InGaN/GaN quantum well structures with silicon doping and the mechanisms for radiative efficiency improvement,” *Phys. status solidi*, vol. 1096, no. 4, pp. 1093–1096, 2003.
- [158] Y. C. Cheng, E. C. Lin, C. M. Wu, C. C. Yang, J. R. Yang, A. Rosenauer, K. J. Ma, S. C. Shi, L. C. Chen, C. C. Pan, and J. I. Chyi, “Nanostructures and carrier localization behaviors of green-luminescence InGaN/GaN quantum-well structures of various silicon-doping conditions,” *Appl. Phys. Lett.*, vol. 84, no. 14, pp. 2506–2508, 2004.
- [159] C. Du, X. Huang, C. Jiang, X. Pu, Z. Zhao, L. Jing, W. Hu, and Z. L. Wang, “Tuning carrier lifetime in InGaN/GaN LEDs via strain compensation for high-speed visible light communication,” *Scientific Reports*, vol. 6, no. 1, p. 37132, 2016.

- [160] D. Wickramaratne, J. X. Shen, C. E. Dreyer, A. Alkauskas, and C. G. Van De Walle, “Electrical and optical properties of iron in GaN, AlN, and InN,” *Physical Review B*, vol. 99, no. 20, pp. 1–13, 2019.
- [161] R. Liu, E. Tucker, S. M. Lee, K. Kasarla, C. McCormick, and C. Bayram, “Cp₂Mg-induced transition metal ion contamination and performance loss in MOCVD-grown blue emitting InGaN/GaN multiple quantum wells,” *Appl. Phys. Lett.*, vol. 116, no. 19, p. 192106, 2020.

APPENDIX A

INSTRUMENTS AND EQUIPMENT

A.1 X-Ray Diffraction

X-ray diffraction (XRD) was completed on a PANalytical Phillips X'Pert MRD system with Cu K-alpha 1 as the X-ray source ($\lambda = 0.154056$ nm), line focus beam, high-resolution parallel beam configuration with hybrid mirror with x-ray mirror, 2-bounce monochromator (beam divergence = 30 arc-sec), and a high-speed line detector PIXcel© with scatter slit. The motor stage allows for six axes of motion, x, y, z, Ω , Φ , and Θ , for alignment for a wide range of scattering planes (Figure A.1). A typical scanning parameter setup for the (102) plane of GaN is shown in Figure A.2. The operating procedures are as follows:

1. Omega psi omega
2. 002 scan
3. 2theta= 34.59500 (d = 2.590693)
4. Fringe = 15 nm
5. omega scan
6. 5 deg, 0.01 deg step, 1 sec step time (fwhm = 0.05230)
7. (105) scan
8. Change unit cell to GaN 105, recalculate, fix psi from previous
9. Phi scan 200 deg, 0.5 deg step, 0.5s step time
10. Move to peak (267.010)
11. Omega scan 1 deg, 0.02 deg step, 0.5 s time
12. Move to peak (31.8895)
13. Phi scan 5.95 deg, 0.05 deg, 0.5s time
14. Move to peak (268.42)
15. Omega scan 0.1 deg, 0.002 deg step, 0.5 s time
16. Type 2theta peak position in position (105.0065), fix offset

17. omega scan 2.5 deg, 0.01 deg, 1s step (4'12")
18. (102) scan
19. Position/crystal GaN, 1 0 2 unit cell, click to update
20. Phi Scan, 200 deg, 0.5 deg, 0.5 s (3'22")
21. Should see intermediate peaks spaced at 60deg apart, about 3k cps
22. Move to peak (-1.45)
23. Psi Scan 4.45 deg, 0.05 deg, 0.5s (49")
24. Move to peak
25. Phi Scan 4.45 deg, 0.05 deg, 0.5s (47")
26. Move to peak (-1.32)
27. omega Scan 4.45 deg, 0.05 deg, 0.5s (48")
28. Move to peak (24.07130)
29. 2theta omega scan
30. Move to peak (48.130) (d space = 1.889778), restore correct offset
31. omega Scan 2.5 deg, 0.01 deg, 1s (4'12") (fwhm = 0.07933)

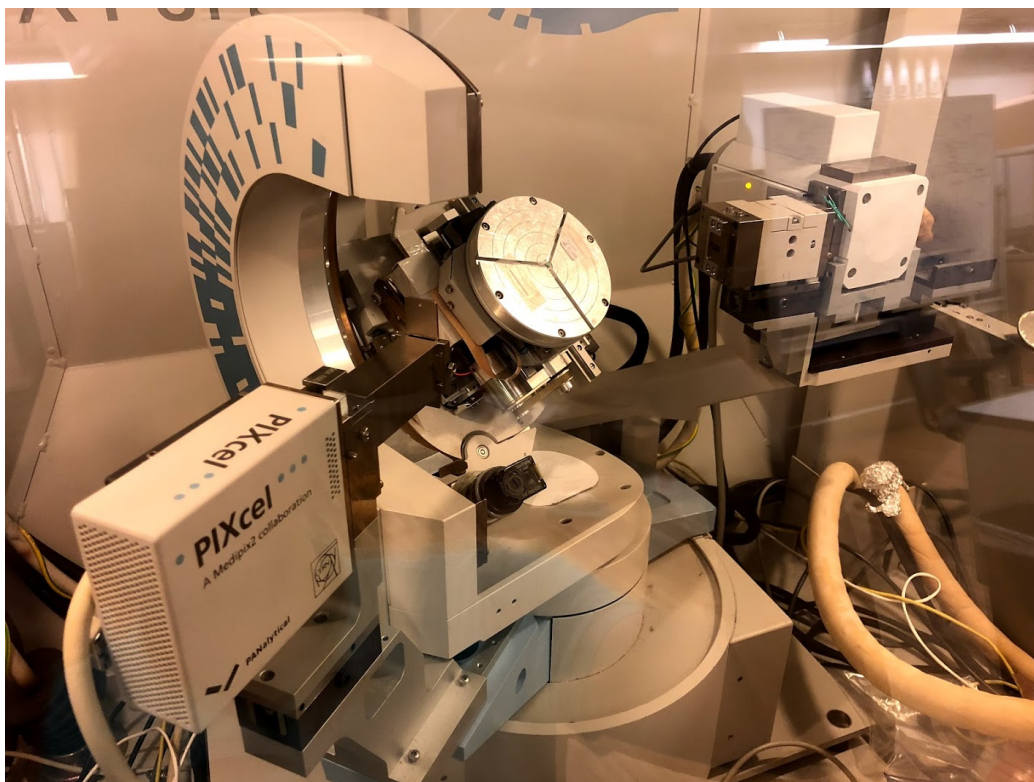


Figure A.1: PANalytical Phillips X'Pert XRD system. The stage is oriented to analyze the (102) plane of h-GaN.

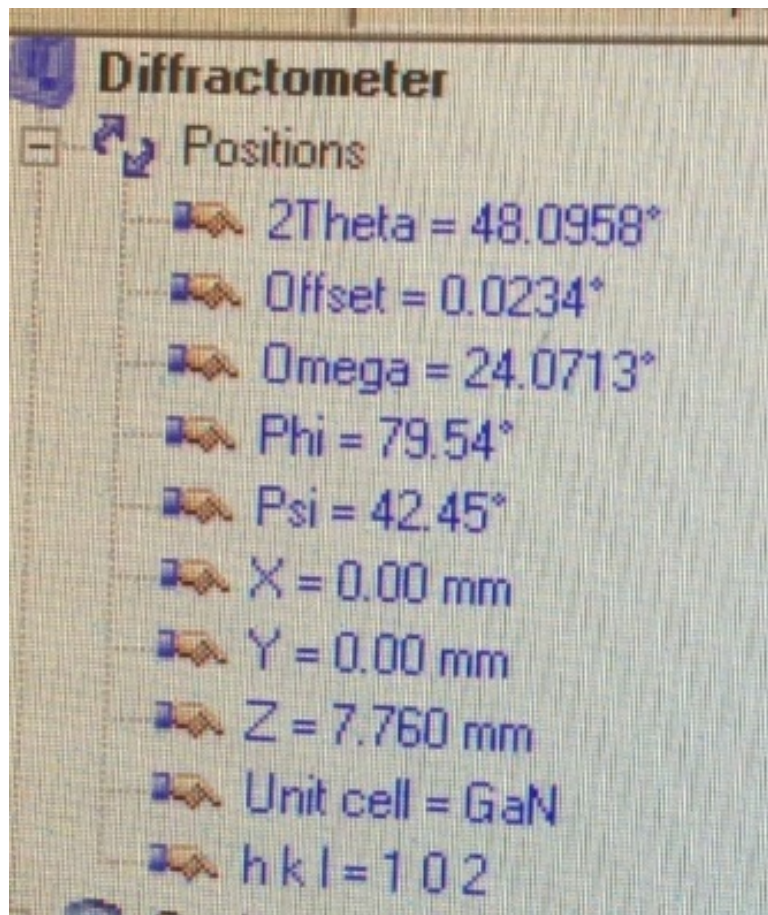


Figure A.2: Typical scanning setup for probing the (102) plane of h-GaN.

A.2 Reactive Ion Etching

Anisotropic dry etching of SiO₂ was completed using a PlasmaLab reactive ion etcher (RIE), as shown in Figure A.3. The RIE is connected to five gases: CHF₃, CF₄, SF₆, O₂, and Xe. CHF₃ was used for its high anisotropy and the vertical sidewalls. The RIE utilizes a 100 W power supply at a frequency of 13.56 MHz. The mass flow controller has a capacity of 200 sccm. For the etching, the following recipe is used:

Gas flow: 30 sccm

Chamber pressure: 35 mTorr

Power: 20

The etch rate was found to be 137 Å/min for thermally grown SiO₂. Thus, ≈37 minutes was needed to etch away 500 nm of thermal SiO₂. The operating procedure is as follows:

1. Close the cylinders, turn T-valve to point in the middle (both lines closed)
2. Turn key from manual to changed parameter
3. Press read + parameter key to read value
 - a. Set + Gas1 (needs multiple presses), punch in 30.0\% (press 3,0,0, 200MFCsccm*0.5ConversionF*30\%=30 sccm, which is 35 mTorr pressure CHF3), enter
 - b. Power = 20\% (for 93W)
 - c. Throttle = 35 sccm
 - d. Gas2 = 0 (no O2)
 - e. Read + timer (to see time setting), Set + timer (to change)
4. Turn key to manual, press manual + Gas1, pressure should read around 30 sccm, then drops (this opens the line for evac)
5. Close(manual + gas 1)
6. Press manual + vent (N2, vent, N2 vent)
7. Wait 30s after vent LED is solid, use joystick and button to raise chamber lid
8. Manual + vent to stop venting
9. Load sample, 4" uniformity is good according to Yaguang
10. Open gas valves (high, low, T)
11. Lower the lid and press "run"
 - a. Valve position will lower to zero

- b. Roughing starts
- c. If hissing is heard, press the power button immediately
- d. Roughing stops at around 9.6 minute mark (count down from 12)
- e. Wait 1 minutes, then HiVac LED will flash and then solid
- f. Throt will blink automatically to stabilize pressure
- g. Beep, reverse power (~80W), DC bias on, reverse power off, forward power (~90W) plasma on, timer starts
- h. 320 V DC bias, 93 W forward power
- 12. After process done, chamber should vent automatically
 - a. If not, press stop and then vent (button has poor contact)
- 13. Take sample out, close chamber lid and
- 14. Close cylinder valves, close T valve
- 15. Manual + rough (hissing sound good, beeping bad), 1 min till hi-vac
- 16. After hi vac stops flashing open gas 1
- 17. (manual + gas1, press many times until flashing)
- 18. Wait till pressure and flow are below 1
- 19. Close gas 1
- 20. Open t and cylinder bales for CF4
- 21. Turn the key to change parameter, Change flow rate of Gas1 back to 35% (for CF4)
- 22. Turn T-valve to CF4

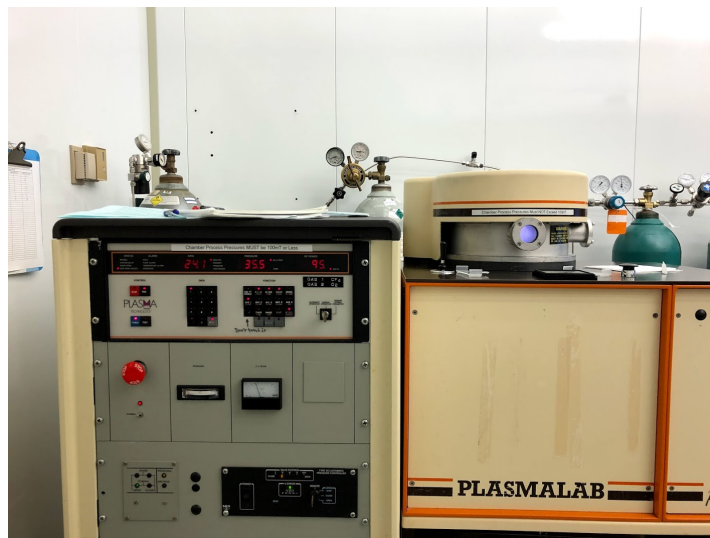


Figure A.3: PlasmaLab RIE running CHF_3 process.

A.3 Dynatex DX-III Scribe Breaker

The 4 inch wafers used for the fabrication of the nano-patterned silicon substrates were cleaved using a Dynatex DX-III scribe breaker system (Figure A.4). After Ni hardmask is deposited on the 4-inch silicon wafer, it is mounted on a low-adhesion semiconductor blue tape held in place by a pair of snap-in retention rings (Figure A.5). The assembly is then placed on the vacuum holder on the Dynatex (Figure A.6). Computer controlled scribing and anvil breaker enables very precise, repeatable, and accurate chip liftout (Figure A.7).



Figure A.4: Dynatex DX-III scribe breaker system.

Turn vacuum, N₂ valves on

Turn on DX-III, PC, monitors

Mount blue tape on extender/grip rings

Mount sample on tape by flipping and rub blue tape on. Avoid bubbles

1. PC/setup

a. Wafer diameter: 100 mm

b. Thickness: 500 μm

c. Geometry: circular

d. Mode: scribe and break

2. PC/scribe parameter
 - a. Method:
 - i. Continuous: cut across until scribe sees edge
 - ii. Edge: cut a pre-defined length
 - b. Scribe length: 1.5~5 mm
 - i. Force: 2920 cts
 - ii. Angle 32°
 - iii. Speed 6 mm/s
 - iv. Approach speed 960 $\mu\text{m/s}$
 - c. Impact bar height: 255 μm
3. PC/break parameter:
 - a. Anvil height: 0.944mm
 - b. Pressure: 176.5 kPa
 - c. Anvil gap: 0.652 μm
4. Exit, save
5. Mount sample on machine (maybe cut tape corner)
6. PC/interactive mode (Activates vacuum)
 - a. Use joystick to find flat, x and y jog for fine movement
 - b. Use theta knob to align flat to y axis movement
 - c. Press accept theta alignment
7. Press single scribe
 - a. First run is to find the correct scribe extension length for the correct force
 - b. Subsequent runs are actual scribes
 - c. Multiple scribes are repetitive scribes until stopped.
8. Press single break
 - a. First run will move sample to the left for impact bar height homing
 - b. Subsequent runs move the sample to the right under the anvil for impact

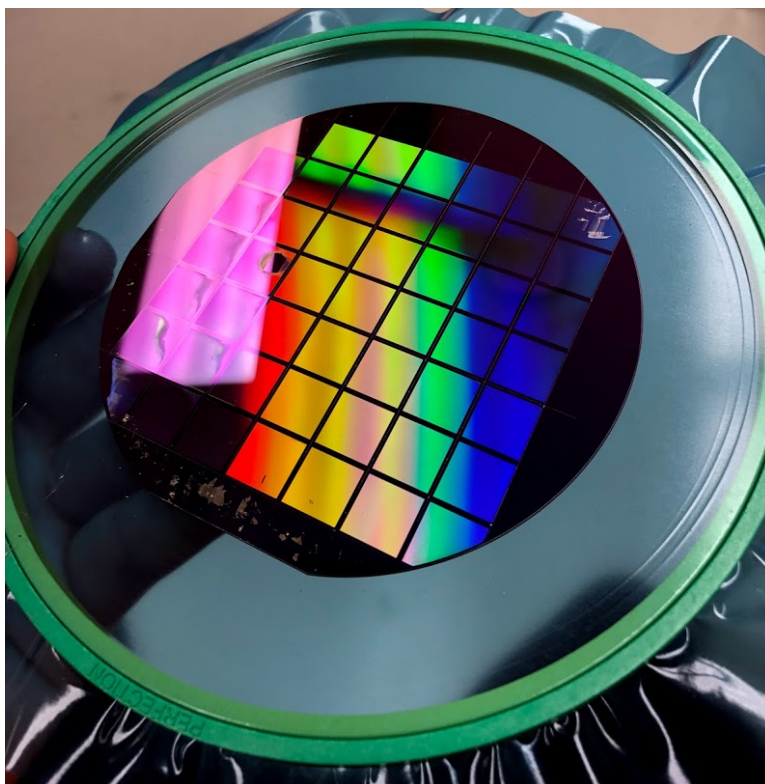


Figure A.5: 4 inch silicon wafer mounted on blue tape held in place by two retention rings.

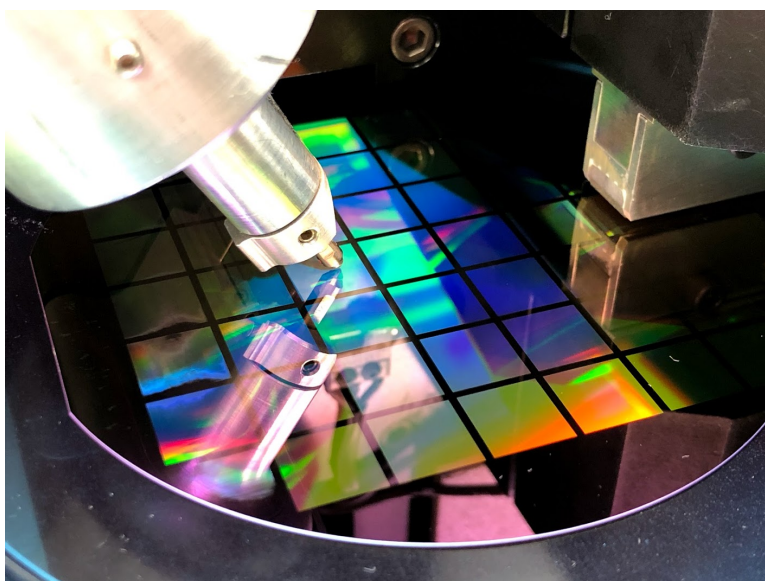


Figure A.6: Scribing in progress.

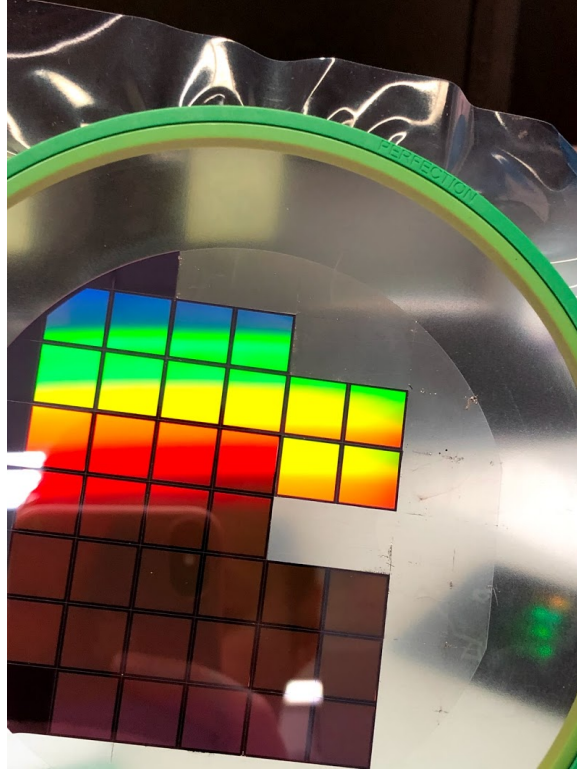


Figure A.7: After scribing and breaking, each individual piece can be lifted out with precision.

A.4 Scanning Electron Microscopy and Electron Backscatter Diffraction

The SEM images were taken on a JEOL 7000F field emission scanning electron microscope. The electron acceleration voltage used is 10 kV and the current is ~ 1 nA. The working distance is typically 6 – 10 mm. Cross-sectional images were taken with the sample clamped on a “mini-vice” sample mount. Electron backscatter diffraction is also performed on this instrument. Oxford Instruments’ EBSD detector is mounted on the back of the SEM. Phase detection and analysis are done via Oxford Instruments’ (formerly known as HKL technology) EBSD analytical software CHANNEL5. An image of the SEM is shown in Figure A.8. The EBSD detector is mounted on the back side of the SEM, as indicated by the red arrow.

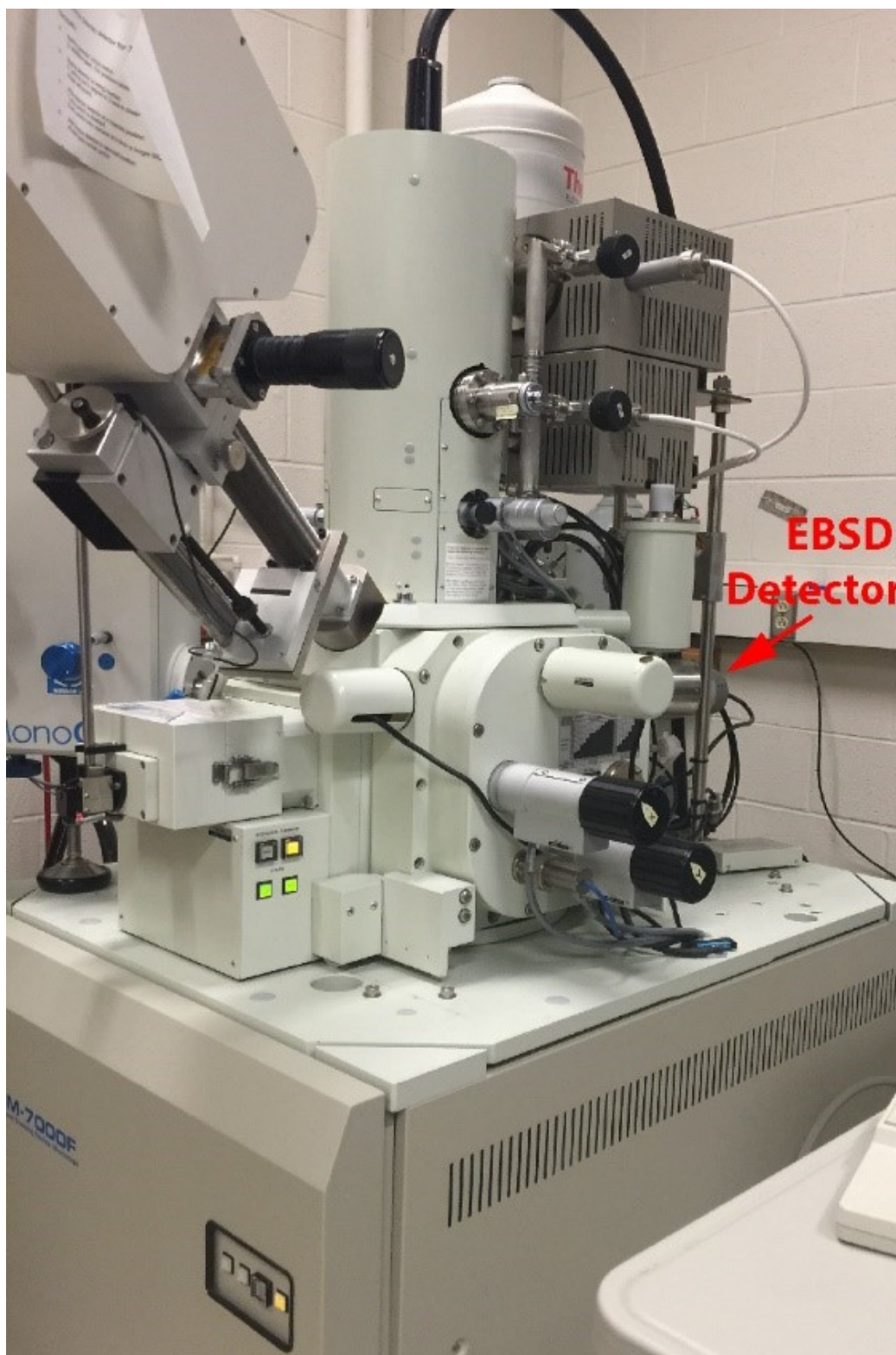


Figure A.8: JEOL 7000F SEM with EBSD detector mounted on the back.

A.5 Silicon Anisotropic Etching Recipe

The recipe to create U-groove nanopatterns on Si(100) substrates from as-deposited photoresist is shown in Table A.1.

Table A.1: U-groove nanopatterning fabrication steps

Step	Parameter	Equipment
1. Ni Deposition	40 nm	AJA Evaporator 4 or Lesker
2. CHF ₃ RIE	20% power, 30 sccm CHF ₃ flow, pressure 30 mTorr, 37 min	PlasmaLab RIE
3. O ₂ plasma	100W RIE, 300W ICP, 15 sccm flow, 10 mTorr, 10 min,	PlasmaTherm ICPRIE
4. Ni liftoff	5 min, ~80°C, manual agitation	AZ400T, hotplate setting at ~ 160 °C
5. BOE etch	10:1 BOE, 10 sec, room temperature	Acid hood, PMP beakers, do KOH after this step immediately (< 20 seconds)
6. KOH etch	45%, 50°C, 35 seconds, saturated with IPA	temperature-controlled hotplate, glassware, PMP tweezers

Potassium hydroxide (KOH) 45% solution was purchased from TranseneTM in a 1 gallon bottle. For the KOH solution, isopropyl alcohol (IPA) is added to the mix to reduce surface tension to allow H₂ bubbles to escape the sample freely. This prevents micromasking of the etching of Si underneath the bubbles. The temperature is then raised to 50 °C and maintained for the duration. The IPA in the KOH solution is kept at saturation. This will manifest as another layer of liquid on the surface of KOH (Figure A.9). Maintaining this layer will ensure the IPA in KOH is kept at saturation. Adding additional IPA during the process will decrease the temperature of the solution, and the etch rate will be affected. The solution must be left on the hotplate for additional time for the solution to reach equilibrium again. Samples can be either handheld by polymethylpentene (PMP) tweezers or in a polytetrafluoroethylene (PTFE), Teflon, dipper.

Thirty five seconds in 45% KOH at 50 °C corresponds to ≈78 nm of etch depth. This is verified using a SEM to look at the cross section of the grooves.

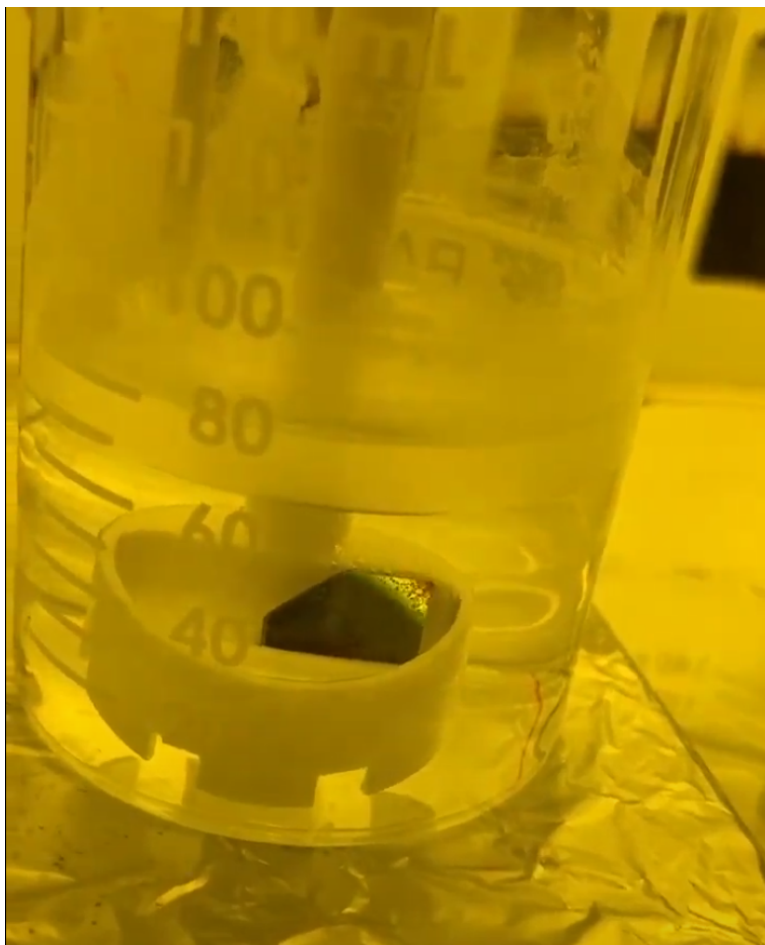


Figure A.9: KOH solution during etching. A layer of IPA is visible on the top. Formation of H_2 bubbles is visible on the sample, but the bubbles do not stick to the sample's surface due to the reduced surface tension by the addition of IPA in the KOH solution. A PTFE dipper was used for the handling of the sample.

A.6 KOH Etch Setup with Temperature Feedback Loop

Aqueous anisotropic KOH etching of Si(100) was completed in a fume hood using a Labnet AccuPlate (D0400) fitted with a Teflon-coated thermometer (D0462) for external temperature control via a feedback loop (Figure A.10). Since the KOH etch process is highly temperature-dependent, the temperature feedback loop is necessary to ensure a consistent environment for the etchant. The temperature used in this experiment varied between 50 and 60 °C. It generally takes about 15 minutes for 100 mL of KOH and isopropanol alcohol solution to reach steady state. Glass beakers and Teflon dippers and tweezers are used for sample handling.

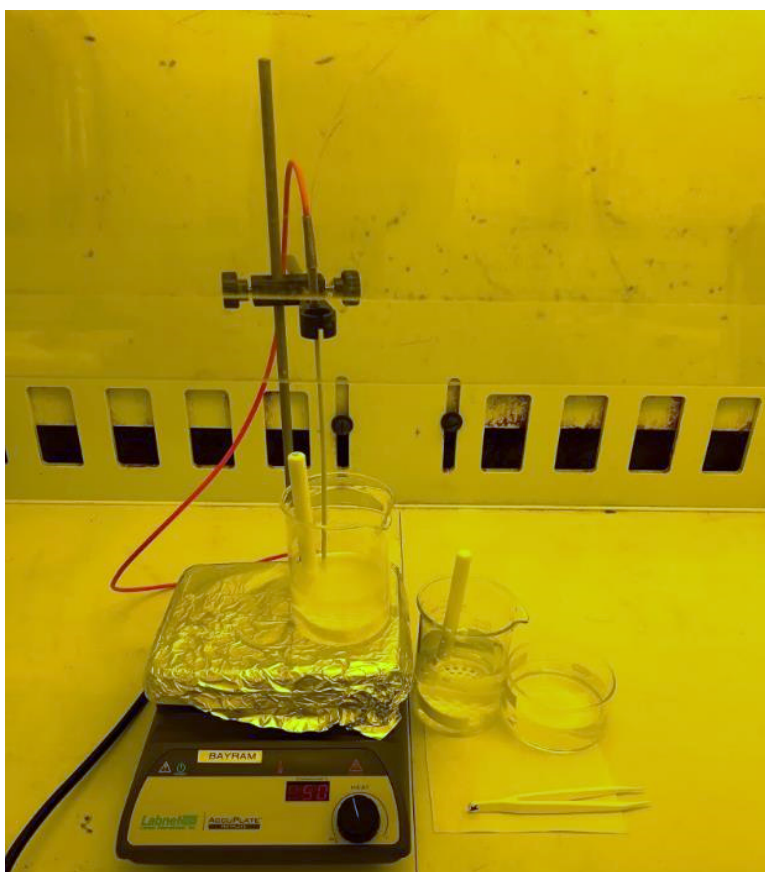


Figure A.10: KOH etching setup using a temperature feedback loop, a glass beaker with KOH, another glass beaker with DI water for quenching, a crystallizer for rinse, and PTFE dippers and PMP tweezers for sample handling.

A.7 Atomic Force Microscopy

The AFM study was conducted on an Asylum Cypher Atomic Force Microscope mounted on an optical table with continuous nitrogen flow supports. The tips used were BudgetSensors silicon AFM tips coated with aluminum (BS-Tap300Al). The system is capable of < 5 nm height resolution with a maximum lateral scan dimension of 30×30 μm and vertical maximum dimension of 5 μm .

A.8 Transmission Electron Microscopy

Transmission electron microscopy was conducted on a JEOL 2010 LaB6 TEM attached with Gatan MatScan 1k \times 1k CCD and a DigitalMicrograph computer control. The electron acceleration voltage is 200 kV, which yields a point resolution of 2.8 Å. A cross-sectional piece of the U-grooves is taken out and thinned to ~ 50 nm by a focused ion beam (FEI Helios). An image of the TEM with the U-groove sample mounted and its image projected on the phosphor screen is shown in Figure A.11.

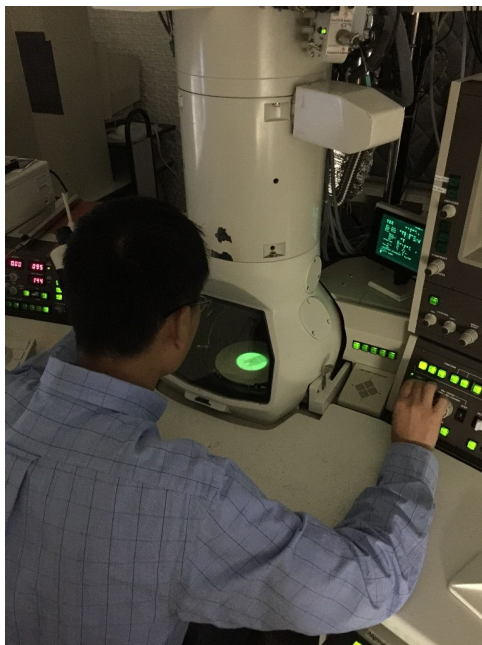


Figure A.11: JEOL 2010 TEM with an U-groove image showing on the phosphor screen.

A.9 Raman Spectroscopy

Raman spectroscopy was conducted on a Horiba LabRAM HR 3D confocal Raman imaging microscope with a 405 nm laser and a 100x, NA 0.95 objective lens (Figure A.12). The signal was collected using a 1800 g/mm grating blazed at 500 nm and a Horiba Synapse back-illuminated deep-depletion CCD camera.



Figure A.12: Horiba Raman Confocal Imaging Microscope (image taken from UIUC Beckman Institute's website at: itg.beckman.illinois.edu/)

A.10 Cathodoluminescence

Cathodoluminescence was conducted on the same JEOL 7000F field emissions scanning electron microscope fitted with a Gatan MonoCL3 system. Signal collection was achieved using an imaging CCD (sensitive in the 300-900 nm range) with a 1200 g/mm grating blazed at 500 nm and a paraboloid mirror inserted in the specimen chamber. A liquid helium flow stage with heating coil is fitted for cryo-CL studies that is capable of temperature control range of 5.65 – 300 K. The instrument with its specimen chamber opened is shown in Figure A.13. The brass-colored helium flow stage is seen being mounted in the specimen control stage. The spectrometer (Gatan MonoCL) with a CCD attached (brown) is mounted on the left of the SEM through a port opening for the insertion of the paraboloid mirror.

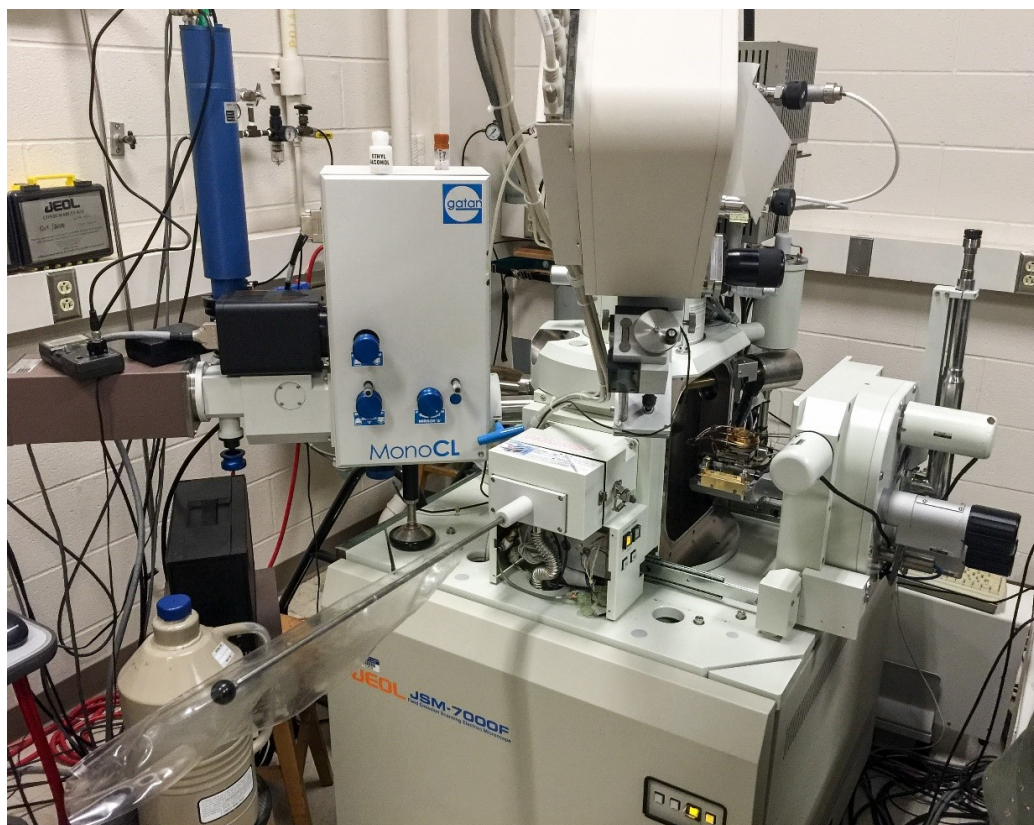


Figure A.13: JEOL 7000F with Gatan MonoCL3 and cryogenic stage being fitted in the specimen chamber.

A.11 Photoluminescence

Time-integrated photoluminescence and polarization-dependent PL were conducted using an unpolarized 266 nm continuous wave frequency-quadrupled Nd:YAG laser with an average output power of 10 mW with a UV-compatible wire grid polarizer fitting in front of a Princeton Instruments Acton SP-300i spectrometer using 1200l/mm grating blazed at 500 nm and a Princeton Instruments PIXIS high-performance CCD camera. The sample and luminescence collection optics are set up in a cardboard black box to isolate the CCD from stray light and potentially harmful scattered UV light. The PL setup outside and inside the black box is shown in Figures A.14 and A.15, respectively.

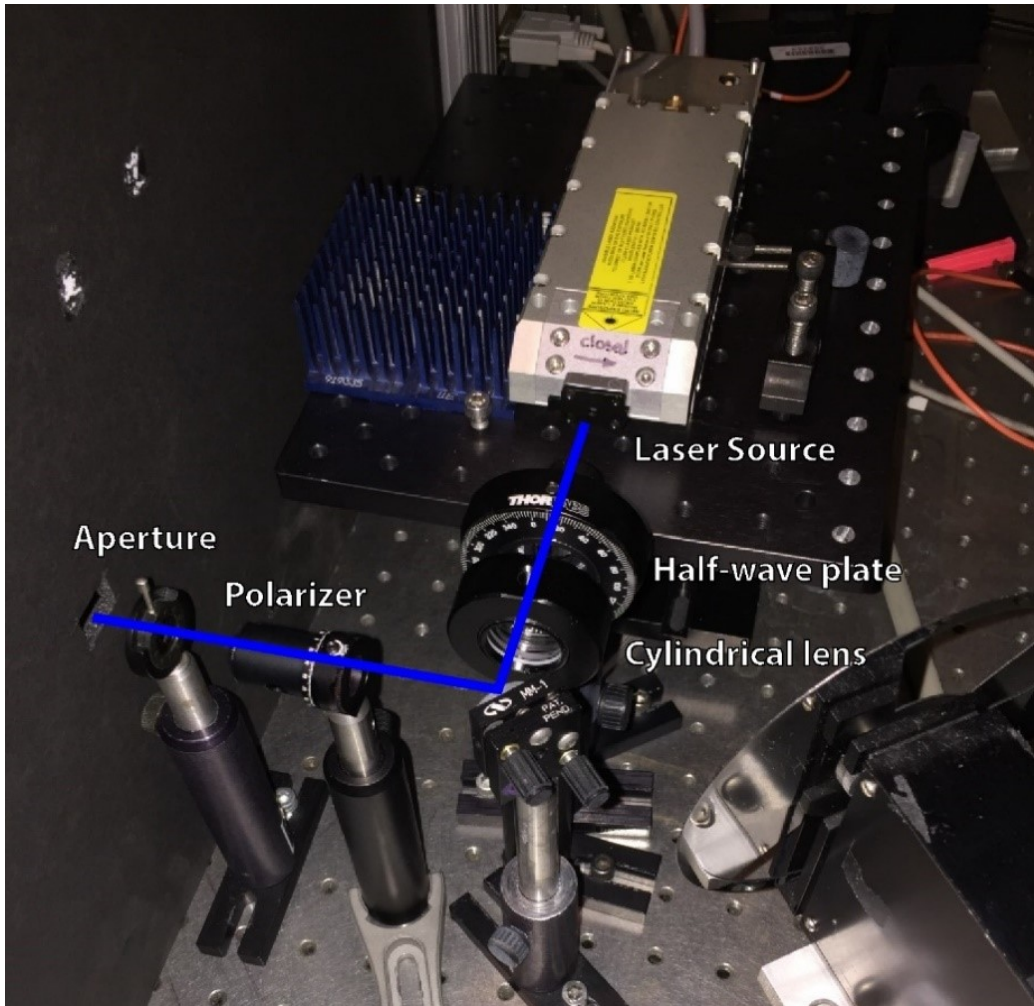


Figure A.14: PL setup outside the black box with 266 nm laser showing in blue.

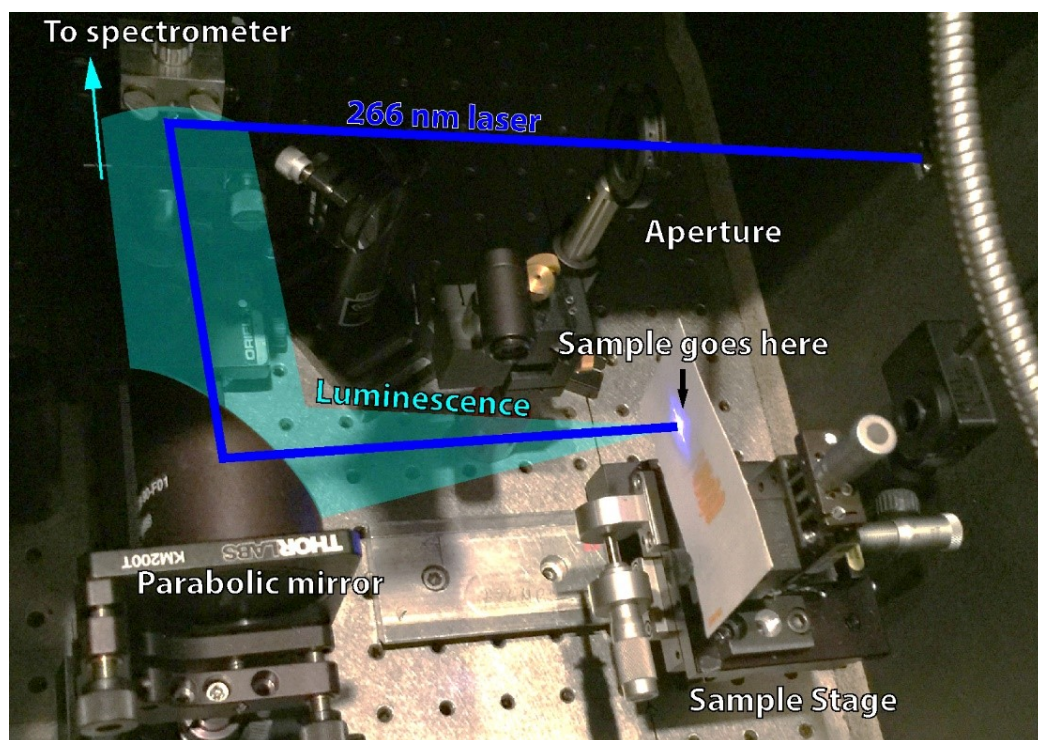


Figure A.15: PL setup inside the black box showing laser beam in blue and sample luminescence in turquoise.

A.12 Cryo-Photoluminescence

Temperature-dependent (1.4 K - 300 K) photoluminescence study was conducted on a custom-built benchtop setup with a helium bath cryostat with quartz windows (Figure A.16). The 266 nm laser from the regular PL setup, along with the optics for focusing and shaping the beam, were repurposed in the cryo-PL setup (Figure A.17). Another Princeton Instruments spectrometer fitted with gratings ranging from 150, 300, and 600 lines/mm and a silicon-based CCD camera. The temperature control was achieved using a PID temperature controller and thermometer.

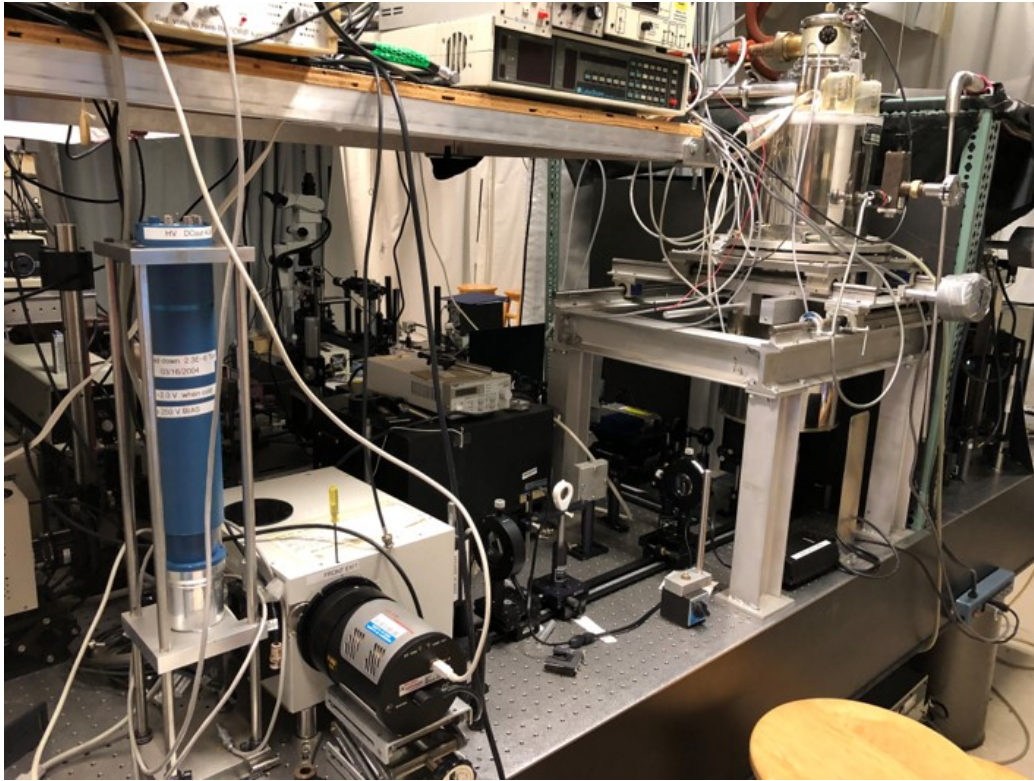


Figure A.16: PL setup inside the black box showing laser beam in blue and sample luminescence in turquoise.

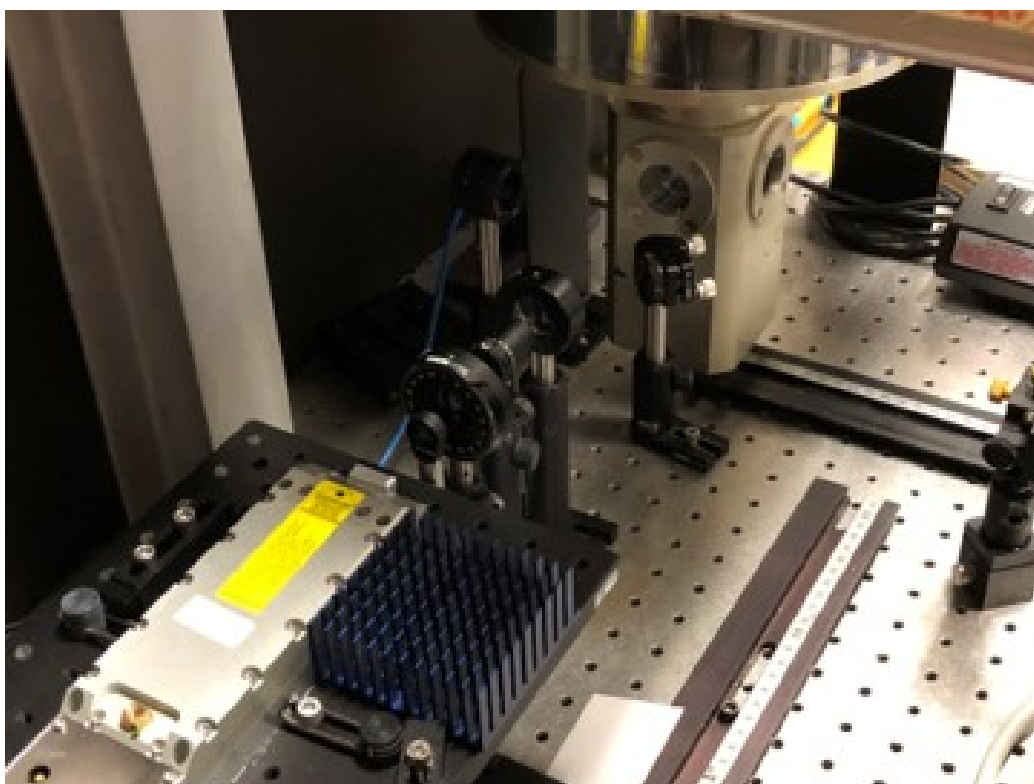


Figure A.17: PL setup inside the black box showing laser beam in blue and sample luminescence in turquoise.

A.13 Time-resolved Photoluminescence

Time-resolved photoluminescence study was conducted at the Center for Nanoscale Materials at Argonne National Laboratory using a frequency-tripled Tsunami Ti:sapphire pulsed laser with an average output power of ~ 5 mW with 100 fs pulses at 80 MHz. Signal was collected using a Hamamatsu streak camera system capable of < 1 ps resolution with a diffraction grating of 600 1/mm. Due to camera restrictions, no images of the facility were taken. A representative image of the TRPL setup taken from the website of Argonne National Laboratory is shown in Figure A.18. A raw data image is shown in Figure A.19.



Figure A.18: Ultra-fast time-resolved photoluminescence setup at Center for Nanoscale Materials (image taken from ANL's website at: anl.gov/cnm/group/terahertz-ultraviolet-ultrafast-spectroscopy).

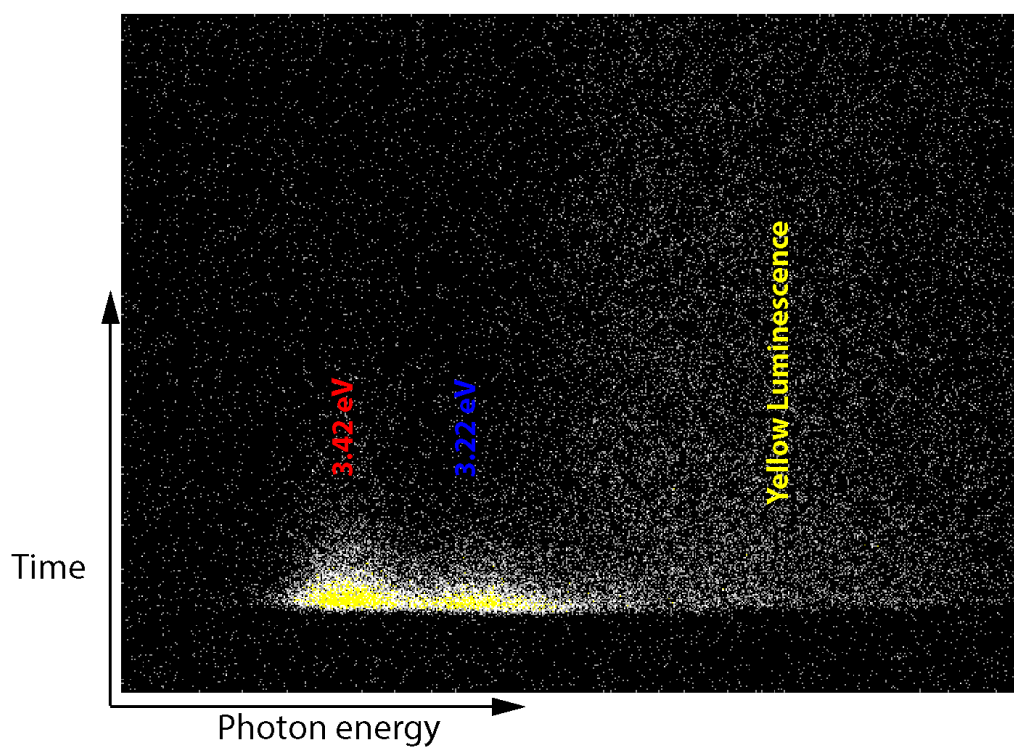


Figure A.19: Streak camera data image. The leftmost photon cluster corresponds to the h-GaN emission (marked by red 3.42 eV). The middle cluster corresponds to c-GaN emission (blue 3.22 eV). The broad and slow-decaying photon cluster on the right is the defect yellow luminescence.

APPENDIX B

COURSE LAB MODULES

B.1 Lab 1: NanoLab Walkthrough and Safety

Due: one week after your lab, email to Dicky Liu in PDF format (rliu37@illinois.edu)

INTRODUCTION:

Nanofabrication Laboratory (NanoLab), the cleanroom located at the middle of the ECE building, is the centerpiece of this university and the department of electrical engineering. It is built in a way that maximizes exposure to attract all kinds of attention from prospective student, visiting scientists, potential donors, state law makers, and plebs. Its yellow illumination and cleanroom bunny suits are the epitome of semiconductor engineering. More often than not, visitors cannot help but whip out their phones to take pictures of this magnificent and yet enigmatic space and its quantum-confined engineers. You are part of this club now.

ABSTRACT:

1. Write a few sentences about the purpose of this report and its content. What's special about cleanrooms? What safety precautions are outlined in this report? (10pts)

Read the handouts sent for this report and answer the following questions:

I. General Safety.pdf

2. Up to how many people should be allowed in the gown room? (4pts)
3. What's the rule regarding safety glasses, prescription glasses, and contact lenses? (4pts)
4. What items are forbidden in the cleanroom? (4pts)

5. What's the appropriate attire for entering the cleanroom? (4pts)
6. What are fume hoods? What equipment is required when using the fume hood? (4pts)
7. What special precaution must be taken when handling the heavy nitrile gloves? (4pts)
8. In an emergency, what must you dial from a campus phone to reach help? (4pts)
9. What's the address and the room number of the NanoLab? (4pts)

II. Regarding Hydrofluoric Acid (HF)

Even though we will not be dealing with HF directly, the acid is present in the lab, and we must know how to handle it safely as a precaution.

10. Although HF is a weak acid, it is potentially fatal if left untreated. Through what chemical reaction does HF cause hypocalcemia and hypomagnesemia? (5pts)
11. Briefly describe how we prevent accidental HF exposure? (5pts)
12. Briefly describe how we treat accidental HF exposure. (5pts)

III. Life Safety – Facilities.pptx

13. Using a computer software of your choice (Adobe Illustrator, MS Paint, etc.) draw and paste here a rough sketch of the layout of the NanoLab detailing the following: (8pts)
 - 4 exits to atrium and loading dock
 - 3 chemical eyewash and showers
 - 2 fire alarm pull stations
 - 3+2 fire extinguishers
14. What is a difference between normal gold and gold nanoparticles? (5pts)
15. What is the range of the sizes of nanomaterials (in nanometers)? (5pts)

16. What kind of personal protective equipment (PPE) can be used when handling nanomaterial (list 6)? (5pts)

IV. Nanomaterial Risk management.pptx

17. What is a difference between normal gold and gold nanoparticles? (5pts)
18. What is the range of the sizes of nanomaterials (in nanometers)? (5pts)
19. What kind of personal protective equipment (PPE) can be used when handling nanomaterial (list 6)? (5pts)

IV. NanoLab Safety Policies.pptx

20. How long are nanomaterials allowed to be stored in the lab? (5pts)
21. How to dispose of nanomaterial waste and nanomaterial contaminated waste? (5pts)
22. What is the required PPE (5) for entering the UIUC NanoLab? (5pts)
23. What is the additional piece of equipment required when handling **nanomaterials**? (5pts)
24. What is the additional piece of equipment required when working with **chemicals**? (5pts)
25. Make sure you've included a title for this report, your names, an abstract and the 4 sections.

Compile it into a PDF file and send it to Dicky. (10 pts) Aim for 2 pages.

Total: 115 points

B.2 Lab 2: Scanning Electron Microscopy

Due: one week after your lab 11:59 PM via email in PDF format to TA
Dicky (rliu37@illinois.edu)

ABSTRACT:

The versatility, ease of use, and non-destructive nature of Scanning Electron Microscopy (SEM) allows it to be one of the most useful tool in semiconductor, nanotechnology, biology, and comparative literature. The wave-particle duality nature of electrons allows us to image at a resolution many times greater than traditional optical microscopes.

1. After you finished lab write-up, write an abstract: (1) the purpose of this report, and its (2) theoretical calculations and (3) experimental contents. (10 pts)

I. Diffraction Limit

The diffraction limit is the theoretical limit of how small of a feature a microscope can resolve. The expression for the diffraction limit is given by:

$$d = \frac{\lambda}{2NA}$$

where d is the resolution, λ is the wavelength, NA is the numerical aperture.

1. (6 pts) Assume **NA as 1.4** calculate the diffraction limit of:
 - (a) Mid infrared (10 μm),
 - (b) blue (450 nm),
 - (c) mercury I-line (365 nm)
 - (d) low pressure Hg lamp (254 nm)
 - (e) Intel's crappy lithography, ArF laser (193 nm)
 - (f) TSMC extreme UV lithography (13.5 nm)

II. Scanning Electron Microscope

2. (4 pts) Look up and draw a schematic of a SEM, including:
 - (a) Electron gun
 - (b) 2 \times condenser lenses
 - (c) Objective lens
 - (d) Low res secondary electron detector

3. (10 pts) When the electron beam (primary electrons) hits the sample, it creates an interaction volume that gives off many different types of particles. Draw an interaction volume (hand drawn + insert as a picture works) and label the regions where the following particles are emitted, and briefly (1 sentence) explain what they are:
 - (a) Auger electrons
 - (b) Secondary electrons
 - (c) Back scattered electrons
 - (d) X-rays
 - (e) cathodoluminescence
4. (2 pts) In a SEM, we can accelerate electrons with a potential ranging from roughly 1–30 kV, resulting in electrons with 1–30 keV of kinetic energy. Calculate the range of wavelengths of electrons a SEM can generate (hint: de Broglie wavelength).
5. (1 pt) Calculate the theoretical diffraction limit of a SEM operating at 15 kV, assuming a NA of 0.6.
6. (2 pts) In reality, SEM can only resolve to ~1 nm due to other limitations. List two of them. Hint: you drew one.
7. (1 pt) What does the “scanning” part of SEM mean?
8. (2 pt) Describe what astigmatism is. What are the names of the knobs we turn to correct for this?

III. Image Analysis

You will use the FEI DB835 dual beam FIB/SEM in the Nanolab to take four images of the LED mesa sample.

- i Plane-view of an entire mesa (make sure each individual defect can be sufficiently distinguished).
- ii Plane-view of a defect on a mesa at high res.
- iii 30° tilted view of a mesa corner at low res.
- iv 30° tilted view of a defect on a mesa at high res.

- 9 (4 pts) Print the 4 images on a single sheet of paper, attach them to the end of your report. Label them i iv.
- 10 (2 pts) Using (ii), measure the approximate diameter of a volcano. Comment on the shape and make an educated guess on the type of crystal.
- 11 (2 pts) Using trig and (iii), estimate the height of the mesa.
- 12 (2 pts) Using trig and (iv), estimate the height of a volcano.
- 13 (3 pts) Count the number of defects in (i) and express it as a density in the unit of cm^{-2} .
- 14 (6 pts) Format. Aim for 1+1 pages.
- (a) Filename: "ECE443 lab3 firstname"
 - (b) PDF, Page number
 - (c) Title, name, date of submission, abstract

Congratulations. You can now put Scanning Electron Microscopy on your resume!

Total possible points: 60

B.3 Lab 3: Light Emitting Diodes 1

Due: one week after your hands-on lab at 11:59 PM via email in PDF format to sanatp2

Abstract

Light emitting diodes have transformed how much impact photonics has on our everyday lives. When you look up some dank memes on the internet, it's the LED backlight of your smart phones that illuminate the polarizer that displays information.

Write in a few sentences about (1) the purpose of this report and (2) its content. (10 pts)

I. The “White” LED

Concentrated in the middle of our eyes (fovea), we have three kinds of cone retinal cells: S-, M-, L-cones. While most primates are trichromats (blue green red), the majority of the animals are dichromats (blue and green). In the most fundamental biological sense, humans are only capable of sensing the three colors. Any mixed excitation of these channels results in a different perceived color. To produce a perceived yellow light, we don’t necessarily need to produce light at 570 nm, but a green plus red light with the appropriate intensity ratio will suffice (photons don’t add). “White” is the excitation of all three cones. The color temperature of the “white” refers to the blackbody radiation (heat-generated light) spectrum approximation of the light source.

The most common method is to use a blue (In_{0.1}Ga_{0.9}N/GaN) LED coated with some types of phosphor. The phosphor (rare element-based) down converts the blue photons into lower energy photons. While the LED’s emission is Gaussian distributed (in energy space), the phosphors’ emission is usually more convoluted.

In NanoLab, collect the following data. Adjust the integration time so the intensity of the highest peak is between 40K and 60 K:

- Use the macro lens to take a picture of the white part of the probe station screen to see individual subpixels.
 - Use the Avantes fiber spectrometer to acquire spectra of:
 - The Keithley probe station screen
 - Smartphone flashlight
- 1 Attach your macro image of the subpixels. Make sure to zoom in and crop so they are large enough to be seen. (5 pts)
 - 2 Plot the spectra of the screen and flashlight as **functions of energy (eV)** in a single plot using OriginPro. Make sure to include (i) axis titles, (ii) units, and (iii) the correct legend. A low-quality example is shown in Figure B.1. (20 pts)

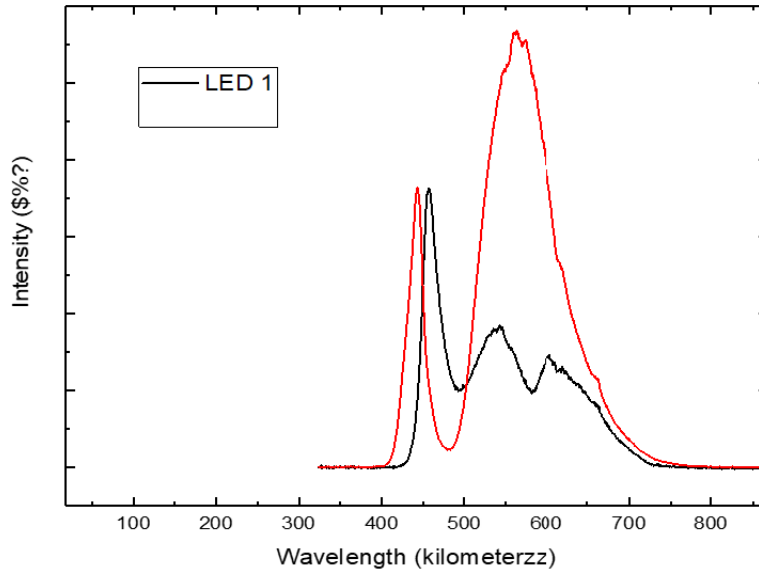


Figure B.1: A low quality sample plot of the two white LEDs measured in lab with several errors/mistakes incorporated.

- 3 Add arrows pointing to the peaks that are produced by semiconductors on the plot and text saying “InGaN”. (2 pts)
- 4 Add arrows pointing the peaks that are produced by phosphors and text saying “phosphor”. (3 pts)
- 5 Find the energies of these five peaks, and find the equivalent $\text{In}_x\text{Ga}_{1-x}\text{N}$ composition for these energies. Assume zero bowing factor and $E_{\text{gGaN}} = 3.4 \text{ eV}$, $E_{\text{gInN}} = 0.7 \text{ eV}$. Answer in a table (15 pts)

Peak	Peak Energy	InGaN equivalent
Monitor phosphor 1	2 eV	$\text{In}_{0.99}\text{Ga}_{0.01}\text{N}$

- 6 In the blue + yellow “white” LED, the InGaN LED is coated with yellow phosphor that’s made from Cerium doped yttrium aluminum garnet (Ce:YAG). Find what are the green and red phosphors used in the monitor (4 pts)

II. LEDs for Displays

- 7 List 3 disadvantages of producing white light for displays using the blue LED + phosphor approach. (6 pts)

- 8 Comment on what would the “white” spectrum look like from a phosphor-free RGB LEDs. How would they differ from the spectrum of the monitor you took for Q1? (5 pts)

Place an OLED light source under the microscope and take the spectrum using the spectrometer. Adjust integration time so intensity is between 40K – 60K.

- 9 Plot the OLED’s spectrum as functions of energy (eV) in another plot using OriginPro. See the same terms and conditions from Q2 (10 pts).
- 10 Find the approximate efficiencies of blue, green and red solid-state LEDs. Use department of energy + LED efficiency in your google search query is a good starting point. (6 pts)
- 11 What’s the biggest hurdle to use three solid-state LEDs (RGB) to produce white instead of using OLEDs? (2 pts)
- 12 Do a brief literature search and list 3 short comings of the OLEDs (vs solid state LEDs). (6pts)

Following their pending divorce, Apple is investing heavily on a technology called micro LEDs in order to reduce their reliance on Samsung’s production capacity. Thus, Apple Inc. is hiring aggressively in the LED field. What better place to look for an LED engineer other than UIUC?

- 13 State the approximate numbers (in orders of magnitude) of LED used in a display based on conventional LED backlight, mini LED, and micro LED. (3 pts)

III. MEASURING THE BLUE LED

- 14 Draw a simple cross-sectional diagram of the LED “mesa” you probed in the lab. Show where the p-type, intrinsic, and n-type materials would be located in the LED “island”. Also label the n- and p- contacts. (10 pts)

Make contact to a functional on-wafer LED. Do a voltage linear sweep from 0 – 9V.

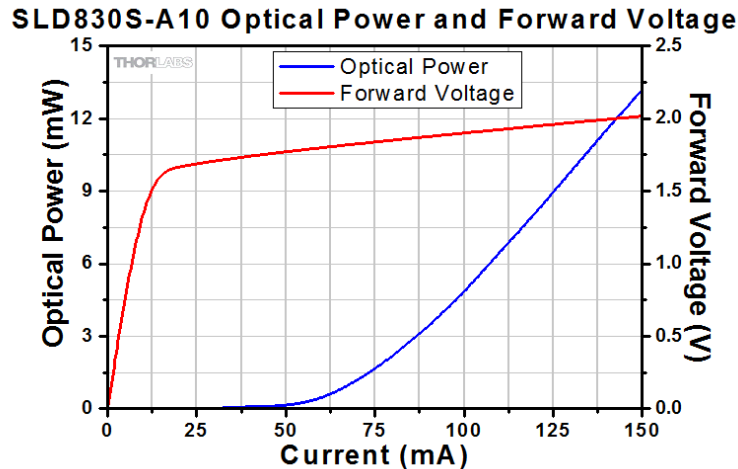


Figure B.2: Standard LIV plot for a LED.

Bias the current at 80 mA and optimize the light collection and integration time so the intensity reads between 40K - 60K. Save the spectrum. Without changing anything, measure the spectrum at 70, 60, 50, 40, 30, 20, 10 mA.

Use your cell phone and snap a picture of a glowing LED through the eye piece of the microscope.

- 15 Plot the spectra of the LED at the 8 different current levels using OriginPro. See the same terms and conditions from Q2 (10 pts).
- 16 Find the intensities of the highest peak at all current biases, and plot them against current. See the same terms and conditions from Q2 (10 pts).
- 17 Place your glowing image here. Zoom in and crop for an appropriate presentation. (5 pts)

In the industry, the specification of LED or laser diodes will usually include a L-I-V plot (Figure B.2).

We'll create one for our on-wafer LEDs.

- 18 Q18. Create a L-I-V plot, which is a "double Y plot". L is the intensity (use numbers from Q16), I is the current, V is the voltage. (30 pts)
 - (a) Use L (counts) as y1, I as x, and V as y2

- (b) Create a single legend that includes both curves
- (c) Color the curves differently
- (d) Include: 3 axis titles, units
- (e) Top line
- (f) Grid
- (g) Align the zeroes

- 19 Estimate the turn on voltage from your plot. (2 pts)
- 20 Calculate the peaks' approximate In-mole fraction in the $\text{In}_x\text{Ga}_{1-x}\text{N}$ layer. Using the same assumptions from Q5. (5pts)
- 21 Make sure you've included a title for this report, your names, an abstract (Q0) and the 2 sections. Compile it into a PDF file and email it to sanatp2. Name your files as: (5 pts)

2020ECE443_Firstname_Lastname_Fab3.pdf

Aim for 3 pages max. (4 pts)

Total points: 170

B.4 Fab 4: LED Temperature and Efficiency Droop

Abstract

Bandgaps of semiconductors are a function of temperature according to Varshni's equation:

$$E_g(T) = E_g(0) - \frac{\alpha T^2}{(T + \beta)} \quad (\text{B.1})$$

where α is Varshni's coefficient, β is the Debye temperature and $E_g(0)$ is the bandgap energy at absolute zero. This behavior dictates the design of LEDs, solar cells, and laser diodes. Say the word "Varshni" in any semiconductor courses at UIUC will impress the pants off your professors.

Write 2 sentences about the purpose of this report and its two components. (5 pts)

Collect the following data:

- 1 *Electroluminescence* – at 20, 30, 40, 50, 60, 70, 80, 85°C, do a voltage linear sweep 0 to 8 V, 0.1 V step and take a spectrum at 60 mA current bias on the on-wafer LED.
- 2 *Radiometry* – do a current linear sweep 0 – 100 mA and record the watt flux from a LED.

I. ELECTROLUMINESCENCE

- 1 Q1. Plot your IV curves of the LED at 20 °C to 85 °C in one figure. (10 pts)
- 2 Find the voltage required for 60 mA of current at 20 °C. (1 pts)
- 3 Find the reduction voltage (ΔV) required for 60 mA of current at the remaining temperatures compare to that of $T = 20\text{ °C}$, and make a plot of: (8 pts)
 - (a) x-axis: temperature
 - (b) y- axis: $\Delta V_{I=60\text{mA}}$
- 4 . Comment on the (i) direction and (ii) slope of this shift in voltage when temperature increases. (2 pts)
- 5 . Plot the spectra of the LED at 60 mA of forward current across the temperature range in a single plot: (4 pts)
 - (a) x-axis: Energy (eV)
 - (b) y- axis: intensity
- 6 . Sum the entire intensity column as “optical intensity”, normalize to that of 20 °C, and plot: (4 pts)
 - (a) X-axis: temperature (T)
 - (b) Y-axis: normalized optical intensity

II. RADIOMETRY

- 7 Using the integrating sphere’s data, plot the VI curve as: (3 pts)
 - (a) x-axis: current (I)

- (b) y- axis: voltage (V)
- 8 Using the integrating sphere's data, plot the LI curve as: (3 pts)
 - (a) x-axis: current (I)
 - (b) y- axis: optical power (L)
- 9 Combine the plots from Q6, Q7 into a LIV plot as: (2 pts)
 - (a) X-axis: current (I)
 - (b) Left y-axis: optical power (L)
 - (c) Right y-axis: voltage (V)
- 10 Plot: (3 pts)
 - (a) X-axis: current (I)
 - (b) Y-axis: optical power (L)
- 11 Calculate the input power ($P=IV$) and wall-plug-efficiency ($WPE = L/P$), and plot it as: (3 pts)
 - (a) X-axis: current (I)
 - (b) Y-axis: efficiency (WPE)
- 12 Combine your plots from Q10 and Q11 into: (2 pts)
 - (a) X-axis: current (I)
 - (b) Left y-axis: optical power (L)
 - (c) Right y-axis: WPE
- 13 The loss of efficiency at a given current level compared to the max WPE is called efficiency droop. Plot the efficiency droop as: (3 pts)
 - (a) X-axis: current (I)
 - (b) Y-axis: absolute value ΔWPE (ignore values before max was achieved.)
- 14 Include a title for this report, your names, date of submission, an abstract (Q0), page number. This time we'll do double column body. (use layout/breaks/section breaks/continuous). Send the PDF file to rliu37. Name your files as: (7 pts)

B.5 Fab 5: Solar Cells

Abstract Write 2 sentences about the purpose of this report and its content.
(4 pts)

I. IV CURVES

A solar cell is a p-i-n diode with engineered structure to produce a photovoltaic effect to produce electricity from solar irradiation. The solution to our imminent extinction – the solar cell, is also the reason why 80% of you took this course. For the experiment, we have two types of solar cells: RadioShack crystalline silicon (Si) and eBay thin-film Copper Indium Diselenide (CIS) solar cells.

Collect the following IV curves, for the lit condition, use the microscope's built-in LED.

A Single Si solar cell, dark and lit.

B Two Si solar cells in parallel and series, lit.

C Single CIS solar cell, dark and lit.

D Two CIS solar cells in parallel and series, lit.

E A Si and a CIS solar cell in parallel and series, lit.

- 1 Plot the IV curves of A and B in one plot, complete with legends, axis title, and units. Make sure the figure is enclosed by borders on all sides for all your graphs (see example to the right). (5 pts)
- 2 Extract the ISC and VOC for the three lit conditions from A and B. (6 values, 6 pts)
- 3 Write a one sentence observation on the ISC and VOC when two similar Si solar cells are arranged in series/parallel. Make sure to include numerical values. (2 pts)

- 4 Plot the IV curves of C and D in one plot. (5 pts)
- 5 Extract their ISC and VOC. (6 values, 6 pts)
- 6 Write a one sentence observation on the ISC and VOC when two similar CIS solar cells are arranged in series/parallel. (2 pts)
- 7 Plot the IV curves of A (lit only), C (lit only), and E in one plot. (4 pts)
- 8 Extract the ISC and VOC from E. (4 values, 2 pts)
- 9 Comment on which solar cell is limiting ISC when you connect Si and CIS cells in series (Si+CIS) and limiting VOC when in parallel (Si//CIS) (2 pts)
- 10 If you have access to unlimited number of solar cells, how would you increase ISC of Si+CIS to that of Si, and increase VOC of Si//CIS to that of CIS? Draw two circuit diagrams for your answers. (2 pts)
- 11 Calculate the power generated ($P = \text{Reverse } I \times V$) for single Si and single CIS (A). Find the maximum power (P_{max}) and its corresponding current (I_{max}) and voltage (V_{max}). (4 pts)
- 12 Calculate the fill factors (ff) for the single Si and single CIS solar cell using their ISC, VOC, I_{max} , V_{max} . (2 pts)
- 13 Plot in two graphs the reverse current vs voltage vs power (IVP) graph for lit single Si, single CIS: (2×5 pts)
 - (a) Left y: Reverse current
 - (b) Bottom x: voltage
 - (c) Right y: power
 - (d) add a colored rectangle with the vertices at (0,0) and (V_{max} , I_{max})

I am looking for something similar to Figure B.3:

- 16 Tabulate the ISC and VOC values from all lit conditions (additional 24 values) in a table like Figure B.4: (15 pts)

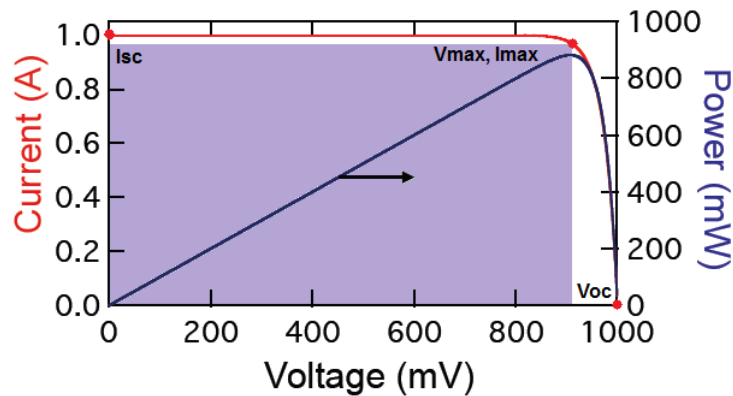


Figure B.3: Sample solar cell fill factor/ power plot.

Sample Config.	I_{sc} (mA)	V_{oc} (V)	I_{max} (mA)	V_{max} (mA)	P_{max} (mW)	ff (%)
Si						
Si + Si						
Si // Si						
CIS	Green =					
CIS + CIS	extract from					
CIS // CIS	previous Qs					
Si + CIS						
Si // CIS						

Figure B.4: Summary of solar cell parameters.

17 Format: filename, PDF, page number, title, name, date, abstract, single column title, double column body (9 + 4 pts)

Total points: 80

B.6 Fab 6: Design of Experiment: Temperature Dependence of Solar Cells

Abstract

(finish this last) Write three sentences about the purpose and approach of this report, the type/range of data collected, and its findings. (6 pts)

For the silicon solar cell, collect the IV curve at 20, 40, 60, 80, 100°C under dark and lit condition.

I. INTRODUCTION.

In two paragraphs, explain:

- 1 Motivation: why do we care about solar cells, its temperature dependence, and the potential impact of this knowledge. (5 pts)
- 2 Hypothesis: how does temperature affect bandgap? How does the altered bandgap change the lower absorption threshold? How should this affect the parameters of the silicon solar cell? You can include equations/diagrams if they help. (5 pts)

II. EXPERIMENTAL PROCEDURE.

- 3 In one paragraph, describe: how do you go about setting the experiment up? How are the solar cells connected? How do you vary the temperature? How do you account for ambient light? What kind of light source should you use? (10 pts)
- 4 Draw a diagram to convey your setup. (5 pts)

III. DATA/ANALYSIS:

Produce the following Plot the following complete with legends, axis title, units, borders.

- 5 Dark IV curves for all temperatures in one graph. (5 pts)
- 6 Describe what happens to their voltages required for 80 mA (V_{80mA}), and its temperature dependence ($\Delta V_{80mA} / ^\circ C$). (3 pts)
- 7 A double Y-plot with (5 pts):
 - (a) Left Y: Lit reverse current for all temperatures
 - (b) Right Y: Power generated
 - (c) Bottom X: Voltage
- 8 Extract ISC, VOC, I_{max}, V_{max} from Q4, and create a double Y plot using (7 pts):
 - (a) Left Y: Current (ISC, I_{max})
 - (b) Right Y: Voltage (VOC, V_{max})

(c) Bottom X: Temperature

- 9 Describe what happens to ISC and I_{max} when the temperature increases. Add their slopes (mA/°C) to your plot in Q6. (4 pts)
- 10 Describe what happens to VOC and V_{max} when the temperature increases. Add their slopes (mV/°C) to your plot in Q6. (4 pts)
- 11 Plot the fill factor (ff) with respect to temperature. (3 pts)
- 12 Describe what happens to ff when the temperature increases. Add its slope (°C⁻¹) to your plot in Q13. (2 pts)
- 13 Plot the normalized (to their respective 20°C values) V_{80mA}, ISC, VOC, P_{max}, I_{max}, V_{max}, ff values with respect to temperature. (10 pts)
- 14 Find their dependence on temperature (slope) in the form of %/°C, and tabulate them as below (7 pts):

Parameter	Temp-dependence (% / °C)
V _{80 mA}	
ISC	
VOC	
P _{max}	
I _{max}	
V _{max}	
<i>ff</i>	

- 15 Write a one paragraph conclusion about the thermal dependence of the parameters of silicon solar cell. (10 pts)
- 16 Format: filename, PDF, page number, title, name, date, abstract, single column title, name, date, abstract double column body. Aim for < 4 pages. (9 + 6 pts)
- 17 Give your report a journal-esque header. (+2 points)

Total points: 100 + 2